



**HAL**  
open science

# Integration of epitaxial piezoelectric thin films on silicon

Shi Yin

► **To cite this version:**

Shi Yin. Integration of epitaxial piezoelectric thin films on silicon. Other. Ecole Centrale de Lyon, 2013. English. NNT: 2013ECDL0039 . tel-01139336

**HAL Id: tel-01139336**

**<https://theses.hal.science/tel-01139336>**

Submitted on 4 Apr 2015

**HAL** is a multi-disciplinary open access archive for the deposit and dissemination of scientific research documents, whether they are published or not. The documents may come from teaching and research institutions in France or abroad, or from public or private research centers.

L'archive ouverte pluridisciplinaire **HAL**, est destinée au dépôt et à la diffusion de documents scientifiques de niveau recherche, publiés ou non, émanant des établissements d'enseignement et de recherche français ou étrangers, des laboratoires publics ou privés.

**ÉCOLE CENTRALE DE LYON**

# **THÈSE**

Présentée publiquement en vue de l'obtention du grade de

**DOCTEUR DE L'ÉCOLE CENTRALE DE LYON**

École doctorale : Matériaux

Spécialité : Dispositifs de l'Électronique Intégrée

par

**Shi YIN**

---

## **Integration of epitaxial piezoelectric thin films on silicon**

---

*Thèse préparée à l'INL - Ecole Centrale de Lyon  
sous la direction d'Yves ROBACH*

Soutenance le 27/11/2013 devant la commission d'examen composée par

M. Gilles POUILLAIN	Professeur, CRISMAT, Caen	Rapporteur
Mme Laurence MECHIN	Chargée de recherches, GREYC, Caen	Rapporteur
M. Lucian PINTILIE	Chercheur, NIMP, Bucharest	Examineur
Mme Pascale ROY	Directeur de recherches, Synchrotron Soleil, Saclay	Examineur
M. Jérôme WOLFMAN	Chargé de recherches, LEMA, Tours	Examineur
M. Gwenaël LE RHUN	Chercheur, CEA-LETI, Grenoble	Co-encadrant
M. Bertrand VILQUIN	Maître de conférence, ECL-INL, Ecully	Co-encadrant
M. Yves ROBACH	Professeur, ECL-INL, Ecully	Directeur de thèse

---

---

## ACKNOWLEDGEMENT

---

---

First and foremost I would like to offer my sincerest gratitude to my thesis director Prof. Yves Robach. He is not only a knowledgeable and experienced professor with extensive information in scientific researches and communities but also a patient and responsible teacher who has supported me throughout all my thesis with his time, enthusiasm, and funding to make my research productive and stimulating. He kindly helped and encouraged me for my thesis writing which became the hardest period in my PhD study. I could not imagine that I can complete the researches and obtain my PhD degree smoothly without his instructions. The work experience with him will definitely turn to my precious and indispensable treasure during my future life and career.

This PhD research was initialized by the collaboration of l'Institut des Nanotechnologies de Lyon (INL) in l'Ecole Centrale de Lyon (ECL) and Laboratoire d'électronique des technologies de l'information (LETI) in Commissariat à l'énergie atomique et aux énergies alternatives (CEA) under the project ANR « MOCA 2010-NANO-020 » and « MINOS ANR-07-BLAN-0312 ». Here, I would like to express my best appreciation to my supervisors Prof. Bertrand Vilquin and Dr. Gwenaël Le Rhun for their instructions and advices on my researches. At INL, I worked with Prof. Bertrand Vilquin during the first one and half years. His joyful smile always resounded in the coffee room which relieved our working pressure using his interesting conversations after lunch. His large academic network definitely provided an exclusive and convenient condition for me to reach the scientific communities and access the advanced facilities. Moreover, he is very helpful in my daily life as I live in a foreign country with a different culture from that of China. Dr. Gwenaël Le Rhun is employed in LETI as a senior researcher in the domain of micro-actuator components. He is the first interviewer who enrolled me into this PhD project. As I remember the first interview for my PhD enrollment, he deeply impressed me his exhaustive, serious and meticulous attitude in scientific research and project management. Different from academics, he is an experienced expert and technician in MEMS manufacture who brought me into the world of semiconductor industry.

Beside, I'd like to address my great gratitude to the group members at INL who support my PhD researches from either scientific or technical aspects. Saint-Girons Guillaume often inspired me with his useful knowledge, novel ideas, and great passion during scientific discussions. His view always directed me in the research. Gendry Michel is the director of our laboratory team "hétéroépitaxie et nanostructures" who also contributed his knowledge and opinion without

reservation in the discussion. I wish to thank him for the management of all the projects in our group. Regreny Philippe was our research engineer on the ground floor who offered his advices and opinion on the problem of our equipment and facilities. I also would like to thank Benamrouche Aziz for his helpful assistance in Atomic Force Microscopy (AFM). I still remember my first training on AFM by him and he paid his great patience in step-by-step introduction of the manipulation. Botella Claude was responsible for all the electronics and mechanics in our laboratory and was the master of RHEED, XPS. Without his help, automation of the equipment is impossible. Goure Jean-Baptiste was an experienced technician who was mainly in charge of our equipment, including the core component - Molecular Beam Epitaxy (RIII). Ultrahigh vacuum and stable high-temperature effusion cell were definitely attributed to his hard work during the daily maintenance. I also thank Bachelet Romain for the SrTiO<sub>3</sub>/Si templates which he prepared during my stay in Grenoble. Besides, my PhD research closely concerned the cleanroom technologies which were supported by a group team of technicians at INL. Here, I would like to thank Mazurczyk Radoslaw and Cremillieu Pierre for their kind help in the manipulation of the cleanroom facilities and the chemicals. Lopez Raphaël and Devif Brice are our computer experts in cyber security and software management and thank them for their jobs to provide a safe and tranquil condition in the use of computer and internet. Besides, I also would like to thank José Penuelas (the expert of XRD and TEM) and Nicolas Blanchard (the expert of XPS). In addition, I would thank the senior Chinese doctor Gang Niu who did a lot of pioneer work on the epitaxy of STO on Si. During the first year, he carefully introduced me how to manipulate RIII nearly hand by hand since it was really a monster to me when I first saw the big machine. He also contributed his time, patience and experience without any reservation to help me not only in scientific discussion but also during the daily life. In addition, I would like to thank the other group members at INL together: Khlid (PhD student in nanowire), Jun (Chinese PhD student majored in V-III semiconductor), Sylvain (He worked in INSA for the most of the time), Azza (Our Tunisian PhD student majored in V-III semiconductor), Qiang Liu (new PhD student majored in ferroelectric film), Nasser, Lamis, Lucie. At INSA, I would like to thank Gautier Brice for his kind and helpful lectures on the operation of PFM, Albertini David for his kind help in PFM characterization, Borowiak Alexis (PhD student in PFM), Waël Hourani (PhD student at INSA). At last, I would express my gratitude to our kindly secretaries: Martin Thérèse, Goncalves Sylvie, Dufaut Patricia.

When I worked in the group at LETI during the second one and half years, my PhD research was also supported by numerous helpful assistances from all the group members in the laboratory of LCMA (Laboratoire de Composant Micro-Actuateur). First, I would like to thank Emmanuel Defay for his intellectual knowledge, ideas, and instruction. Although he was not my official thesis supervisor, he always tracked my research process and contributed his minds and

intelligence during the discussion. Moreover, he behaved like a spiritual leader for me to follow not only in the scientific research but also in the daily life. Another person I should appreciate in our group is Julie Abergel who is a very nice and warm-hearted girl. She always has a big group of friends around her sharing the happiness, travel experience, and party beer. She helps me a lot in the researches, like coordination with the cleanroom technicians and discussion on the equipment operation. Besides, she also introduced me to her friends and social activities in France to allow me participate in French culture instead of staying alone. Recently, she and her boyfriend Matthieu Cueff, another LCMA guy, got a new born baby and I wish that they could enjoy this happiest moment. I also wish to express my best gratitude to other group members in LCMA: Thibault Ricart who helped me on the finite element method and the usage of the software Comsol, Marjolin who helped me for the cleanroom technologies, Bruno (senior engineer at LCMA), and so on.

In addition, I gratefully thank our sincere collaborators during my PhD research. Prof. Pascale Roy kindly provided the beam time at Soleil for the experiment of infrared transmission. She also helpfully introduced the facilities and the physical principle during my stay at Soleil. The discussion with her greatly contributes to the explanation of the experimental result. I would also thank Prof. Lucian Pintilie for his kind invitation that I could visit NIMP institute in Bucharest and travel in the fantastic country near the Black Sea. Without the SrRuO<sub>3</sub> bottom electrode he helps to deposit, our PZT films just on doped Si substrate cannot be measured as ferroelectric properties. At NIMP, I would like to thank Cristina Dragoi for her help on PLD deposition of SrRuO<sub>3</sub> film, Lucian Trupina for his help on PFM measurement, Aurelian Catalin Galca and Ioana Pintilie for their invitation of the travel in Romania. And I like to thank the other people who contributed in the project of MOCA: Sylvain Ballandras and Sébastien Alzuega (FEMTO-ST), Prof. Brahim Dkhil (Ecole Centrale de Paris), Emilien Bouyssou (ST-Tour). Moreover, I would like to offer my great appreciation to the professors who kindly accepted my invitation as the members of the defense committee. They are Prof. Gilles Poullain from CRISMAT laboratory (UMR CNRS 6508) in Caen, Prof. Laurence Mechin from GREYC laboratory (UMR CNRS 6072) in Caen, Prof. Jérôme Wolfman from GREMAN laboratory (UMR CNRS 7347) in Tours, and also Prof. Pascale Roy, Prof. Lucian Pintilie.

I cannot forget my happiest foreign experience in France with my Chinese PhD colleges during these years. They are Taiping Zhang, Xianqin Meng, Zhugen Yang, Sui Ning, Nanhao Zhu, Boyang Gao, Tianli Huang, Jingwei Miao, Gang Niu, Tao Xu, Yun Zhou, Ningning Liu, He Ding, Huanhuan Liu, Xuchen Liu, Zhen Li, Fengyuan Sun ...

At last, I wish to express my great thankfulness to my parents. Without their solid support, I could not continue my study to the doctoral degree and complete my PhD thesis this year. All my

achievement until now should be contributed to their long-lasting and selfless love. And I also like to thank my girlfriend Chun Hao that she gave me the support and courage while sharing the happy moment together. Finally, I would like to express my most heartfelt gratitude to all the people in my life who have supported and helped me until now. And I will continue being your dutiful friend in all the rest life.

---

---

## Content of the thesis

---

---

<b>General Introduction .....</b>	<b>1</b>
<b>Chapter I - Physical principles and motivations .....</b>	<b>5</b>
<b>I.1) Piezoelectric MEMS overview .....</b>	<b>6</b>
<b>I.2) Piezoelectricity and ferroelectricity .....</b>	<b>10</b>
I.2.1) Piezoelectricity .....	10
I.2.2) Ferroelectricity .....	13
I.2.3) Piezoelectric and ferroelectric materials .....	15
I.2.3.1) Wurtzite structure .....	15
I.2.3.2) Perovskite structure .....	17
I.2.3.3) Summary .....	19
<b>I.3) Physical principle of piezoelectric MEMS .....</b>	<b>19</b>
I.3.1) Operation modes and figures of merit .....	20
I.3.2) Influence of ferroelectric thin films .....	21
I.3.2.1) Effect of film orientation .....	21
I.3.2.2) Effect of residual stress .....	23
<b>I.4) Single crystal piezoelectric films on Si: state of the art .....</b>	<b>25</b>
I.4.1) Epitaxial PZT films .....	25
I.4.2) Epitaxial PMN-PT films .....	28
I.4.3) Summary .....	29
<b>I.5) Objectives of the thesis .....</b>	<b>30</b>
<b>I.6) Reference .....</b>	<b>31</b>
<b>Chapter II - Epitaxial growth and characterization technologies .....</b>	<b>45</b>
<b>II.1) Introduction .....</b>	<b>46</b>
<b>II.2) Deposition technologies for epitaxial growth .....</b>	<b>46</b>
II.2.1) General features of epitaxial growth .....	46
II.2.2) Molecular Beam Epitaxy .....	49
II.2.3) Pulsed Laser Deposition .....	53
II.2.4) Sol-gel deposition .....	55
<b>II.3) Characterizations techniques .....</b>	<b>57</b>

II.3.1) X-Ray Diffraction .....	57
II.3.2) Transmission Electron Microscopy .....	62
II.3.3) Electrical measurement .....	63
II.3.3.1) Impedance meter .....	63
II.3.3.2) Polarization hysteresis loop .....	68
II.3.4) Piezoresponse Force Microscopy .....	69
II.3.5) Mechanical characterization .....	71
<b>II.4) Reference .....</b>	<b>72</b>
<b>Chapter III - Integration of epitaxial PZT thin film on Si substrate .....</b>	<b>77</b>
<hr/>	
<b>III.1)Introduction .....</b>	<b>78</b>
<b>III.2)Evaluation of SrTiO<sub>3</sub> film on Si(001) for the use of buffer layer .....</b>	<b>78</b>
III.2.1)Experimental details .....	78
III.2.1.1) Chemical treatment of Si(001) substrate .....	78
III.2.1.2) Passivation of Si(001) surface using Sr .....	80
III.2.1.3) Two-step growth method .....	81
III.2.2)Crystalline structure and surface topography of epitaxial SrTiO <sub>3</sub> film .....	83
III.2.3)Conclusion .....	84
<b>III.3)Sol-gel deposition of PZT film on SrTiO<sub>3</sub>/Si(001) .....</b>	<b>85</b>
III.3.1)Sol-gel deposition of PZT film .....	85
III.3.2)Influence of annealing temperature .....	86
III.3.2.1) Crystalline structure .....	87
III.3.2.2) Surface topography .....	90
III.3.2.3) Electrical characterization .....	90
III.3.3)Microscopic structure of PZT/SrTiO <sub>3</sub> /Si(001) stack .....	92
III.3.4)Chemical profile of PZT/SrTiO <sub>3</sub> /Si(001) stack .....	94
III.3.5)Conclusion .....	97
<b>III.4)Use of SrRuO<sub>3</sub> bottom electrode for integration of PZT on Si .....</b>	<b>97</b>
III.4.1)Introduction .....	97
III.4.2)Pulsed laser deposition of SrRuO <sub>3</sub> film on SrTiO <sub>3</sub> /Si(001) .....	99
III.4.3)Sol-gel deposition of PZT film on SrRuO <sub>3</sub> /SrTiO <sub>3</sub> /Si(001) .....	101
III.4.3.1) Crystalline structure .....	102
III.4.3.2) Microscopic structure .....	104
III.4.3.3) Electrical characterizations .....	107
III.4.3.4) Microscopic piezoelectric properties .....	112
<b>III.5)Conclusion .....</b>	<b>114</b>

III.6) Reference .....	115
------------------------	-----

**Chapter IV - Integration of epitaxial PMN-PT films on Si substrate ..... 125**

---

<b>IV.1) Introduction .....</b>	<b>126</b>
IV.1.1) Relaxor ferroelectrics .....	126
IV.1.2) PMN-PT solid solution .....	127
<b>IV.2) Sol-gel deposition of PMN-PT film on SrTiO<sub>3</sub>/Si(001) .....</b>	<b>130</b>
IV.2.1) Introduction .....	130
IV.2.2) Sol-gel deposition of PMN-PT films .....	131
IV.2.3) Crystalline structure and surface topography .....	132
IV.2.4) Microstructure of epitaxial PMN-PT film .....	134
IV.2.5) Phase transition studied by infrared transmission .....	136
<b>IV.3) Use of SrRuO<sub>3</sub> as bottom electrode for integration of PMN-PT on Si .....</b>	<b>139</b>
IV.3.1) Structural characterization by XRD .....	139
IV.3.2) Electrical properties .....	140
<b>IV.4) Conclusion .....</b>	<b>142</b>
<b>IV.5) Reference .....</b>	<b>143</b>

**Chapter V - Microfabrication and characterization of piezoelectric devices ..... 153**

---

<b>V.1) Introduction .....</b>	<b>154</b>
<b>V.2) Microfabrication process .....</b>	<b>155</b>
V.2.1) Piezoelectric membrane .....	155
V.2.2) Piezoelectric cantilever .....	159
<b>V.3) Finite Element Method and analytic model .....</b>	<b>162</b>
V.3.1) Introduction .....	162
V.3.1.1) Finite Element Method .....	162
V.3.1.2) Analytic Method .....	163
V.3.2) Characterization on piezoelectric membrane .....	165
V.3.3) Characterization on piezoelectric cantilever .....	167
<b>V.4) Conclusion .....</b>	<b>169</b>
<b>V.5) Reference .....</b>	<b>169</b>

**General conclusion and perspectives ..... 175**

---

<b>Appendix .....</b>	<b>179</b>
<b>A) Attempt to integrate PZT films on Si(111) using Gd<sub>2</sub>O<sub>3</sub> buffer layer .....</b>	<b>180</b>
A.1) Introduction .....	180
A.2) Deposition of Gd <sub>2</sub> O <sub>3</sub> film on Si(111) by Molecular Beam Epitaxy .....	182
A.3) Structural characterization of Gd <sub>2</sub> O <sub>3</sub> /Si(111) substrate .....	184
A.4) Sol-gel deposition of PZT film on Gd <sub>2</sub> O <sub>3</sub> /Si(111) substrate .....	185
A.5) Conclusion .....	188
<b>B) Finite Element Method .....</b>	<b>188</b>
<b>C) Reference .....</b>	<b>191</b>

## **General Introduction**

---

---

Due to their intrinsic piezoelectric properties, ferroelectric films naturally become promising materials for micro electromechanical system (MEMS) devices, especially for those lead-based ferroelectric oxides which possess large piezoelectric coefficients and tunable chemical compositions. Modern electronics and the tendency of monolithic packaging increasingly require the silicon-based integration of ferroelectric films in order to reduce the manufacture cost, increase the sensitivity, and assemble different functional components into one single chip. The most commonly used heterostructure in the industry is traditionally based on platinized silicon substrate, which provides low resistivity as a bottom electrode and relatively robust chemical stability on silicon. However, ferroelectric films usually have lower performances on Si than its bulk counterpart due to many defects induced by the substrate and the growth conditions. Continuous development of MEMS devices requires better quality films to achieve high performances, leading to increasing researches on the optimization of growth process and to developing the innovative heterostructures during recent years.

A high quality oxide film on Si is also required, not only for piezoelectricity but also for other applications of oxide films, involving a wide range of dielectric, pyroelectric and optical properties, such as FeFET (Ferroelectric Field Emission Transistor), FeRAM (Ferroelectric Random Access Memory), infrared sensors, and light modulators. Although platinized Si substrate is often used in the industry, its own drawbacks, such as polycrystalline structure, dead layer, pyrochlore phase, will prevent further promotion of its piezoelectric and other properties. The strategy that replaces by an oxide-terminated Si substrate, like YSZ (Yttrium-Stabilized Zirconia),  $\text{TiO}_2$ ,  $\text{SrTiO}_3$ , to grow epitaxial piezoelectric films has been proposed to check if the properties could be enhanced. Actually, the technical obstacle hindering the heteroepitaxy of oxide films is the formation of native silica layer on Si. In 1998, a commensurate  $\text{SrTiO}_3/\text{Si}$  interface was successfully obtained using Molecular Beam Epitaxy (MBE) technique. MBE system having extremely high vacuum allows a precise control of the interface, composition and thickness of growing structures at atomic level. Based on such oxides/Si substrate, heteroepitaxy of functional materials, such as III-V, Ge, and also the perovskite ferroelectric oxides, could be available by different deposition techniques. High performances and large piezoelectric coefficients of such epitaxial ferroelectric films have been already demonstrated by different MEMS devices using this new heterostructures.

## *General Introduction*

---

In this context, the main objectives of this thesis are (i) to develop a strategy for the epitaxial growth of ferroelectric films, like PZT and PMN-PT (ii) to evaluate the piezoelectric properties of the as-deposited epitaxial films by realizing some simple MEMS devices, such as membranes and cantilevers and (iii) to verify if the performances of monocrystalline piezoelectric layers are increased compared to the polycrystalline layers. We have focused our researches on Si(001) substrate with SrTiO<sub>3</sub> buffer layer and SrRuO<sub>3</sub> bottom electrode, since these two oxides have the same perovskite ABO<sub>3</sub> crystal structure and lattice constants similar to the ferroelectric materials we studied. PZT and PMN-PT have been grown on Si substrate using sol-gel method since the sol-gel method is the easiest way to homogeneously spread ferroelectric films on a large inch Si wafer with compatibility of standard cleanroom technologies.

This PhD thesis involves the collaboration between two French laboratories, i.e. CEA LETI (CEA: Commissariat à l'Energie Atomique et aux Energies Alternatives, LETI: Laboratoire d'Electronique et de Technologie de l'Information) in Grenoble and INL (Institut des Nanotechnologies de Lyon) in Ecole Centrale de Lyon. This work, partly realized on NANOLYON platform, has been supported by the French Agence Nationale de la Recherche (ANR) through the project MOCA 2010-NANO-020 and the project MINOS ANR-07-BLAN-0312.

This manuscript consists of five chapters. In chapter 1, the state-of-art technologies in piezoelectric MEMS (micro electromechanical system) and epitaxial oxide film on silicon substrate is presented. The motivations for developing a benchmark of epitaxial oxide films on Si and their simple MEMS structures are addressed with review of recent researches published during the past years.

Chapter 2 mainly discusses on the technologies used for film deposition and various characterizations. Three technologies, including MBE, Pulse Laser Deposition, and sol-gel method, are introduced for film deposition. Structural, electrical characterization, and the characterization for MEMS devices are also presented.

Chapter 3 will be dedicated to the deposition and the characterization of epitaxial PZT films on Si substrate. The candidates for the use of template is SrTiO<sub>3</sub> on Si(001). The deposition of PZT films is processed by sol-gel method. Structural measurement on the PZT films shows that the SrTiO<sub>3</sub> template can generate an epitaxial PZT film with pure perovskite phase. Various structural measurements confirm an epitaxial single-crystal PZT film with pure perovskite phase up to  $\mu\text{m}$  thickness. On the other hand, to access the electrical measurement, a bottom electrode must be considered. In this thesis, SrRuO<sub>3</sub> is chosen for this purpose since it has a relatively low resistivity and a lattice compatible structure with SrTiO<sub>3</sub> and PZT. Based on SrRuO<sub>3</sub> bottom

## *General Introduction*

---

electrode, the ferroelectric properties of PZT films are evidenced by the electrical measurement. Moreover, in this chapter the optimal deposition of SrTiO<sub>3</sub> and SrRuO<sub>3</sub> films are also addressed.

In Chapter 4, another ferroelectric material, i.e. 0.9Pb(Mg<sub>1/3</sub>Nb<sub>2/3</sub>)O<sub>3</sub>-0.1PbTiO<sub>3</sub> (PMN-PT) which is a typical relaxor ferroelectric, will be discussed as concern its epitaxial deposition and characterizations. The epitaxial PMN-PT film is successfully deposited by sol-gel method on SrTiO<sub>3</sub>/Si(001) without the help of a seeding layer. Electrical measurements based on SrRuO<sub>3</sub> bottom electrode and infrared transmission spectroscopy demonstrate a diffused phase transition across a large range of temperature for the epitaxial PMN-PT film, which we attribute to the existence of residual stress in the film.

The microfabrication process of simple MEMS devices, i.e. cantilever and membrane, based on epitaxial PZT films will be presented in Chapter 5, including the mechanical characterization and the simulations. Due to the lack of a reliable bottom electrode at the beginning of this elaboration, PZT/SrTiO<sub>3</sub>/Si stack is used for fabrication of membranes which is realized by back-etching of Si substrate to access the bottom of the PZT film. PZT films deposited on SrRuO<sub>3</sub>/SrTiO<sub>3</sub>/SOI (silicon-on-insulator) are used for fabrication of cantilevers whose thickness is simply defined by the SOI structure. Piezoelectric response under a given dc voltage is characterized by interferometer for both cantilever and membrane structures. Hysteresis loop evidences a real piezoelectric effect exerting on the MEMS devices. Besides, simulations by finite element method and analytical modeling are performed to study the characterization results.

## *General Introduction*

---

**Chapter I - Physical principles and motivations**

---

---

<b>I.1) Piezoelectric MEMS overview .....</b>	<b>6</b>
<b>I.2) Piezoelectricity and ferroelectricity .....</b>	<b>10</b>
I.2.1) Piezoelectricity .....	10
I.2.2) Ferroelectricity .....	13
I.2.3) Piezoelectric and ferroelectric materials .....	15
I.2.3.1) Wurtzite structure .....	15
I.2.3.2) Perovskite structure .....	17
I.2.3.3) Summary .....	19
<b>I.3) Physical principle of piezoelectric MEMS .....</b>	<b>19</b>
I.3.1) Operation modes and figures of merit .....	20
I.3.2) Influence of ferroelectric thin films .....	21
I.3.2.1) Effect of film orientation .....	21
I.3.2.2) Effect of residual stress .....	23
<b>I.4) Single crystal piezoelectric films on Si: state of the art .....</b>	<b>25</b>
I.4.1) Epitaxial PZT films .....	25
I.4.2) Epitaxial PMN-PT films .....	28
I.4.3) Summary .....	29
<b>I.5) Objectives of the thesis .....</b>	<b>30</b>
<b>I.6) Reference .....</b>	<b>31</b>

### **I.1) Piezoelectric MEMS overview**

As a new technical discipline born in 1980s, piezoelectric MEMS (Micro-ElectroMechanical System) become a rapidly evolving area in the research and development of MEMS field. The basic principle of piezoelectric MEMS is based on the intrinsic electromechanical coupling effect of piezoelectric materials to transform the energies between electrical and mechanical forms. In piezoelectric materials, elastic strain is induced by application of an electric field (converse effect), or electric charges appear on the surfaces of a piezoelectric element (direct effect) upon application of an elastic stress. This exclusive advantage of piezoelectric materials promotes the requirement of MEMS sensors and actuators in many applications, such as ultrasonic transducer <sup>[1]</sup>, accelerometer <sup>[2, 3]</sup>, micro pump <sup>[4]</sup>, gas sensors <sup>[5]</sup>, and energy harvesting <sup>[6]</sup>. For most of the applications, the use of bulk piezoelectric materials has already existed for a long time. The miniaturization of piezoelectric devices into MEMS scale is primarily promoted by the requirement of exchanging minimal amount of energy and obtaining improved performances, like higher resonance frequencies, low operation voltages, and high sensitivities. Various illustrative applications of piezoelectrics MEMS are listed in Table I.1:

**Table I.1 – List of some piezoelectric MEMS devices.**

<b>Sensors</b>	<b>Actuators</b>	<b>RF MEMS</b>	<b>Others</b>
Mass sensor <sup>[7]</sup>	Micro mirror <sup>[15]</sup>	Contact switches <sup>[21]</sup>	Optical modulator <sup>[25]</sup>
Pressure sensor <sup>[8]</sup>	Micro pump <sup>[16]</sup>	Signal filters <sup>[22]</sup>	Energy harvesting <sup>[26, 27]</sup>
Hydrophone <sup>[9]</sup>	Micro valve <sup>[17]</sup>	Tunable capacitor <sup>[23]</sup>	
Microphone <sup>[10]</sup>	Printhead <sup>[18]</sup>	Bulk acoustic resonator <sup>[24]</sup>	
Accelerometer <sup>[11]</sup>	Ultrasonic motor <sup>[19]</sup>		
Gyroscope <sup>[12]</sup>	Camera autofocus <sup>[20]</sup>		
Infrared detector <sup>[13]</sup>			
Piezoelectric micromachined ultrasonic transducers (pMUTs) <sup>[14]</sup>			

Sensors and actuators represent two principal categories of piezoelectric MEMS devices. Typically, piezoelectric sensors are configured as direct mechanical transducers by using direct piezoelectric effect to generate an electrical output signal, or as resonators for which the resonance frequency and amplitude are influenced by input physical quantities. Taking mass sensor as an example, a surface acoustic wave is usually generated on piezoelectric film by applying ac voltage. Absorbed particles on the surface can shift the resonance frequency of the acoustic wave. By sweeping the frequency, the frequency shift is detected and consequently the mass of the absorbed particles is measured. Piezoelectric actuators are commonly designed in either bimorph or expansion structure to obtain the elastic displacement. In the former one, bimorph structure with piezo-active layer and piezo-inactive elastic layer is used to amplify the

in-plane piezoelectric strain into beam deflection [28]. The design of bimorph structure can be a beam, like in a contact radio frequency (RF) switch or a membrane, like in a micro pump. In a contact RF switch, piezoelectric beam is used to perform the mechanical movement to switch between short and open circuits. Such RF switch operates with a low insertion loss at GHz band thanks to the high-quality factors [21], which provides tremendous advantages over GaAs and silicon switching devices. In expansion structure, mechanical displacement is obtained directly from longitudinal electric-field-induced strain [29]. Therefore, the structure has a relatively simpler design compared to bimorph structure, but a smaller displacement. Another application can be found in optical modulation by using various electro-optic properties of piezoelectric materials. Usually, piezoelectric materials have good electro-optic switching times and modest half-wave voltages, especially for relaxor ferroelectrics, so that the phase, amplitude, frequency or polarization of a light beam can be modulated at the GHz band [30]. Energy harvesting using piezoelectric MEMS is another emerging technology that was developed in the late 1990s, where the piezoelectric materials convert the environmental vibrations, like seismic vibrations and acoustic noise, into electrical energy. The produced power (few mW) is usually sufficient for most of handheld devices and passive sensors. Wang *et al* published their work in 2006 on piezoelectric nano-brushes which can be integrated into clothes to harvest the energy of human motions [27].

Piezoelectricity is not the only choice for MEMS devices. Other physical principles, like electrostatic interaction [31], thermomechanical bimorph effect [32], and magnetostrictive effect [33], are also available in MEMS design. Due to its relatively simple fabrication process, electrostatic MEMS has been successfully commercialized for different kinds of actuators [34], as also for sensors [35] and transducers [36]. Even with the disadvantage of nonlinearity, electrostatic devices can reach an electro-mechanical coupling coefficient  $k^2$  of 100% in small signal limit [37], which is larger than that of piezoelectric effect. Another competing technology is thermomechanical bimorph effect, which utilizes the difference of in-plane thermal expansion of two parallel layers to generate the deflection in the cantilever or membrane [38]. However, this effect is naturally of high power consumption due to the large heat dissipation. Further possibilities are magnetostrictive and electromagnetic effects, but they require a special coil structure and the resistive loss is inevitable. But for those applications where a remote power supply is mandatory, they remain of the preferred choice [39]. Compared with other physical principles employed in MEMS, piezoelectricity has following advantages for applications:

- (1) Large actuation force and low operating voltage: Many ferroelectric materials, like lead-based ferroelectrics  $\text{Pb}(\text{Zr}_x\text{Ti}_{1-x})\text{O}_3$  (PZT) [40], possess large piezoelectric coefficients (either  $d_{33}$  or  $e_{31}$ ) which can generate large force actuation and large displacement, especially by

using the curvature of bimorph structure. Piezoelectric thin film actuators can be driven by high-frequency circuit to enable high contact force, high restoring force, and temperature-stable switches operating at  $\leq 10$  V thanks to their high dielectric constants <sup>[41]</sup>. Although such low-voltage actuation switches have been realized using electrostatic actuation, these actuators lack the restoring force necessary for long cycle lifetimes.

- (2) Low dielectric loss, namely high efficiency and high quality factor Q: Indeed, the performance of piezoelectric MEMS largely depends on the film quality, like crystalline quality, formation of dead layer, chemical stoichiometry, presence of charge traps, etc., which is strongly affected by the fabrication process. Varieties of deposition technologies are available to deposit high-quality piezoelectric films with different heterostructure designed for specific requirements. Using optimal growth condition, piezoelectric films with low insertion loss, high piezoelectric coefficients, and high quality factor Q, can be achieved.
- (3) High-speed and high-frequency operation: Shrinking dimension of MEMS devices down to  $\mu\text{m}$ -level provides the possibility to work at the frequency range from high MHz to low GHz, i.e. RF band. Resonance frequency of piezoelectric RF MEMS is mainly determined by lithography through the shape of both the electrode and piezoelectric components. Using the non-linear part of the piezoelectric response such resonance frequency can be dynamically tuned by applying dc bias voltage. On the other hand, the high-frequency losses of films may be smaller than those of bulk materials if crystalline orientation and domain wall mobility are controlled during thin film deposition. Moreover, it was demonstrated that, using the interface of two materials with different piezoelectric coefficients, THz acoustic wave can be possibly detected <sup>[42]</sup>, which largely widens the frequency domain of the piezoelectric MEMS.
- (4) Linear piezoelectric response between electric signal and elastic stress: In most cases, piezoelectric response maintains linear relationship between electric signal and elastic stress. The linear effect largely simplifies the design of piezoelectric MEMS and electronic controller. On the contrary, the nonlinear electrostatic effect is determined by both electric voltage and the distance between two electrodes. The *so-called* “pull-in” instability must be carefully considered during the design since the applied voltage could exceed a certain critical voltage and induce a short circuit <sup>[43]</sup>.
- (5) The possibility to scaling down to Nano-ElectroMechanical System (NEMS): Piezoelectric NEMS with smaller dimension results in higher frequency, higher quality factor and ultrahigh sensitivity compared with MEMS counterpart. For instance, based on a nanoscale

piezoelectric beam, the attogram-scale mass, like protein molecule, can be measured by using beam resonance <sup>[44, 45]</sup>. The enhanced performances in NEMS provide the opportunity to perform new experimental researches in the fields, like medical testing and biological research.

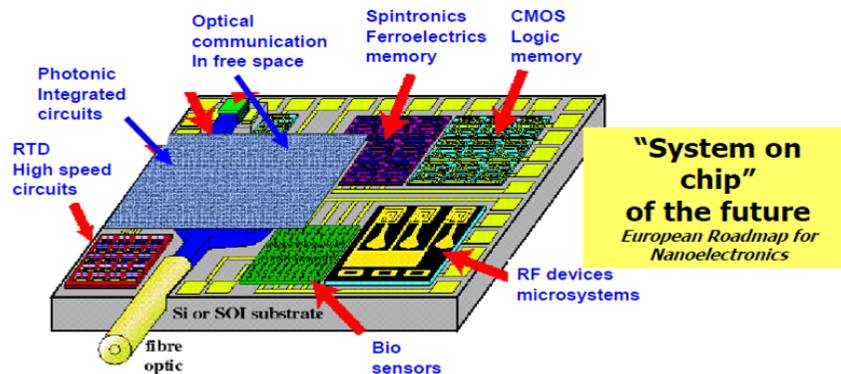


Figure I.1 - Monolithic integration of different components on the same silicon substrate <sup>[46]</sup>.

Integration of piezoelectric MEMS on conventional CMOS (complementary metal-oxide semiconductor) substrate permits the monolithic fabrication, allowing a way to promote production yield, shrink device dimension, and decrease the manufacture cost. MEMS packaging takes the majority of the cost since the device which contains various mechanical structures, chemical active surface, for instance, must be compatible with application-specific environment that requires not only the electromagnetic isolation but also the transfer of measured physical quantity from outside space. Therefore, monolithic integration can effectively decrease the cost by combining the package processes of each individual component. Even before the term “MEMS” was coined, sensors had been already integrated into the electronics to monitor the operating condition, which acted as an “eye” for the electronics to “see” the real physical world. Nowadays, most significant MEMS products, like printheads <sup>[47]</sup>, accelerators <sup>[48]</sup>, digital light processors <sup>[49]</sup>, are actually integrated with ASIC electronics (Application-Specific Integrated Circuit) to realize additional functions, such as environmental monitoring, energy management, temperature stabilization, and simple computation. Moreover, according to European Roadmap for Nanoelectronics, systems-on-a-chip that will amalgamate different components, like optical communication, energy harvester, sensor, and actuator, on a single die has been proposed to satisfy the application-specific requirement (Figure I.1) <sup>[46]</sup>. On the other hand, more and more emerging techniques appear, like spintronics <sup>[50]</sup>, photonics <sup>[51]</sup>, microfluidics <sup>[52]</sup>, molecular electronics <sup>[53]</sup>, and nano-electronics <sup>[54]</sup>. If all these principles could be integrated, devices with new functions and applications can be fabricated with shrinking dimension. Smart devices, like smart dust <sup>[55]</sup> and drug delivery <sup>[56]</sup>, would be available for special applications in the future. This *so-called* “Beyond Moore’s Law” is apart from the development of conventional electronics

which doubles its performance each 18 months. Obviously, due to different crystalline structure and chemical context monolithic integration must involve several prerequisite considerations, like Si passivation, template layer, bottom electrode, etc., for the deposition of functional materials on the commonly used Si wafer. Another issue must be considered such that the thin film materials usually have modified properties different from those of the bulk one. Many effects, like elastic stress, oxygen vacancies, interfacial states, film thickness, can degrade or enhance the performance of the thin film materials and, therefore, the device can be engineered by changing the growth condition for specific purpose.

## **I.2) Piezoelectricity and ferroelectricity**

### **I.2.1) Piezoelectricity**

The term “piezoelectricity” describes an intrinsic electromechanical property of piezoelectric materials that can convert electrical energy into mechanical energy, and vice versa. In the direct effect, when piezoelectric material undergoes an elastic stress, electrical charges accumulate on the surfaces of the material. In the converse effect, elastic strain is induced when an electric field is applied on the material. From crystallographic perspective, the appearance of piezoelectric properties can be predicted by knowing the symmetry of the crystalline structure. Those crystalline materials having a centrosymmetric structure are not piezoelectric, which is attributed to the fact that the opposite electric charges in the centrosymmetric lattice cannot be separated by the uniaxial deformation of the lattice, i.e. elastic strain. However, these 11 centrosymmetric crystalline structures out of 32 crystalline classes can still reduce their dimension along the direction of applied electric field, which is caused by the electrostatic attraction between electric-field-induced dipoles. This phenomenon is called “electrostriction” and occurs in all the dielectrics but is much weaker than piezoelectric effect. The induced strain by electrostriction effect is usually proportional to the square of the induced polarization and no reversal effect exists, namely the elastic stress cannot induce the polarization by electrostriction effect. The remaining 21 non-centrosymmetric crystals are piezoelectric except for class-432. In those 20 non-centrosymmetric crystalline structures, the uniaxial deformation of the lattice caused by elastic stress can shift the positive and negative charges along the opposite directions, leading to the formation of electric dipole. This reversible physical process has a linear relationship between the applied elastic stress and the induced polarization. Switching the direction of the applied electric field also change the sign of the induced strain, and vice versa. It is different from the quadratic effect of the electrostriction which is always compressive strain. To summarize, Figure I.2 shows the categories among those 32 crystalline classes according to their electrical properties.

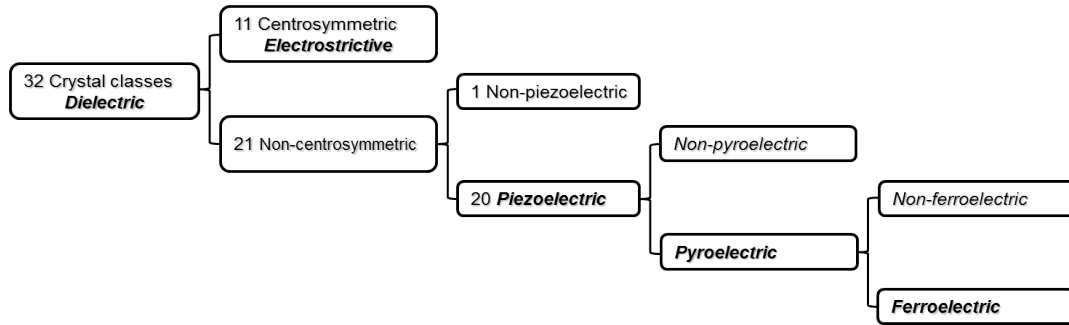


Figure I.2 - 32 crystalline classes categorized by their electrical properties.

Generally, the linear relationship in piezoelectric effect can be simply represented by the definition of piezoelectric coefficient in following equation:

$$d = \frac{P}{\sigma} = \frac{S}{E} \quad \text{Equ. I.1}$$

where  $P$  is the polarization density induced by the applied stress  $\sigma$  in the direct effect, and  $S$  is the elastic strain induced by the applied electric field  $E$  in the converse effect, as illustrated in Figure I.3. The unit of measurement for piezoelectric coefficient  $d$  can be either C/N for the direct effect or m/V for the reverse effect. Theoretically, the two piezoelectric coefficients derived from direct and converse effects are physically equal for a free-standing piezoelectric material, which is, however, not true for a thin film piezoelectric material clamped by the substrate.

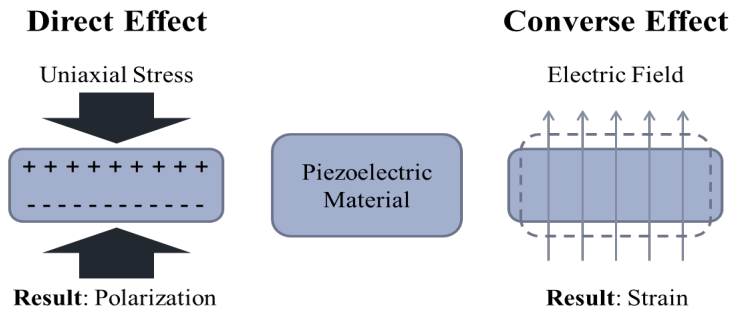


Figure I.3 - Schematic of the direct and converse effects of piezoelectricity.

In practice, a more universal equation of piezoelectricity that can incorporate both mechanical and electrical aspects is required. The equation should also involve the rotational transformation in 3D space. The so-called “coupled equations” dedicated for the requirement are shown as follows for a free-standing piezoelectric material:

$$\begin{aligned} S &= s_E \cdot T + d^t \cdot E \\ D &= d \cdot T + \varepsilon_T \cdot E \end{aligned} \quad \text{Equ. I.2}$$

where  $s_E$  is the mechanical compliance,  $d$  is the piezoelectric coefficient and  $\epsilon_T$  is the dielectric constant. These 3 constants concern the intrinsic properties of piezoelectric material. The remaining physical quantities in coupled equations are the induced strain  $\mathbf{S}$ , the applied stress  $\mathbf{T}$ , the electric field  $\mathbf{E}$  and the induced electrical displacement  $\mathbf{D}$ . All the values are rank-2 tensors that usually take the reduced notation, i.e. Voigt notation. Within, the converse piezoelectric coefficient  $d'$  is mathematically the transpose matrix of the direct piezoelectric coefficient  $d$ . For orthotropic piezoelectric materials, due to the lattice symmetry there are only  $9 + 5 + 3 = 17$  constants in the coupled equations whose physical quantities are shown in the form of matrix as follows:

$$\begin{aligned}
 s_{(6 \times 6)} &= \begin{bmatrix} s_{11} & s_{12} & s_{13} & & & \\ & s_{22} & s_{23} & & 0 & \\ & & s_{33} & & & \\ & & & s_{44} & & \\ & \text{sym.} & & & s_{55} & \\ & & & & & s_{66} \end{bmatrix} \\
 d_{(3 \times 6)} &= \begin{bmatrix} 0 & 0 & 0 & 0 & d_{15} & 0 \\ 0 & 0 & 0 & d_{24} & 0 & 0 \\ d_{31} & d_{32} & d_{33} & 0 & 0 & 0 \end{bmatrix} \\
 \epsilon_{(3 \times 3)} &= \begin{bmatrix} \epsilon_{11} & 0 & 0 \\ 0 & \epsilon_{22} & 0 \\ 0 & 0 & \epsilon_{33} \end{bmatrix}
 \end{aligned} \tag{Equ. I.3}$$

Piezoelectric thin films are usually treated as transversally isotropic by averaging the in-plane physical quantities. Then, the number of independent constants in the coupled equation is reduced to  $4 + 2 + 1 = 7$  according to the following relations:

$$\begin{aligned}
 s_{11} = s_{22}, s_{23} = s_{13}, s_{55} = s_{44}, s_{66} = \frac{s_{11} - s_{12}}{2} \\
 d_{24} = d_{15}, d_{32} = d_{31}, \epsilon_{11} = \epsilon_{22}
 \end{aligned} \tag{Equ. I.4}$$

In thin films,  $d_{31}$  or  $d_{32}$  indicates the in-plane (or transversal) piezoelectric coefficient, and  $d_{33}$  indicates the out-of-plane (or longitudinal) one. And,  $d_{24}$  or  $d_{15}$  represents the relationship between the shear strain and the applied electric field. By using Piezoresponse Force Microscopy (PFM) in lateral or vertical mode,  $d_{24}/d_{15}$  or  $d_{33}$  can be measured<sup>[57]</sup>. Besides,  $d_{31}$  and  $d_{32}$  can be determined by measuring the electric-field-induced deflection of a piezoelectric cantilever<sup>[58]</sup>. The above coupled equations are taken in the “*Strain-Charge*” form. The other forms of the coupled equations and the corresponding piezoelectric coefficients used in different thermodynamic contexts are represented as follows:

## Chapter I - Physical principles and motivations

**Table I.2 - 4 different forms of coupled equations and the corresponding piezoelectric coefficients.**

	“Stress [T]” (N/m <sup>2</sup> )	“Strain [S]” (m/m)
“Charge [D]” (C/m <sup>2</sup> )	$T = c_E \cdot S - e^t \cdot E$ $D = e \cdot S + \epsilon_S \cdot E$ $e_{ij} = \left( \frac{\partial D_i}{\partial S_j} \right)^E = - \left( \frac{\partial T_j}{\partial E_i} \right)^S$	$S = s_E \cdot T + d^t \cdot E$ $D = d \cdot T + \epsilon_T \cdot E$ $d_{ij} = \left( \frac{\partial D_i}{\partial T_j} \right)^E = \left( \frac{\partial S_j}{\partial E_i} \right)^T$
“Voltage [E]” (V/m)	$T = c_D \cdot S - h^t \cdot D$ $E = -h \cdot S + \epsilon_S^{-1} \cdot D$ $h_{ij} = - \left( \frac{\partial E_i}{\partial S_j} \right)^D = - \left( \frac{\partial T_j}{\partial D_i} \right)^S$	$S = s_D \cdot T + g^t \cdot D$ $E = -g \cdot T + \epsilon_T^{-1} \cdot D$ $g_{ij} = - \left( \frac{\partial E_i}{\partial T_j} \right)^D = \left( \frac{\partial S_j}{\partial D_i} \right)^T$

Within the table, the matrix of  $c$  (stiffness coefficients) is the inverse of that of  $s$  (compliance coefficients), i.e.  $c = s^{-1}$ . In the definition of piezoelectric coefficient in Table I.2, the first term is related to the direct effect, and the second term is related to the converse effect.

### I.2.2) Ferroelectricity

As shown in Figure I.2, ferroelectric materials are a subclass of pyroelectric materials which maintains a permanent electric dipole in crystalline lattice when the external electric field is absent. Pyroelectric materials can respond to a temperature variation by accumulating electric charges on the surface. Essentially, the permanent dipole is determined by the lattice geometry of the pyroelectric material. Temperature variation changing the lattice constants can change the length of the permanent dipole, and therefore change the dipole moment. Different from the lattice deformation induced by uniaxial stress, temperature-induced deformation cannot separate the opposite charges if no permanent dipole develops in the lattice, i.e. non-pyroelectric materials. However, not all the pyroelectric materials are ferroelectric as some might be paraelectric, for which the permanent dipoles are randomly distributed due to thermal excitation, and no macroscopic spontaneous polarization happens. Only those pyroelectric materials whose permanent dipoles align along a preferred direction in the whole ferroelectric domain are called ferroelectrics. Unlike paraelectric pyroelectrics, the removal of the applied electric field does not lead to the disappearance of the spontaneous polarization in ferroelectric material. Moreover, the electric field can change and switch the spontaneous polarization, and therefore tune the properties of the ferroelectric material. Figure I.4 shows a typical P-E hysteresis loop, i.e. polarization vs. electric field, of ferroelectric material, where the polarization is not only determined by the applied electric field but also by the historical state. Usually, poling process is necessarily carried out before utilization to align the ferroelectric domains in a preferred direction in the *as-prepared* material. Then, increasing the applied electric field will increase the polarization since more ferroelectric domains are switched in the same direction. After all the

ferroelectric domains are aligned, the polarization undergoes a linear increase due to dielectric polarization. The intersection of such linear line with polarization axis is called “saturated polarization” ( $P_s$ ), which indicates the intrinsic spontaneous polarization in the material. Afterwards, the polarization will decrease with reducing the electric field since the ferroelectric domains partially switch back to random distribution. But the majority of the ferroelectric domains keep along the preferred direction, forming the remnant polarization ( $P_r$ ) at zero electric field. The electric field required to cancel the remnant polarization is called “coercive electric field ( $E_c$ )”.

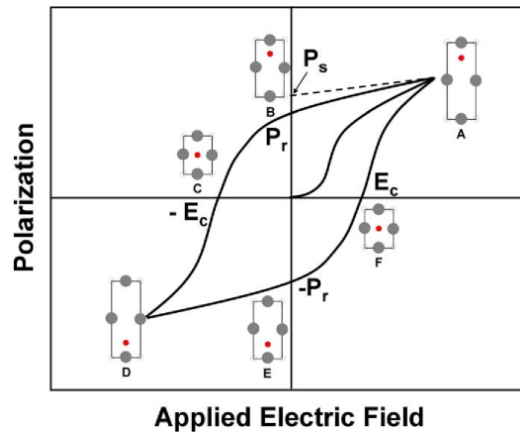


Figure I.4 - A typical hysteresis loop for ferroelectric material.

Another important factor that strongly determines the spontaneous polarization in ferroelectric material is the temperature. The spontaneous polarization can be theoretically depicted by the Landau-Ginzburg-Devonshire free energy, which is shown as follows for the case of tetragonal lattice with no stress and electric field applied on the ferroelectric material.

$$G = a_1 P^2 + a_2 P^4 + a_3 P^6 \quad \text{Equ. I.5}$$

where  $P$  is the spontaneous polarization,  $a_i$  are the dielectric stiffness coefficients. The first-order dielectric stiffness  $a_1$  is given by the Curie-Weiss law,  $a_1 = (T - T_C)/2\epsilon_0 C$ , where  $T_C$  and  $C$  are the Curie temperature and constant, respectively. Therefore, the free energy as a function of polarization also varies with the temperature (Figure I.5 (a)). When the temperature is below  $T_C$ ,  $a_1$  becomes negative. The free energy shows two minima at  $+P_s$  and  $-P_s$ , suggesting two possible states of spontaneous polarization. An applied electric field larger than the energy barrier between the two states can switch the spontaneous polarization. With increasing the temperature, the spontaneous polarization usually decreases and eventually vanishes at the Curie temperature (Figure I.5 (b)), corresponding to the ferroelectric-paraelectric phase transition. The minimal free energy only happens at  $P_s = 0$  when  $T > T_C$ , i.e. no spontaneous polarization. The typical P-E hysteresis loop of ferroelectric material disappears and follows a nonlinear relationship (Figure

I.5 (c)). Such nonlinear dielectric response results from the permanent polarization which cannot develop in the entire ferroelectric domain and cannot keep the preferred direction at zero electric field. In addition, the nonlinear dielectric response at an elevated temperature tends to be linear due to the fact that the permanent polarization is weakened by thermal excitation.

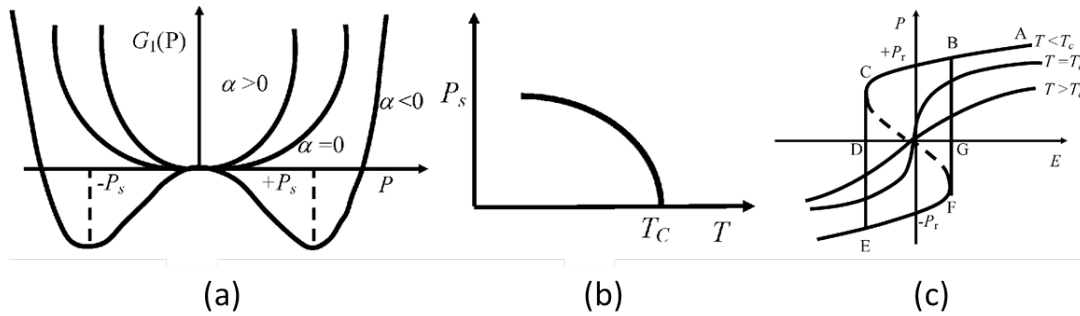


Figure I.5 - Temperature-dependent properties of ferroelectric material: (a) the free energy, (b) the spontaneous polarization, and (c) the P-E loop.

### I.2.3) Piezoelectric and ferroelectric materials

Piezoelectricity can be realized by a large number of materials spanning from common biologic tissues, like seashell <sup>[59]</sup>, human bones <sup>[60]</sup>, and high polymers <sup>[61]</sup> to the conventional piezoelectric materials used in the research and industry, like AlN <sup>[62]</sup>, ZnO <sup>[63]</sup>, and PZT <sup>[64]</sup>. For piezoelectric MEMS, two principal crystalline structures are concerned, i.e. wurtzite and perovskite structures, which we will discuss in this section with introduction of the common used piezoelectric materials.

#### I.2.3.1) Wurtzite structure

Wurtzite structure originates from the name of a zinc iron sulfide mineral ((Zn, Fe)S), whose crystalline structure belongs to the hexagonal crystal system. The structure is mainly adopted by the ferroelectric materials ZnO and AlN. Taking ZnO as an example, the hexagonal structure of wurtzite ZnO is schematically presented in Figure I.6. The wurtzite structure of ZnO can be regarded as two interconnecting sublattices of  $Zn^{2+}$  and  $O^{2-}$ , such that each Zn ion is surrounded by a tetrahedra of O ions, and vice-versa. In the ideal wurtzite structure, these two sublattices relatively shift  $3/8$  of the lattice constant along c-axis, leading to that the ratio  $c/a$  is  $(8/3)^{1/2}$ , i.e. 1.6330. For ZnO, the hexagonal structure has a space group of  $P6_3mc$ , which has no inversion symmetry and results in the piezoelectricity, with the lattice constants of  $a = 3.2495 \text{ \AA}$  and  $c = 5.2069 \text{ \AA}$ , i.e.  $c/a = 1.60$  close to that of the ideal one, and the density of  $5.605 \text{ g/cm}^3$  <sup>[65]</sup>. The shift of two sublattices is about 0.3836 along c-axis for ZnO, leading to the formation of

spontaneous polarization in the lattice, i.e. pyroelectricity<sup>[66]</sup>. In addition, ZnO is also known to crystallize in the cubic zincblende and rocksalt (NaCl) structures. The cubic zincblende structure forms by growth on cubic substrate<sup>[67, 68]</sup>, and the rocksalt structure is a high-pressure metastable phase at ~10 GPa<sup>[69]</sup>.

The zincblende ZnO also possesses the piezoelectric properties but is lack of pyroelectric properties. Moreover, ZnO has a wide band gap of 3.4 eV<sup>[70]</sup> with intrinsic carrier concentration of  $\sim 10^{16} \text{ cm}^{-3}$ . Due to the large exciton binding energy of 60 meV at 300 K, ZnO becomes an important candidate for blue and ultra-violet optical devices. As a ferroelectric material, ZnO has a spontaneous polarization of  $-0.057 \text{ C/m}^2$ <sup>[71]</sup> and the piezoelectric coefficient is  $0.89 \text{ C/m}^2$ ,  $-0.51 \text{ C/m}^2$ , and  $-0.45 \text{ C/m}^2$  for  $e_{33}$ ,  $e_{31}$ , and  $e_{15}$ <sup>[72]</sup>. Other promising advantages of ZnO include its broad fabrication methods, such as sol-gel<sup>[73]</sup>, sputtering<sup>[74]</sup>, metal organic chemical vapor deposition<sup>[75]</sup>, and pulsed laser deposition (PLD)<sup>[76]</sup>, low power threshold for optical pumping<sup>[77]</sup>, piezoelectricity<sup>[27]</sup>, radiation hardness<sup>[78]</sup> and biological compatibility<sup>[79]</sup>. Together, these properties enable ZnO to be an ideal candidate for a variety of devices ranging from sensors through to ultra-violet laser diodes and nanotechnology-based devices such as displays.

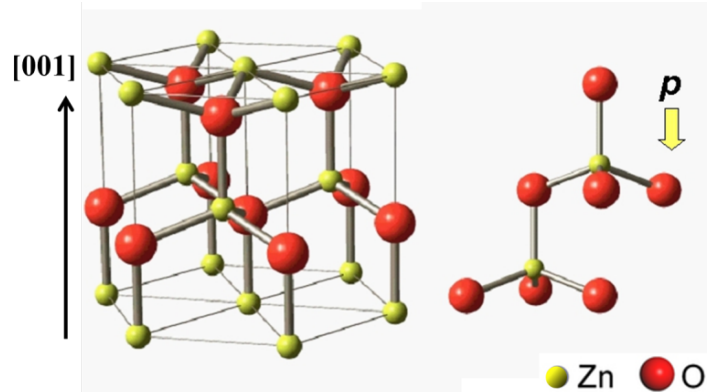


Figure I.6 - The atomistic model of wurtzite ZnO structure.

AlN is another example of wurtzite structure with covalent bonds and lattice constant of  $a = 3.112 \text{ \AA}$  and  $c = 4.982 \text{ \AA}$ <sup>[80]</sup>. The two sublattices of AlN relatively shift a distance of  $0.38 c$ -axis lattice constant, leading to the spontaneous polarization of  $-0.081 \text{ C/m}^2$  along  $c$ -axis with the piezoelectric coefficients of  $1.46 \text{ C/m}^2$ ,  $-0.60 \text{ C/m}^2$ , and  $-0.48 \text{ C/m}^2$  for  $e_{33}$ ,  $e_{31}$ , and  $e_{15}$ . The piezoelectricity of AlN is primarily generated by changing the N-Al-N bond angle, rather than changing the Al-N bond length. However, reorientation of the polarization requires breaking primary chemical bonds, so AlN is not ferroelectric and, therefore, yields piezoelectric constants that are very stable as a function of temperature, frequency, and the amplitude of the drive electric field<sup>[81]</sup>. AlN has some advantages over ZnO. First, AlN is widely used in the industry

due to the perfect compatibility with silicon semiconductor technology, whereas ZnO has the problem of fast diffusion. On the other hand, wurtzite AlN has a wide band gap of 6.2 eV with a large resistivity and good film quality are reported to grow between 100°C and 900°C [82]. On the contrary, with a smaller band gap, i.e. 3.4 eV, ZnO is a semiconductor which is easier to be doped, e.g. Zn interstitials [83], leading to a high dc conductivity. For those sensors and actuators working at frequencies below about 10 kHz, the use of ZnO is limited. Moreover, AlN and AlGaIn are usually used to fabricate light-emitting diodes operating in blue to ultraviolet region [84, 85] due to its wide band gap.

### I.2.3.2) Perovskite structure

Perovskite oxides is a large family of oxide materials with a general chemical formula of  $A^{2+}B^{4+}O_3$  [86, 87, 88]. In the formula, both A and B cations can be doped by different atoms to modulate the electrical properties. Taking PZT as an example, Figure I.7 exhibits the crystalline structure of PZT material. In the unit cell, eight Pb atoms occupy each corner, and Zr or Ti atoms randomly locate near the center of the lattice. The central Zr or Ti atom is surrounded by an octahedron that consists of eight oxygen anions at the face center of the lattice. Usually, A and B cations have very different radius in ferroelectric materials. For PZT, the radius of Pb atom (175 pm) is larger than that of Zr (160 pm) and Ti (147 pm). Goldschmidt tolerance factor indicates such incompatibility of ionic radius in a crystal structure, which is defined as follows for perovskite material:

$$t = \frac{r_A + r_o}{\sqrt{2}(r_B + r_o)} \quad \text{Equ. I.6}$$

where  $r_A$ ,  $r_B$  and  $r_o$  represent the radius of A, B and oxygen respectively. For those A and B cations having ideal radius like SrTiO<sub>3</sub> (STO),  $t$  is less than one and B atom steadily locates at the center of the cubic lattice, resulting in the non-piezoelectric properties. On the contrary, the tolerance factor of PZT is larger than one. The relatively large free space in the oxygen octahedron provides the possibility to generate permanent dipole by shifting the B cation away from the center of the lattice.

PZT ferroelectric material is actually a solid solution whose crystalline structure varies with the ratio of rhombohedral PbZrO<sub>3</sub> and tetragonal PbTiO<sub>3</sub> (PT). Figure I.8 (a) shows the phase diagram of PZT solid solution. When PT > 48%, ferroelectric tetragonal structure is energetically stable, where the permanent dipole has 6 possible orientations along the longest axis of the tetragonal lattice, i.e. <100> direction. In the rhombohedral region where PT < 48%, the favorable orientation of the permanent dipole is along the space diagonal of the lattice, i.e. <111> direction, and so there exists 8 possible orientations. The piezoelectric coefficients of PZT

increase with the chemical composition approaching the *so-called* Morphotropic Phase Boundary (MPB) at PT = 48%. The piezoelectric coefficient varying with chemical composition can be theoretically predicted by Haun's model [89]. Near MPB, PZT material exhibits an average crystalline structure in either tetragonal or rhombohedral lattice by conventional XRD measurement (X-Ray Diffraction). Both PZT phases are energetically favorable, so there are 14 possible polarization directs and the piezoelectric properties are largely enhanced. Moreover, high-resolution synchrotron XRD reveals a local monoclinic crystalline structure in PZT material near MPB [90]. In the Zr-rich composition, the local monoclinic lattice randomly distributed in three preferred orientations results in the rhombohedral symmetry [91], and in the Ti-rich composition the local monoclinic lattice with four preferred orientations results in the tetragonal symmetry [92]. Such composition dependency of electrical properties can be observed in Figure I.8 (b) [93], where the symbols are for  $e_{31,f}$  data and the lines are for  $d_{33,f}$  data. Both bulk PZT ceramics and thin films often show the maxima in the piezoelectric  $d$  and  $e$  coefficients generally appeared at the MPB [94, 95]. This phenomenon does not have a strong deposition dependent correlation with the factors like deposition method, film orientation, film thickness. At MPB, monoclinic phase exists within a certain width in chemical composition near MPB which narrows with increasing the temperature. Above the Curie temperature, the crystalline lattice of PZT becomes cubic and the Zr or Ti cation exactly locates at the center of the lattice, leading to the phase transition of PZT materials into the paraelectric phase.

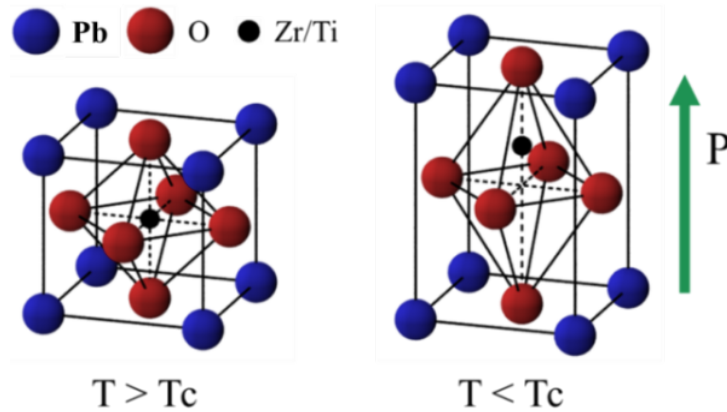


Figure I.7 - Schematic of PZT crystalline lattice and the origin of permanent dipole in tetragonal lattice.

PMN-PT ( $x\text{Pb}(\text{Mg}_{1/3}\text{Nb}_{2/3})\text{O}_3-(1-x)\text{PbTiO}_3$ ) system is a solid solution doping relaxor ferroelectric  $\text{Pb}(\text{Mg}_{1/3}\text{Nb}_{2/3})\text{O}_3$  (PMN) by ordinary ferroelectric PT and possesses the same perovskite structure. The relaxor properties of PMN are mainly attributed to the compositional fluctuation of Mg and Nb at the B site. The addition of PT can generally change the relaxor properties of PMN into an ordinary ferroelectric one [96]. Such phase boundary exists at  $x = 0.4$

separating pseudocubic phase (relaxor ferroelectric) and tetragonal phase (normal ferroelectric) [97]. Near the MPB, monoclinic crystalline structure is energetically favorable, which has several energetically equivalent orientations for the permanent polarization, so that the maximal dielectric constants and piezoelectric coefficients occur. At  $x < 0.4$ , PMN-PT has a pseudocubic structure with space group  $Pm3m$  at room temperature with no evidence of long range ordering of the dissimilar B site cation in  $ABO_3$  perovskite structure. Those local nano-sized ferroelectric domains randomly distributed in the paraelectric host material were found to be responsible for many anomaly electrical properties of PMN-PT, like huge dielectric constant ( $> 20000$ ), giant piezoelectric coefficient, temperature-dependent electrical properties, etc. In Chapter 4, more discussion will be addressed in detail on the nature of relaxor properties and the epitaxial growth of PMN-PT films on Si substrate.

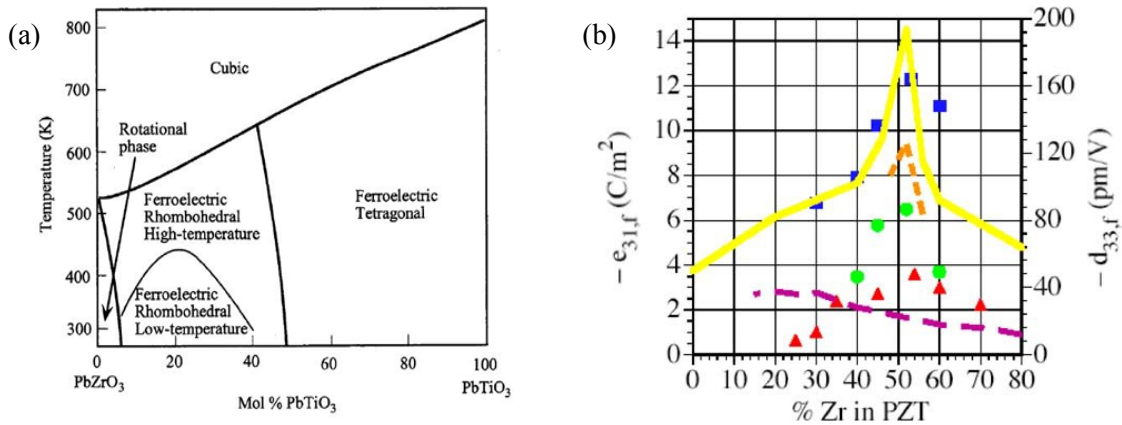


Figure I.8 - Phase diagram of PZT solid solution [98] and the composition dependence of the relative piezoelectric response in PZT thin films [95].

### I.2.3.3) Summary

From crystallographic aspect, piezoelectricity is intrinsically induced by those crystalline structures with no inversion symmetry. Two major categories, i.e. wurtzite and perovskite, of piezoelectric materials are widely used in the research and industry, as we mainly discuss on 4 important piezoelectric materials, such as ZnO, AlN, PZT, and PMN-PT. Since those lead-based ferroelectric materials having large piezoelectric coefficients is essential for MEMS applications, we will study these two ferroelectric materials, i.e. PZT and PMN-PT, in this thesis with epitaxial growth on silicon and various characterizations on the thin films.

## I.3) Physical principle of piezoelectric MEMS

### I.3.1) Operation modes and figures of merit

Piezoelectric MEMS devices can operate in different modes using corresponding electrode configuration and figure of merit. Taking cantilever as an example, several piezoelectric coefficients are used in MEMS devices, as shown in Figure I.9. The first configuration with the electrodes on top and bottom surfaces utilizes the transverse piezoelectric coefficient ( $e_{31,f}$  - the subscript  $f$  after a piezoelectric coefficient denotes an effective coefficient for a thin film). Remnant polarization is poled along the norm of the thin film under the electric field with the same direction, leading to the strain in the thickness direction and the stress in the in-plane directions. The unimorph structure of the cantilever bends when the induced stress of the piezoelectric layer acts on the passive elastic layer. Alternatively, interdigitated electrodes can be patterned on the ferroelectric film surface if the film is deposited on an insulating substrate. With such configuration, remnant polarizations are induced between two electrode fingers along the in-plane direction. The longitude piezoelectric coefficient is used to produce the in-plane strain, on actuation with an electric field, to deflect the unimorph structure of the cantilever. Moreover, although the surface displacement induced by the out-of-plane  $d_{33}$  coefficient with the top and bottom electrodes is modest, the so-called piston motion as shown in Figure I.9 (c) can be useful in some potential electronics applications<sup>[99]</sup>.

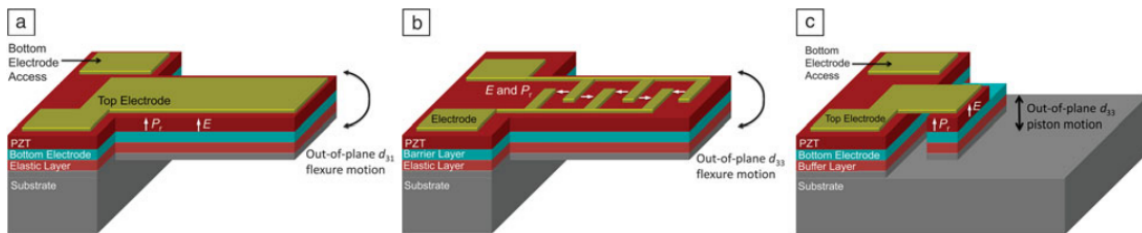


Figure I.9 - Illustration of common sensing and actuation modes in piezoelectric MEMS.

Except for the piezoelectric coefficients discussed above, other parameters in Table I.3 are also important and of interest in addition to force, deflection and piezoelectric charge (current). For piezoelectric energy harvesting with deflected laminated structure, the true power generation figure of merit concerns both the piezoelectric coefficient as well as the relative dielectric constant, i.e.  $d_{31,f}/\epsilon_0\epsilon_{33}$ . This figure of merit averages the generated power of the cantilever with consideration of cantilever power loss by transfer of energy to the piezoelectric layer. Coupling coefficient ( $k^2$ ) describes the effectiveness of energy transformation from electrical to mechanical energy, which is essential for resonating structures. Part of the electrical energy is dissipated and transformed to heat, which is defined by dielectric loss tangent ( $\tan \delta$ ). In piezoelectric sensor, dielectric loss also imposes limits to the resolution by generating a noise current or voltage, i.e. the signal-to-noise ratio. Table I.3 also lists those parameters for three common used piezoelectric materials. Among those materials, lead-based materials PZT have the

## Chapter I - Physical principles and motivations

largest piezoelectric coefficient and dielectric constant. However, for application of energy harvesting small dielectric constant is of advantage since that generates large output voltage and current and, therefore, AlN and ZnO with small piezoelectric coefficient is useful.

**Table I.3 - Thin film piezoelectric and dielectric properties.**

Physical parameter	Coefficients/figures of merit	ZnO	AlN	PZT
Deflection force, piezoelectric charge of deflected piezoelectric laminated structure	$e_{31,f}$ (C/m <sup>2</sup> )	-1.0	-1.05	-8 ~ -12
Longitude piezoelectric coefficient	$d_{33,f}$ (pm/V)	5.9	3.9	60 ~ 130
Dielectric constant of planar capacitor structure	$\epsilon_{33}$	10.9	10.5	300 ~ 1300
Piezoelectric voltage in deflected piezoelectric laminated structure	$d_{31,f}/\epsilon_0\epsilon_{33}$ (GV/m)	-10.3	-11.3	-0.7 ~ -1.8
Coupling coefficient for plate wave	$e_{31,f}^2/\epsilon_0\epsilon_{33}$ (GPa)	10.3	11.9	6 ~ 18
Dielectric loss tangent	$\tan\delta$ (@ 1 to 10 kHz, 10 <sup>5</sup> V/m)	0.01 ~ 0.1	0.003	0.01 ~ 0.03
Signal-to-noise ratio	$e_{31,f}/\sqrt{\epsilon_0\epsilon_{33}\tan\delta}$ (10 <sup>5</sup> Pa <sup>1/2</sup> )	3 ~ 10	20	4 ~ 8
Coupling coefficient for thickness wave	$d_{33,f}^2 \cdot c_{33}^E/\epsilon_0\epsilon_{33}$	7.4 %	6.5 %	7 % ~ 15 %

### I.3.2) Influence of ferroelectric thin films

#### I.3.2.1) Effect of film orientation

Since the piezoelectric properties of ferroelectric materials originate from spontaneous polarization, piezoelectric coefficients can be defined from the perspective of electrostriction which determines the elastic strain induced by the interaction of electric dipoles:

$$d_{im} = \epsilon_{ik} Q_{mik} P_k \quad \text{Equ. I.7}$$

where  $Q$  is the electrostriction coefficients, and  $P$  is the spontaneous polarization. In the particular case of tetragonal structure where the spontaneous polarization  $P$  aligns in the longest axis of the lattice, the piezoelectric coefficients can be defined as below:

$$\begin{aligned} d_{33} &= 2\epsilon_{33} Q_{33} P_3 \\ d_{31} &= d_{32} = 2\epsilon_{33} Q_{13} P_3 \\ d_{15} &= d_{24} = 2\epsilon_{11} Q_{44} P_3 \end{aligned} \quad \text{Equ. I.8}$$

The other piezoelectric coefficients in Equation I.3 are equal to zero due to the rotational symmetry. For thin film, the “3” subscript usually indicates the normal to the film surface, and  $d_{33}^*$  constant represents the effective longitudinal piezoelectric coefficient, which is not

necessarily parallel to the permanent polarization. Considering a piezoelectric film with  $n^{(3)}$  normal direction applied by an electric field  $E_3$  in the same direction,  $d_{33}^*$  constant is also determined by the relative orientation of spontaneous polarization in the film, which can be derived by rotational transform (the summation is taken over repetitive suffixes):

$$d_{33}^* = d_{kij} n_k^{(3)} n_i^{(3)} n_j^{(3)} \quad (i, j, k = 1, 2, 3) \quad \text{Equ. I.9}$$

where  $n_k^{(3)}$ ,  $n_i^{(3)}$ , and  $n_j^{(3)}$  are the components of the normal vector of the surface in the Cartesian coordinates of the crystalline lattice.

On the other hand, ferroelectric thin film is often involved in a composite structure interacting with the other layers of the heterostructure, like elastic layer, silicon substrate, template, for instance, which can be regarded as a mechanically closed system, as shown in Figure I.10 for piezoelectric cantilever.

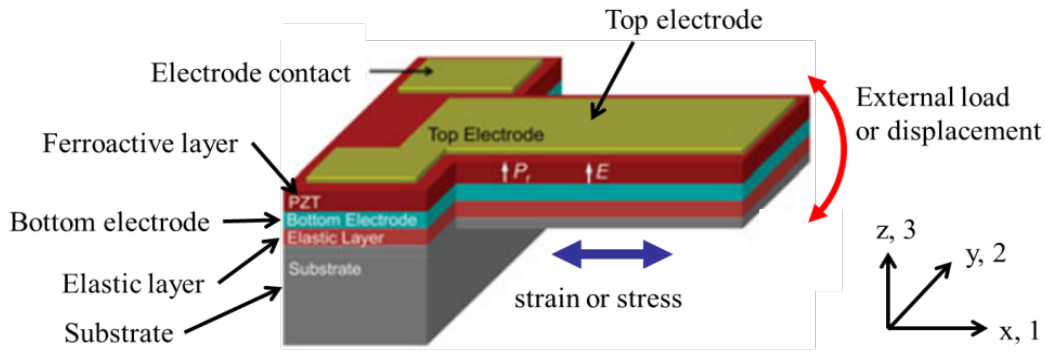


Figure I.10 - Actuator and sensor applications for piezoelectric laminated cantilever.

Such interaction with the substrate is very anisotropic, leading to the identical strains along the in-plane directions (indices 1, 2) and the zero stress perpendicular to the film surface (index 3). Therefore, the effective deformation of the thin film is dependent of not only one piezoelectric coefficient. For the film on a very thick (or rigid) substrate, the *so-called* effective piezoelectric coefficient is available with consideration of the compliance tensor ( $S$ ) and the piezoelectric coefficient ( $d$ ):

$$e_{31,f} = \frac{d_{31}}{s_{11}^E + s_{12}^E} \quad \text{and} \quad d_{33,f} = d_{33} - \frac{2s_{13}^E}{s_{11}^E + s_{12}^E} d_{31} \quad \text{Equ. I.10}$$

The above equations turn out that  $d_{33,f}$  is always smaller than  $d_{33}$  and that the absolute value of  $e_{31,f}$  is always larger than that of  $e_{31}$ , both of which can be measured directly. Another effect of substrate clamping is the inequality of direct and converse piezoelectric coefficients in the form of thin film <sup>[100]</sup>. Figure I.11 theoretically predicts the effective longitudinal piezoelectric

coefficient  $d_{33}^*$  for two PZT materials, i.e. tetragonal PZT (50:50) and rhombohedral PZT (52:48), which are clamped on silicon and STO substrates <sup>[101]</sup>. For both tetragonal and rhombohedral PZT films, the maximum  $d_{33}^*$  is found in the direction along or very close to the pseudocubic [001] direction. The converse piezoelectric coefficient is not substrate-dependent, while the direct piezoelectric coefficient exhibits a larger value for the film on a relatively soft substrate (Si) than on a relatively rigid substrate (STO). However, both direct and converse piezoelectric coefficients show a smaller value than that of bulk material due to the clamping effect of the substrate.

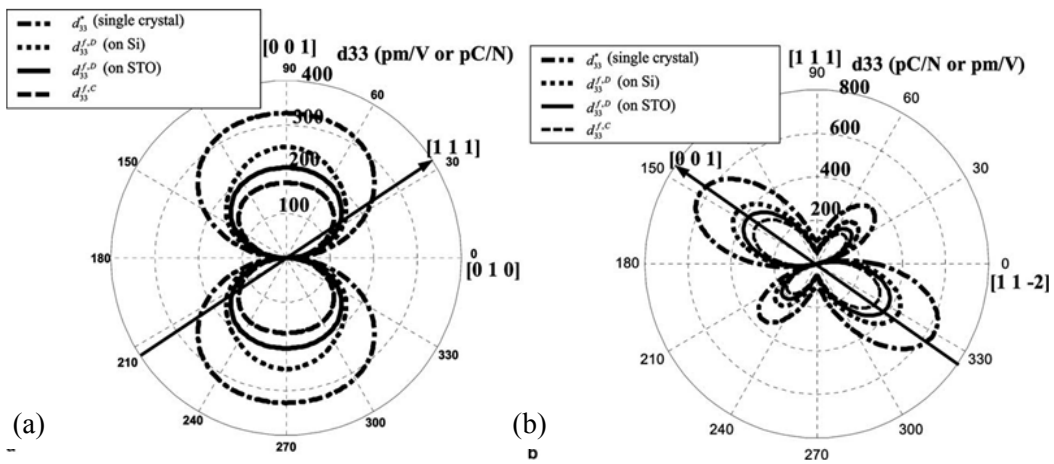


Figure I.11 - Effective longitudinal piezoelectric coefficient  $d_{33}^*$  as a function of film orientation for the case of (a) tetragonal PZT (50/50) film and (b) rhombohedral PZT (52/48) film on various substrates <sup>[102]</sup>.

### I.3.2.2) Effect of residual stress

Residual stress is another important effect relating with the dielectric constant <sup>[103]</sup> and the piezoelectric properties <sup>[104,105,106]</sup> of the epitaxial ferroelectric films. Generally, three types of residual stress possibly develop in the epitaxial films, such as epitaxial stress, thermal stress and transformation stress <sup>[107]</sup>. Epitaxial stress results from the lattice mismatch between the film lattice parameter ( $a_0$ ) and the substrate lattice parameter ( $a_s$ ) at growth temperature. Since the substrate thickness is much greater than that of the film, the induced epitaxial stress is tensile when  $a_s > a_0$  or compressive when  $a_s < a_0$ . The lattice mismatch is defined as follows:

$$f = (a_s - a_0)/a_0 \quad \text{Equ. I.11}$$

Epitaxial stress can be released by forming dislocations at film/substrate interfaces or increasing the film thickness. Thermal stress develops due to the different thermal expansion coefficients between the film and the substrate during cooling process in the fabrication. Taking epitaxial PZT film on silicon substrate as an example, the thermal expansion coefficient of PZT is about

$7.0 \times 10^{-6} \text{ K}^{-1}$ , larger than that of silicon ( $2.6 \times 10^{-6} \text{ K}^{-1}$ ). During the cooling process, PZT film contracts less than the bulk one due to the clamping of silicon substrate, leading to a tensile residual stress. Lee *et al* investigated the effect of thermal residual stress in PZT film <sup>[108]</sup>. It was concluded that higher remnant polarization ( $P_r$ ) and higher saturation polarization ( $P_s$ ) will be induced when compressive stress occurs, while piezoelectric properties will be enhanced when tensile stress occurs. Transformation stress involves the ferroelectric-paraelectric phase transition in ferroelectric materials, leading to the multiply preferred orientations of the lattice. Figure I.12 (a) demonstrates the three possible variants of tetragonal lattice originated from initial cubic lattice when the temperature decreases below the Curie temperature <sup>[109]</sup>. The free energy may increase due to the domain interfaces and the lattice mismatch between the film and the substrate. To minimize the free energy, textured structure of ferroelectric domains will develop in the film. The architecture of ferroelectric domains can be either *a/c/a/c* 2-domain structure for small *c*-domain fractions (Figure I.12 (b)) or 3-domain structures in cellular arrangement for relatively large *c*-domain fractions (Figure I.12 (c)). Moreover, for lead-based ferroelectric materials, pyrochlore phase probably forms depending on the growth conditions. The study of process-dependent PZT film exhibits that pyrochlore-free PZT film has less internal stress than that of pyrochlore-containing PZT film <sup>[110]</sup>.

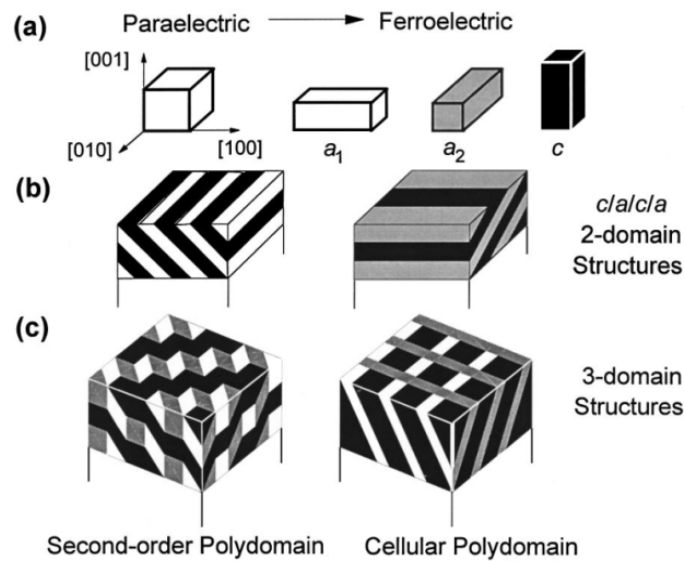


Figure I.12 - (a) the cubic-tetragonal transform of crystalline structure at the Curie temperature, (b) the formation of *c/a/c/a* 2-domain architecture, and (c) the formation of 3-domain architecture below the Curie temperature <sup>[111]</sup>.

#### I.4) Single crystal piezoelectric films on Si: state of the art

Two important ferroelectric materials are mainly concerned in this thesis, namely PZT and PMN-PT, for their epitaxy on silicon substrate. Both materials are lead-based ferroelectrics

holding large dielectric constant and piezoelectric coefficients, especially for PMN-PT which is a typical relaxor ferroelectric material. In this section, we will introduce the historical development and the state-of-art technology for the integration of those two materials on Si.

#### **I.4.1) Epitaxial PZT films**

Most applications of PZT films, which cover from dynamic random access memories, field effect transistors, ferroelectric random access memories, to piezoelectric MEMS <sup>[111, 112]</sup>, require the growth of high-quality PZT films on silicon to promote their performances. Intermediate template layer and chemical barrier must be carefully considered to prevent undesired inter-diffusion between the substrate and the PZT film and oxidation reactions <sup>[113]</sup>. In the applications, PZT films are usually inserted between conductive top and bottom electrodes in order to form a metal-insulator-metal heterostructure. Due to simple fabrication and excellent conductivity, platinumized silicon substrate is widely used as template. Thin Ti adhesive layer is usually deposited between Pt electrode and Si substrate to ameliorate crystalline quality and therefore electrical properties of the PZT films: this is mainly due to the formation of an additional TiO<sub>2</sub> layer on Pt surface <sup>[114]</sup>. In fact, Pt layer does not inhibit the diffusion of Ti to its surface so that Ti reacts with oxygen into TiO<sub>2</sub> during the thermal treatment <sup>[115]</sup>. The additional TiO<sub>2</sub> layer plays the role of nucleation centers for growth of PZT films, giving better crystalline structure and therefore enhanced electrical properties compared with those PZT films directly grown on Pt electrode <sup>[116]</sup>. However, epitaxial growth of PZT films on polycrystalline metallic electrode often generates high-density defects which prevent the movement of ferroelectric domain walls <sup>[117]</sup>. Polarization switching is therefore suppressed due to such pinning effect, giving rise to the dead-layer problem <sup>[118]</sup>. Moreover, the fatigue problem which occurs in the PZT films on metallic electrode is attributed to the oxygen vacancies trapped near metal/oxide interface. The trapped oxygen vacancies have been also identified as being responsible for the increase of leakage current (dc degradation) in the capacitors <sup>[119, 120]</sup>, and would build an internal electric field in the films to prevent further domain switching. To delay apparition of the fatigue, use of oxide template on Pt layer has been proven as an effective approach. Besides, better fatigue resistance of PZT films can be intentionally obtained when both top and bottom electrodes are conductive oxides <sup>[121]</sup>. Actually, the enhanced fatigue resistance of PZT films is due to the fact that the oxide acts as an “oxygen sink” which can fill the oxygen vacancies during switching cycle <sup>[122]</sup>. Several oxide electrodes, like RuO<sub>2</sub> <sup>[123, 124]</sup>, SrRuO<sub>3</sub> (SRO), YBa<sub>2</sub>Cu<sub>3</sub>O<sub>7-δ</sub> (YBCO) <sup>[125]</sup>, LiNbO<sub>3</sub> <sup>[126, 127]</sup>, La<sub>x</sub>Sr<sub>1-x</sub>CoO<sub>3</sub> (LSCO) <sup>[128]</sup> have been proposed for PZT capacitors.

PZT film was deposited by sol-gel method with RuO<sub>2</sub> top and bottom electrodes <sup>[129]</sup>. It was observed that the film shows no polarization fatigue up to 10<sup>11</sup> switching cycles. The enhanced

fatigue resistance is also attributed to the increased stability of RuO<sub>2</sub>/PZT interface which has a low lattice mismatch, a more favorable contact potential, and a sharp interface structure without virtual inter-diffusion. In the same way, PZT film with YBCO top and bottom electrodes shows very little polarization fatigue up to the same number of switching cycles. On the contrary, a Pt/PZT/Pt capacitor typically exhibits fatigue-free behavior only to 10<sup>8</sup> - 10<sup>9</sup> cycles [130]. These PZT films deposited on oxide/Pt template are often polycrystalline with certain orientation preference. Thus, the piezoelectric performances can be further promoted if the textured structure of PZT film is improved. R. Ramesh *et al.* reported the use of yttria-stabilized zirconia (YSZ) deposited by RF sputtering to completely substitute metallic template [125, 128]. Highly oriented PZT films were deposited with either YBCO or LSCO electrode on YSZ-buffered Si substrate. The fatigue problem was dramatically decreased, leading that the PZT capacitor shows a larger remnant polarization  $\Delta P$  of 25-30  $\mu\text{C}/\text{cm}^2$  for an applied field of only 70 kV/cm ( $\Delta P$  = switched polarization - non-switched polarization). Besides, better fatigue resistance was observed with symmetrical electrodes, i.e. oxide/ferroelectric/oxide, as compared with the one with single oxide electrode [131].

In parallel, R. A. McKee *et al.* demonstrated a successful method to grow a layer of commensurate crystalline STO on silicon substrate with an abrupt oxide/Si interface, using Molecular Beam Epitaxy (MBE) [132, 133]. The availability of such a high-quality perovskite-terminated Si(001) substrate attracted increasing interest to integrate various functional oxides on Si wafer, like Sr<sub>x</sub>Ba<sub>1-x</sub>TiO<sub>3</sub> [134], BiFeO<sub>3</sub> [135], LaAlO<sub>3</sub> [136]. In 2001, researchers in Motorola Lab published a pioneer work concerning the successful integration of epitaxial PZT films on Si substrate by using STO template and LSCO electrode [137]. Compared with YSZ template, this heterostructure is relatively simple and the STO template has the same perovskite structure as PZT. Clean and sharp interfaces between layers are observed with negligible inter-diffusion. Larger piezoelectric coefficients and smaller dielectric constants were obtained as compared to YSZ-buffered Si substrate, which was associated with the smaller in-plane lattice mismatch [138]. The epitaxial relationship in the heterostructure was verified by XRD as (100) PZT [001] // (100) LSCO [001] // (100) STO [001] // (110) Si [001]. Systematic study of the influence of different substrates, like Pt/Si, LSCO/Pt/Si and LSCO/STO/Si, showed an enhanced piezoelectric coefficient ( $d_{33}$ ) with increasing the crystalline quality of PZT films (Figure I.13). Highest piezoelectric coefficient was found in the epitaxial PZT film on LSCO/STO/Si substrate, i.e. 125 pm/V for PZT(40/60) and 200 pm/V for PZT(52:48). The values are closed to the theoretical prediction if the clamping effect of silicon substrate is taken into consideration [139].

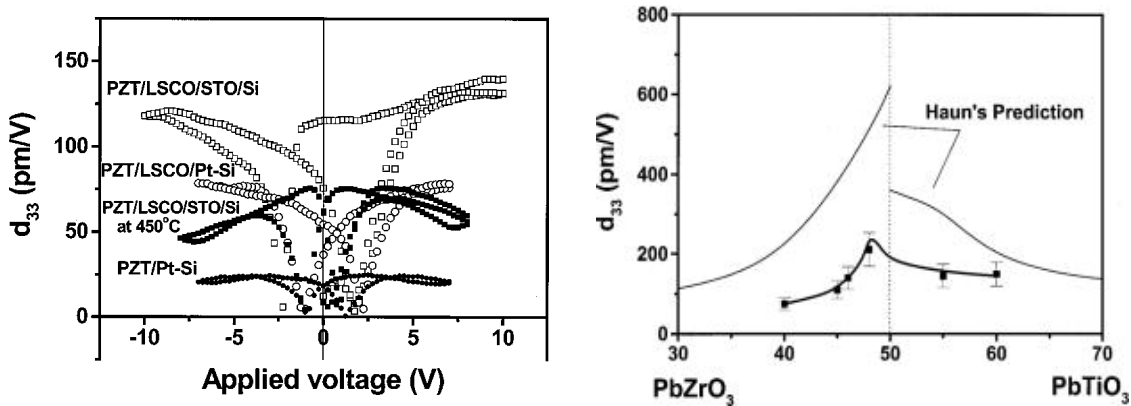


Figure I.13 - Piezoelectric hysteresis loops measured using PFM for (left) 4 heterostructures and (right) the different chemical compositions <sup>[141]</sup>.

Then, different deposition technologies with various oxide electrodes have been proposed to integrate PZT films on STO-buffered Si substrate, like PLD with SRO <sup>[140]</sup> or  $(\text{La}_x\text{Sr}_{1-x})\text{MnO}_3$  <sup>[141]</sup> electrodes, sol-gel method with SRO <sup>[140]</sup> or LSCO <sup>[142]</sup> electrode, off-axis magnetron sputtering with SRO electrode <sup>[143]</sup>. The diversity of fabrication technologies largely excites the research interest to employ epitaxial PZT films in MEMS devices. E. K. Reilly and P. K. Wright presented their first MEMS device which was based on PLD-deposited PZT film with STO buffer layer and SRO bottom electrode on Si substrate <sup>[144]</sup>. Then, a similar device has been demonstrated using off-axis magnetron sputtering <sup>[145]</sup>, which gave a piezoelectric coefficient ( $d_{31}$ ) of 130 pm/V for PZT(20:80). The quality factor  $Q$  of an epitaxial PZT/Si cantilever reached 169 in air and 284 in vacuum at the resonance. Vibration energy harvester based on PZT/SRO/STO/SOI heterostructure was successfully fabricated, as illustrated in Figure I.14 <sup>[146]</sup>, <sup>[147]</sup>. Large piezoelectric coefficient ( $e_{31} = -18.2 \pm 0.9 \text{ C/m}^2$ ) together with low dielectric constant ( $\epsilon = 150$ ) of the epitaxial PZT(20:80) film is the key advantage to realize high performance piezoelectric energy harvesters. Power density as high as  $105 \mu\text{W}\cdot\text{g}^{-2}\cdot\text{mm}^{-3}$  was generated with small resistive load and high electric current. The low optimal load resistance is considered as being easily matched with standard electronics. It is superior to what is obtained by polycrystalline PZT and AlN films whose high impedance limits the output current.

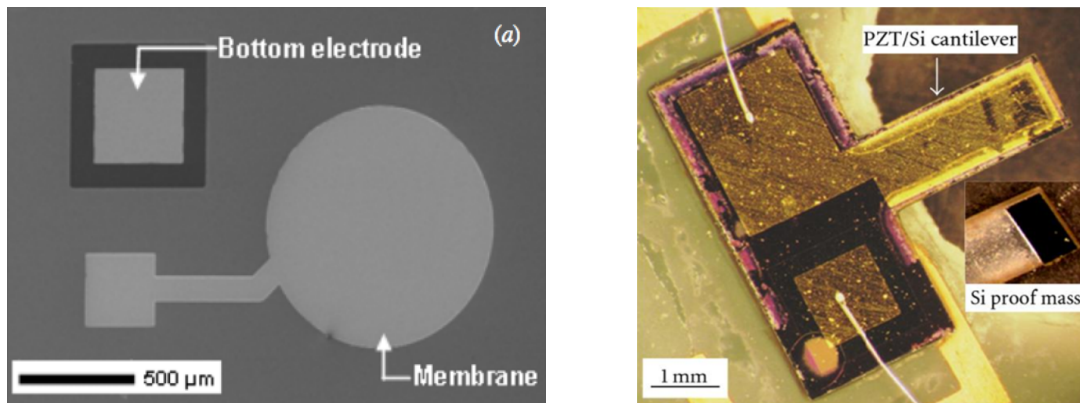


Figure I.14 - The epitaxial PZT/Si membrane in Ref. 146 (left) and the energy harvester with a Si proof mass in Ref. 146 (right) .

#### I.4.2) Epitaxial PMN-PT films

Due to its compositional complexity and poor thermodynamic stability, epitaxial growth of good quality PMN-PT films is much difficult [148,149]. In order to obtain epitaxial single-crystal PMN-PT films, early researches are mainly based on oxide substrates, like MgO [150, 151] and STO [148, 152]. C. B. Eom *et al* reported their first use of vicinal (001) STO substrate with  $>4^\circ$  miscut to stabilize the perovskite PMN-PT phase and successfully obtained the almost PMN-PT pure phase with good stoichiometry [153]. Compared with exact (001) STO substrate, the high-density steps on the top surface of the miscut STO substrate can effectively depress the formation of pyrochlore PMN-PT phase. On the other hand, platinized Si was firstly proposed for integration of PMN-PT on Si. However, epitaxial PMN-PT films grown on platinized Si often show a textured perovskite phase with (111)-preferred orientation along the norm of the film surface and the randomly distributed in-plane orientations, leading to a polycrystalline structure in the film. This textured polycrystalline structure with high-density grain boundaries and the dead layer induced by oxide/Pt interface will deteriorate the piezoelectric performance of PMN-PT films. Therefore, in order to promote the formation of high-quality perovskite PMN-PT structure, oxide seeding layers on Pt/Si were employed, like LSCO [154], BaTiO<sub>3</sub> [155], LaNiO<sub>3</sub> [156, 157] and TiO<sub>2</sub> [158]. Furthermore, a CeO<sub>2</sub>/YSZ/Si substrate was proposed to completely replace the metallic template for highly c-axis oriented PMN-PT film on Si [159, 160, 161]. However, a critical thickness of about 700 nm still limits the film quality of such epitaxial PMN-PT film, above which pyrochlore phase appears in the matrix of perovskite PMN-PT. In 2011, C. B. Eom's group successfully combined two technologies, namely STO buffer layer and miscut Si wafer ( $\sim 4^\circ$ ), to deposit epitaxial 0.67PMN-0.33PT films on silicon, where SRO was used for bottom electrode [162]. The  $\mu\text{m}$ -thick PMN-PT film shows a dramatic improvement in both phase purity and epitaxial pyrochlore-free phase (Figure I.15). Micro-cantilever structure was fabricated, showing

a well-defined linearity of piezoelectric response under ac and dc voltage. After pre-poling process, an effective  $e_{31,f}$  coefficient as high as  $-27 \pm 3$  C/m<sup>2</sup> was measured, which are the highest reported  $e_{31,f}$  value for any piezoelectric thin films. A large figure of merit for energy harvesting ( $\sim 50$ ) was determined, exceeding all the previously reported values for ferroelectric energy harvester. With such large transversal piezoelectric coefficients, the required actuation voltage can decrease below 2.5 V while keeping a sufficiently large electric-field-induced displacement. Such low actuation voltage is compatible with the low-voltage CMOS circuits. Therefore, the excellent piezoelectric performance of epitaxial PMN-PT films can provide a wide range of piezoelectric device applications, such as ultrasound medical imaging, microfluidic control, piezotronics, and energy harvesting.

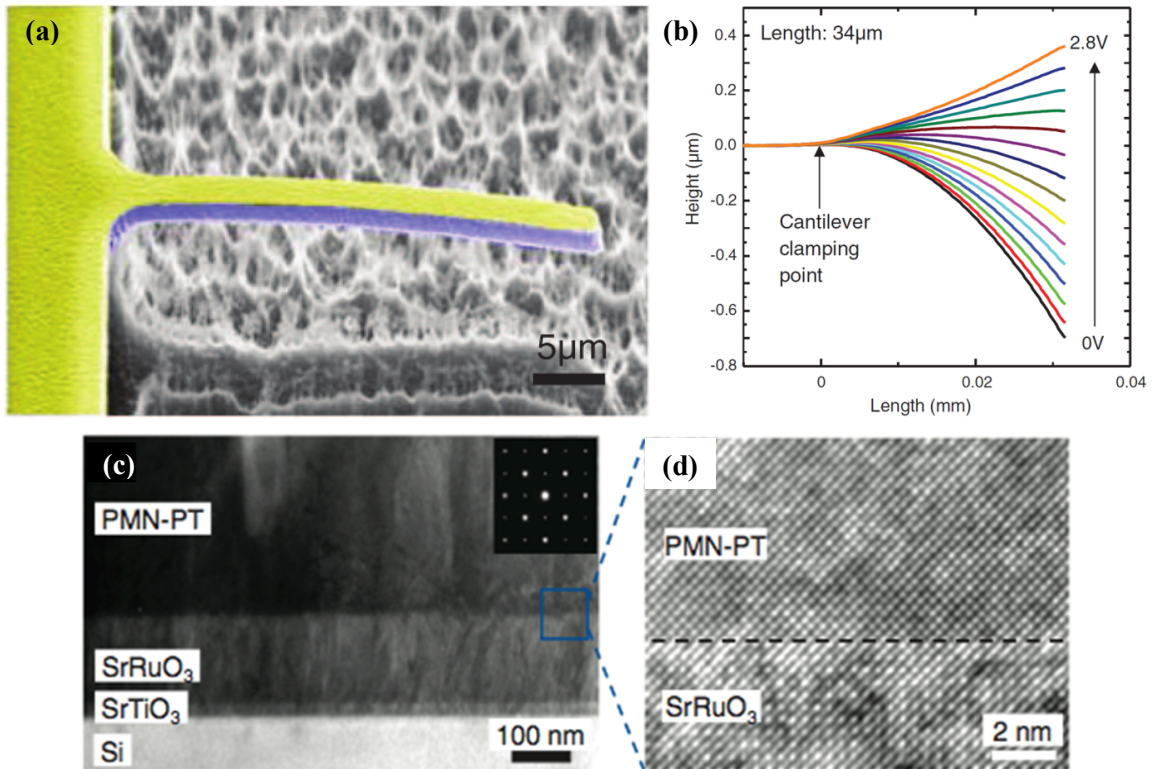


Figure I.15 - Fabrication and characterization of PMN-PT micro-cantilevers. (a) SEM image of PMN-PT cantilever. (b) Cantilever profile as a function of dc voltage. (c) Bright-field cross-sectional TEM image near the PMN-PT/SRO interface. (d) High-resolution TEM image of PMN-PT/SRO interface <sup>[162]</sup>.

### I.4.3) Summary

As we discussed above, the effective strategy to enhance piezoelectric properties of ferroelectric films on silicon is the epitaxial deposition of high-quality single-crystal films. To satisfy such requirement, two approaches can be taken: (i) utilizing perovskite oxide to substitute

metallic template on silicon to have a commensurate oxide/Si interface, and (ii) introducing oxide bottom electrode as oxygen sink, thus leading to low oxygen vacancies and better electrical performance. In this thesis, we will utilize sol-gel method to deposit ferroelectric thin film, i.e. PZT and PMN-PT, on silicon wafer by using STO template and SRO bottom electrode.

### **I.5) Objectives of the thesis**

The research work of the thesis was carried out in the framework of and funded by a French National Research Agency (ANR) project, Single crystal dielectric thin films for integrated capacitors (MOCA), ANR-10-NANO-0020. MOCA brought together 4 major French laboratories, Laboratoire d'Electronique et de Technologie de l'Information (LETI), Institut des Nanotechnologies de Lyon (INL), Laboratoire Structures, Propriétés et Modélisation des Solides (SPMS), Institut Franche-Comté Electronique Mécanique Thermique et Optique - Sciences et Technologies (FEMTO-ST) and a private company STmicroelectronics in Tours, to develop and provide a clear status on the superiority of the epitaxial single-crystal thin films in various targeted proofs of concept, like acoustic resonators, high-K capacitors and piezoelectric actuators, compared to their polycrystalline counterpart. The MOCA project involves the research of heterogeneous integration of functional materials on Si substrate to increase the interaction, like sensing, actuation, time reference, frequency filters, integrated capacitors, as close as possible to the microelectronic one, which allows envisioning new devices associated with the “More Moore” concept. Beyond miniaturization, more functions can be added onto the existing Si technologies (diversification) in a “more than Moore” approach where the European semiconductor industry plays a worldwide leading role. The properties of single crystal perovskite materials which exhibit an impressive series of outstanding coupling properties, like dielectric constant, piezoelectric coefficient, pyroelectric coefficient, are expected to overcome those of corresponding polycrystalline films. Therefore, it appears very promising to develop technological routes allowing the synthesis of single crystal ferroelectric materials on Si substrates and decrease the technology cost without any trade-off concerning the material quality. This approach will induce a huge societal impact by allowing in one hand for a more in-depth penetration in the mass market of new functionalities related to these materials as the technology proposed is compatible with existing mass fabrication plants and on the other hand notable advances in state-of-the-art material quality.

In this thesis, two piezoelectric oxides are mainly developed and researched, namely PZT (52:48) and 0.9PMN-0.1PT, for their epitaxial growth on silicon substrate and various characterizations. The research will address the special issue of the integration of single crystal thin films with silicon-based technologies by a bottom-up approach (epitaxy). As this technology

constitutes a high breakthrough compared to the standard way, the research will be proposed in the “fundamental research” framework. In this approach, the originality of the research is to obtain silicon-compatible epitaxial high quality materials by using different deposition tools derived from the microelectronic industry: MBE, sol-gel and PLD. In the partners of the project, INL has a strong experience on the growth of STO single crystal layers on Si by using MBE method. For the application, the deposition of low resistivity bottom electrode is a mandatory requirement for most devices, which is accessible by using PLD method in NIMP (National Institute of Materials Physics, Romania). Besides, LETI could process the sol-gel layers deposited on STO buffered layers, which has been conventionally utilized for a long time to grow ferroelectric films on 200 mm Si wafer in their MEMS research. The research will therefore give the opportunity to benchmark sol-gel, PLD and MBE techniques. This innovative approach will provide original and important data on the ability to provide high quality films with standard technologies which is a crucial point to go through integration.

## I.6) Reference

- 
- [1] P. A. Payne, J. V. Hatfield, A. D. Armitage, Q. X. Chen, P. J. Hicks and N. Scales, “Integrated ultrasound transducers,” in *Proceedings of IEEE Ultrasonics Symposium ULTSYM-94*, 1994, pp. 1523–1526 **vol.3**.
- [2] R. A. Wolf, K. K. Deng, R. J. Davis, and S. Trolier-McKinstry, “Design, fabrication, and measurement of high-sensitivity piezoelectric microelectromechanical systems accelerometers,” *Journal of Microelectromechanical Systems*, **vol. 12**, no. 4, pp. 433–439, Aug. 2003.
- [3] H. G. Yu, L. Zou, K. Deng, R. Wolf, S. Tadigadapa, and S. Trolier-McKinstry, “Lead zirconate titanate MEMS accelerometer using interdigitated electrodes,” *Sensors and Actuators A: Physical*, **vol. 107**, no. 1, pp. 26–35, Oct. 2003.
- [4] Kenji Uchino, (1997). “*Piezoelectric Actuators and Ultrasonic Motors*”. Kluwer Academic Publishers.
- [5] N. Ledermann, P. Muralt, J. Baborowski, M. Forster, and J.-P. Pellaux, “Piezoelectric  $\text{Pb}(\text{Zr}_x\text{Ti}_{1-x})\text{O}_3$  thin film cantilever and bridge acoustic sensors for miniaturized photoacoustic gas detectors,” *Journal of Micromechanics and Microengineering*, **vol. 14**, no. 12, pp. 1650–1658, Dec. 2004.
- [6] H.-B. Fang, J.-Q. Liu, Z.-Y. Xu, L. Dong, L. Wang, D. Chen, B.-C. Cai, and Y. Liu, “Fabrication and performance of MEMS-based piezoelectric power generator for vibration energy harvesting,” *Microelectronics Journal*, **vol. 37**, no. 11, pp. 1280–1284, Nov. 2006.
- [7] H. Zhang, E.S. Kim, “Micromachined acoustic resonant mass sensor,” *Journal of Microelectromechanical Systems*, **vol. 14**, no. 4, pp. 699–706, Aug. 2005.

- [8] G. Caliano, N. Lamberti, A. Iula, and M. Pappalardo, "A piezoelectric bimorph static pressure sensor," *Sensors and Actuators A: Physical*, **vol. 46**, no. 1–3, pp. 176–178, Jan. 1995.
- [9] G. Uma, M. Umopathy, S. Jose, V. Natarajan, and M. Kathiresan, "Design and Simulation of PVDF-MOSFET Based MEMS Hydrophone," *Instrumentation Science & Technology*, **vol. 35**, no. 3, pp. 329–339, Apr. 2007.
- [10] S. C. Ko, Y. C. Kim, S. S. Lee, S. H. Choi, and S. R. Kim, "Micromachined piezoelectric membrane acoustic device," *Sensors and Actuators A: Physical*, **vol. 103**, no. 1–2, pp. 130–134, Jan. 2003.
- [11] L.-P. Wang, K. Deng, L. Zou, R. Wolf, R. J. Davis, and S. Trolier-McKinstry, "Micro-electromechanical systems (MEMS) accelerometers using lead zirconate titanate thick films," *IEEE Electron Device Letters*, **vol. 23**, no. 4, pp. 182–184, Apr. 2002.
- [12] A. M. Madni, L. E. Costlow, and S. J. Knowles, "Common design techniques for BEI GyroChip quartz rate sensors for both automotive and aerospace/defense markets," *IEEE Sensors Journal*, **vol. 3**, no. 5, pp. 569–578, Oct. 2003.
- [13] P. W. Kruse, "Uncooled IR focal plane arrays," *Proc. SPIE 2552, Infrared Technology XXI*, pp. 556–63 (1995).
- [14] F. Akasheh, T. Myers, J. D. Fraser, S. Bose, and A. Bandyopadhyay, "Development of piezoelectric micromachined ultrasonic transducers," *Sensors and Actuators A: Physical*, **vol. 111**, no. 2–3, pp. 275–287, Mar. 2004.
- [15] F. Filhol, E. Defaÿ, C. Divoux, C. Zinck, and M.-T. Delaye, "Resonant micro-mirror excited by a thin-film piezoelectric actuator for fast optical beam scanning," *Sensors and Actuators A: Physical*, **vol. 123–124**, pp. 483–489, Sep. 2005.
- [16] N.-T. Nguyen and T.-Q. Truong, "A fully polymeric micropump with piezoelectric actuator," *Sensors and Actuators B: Chemical*, **vol. 97**, no. 1, pp. 137–143, Jan. 2004.
- [17] I. Chakraborty, W. C. Tang, D. P. Bame, and T. K. Tang, "MEMS micro-valve for space applications," *Sensors and Actuators A: Physical*, **vol. 83**, no. 1–3, pp. 188–193, May 2000.
- [18] J. Brünahl and A. M. Grishin, "Piezoelectric shear mode drop-on-demand inkjet actuator," *Sensors and Actuators A: Physical*, **vol. 101**, no. 3, pp. 371–382, Oct. 2002.
- [19] K. Uchino, S. Cagatay, B. Koc, S. Dong, P. Bouchilloux, and M. Strauss, "Micro Piezoelectric Ultrasonic Motors," *Journal of Electroceramics*, **vol. 13**, no. 1–3, pp. 393–401, Jul. 2004.
- [20] M.-H. Lin, H.-T. Hsieh, W.-Y. Hsu, Y.-C. Cheng, C.-H. Wu and G.-D. J. Su, "Auto-focus imaging systems with MEMS deformable mirrors", *Proc. Current Developments Lens Design Opt. Eng. X*, pp.74280Q 2009.

- [21] Hee-Chul Lee, Jae-Yeong Park, Jong-Uk Bu, “Piezoelectrically actuated RF MEMS DC contact switches with low voltage operation,” *IEEE Microwave and Wireless Components Letters*, **vol. 15**, no. 4, pp. 202–204, Apr. 2005.
- [22] G. Piazza, P. J. Stephanou, and A. P. Pisano, “Single-Chip Multiple-Frequency ALN MEMS Filters Based on Contour-Mode Piezoelectric Resonators,” *Journal of Microelectromechanical Systems*, **vol. 16**, no. 2, pp. 319–328, Apr. 2007.
- [23] J. Y. Park, Y. J. Yee, H. J. Nam, and J. U. Bu, “Micromachined RF MEMS tunable capacitors using piezoelectric actuators,” in *2001 IEEE MTT-S International Microwave Symposium Digest (Cat. No. 01CH37157)*, **vol. 3**, pp. 2111–2114.
- [24] R. Ruby, “Review and comparison of bulk acoustic wave FBAR,” *SMR technology Proc. IEEE Ultrasonics Symp.* **vol. 7**, pp. 1029–40, 2007.
- [25] Tim Zander, Andreas Herklotz, Suwit Kiravittaya, Mohamed Benyoucef, Fei Ding, Paola Atkinson, Santosh Kumar, Johannes D. Plumbhof, Kathrin Dörr, Armando Rastelli, and Oliver G. Schmidt, “Epitaxial quantum dots in stretchable optical microcavities,” *Optics Express*, **vol. 17**, Issue 25, pp. 22452–22461 (2009).
- [26] G. K. Ottman, H. F. Hofmann, A. C. Bhatt, and G. A. Lesieutre, “Adaptive piezoelectric energy harvesting circuit for wireless remote power supply,” *IEEE Transactions on Power Electronics*, **vol. 17**, no. 5, pp. 669–676, Sep. 2002.
- [27] Z. L. Wang and J. Song, “Piezoelectric nanogenerators based on zinc oxide nanowire arrays,” *Science (New York, N.Y.)*, **vol. 312**, no. 5771, pp. 242–6, Apr. 2006.
- [28] Q. Q. Zhang, S. J. Gross, S. Tadigadapa, T. N. Jackson, F. T. Djuth, and S. Trolier-McKinstry, “Lead zirconate titanate films for  $d_{33}$  mode cantilever actuators,” *Sensors and Actuators A: Physical*, **vol. 105**, no. 1, pp. 91–97, Jun. 2003.
- [29] S. Koganezawa, Y. Uematsu, T. Yamada, H. Nakano, J. Inoue, and T. Suzuki, “Dual-stage actuator system for magnetic disk drives using a shear mode piezoelectric microactuator,” *IEEE Transactions on Magnetics*, **vol. 35**, no. 2, pp. 988–992, Mar. 1999.
- [30] D. A. McHenry, J. Giniewicz, S. J. Jang, A. Bhalla, and T. R. Shrout, “Optical properties of hot pressed relaxor ferroelectrics,” *Ferroelectrics*, **vol. 93**, no. 1, pp. 351–359, May 1989.
- [31] S. Gorthi, A. Mohanty, and A. Chatterjee, “Cantilever beam electrostatic MEMS actuators beyond pull-in,” *Journal of Micromechanics and Microengineering*, **vol. 16**, no. 9, pp. 1800–1810, Sep. 2006.
- [32] A. Jain, H. Qu, S. Todd, and H. Xie, “A thermal bimorph micromirror with large bi-directional and vertical actuation,” *Sensors and Actuators A: Physical*, **vol. 122**, no. 1, pp. 9–15, Jul. 2005.
- [33] E. Quandt and A. Ludwig, “Magnetostrictive actuation in microsystems,” *Sensors and Actuators A: Physical*, **vol. 81**, no. 1–3, pp. 275–280, Apr. 2000.

- [34] F. Hu, Y. Tang, and Y. Qian, "Design of a MEMS micromirror actuated by electrostatic repulsive force," *Optik - International Journal for Light and Electron Optics*, **vol. 123**, no. 5, pp. 387–390, Mar. 2012.
- [35] J. C. Lötters, J. G. Bomer, A. J. Verloop, E. A. Droog, W. Olthuis, P. H. Veltink, and P. Bergveld, "Design, fabrication and characterization of a highly symmetrical capacitive triaxial accelerometer," *Sensors and Actuators A: Physical*, **vol. 66**, no. 1–3, pp. 205–212, Apr. 1998.
- [36] I. J. O'Sullivan and W. M. D. Wright, "Ultrasonic measurement of gas flow using electrostatic transducers," *Ultrasonics*, **vol. 40**, no. 1–8, pp. 407–411, May 2002.
- [37] A. S. Ergun, G. G. Yaralioglu, and B. T. Khuri-Yakub, "Capacitive Micromachined Ultrasonic Transducers: Theory and Technology," *Journal of Aerospace Engineering*, **vol. 16**, no. 2, pp. 76–84, Apr. 2003.
- [38] I. Zine-El-Abidine, M. Okoniewski, and J. G. McRory, "Tunable radio frequency MEMS inductors with thermal bimorph actuators," *Journal of Micromechanics and Microengineering*, **vol. 15**, no. 11, pp. 2063–2068, Nov. 2005.
- [39] E. Quandt and A. Ludwig, "Magnetostrictive actuation in microsystems," *Sensors and Actuators A: Physical*, **vol. 81**, no. 1–3, pp. 275–280, Apr. 2000.
- [40] B. Piekarski, M. Dubey, E. Zakar, R. Polcawich, D. Devoe, and D. Wickenden, "Sol-Gel PZT for MEMS Applications," *Integrated Ferroelectrics*, **vol. 42**, no. 1, pp. 25–37, Jan. 2002.
- [41] J.-H. Park, H.-C. Lee, Y.-H. Park, Y.-D. Kim, C.-H. Ji, J. Bu, and H.-J. Nam, "A fully wafer-level packaged RF MEMS switch with low actuation voltage using a piezoelectric actuator," *Journal of Micromechanics and Microengineering*, **vol. 16**, no. 11, pp. 2281–2286, Nov. 2006.
- [42] M. R. Armstrong, E. J. Reed, K.-Y. Kim, J. H. Glowina, W. M. Howard, E. L. Piner, and J. C. Roberts, "Observation of terahertz radiation coherently generated by acoustic waves," *Nature Physics*, **vol. 5**, no. 4, pp. 285–288, Mar. 2009.
- [43] Gilberto Flores, Gema A. Mercado, John A. Pelesko, *Proceedings of the International Conference on MEMS, NANO and Smart Systems (ICMENS'03)*.
- [44] Attogram-scale mass sensing is described in M. L. Roukes, and K. L. Ekinici, U. S. Patent 6,722,200 (20 April 2004).
- [45] E. Colinet, L. Duraffourg, S. Labarthe, S. Hentz, P. Robert, and P. Andreucci, "Self-oscillation conditions of a resonant nanoelectromechanical mass sensor," *Journal of Applied Physics*, **vol. 105**, no. 12, p. 124908, 2009.
- [46] R. Compañó, L. Molenkamp, D. J. Paul, *Technology Roadmap for Nanoelectronics*, European Commission IST programme Future and Emerging Technologies, November 2000.
- [47] Sang-Wook Lee, Hyeon-Cheol Kim, Keon Kuk and Yong-Soo Oh, "A monolithic inkjet print head: DomeJet," in *Technical Digest. MEMS 2001. 14th IEEE International Conference on Micro Electro Mechanical Systems (Cat. No.01CH37090)*, pp. 515–518.

- [48] A. Paul Brokaw, Theresa Core, Steven J. Sherman, Robert W. K. Tsang, United States Patent, Appl. No.: US 08/028,922 (1993).
- [49] R. D. Fellman, "Design issues and an architecture for the monolithic implementation of a parallel digital signal processor," *IEEE Transactions on Acoustics, Speech, and Signal Processing*, vol. **38**, no. 5, pp. 839–852, May 1990.
- [50] S. A. Wolf, "Spintronics: A Spin-Based Electronics Vision for the Future," *Science*, vol. **294**, no. 5546, pp. 1488–1495, Nov. 2001.
- [51] B. Jalali and S. Fathpour, "Silicon Photonics," *Journal of Lightwave Technology*, vol. **24**, no. 12, pp. 4600–4615, Dec. 2006.
- [52] G. M. Whitesides, "The origins and the future of microfluidics.," *Nature*, vol. **442**, no. 7101, pp. 368–73, Jul. 2006.
- [53] H. B. Akkerman, P. W. M. Blom, D. M. de Leeuw, and B. de Boer, "Towards molecular electronics with large-area molecular junctions," *Nature*, vol. **441**, no. 7089, pp. 69–72, May 2006.
- [54] W. Lu and C. M. Lieber, "Nanoelectronics from the bottom up.," *Nature materials*, vol. **6**, no. 11, pp. 841–50, Nov. 2007.
- [55] J. M. Kahn, R. H. Katz, and K. S. J. Pister, "Next century challenges," in *Proceedings of the 5th annual ACM/IEEE international conference on Mobile computing and networking - MobiCom '99*, 1999, pp. 271–278.
- [56] G. Voskerician, M. S. Shive, R. S. Shawgo, H. von Recum, J. M. Anderson, M. J. Cima, and R. Langer, "Biocompatibility and biofouling of MEMS drug delivery devices," *Biomaterials*, vol. **24**, no. 11, pp. 1959–1967, May 2003.
- [57] S. V Kalinin, B. J. Rodriguez, S. Jesse, J. Shin, A. P. Baddorf, P. Gupta, H. Jain, D. B. Williams, and A. Gruverman, "Vector piezoresponse force microscopy.," *Microscopy and microanalysis : the official journal of Microscopy Society of America, Microbeam Analysis Society, Microscopical Society of Canada*, vol. **12**, no. 3, pp. 206–20, Jun. 2006.
- [58] E. Defaÿ, C. Zinck, C. Malhaire, N. Baboux, and D. Barbier, "Modified free vibrating beam method for characterization of effective  $e_{31}$  coefficient and leakage resistance of piezoelectric thin films," *Review of Scientific Instruments*, vol. **77**, no. 10, p. 103903, 2006.
- [59] T. Li and K. Zeng, "Nanoscale piezoelectric and ferroelectric behaviors of seashell by piezo-response force microscopy," *Journal of Applied Physics*, vol. **113**, no. 18, p. 187202, 2013.
- [60] C. Halperin, S. Mutchnik, A. Agronin, M. Molotskii, P. Urenski, M. Salai, and G. Rosenman, "Piezoelectric Effect in Human Bones Studied in Nanometer Scale," *Nano Letters*, vol. **4**, no. 7, pp. 1253–1256, Jul. 2004.
- [61] E. Fukada, "History and recent progress in piezoelectric polymers.," *IEEE transactions on ultrasonics, ferroelectrics, and frequency control*, vol. **47**, no. 6, pp. 1277–90, Jan. 2000.

- [62] H. P. Loeb, M. Klee, C. Metzmacher, W. Brand, R. Milsom, and P. Lok, "Piezoelectric thin AlN films for bulk acoustic wave (BAW) resonators," *Materials Chemistry and Physics*, **vol. 79**, no. 2–3, pp. 143–146, Apr. 2003.
- [63] N. W. Emanetoglu, C. Gorla, Y. Liu, S. Liang, and Y. Lu, "Epitaxial ZnO piezoelectric thin films for saw filters," *Materials Science in Semiconductor Processing*, **vol. 2**, no. 3, pp. 247–252, Oct. 1999.
- [64] S. P. Beeby, A. Blackburn, and N. M. White, "Processing of PZT piezoelectric thick films on silicon for microelectromechanical systems," *Journal of Micromechanics and Microengineering*, **vol. 9**, no. 3, pp. 218–229, Sep. 1999.
- [65] D. R. Lide (Ed.), *CRC Handbook of Chemistry and Physics*, 73rd Edition, CRC Press, New York, 1992.
- [66] E. H. Kisi and M. M. Elcombe, "u parameters for the wurtzite structure of ZnS and ZnO using powder neutron diffraction," *Acta Crystallographica Section C Crystal Structure Communications*, **vol. 45**, no. 12, pp. 1867–1870, Dec. 1989.
- [67] A. B. M. A. Ashrafi, A. Ueta, A. Avramescu, H. Kumano, I. Suemune, Y.-W. Ok, and T.-Y. Seong, "Growth and characterization of hypothetical zinc-blende ZnO films on GaAs(001) substrates with ZnS buffer layers," *Applied Physics Letters*, **vol. 76**, no. 5, p. 550, 2000.
- [68] S.-K. Kim, S.-Y. Jeong, and C.-R. Cho, "Structural reconstruction of hexagonal to cubic ZnO films on Pt/Ti/SiO<sub>2</sub>/Si substrate by annealing," *Applied Physics Letters*, **vol. 82**, no. 4, p. 562, 2003.
- [69] C. H. Bates, W. B. White, and R. Roy, "New High-Pressure Polymorph of Zinc Oxide," *Science*, **vol. 137**, no. 3534, pp. 993–993, Sep. 1962.
- [70] S. F. Chichibu, T. Sota, G. Cantwell, D. B. Eason, and C. W. Litton, "Polarized photoreflectance spectra of excitonic polaritons in a ZnO single crystal," *Journal of Applied Physics*, **vol. 93**, no. 1, p. 756, 2003.
- [71] F. Bernardini, V. Fiorentini, and D. Vanderbilt, "Spontaneous polarization and piezoelectric constants of III-V nitrides," *Physical Review B*, **vol. 56**, no. 16, pp. R10024–R10027, Oct. 1997.
- [72] G. Carlotti, G. Socino, A. Petri, and E. Verona, "Acoustic investigation of the elastic properties of ZnO films," *Applied Physics Letters*, **vol. 51**, no. 23, p. 1889, 1987.
- [73] Y. Natsume and H. Sakata, "Zinc oxide films prepared by sol-gel spin-coating," *Thin Solid Films*, **vol. 372**, no. 1–2, pp. 30–36, Sep. 2000.
- [74] Z.-C. Jin, I. Hamberg, and C. G. Granqvist, "Optical properties of sputter-deposited ZnO:Al thin films," *Journal of Applied Physics*, **vol. 64**, no. 10, p. 5117, 1988.
- [75] Y. Liu, C. R. Gorla, S. Liang, N. Emanetoglu, Y. Lu, H. Shen, and M. Wraback, "Ultraviolet detectors based on epitaxial ZnO films grown by MOCVD," *Journal of Electronic Materials*, **vol. 29**, no. 1, pp. 69–74, Jan. 2000.

- [76] E. M. Kaidashev, M. Lorenz, H. von Wenckstern, A. Rahm, H.-C. Semmelhack, K.-H. Han, G. Benndorf, C. Bundesmann, H. Hochmuth, and M. Grundmann, "High electron mobility of epitaxial ZnO thin films on c-plane sapphire grown by multistep pulsed-laser deposition," *Applied Physics Letters*, **vol. 82**, no. 22, p. 3901, 2003.
- [77] D. C. Reynolds, D. C. Look, and B. Jogai, "Optically pumped ultraviolet lasing from ZnO," *Solid State Communications*, **vol. 99**, no. 12, pp. 873–875, Sep. 1996.
- [78] C. Coskun, D. C. Look, G. C. Farlow, and J. R. Sizelove, "Radiation hardness of ZnO at low temperatures," *Semiconductor Science and Technology*, **vol. 19**, no. 6, pp. 752–754, Jun. 2004.
- [79] Z. Li, R. Yang, M. Yu, F. Bai, C. Li, and Z. L. Wang, "Cellular Level Biocompatibility and Biosafety of ZnO Nanowires," *The Journal of Physical Chemistry C*, **vol. 112**, no. 51, pp. 20114–20117, Dec. 2008.
- [80] I. Vurgaftman and J. R. Meyer, "Band parameters for nitrogen-containing semiconductors," *Journal of Applied Physics*, **vol. 94**, no. 6, p. 3675, 2003.
- [81] G. Piazza, P. J. Stephanou, and A. P. Pisano, "Piezoelectric Aluminum Nitride Vibrating Contour-Mode MEMS Resonators," *Journal of Microelectromechanical Systems*, **vol. 15**, no. 6, pp. 1406–1418, Dec. 2006.
- [82] M.-A. Dubois and P. Muralt, "Properties of aluminum nitride thin films for piezoelectric transducers and microwave filter applications," *Applied Physics Letters*, **vol. 74**, no. 20, p. 3032, 1999.
- [83] A. Barker, S. Crowther, and D. Rees, "Room-temperature r.f. magnetron sputtered ZnO for electromechanical devices," *Sensors and Actuators A: Physical*, **vol. 58**, no. 3, pp. 229–235, Mar. 1997.
- [84] V. Adivarahan, W. H. Sun, A. Chitnis, M. Shatalov, S. Wu, H. P. Maruska, and M. A. Khan, "250 nm AlGaIn light-emitting diodes," *Applied Physics Letters*, **vol. 85**, no. 12, p. 2175, 2004.
- [85] Y. Taniyasu, M. Kasu, and T. Makimoto, "An aluminium nitride light-emitting diode with a wavelength of 210 nanometres," *Nature*, **vol. 441**, no. 7091, pp. 325–8, May 2006.
- [86] R. E. Cohen, "Origin of ferroelectricity in perovskite oxides," *Nature*, **vol. 358**, no. 6382, pp. 136–138, Jul. 1992.
- [87] E. Pytte, "Theory of Perovskite Ferroelectrics," *Physical Review B*, **vol. 5**, no. 9, pp. 3758–3769, May 1972.
- [88] S. Mathews, "Ferroelectric Field Effect Transistor Based on Epitaxial Perovskite Heterostructures," *Science*, **vol. 276**, no. 5310, pp. 238–240, Apr. 1997.
- [89] M. J. Haun, Z. Q. Zhuang, E. Furman, S. J. Jang, and L. E. Cross, "Thermodynamic theory of the lead zirconate-titanate solid solution system, part III: Curie constant and sixth-order polarization interaction dielectric stiffness coefficients," *Ferroelectrics*, **vol. 99**, no. 1, pp. 45–54, Nov. 1989.

- [90] B. Noheda, D. E. Cox, and G. Shirane, "Stability of the monoclinic phase in the ferroelectric perovskite  $\text{PbZr}_{1-x}\text{Ti}_x\text{O}_3$ ," *Physical Review B*, **vol. 63**, no. 1, p. 014103, Dec. 2000.
- [91] D. L. Corker, A. M. Glazer, R. W. Whatmore, A. Stallard, and F. Fauth, "A neutron diffraction investigation into the rhombohedral phases of the perovskite series," *Journal of Physics: Condensed Matter*, **vol. 10**, no. 28, pp. 6251–6269, Jul. 1998.
- [92] B. Noheda, J. Gonzalo, L. Cross, R. Guo, S.-E. Park, D. Cox, and G. Shirane, "Tetragonal-to-monoclinic phase transition in a ferroelectric perovskite: The structure of  $\text{PbZr}_{0.52}\text{Ti}_{0.48}\text{O}_3$ ," *Physical Review B*, **vol. 61**, no. 13, pp. 8687–8695, Apr. 2000.
- [93] S. Trolier-McKinstry and P. Muralt, "Thin Film Piezoelectrics for MEMS," *Journal of Electroceramics*, **vol. 12**, no. 1/2, pp. 7–17, Jan. 2004.
- [94] H. D. Chen, K. R. Udayakumar, C. J. Gaskey, and L. E. Cross, "Electrical properties' maxima in thin films of the lead zirconate–lead titanate solid solution system," *Applied Physics Letters*, **vol. 67**, no. 23, p. 3411, 1995.
- [95] D.-J. Kim, J.-P. Maria, A. I. Kingon, and S. K. Streiffer, "Evaluation of intrinsic and extrinsic contributions to the piezoelectric properties of  $\text{Pb}(\text{Zr}_{1-x}\text{Ti}_x)\text{O}_3$  thin films as a function of composition," *Journal of Applied Physics*, **vol. 93**, no. 9, p. 5568, 2003.
- [96] B. Noheda, D. Cox, G. Shirane, J. Gao, and Z.-G. Ye, "Phase diagram of the ferroelectric relaxor  $(1-x)\text{PbMg}_{1/3}\text{Nb}_{2/3}\text{O}_3$ - $x\text{PbTiO}_3$ ," *Physical Review B*, **vol. 66**, no. 5, p. 054104, Aug. 2002.
- [97] T. R. Shrout, Z. P. Chang, N. Kim, and S. Markgraf, "Dielectric behavior of single crystals near the  $(1-x)\text{Pb}(\text{Mg}_{1/3}\text{Nb}_{2/3})\text{O}_3$ - $x\text{PbTiO}_3$  morphotropic phase boundary," *Ferroelectrics Letters Section*, **vol. 12**, no. 3, pp. 63–69, Sep. 1990.
- [98] B. Jaffe, W. R. Cook, and H. Jaffe, *Piezoelectric Ceramics* (Academic, New York, 1971) p. 115.
- [99] D. C. Roberts, J. L. Steyn, O. Yaglioglu, S. M. Spearing, M. A. Schmidt, and N. W. Hagood, "A piezoelectric microvalve for compact high-frequency, high-differential pressure hydraulic micropumping systems," *Journal of Microelectromechanical Systems*, **vol. 12**, no. 1, pp. 81–92, Feb. 2003.
- [100] K. Lefki and G. J. M. Dormans, "Measurement of piezoelectric coefficients of ferroelectric thin films," *Journal of Applied Physics*, **vol. 76**, no. 3, p. 1764, 1994.
- [101] G. Lesoult, C.-A. Gandin, and N. T. Niane, "Segregation during solidification with spongy deformation of the mushy zone," *Acta Materialia*, **vol. 51**, no. 18, pp. 5263–5283, Oct. 2003.
- [102] J. Ouyang and a. L. Roytburd, "Intrinsic effective piezoelectric coefficients of an epitaxial ferroelectric film," *Acta Mater.*, **vol. 54**, no. 2, pp. 531–538, Jan. 2006.

- [103] T. M. Shaw, Z. Suo, M. Huang, E. Liniger, R. B. Laibowitz, and J. D. Baniecki, "The effect of stress on the dielectric properties of barium strontium titanate thin films," *Applied Physics Letters*, **vol. 75**, no. 14, p. 2129, 1999.
- [104] 1991 MRS Fall Meeting, Volume 243.
- [105] Y. C. Zhou, Z. Y. Yang, and X. J. Zheng, "Residual stress in PZT thin films prepared by pulsed laser deposition," *Surface and Coatings Technology*, **vol. 162**, no. 2–3, pp. 202–211, Jan. 2003.
- [106] K. Yao, S. Yu, and F. Eng-Hock Tay, "Residual stress analysis in ferroelectric  $\text{Pb}(\text{Zr}_{0.52}\text{Ti}_{0.48})\text{O}_3$  thin films fabricated by a sol-gel process," *Applied Physics Letters*, **vol. 82**, no. 25, p. 4540, 2003.
- [107] H. Luo, X. J. Zheng, and Y. C. Zhou, "Preparation of Ferroelectric PZT Thin Films by Pulsed Laser Deposition and the Dependence of Substrate Temperature," *J. Chinese Laser*, **vol. 28**, no. 6, p. 570, 2001.
- [108] J.-W. Lee, C.-S. Park, M. Kim, and H.-E. Kim, "Effects of Residual Stress on the Electrical Properties of PZT Films," *Journal of the American Ceramic Society*, **vol. 90**, no. 4, pp. 1077–1080, Apr. 2007.
- [109] A. L. Roytburd, S. P. Alpay, L. A. Bendersky, V. Nagarajan, and R. Ramesh, "Three-domain architecture of stress-free epitaxial ferroelectric films," *Journal of Applied Physics*, **vol. 89**, no. 1, p. 553, 2001.
- [110] R. J. Ong, D. A. Payne, and N. R. Sottos, "Processing Effects for Integrated PZT: Residual Stress, Thickness, and Dielectric Properties," *Journal of the American Ceramic Society*, **vol. 88**, no. 10, pp. 2839–2847, Oct. 2005.
- [111] A. I. Kingon and S. K. Streiffer, "Ferroelectric films and devices," *Current Opinion in Solid State and Materials Science*, **vol. 4**, no. 1, pp. 39–44, Feb. 1999.
- [112] R. W. Whatmore, Q. Zhang, Z. Huang, and R. A. Dorey, "Ferroelectric thin and thick films for microsystems," *Materials Science in Semiconductor Processing*, **vol. 5**, no. 2–3, pp. 65–76, Apr. 2002.
- [113] P. Revesz, J. Li, N. Szabo, J. W. Mayer, D. Caudillo, and E. R. Myers, "PZT Interaction with Metal and Oxides Studied by Rutherford Backscattering Spectrometry," *MRS Proceedings*, **vol. 243**, p. 101, Feb. 2011.
- [114] T. Hase, T. Sakuma, K. Amanuma, T. Mori, A. Ochi, and Y. Miyasaka, "Difference in microstructure between PZT thin films on Pt/Ti and those on Pt," *Integrated Ferroelectrics*, **vol. 8**, no. 1–2, pp. 89–98, Mar. 1995.

- [115] H. N. Al-Shareef, K. D. Gifford, S. H. Rou, P. D. Hren, O. Auciello, and A. I. Kingon, "Electrodes for ferroelectric thin films," *Integrated Ferroelectrics*, vol. 3, no. 4, pp. 321–332, Dec. 1993.
- [116] G. J. Willems, D. J. Wouters, H. E. Maes, and R. Nouwen, "Nucleation and orientation of sol-gel PZT-films on pt electrodes," *Integrated Ferroelectrics*, vol. 15, no. 1–4, pp. 19–28, Feb. 1997.
- [117] E. L. Colla, A. K. Tagantsev, D. V. Taylor, and A. L. Kholkin, "Fatigued state of the Pt-PZT-Pt system," *Integrated Ferroelectrics*, vol. 18, no. 1–4, pp. 19–28, Sep. 1997.
- [118] W. L. Warren, D. Dimos, B. A. Tuttle, R. D. Nasby, and G. E. Pike, "Electronic domain pinning in  $\text{Pb}(\text{Zr},\text{Ti})\text{O}_3$  thin films and its role in fatigue," *Applied Physics Letters*, vol. 65, no. 8, p. 1018, 1994.
- [119] J. F. Scott, C. A. Araujo, B. M. Melnick, L. D. McMillan, and R. Zuleeg, "Quantitative measurement of space-charge effects in lead zirconate-titanate memories," *Journal of Applied Physics*, vol. 70, no. 1, p. 382, 1991.
- [120] J. Chen, M. P. Harmer, and D. M. Smyth, "Compositional control of ferroelectric fatigue in perovskite ferroelectric ceramics and thin films," *Journal of Applied Physics*, vol. 76, no. 9, p. 5394, 1994.
- [121] H. N. Al-Shareef, A. I. Kingon, X. Chen, K. R. Bellur, and O. Auciello, "Contribution of electrodes and microstructures to the electrical properties of  $\text{Pb}(\text{Zr}_{0.53}\text{Ti}_{0.47})\text{O}_3$  thin film capacitors," *Journal of Materials Research*, vol. 9, no. 11, pp. 2968–2975, Mar. 2011.
- [122] I. K. Yoo and S. B. Desu, "Leakage current mechanism and accelerated unified test of lead zirconate titanate thin film capacitors," in *ISAF '92: Proceedings of the Eighth IEEE International Symposium on Applications of Ferroelectrics*, pp. 225–228.
- [123] K. R. Bellur, H. N. Al-Shareef, S. H. Rou, K. D. Gifford, O. Auciello, and A. I. Kingon, "Electrical characterization of sol-gel derived PZT thin films," in *ISAF '92: Proceedings of the Eighth IEEE International Symposium on Applications of Ferroelectrics*, pp. 448–451.
- [124] D. J. Lichtenwalner, R. Dat, O. Auciello, and A. I. Kingon, "Effect of electrodes on the ferroelectric properties of pulsed-laser ablation-deposited  $\text{PbZr}_x\text{Ti}_{1-x}\text{O}_3$  thin film capacitors," *Ferroelectrics*, vol. 152, no. 1, pp. 97–102, Feb. 1994.
- [125] R. Ramesh, W. K. Chan, B. Wilkens, H. Gilchrist, T. Sands, J. M. Tarascon, V. G. Keramidis, D. K. Fork, J. Lee, and A. Safari, "Fatigue and retention in ferroelectric Y-Ba-Cu-O/Pb-Zr-Ti-O/Y-Ba-Cu-O heterostructures," *Applied Physics Letters*, vol. 61, no. 13, p. 1537, 1992.
- [126] C.-C. Yang, M.-S. Chen, T.-J. Hong, C.-M. Wu, J.-M. Wu, and T.-B. Wu, "Preparation of (100)-oriented metallic  $\text{LaNiO}_3$  thin films on Si substrates by radio frequency magnetron

sputtering for the growth of textured  $\text{Pb}(\text{Zr}_{0.53}\text{Ti}_{0.47})\text{O}_3$ ,” *Applied Physics Letters*, **vol. 66**, no. 20, p. 2643, 1995.

[127] M.-S. Chen, T.-B. Wu, and J.-M. Wu, “Effect of textured  $\text{LaNiO}_3$  electrode on the fatigue improvement of  $\text{Pb}(\text{Zr}_{0.53}\text{Ti}_{0.47})\text{O}_3$  thin films,” *Applied Physics Letters*, **vol. 68**, no. 10, p. 1430, 1996.

[128] R. Ramesh, H. Gilchrist, T. Sands, V. G. Keramidas, R. Haakenaasen, and D. K. Fork, “Ferroelectric  $\text{La-Sr-Co-O/Pb-Zr-Ti-O/La-Sr-Co-O}$  heterostructures on silicon via template growth,” *Applied Physics Letters*, **vol. 63**, no. 26, p. 3592, 1993.

[129] H. N. Al-Shareef, K. R. Bellur, O. Auciello, and A.I. Kingon, *5th International Symposium on Integrated Ferroelectrics (ISIFS)*, Colorado Springs, CO (1993).

[130] G. Teowee, E. L. Quackenbush, C. D. Baertlein, J. M. Boulton, and D. R. Uhlmann, “Fatigue and retention behaviors of Pt-PZT-metal capacitors with various top metallizations,” in *Proceedings of 1994 IEEE International Symposium on Applications of Ferroelectrics*, pp. 523–526.

[131] J. Lee, L. Johnson, A. Safari, R. Ramesh, T. Sands, H. Gilchrist, and V. G. Keramidas, “Effects of crystalline quality and electrode material on fatigue in  $\text{Pb}(\text{Zr,Ti})\text{O}_3$  thin film capacitors,” *Applied Physics Letters*, **vol. 63**, no. 1, p. 27, 1993.

[132] R. McKee, F. Walker, and M. Chisholm, “Crystalline Oxides on Silicon: The First Five Monolayers,” *Physical Review Letters*, **vol. 81**, no. 14, pp. 3014–3017, Oct. 1998.

[133] R. A. McKee, F. J. Walker, and M. F. Chisholm, “Physical structure and inversion charge at a semiconductor interface with a crystalline oxide.,” *Science (New York, N.Y.)*, **vol. 293**, no. 5529, pp. 468–71, Jul. 2001.

[134] R. Droopad, Z. Yu, J. Ramdani, L. Hilt, J. Curless, C. Overgaard, J. L. Edwards, J. Finder, K. Eisenbeiser, J. Wang, V. Kaushik, B.-Y. Ngyuen, and B. Ooms, “Epitaxial oxides on silicon grown by molecular beam epitaxy,” *Journal of Crystal Growth*, **vol. 227–228**, pp. 936–943, Jul. 2001.

[135] J. Wang, H. Zheng, Z. Ma, S. Prasertchoung, M. Wuttig, R. Droopad, J. Yu, K. Eisenbeiser, and R. Ramesh, “Epitaxial  $\text{BiFeO}_3$  thin films on Si,” *Applied Physics Letters*, **vol. 85**, no. 13, p. 2574, 2004.

[136] J. W. Reiner, A. Posadas, M. Wang, T. P. Ma, and C. H. Ahn, “Growth and structural properties of crystalline  $\text{LaAlO}_3$  on Si (001),” *Microelectronic Engineering*, **vol. 85**, no. 1, pp. 36–38, Jan. 2008.

[137] Y. Wang, C. Ganpule, B. T. Liu, H. Li, K. Mori, B. Hill, M. Wuttig, R. Ramesh, J. Finder, Z. Yu, R. Droopad, and K. Eisenbeiser, “Epitaxial ferroelectric  $\text{Pb}(\text{Zr,Ti})\text{O}_3$  thin films on Si using  $\text{SrTiO}_3$  template layers,” *Applied Physics Letters*, **vol. 80**, no. 1, p. 97, 2002.

- [138] M. D. Nguyen, M. Dekkers, E. Houwman, R. Steenwelle, X. Wan, A. Roelofs, T. Schmitz-Kempen, and G. Rijnders, "Misfit strain dependence of ferroelectric and piezoelectric properties of clamped (001) epitaxial  $\text{Pb}(\text{Zr}_{0.52}\text{Ti}_{0.48})\text{O}_3$  thin films," *Applied Physics Letters*, **vol. 99**, no. 25, p. 252904, 2011.
- [139] X. Du, J. Zheng, U. Belegundu, and K. Uchino, "Crystal orientation dependence of piezoelectric properties of lead zirconate titanate near the morphotropic phase boundary," *Applied Physics Letters*, **vol. 72**, no. 19, p. 2421, 1998.
- [140] K. Maki, B. T. Liu, Y. So, H. Vu, R. Ramesh, J. Finder, Z. Yu, R. Droopad, and K. Eisenbeiser, "Low-Temperature Fabrication of Epitaxial and Random-Oriented  $\text{Pb}(\text{Zr,Ti})\text{O}_3$  Capacitors with  $\text{SrRuO}_3$  Electrodes on Si Wafers," *Integrated Ferroelectrics*, **vol. 52**, no. 1, pp. 19–31, Feb. 2003.
- [141] A. S. Borowiak, G. Niu, V. Pillard, G. Agnus, P. Lecoeur, D. Albertini, N. Baboux, B. Gautier, and B. Vilquin, "Pulsed laser deposition of epitaxial ferroelectric  $\text{Pb}(\text{Zr,Ti})\text{O}_3$  films on silicon substrates," *Thin Solid Films*, **vol. 520**, no. 14, pp. 4604–4607, May 2012.
- [142] B. T. Liu, K. Maki, Y. So, V. Nagarajan, R. Ramesh, J. Lettieri, J. H. Haeni, D. G. Schlom, W. Tian, X. Q. Pan, F. J. Walker, and R. A. McKee, "Epitaxial La-doped  $\text{SrTiO}_3$  on silicon: A conductive template for epitaxial ferroelectrics on silicon," *Applied Physics Letters*, **vol. 80**, no. 25, p. 4801, 2002.
- [143] A. Sambri, S. Gariglio, A. Torres Pardo, J.-M. Triscone, O. Stéphan, J. W. Reiner, and C. H. Ahn, "Enhanced critical temperature in epitaxial ferroelectric  $\text{Pb}(\text{Zr}_{0.2}\text{Ti}_{0.8})\text{O}_3$  thin films on silicon," *Applied Physics Letters*, **vol. 98**, no. 1, p. 012903, 2011.
- [144] E. K. Reilly and P. K. Wright, "Modeling, fabrication and stress compensation of an epitaxial thin film piezoelectric microscale energy scavenging device," *Journal of Micromechanics and Microengineering*, **vol. 19**, no. 9, p. 095014, Sep. 2009.
- [145] D. Isarakorn, A. Sambri, P. Janphuang, D. Briand, S. Gariglio, J.-M. Triscone, F. Guy, J. W. Reiner, C. H. Ahn, and N. F. de Rooij, "Epitaxial piezoelectric MEMS on silicon," *Journal of Micromechanics and Microengineering*, **vol. 20**, no. 5, p. 055008, May 2010.
- [146] D. Isarakorn, D. Briand, P. Janphuang, A. Sambri, S. Gariglio, J.-M. Triscone, F. Guy, J. W. Reiner, C. H. Ahn, and N. F. de Rooij, "The realization and performance of vibration energy harvesting MEMS devices based on an epitaxial piezoelectric thin film," *Smart Materials and Structures*, **vol. 20**, no. 2, p. 025015, Feb. 2011.
- [147] A. Sambri, D. Isarakorn, A. Torres-Pardo, S. Gariglio, Pattanaphong Janphuang, D. Briand, O. Stéphan, J. W. Reiner, J.-M. Triscone, Nico F. de Rooij, and C. H. Ahn, *Smart Materials Research* Volume 2012, Article ID 426048.

- [148] D. Lavric, R. A. Rao, Q. Gan, J. J. Krajewski, and C.-B. Eom, "Epitaxial thin film heterostructures of relaxor ferroelectric  $\text{Pb}(\text{Mg}_{1/3}\text{Nb}_{2/3})\text{O}_3\text{-PbTiO}_3$ ," *Integrated Ferroelectrics*, **vol. 21**, no. 1–4, pp. 499–509, Sep. 1998.
- [149] G. R. Bai, S. K. Streiffer, P. K. Baumann, O. Auciello, K. Ghosh, S. Stemmer, A. Munkholm, C. Thompson, R. A. Rao, and C. B. Eom, "Epitaxial  $\text{Pb}(\text{Mg}_{1/3}\text{Nb}_{2/3})\text{O}_3$  thin films synthesized by metal-organic chemical vapor deposition," *Applied Physics Letters*, **vol. 76**, no. 21, p. 3106, 2000.
- [150] Y. Takeshima, K. Shiratsuyu, H. Takagi, and K. Tomono, "Preparation of Lead Magnesium Niobate Titanate Thin Films by Chemical Vapor Deposition," *Japanese Journal of Applied Physics*, **vol. 34**, no. Part 1, No. 9B, pp. 5083–5085, Sep. 1995.
- [151] K.-A. Bui-Thi, P. Lecoeur, M. Pham-Thi, and G. Garry, "Phase optimisation of PMN-PT thin films deposited by Pulsed Laser Deposition on MgO substrates and Pt-coated silicon," in *2010 IEEE International Symposium on the Applications of Ferroelectrics (ISAF)*, 2010, pp. 1–4.
- [152] R. Herdier, M. Détalle, D. Jenkins, D. Remiens, D. Gréville, and R. Bouregba, "The properties of epitaxial PMNT thin films grown on  $\text{SrTiO}_3$  substrates," *Journal of Crystal Growth*, **vol. 311**, no. 1, pp. 123–127, Dec. 2008.
- [153] S. D. Bu, M. K. Lee, C. B. Eom, W. Tian, X. Q. Pan, S. K. Streiffer, and J. J. Krajewski, "Perovskite phase stabilization in epitaxial  $\text{Pb}(\text{Mg}_{1/3}\text{Nb}_{2/3})\text{O}_3\text{-PbTiO}_3$  films by deposition onto vicinal (001)  $\text{SrTiO}_3$  substrates," *Applied Physics Letters*, **vol. 79**, no. 21, p. 3482, 2001.
- [154] C. Tantigate and A. Safari, "Preparation of thin films on silicon substrates by pulsed laser deposition," *Microelectronic Engineering*, **vol. 29**, no. 1–4, pp. 115–118, Dec. 1995.
- [155] N. Wakiya, K. Shinozaki, and N. Mizutani, "Stabilization of perovskite  $\text{Pb}(\text{Mg}_{1/3}\text{Nb}_{2/3})\text{O}_3$  thin film by a thin  $\text{BaTiO}_3$  buffer layer on Pt/Ti/SiO<sub>2</sub>/Si," *Thin Solid Films*, **vol. 409**, no. 2, pp. 248–253, Apr. 2002.
- [156] M. Detalle, G. Wang, D. Rémiens, P. Ruterana, P. Roussel, and B. Dkhil, "Comparison of structural and electrical properties of PMN-PT films deposited on Si with different bottom electrodes," *Journal of Crystal Growth*, **vol. 305**, no. 1, pp. 137–143, Jul. 2007.
- [157] M. Detalle, A. Ferri, A. Da Costa, R. Desfeux, C. Soyer, and D. Rémiens, "Nanoscale study by piezoresponse force microscopy of relaxor  $0.7\text{Pb}(\text{Mg}_{1/3}\text{Nb}_{2/3})\text{O}_3\text{-}0.3\text{PbTiO}_3$  and  $0.9\text{Pb}(\text{Mg}_{1/3}\text{Nb}_{2/3})\text{O}_3\text{-}0.1\text{PbTiO}_3$  thin films grown on platinum and  $\text{LaNiO}_3$  electrodes," *Thin Solid Films*, **vol. 518**, no. 16, pp. 4670–4674, Jun. 2010.
- [158] W. L. Li, J. M. Wang, C. Q. Liu, and W. D. Fei, "Effects of annealing technique and  $\text{TiO}_2$  seed layer on the phase composition of  $0.7\text{Pb}(\text{Mg}_{1/3}\text{Nb}_{2/3})\text{O}_3\text{-}0.3\text{PbTiO}_3$  film," *Materials Science in Semiconductor Processing*, **vol. 13**, no. 5–6, pp. 426–429, Dec. 2010.

- [159] J. Jiang, H.-H. Hwang, W.-J. Lee, and S.-G. Yoon, "Microstructural and electrical properties of  $0.65\text{Pb}(\text{Mg}_{1/3}\text{Nb}_{2/3})\text{O}_3-0.35\text{PbTiO}_3$  (PMN-PT) epitaxial films grown on Si substrates," *Sensors and Actuators B: Chemical*, vol. **155**, no. 2, pp. 854–858, Jul. 2011.
- [160] J. Jiang and S.-G. Yoon, "Epitaxial  $0.65\text{PbMg}_{1/3}\text{Nb}_{2/3}\text{O}_3-0.35\text{PbTiO}_3$  (PMN-PT) thin films grown on  $\text{LaNiO}_3/\text{CeO}_2/\text{YSZ}$  buffered Si substrates," *Journal of Alloys and Compounds*, vol. **509**, no. 6, pp. 3065–3069, Feb. 2011.
- [161] K. Shinozaki, S. Hayashi, N. Wakiya, T. Kiguchi, J. Tanaka, N. Ishizawa, K. Sato, M. Kondo, and K. Kurihara, "Fabrication and optical properties of  $\text{Pb}(\text{Mg}_{1/3}\text{Nb}_{2/3})\text{O}_3-\text{PbTiO}_3$  thin films on Si substrates using the PLD method.," *IEEE transactions on ultrasonics, ferroelectrics, and frequency control*, vol. **55**, no. 5, pp. 1023–8, May 2008.
- [162] S. H. Baek, J. Park, D. M. Kim, V. A. Aksyuk, R. R. Das, S. D. Bu, D. A. Felker, J. Lettieri, V. Vaithyanathan, S. S. N. Bharadwaja, N. Bassiri-Gharb, Y. B. Chen, H. P. Sun, C. M. Folkman, H. W. Jang, D. J. Kreft, S. K. Streiffer, R. Ramesh, X. Q. Pan, S. Trolier-McKinstry, D. G. Schlom, M. S. Rzchowski, R. H. Blick, and C. B. Eom, "Giant piezoelectricity on Si for hyperactive MEMS.," *Science (New York, N.Y.)*, vol. **334**, no. 6058, pp. 958–61, Nov. 2011.

**Chapter II - Epitaxial growth and characterization technologies**

---

---

<b>II.1) Introduction .....</b>	<b>46</b>
<b>II.2) Deposition technologies for epitaxial growth .....</b>	<b>46</b>
II.2.1) General features of epitaxial growth .....	46
II.2.2) Molecular Beam Epitaxy .....	49
II.2.3) Pulsed Laser Deposition .....	53
II.2.4) Sol-gel deposition .....	55
<b>II.3) Characterizations techniques .....</b>	<b>57</b>
II.3.1) X-Ray Diffraction .....	57
II.3.2) Transmission Electron Microscopy .....	62
II.3.3) Electrical measurement .....	63
II.3.3.1) Impedance meter .....	63
II.3.3.2) Polarization hysteresis loop .....	68
II.3.4) Piezoresponse Force Microscopy .....	69
II.3.5) Mechanical characterization .....	71
<b>II.4) Reference .....</b>	<b>72</b>

## **II.1) Introduction**

The aim of this chapter is to present the fabrication technologies used in this thesis to grow the different layers involved in the integration of  $\text{Pb}(\text{Zr}_x\text{Ti}_{1-x})\text{O}_3$  (PZT) or  $x\text{Pb}(\text{Mg}_{1/3}\text{Nb}_{2/3})\text{O}_3-(1-x)\text{PbTiO}_3$  films on Si, as well as the main characterization tools that allowed the optimization of growth conditions. Different fabrication technologies were used according to the different layers of our samples: Molecular Beam Epitaxy (MBE) for the oxide buffer layer on Si, Pulsed Laser Deposition (PLD) for the conductive oxide layer and sol-gel method for the piezoelectric film. Each of these technologies will be briefly introduced. The main characterization tools used in this thesis concern structural characterization, such as X-Ray Diffraction (XRD), Transmission Electron Microscopy (TEM), and electrical or piezoelectric characterization. The different experimental tools will be presented with emphasis on the available information.

## **II.2) Deposition technologies for epitaxial growth**

### **II.2.1) General features of epitaxial growth**

The technical term “epitaxy” derives from two Greek roots: *epi-* which means “above” and *taxis-* which means “in ordered manner”. Epitaxy refers to the growth of a crystalline film on a crystalline substrate, where one or more preferred orientations of the substrate are preserved in the epitaxial film. It is widely used in semiconductor manufacturing to grow high-quality functional films for specific applications <sup>[1, 2, 3, 4, 5]</sup>. Figure II.1 illustrates the atomistic processes involved in the epitaxial growth. First, atoms sublimated from target material arrive at substrate surface in high vacuum and condense by the way of chemical or physical adsorption. Driven by thermal diffusion, the adsorbed atoms migrate on the substrate surface and form crystalline nuclei by colliding between them. Usually, physical adsorption whose bonding energy is weaker than that of chemical adsorption has a longer diffusion length, providing larger possibility for the atoms to jump to the sites of minimal energy. The crystalline substrate provides the periodical adsorbing sites on the surface for bonding and nucleation of adsorbed atoms. Some surface defects on substrate caused by a slight misorientation, like step edges and kinks, have a relatively small bonding energy, and behave as preferential nucleation centers. In addition, a screw dislocation on substrate surface with spiral edge can provide a continuous mechanism to grow single crystalline film within a much longer duration at low activation energy. Epitaxial growth of high-quality crystalline film is only possible when the crystalline structures of film material and substrate are compatible and the lattice mismatch between them is small.

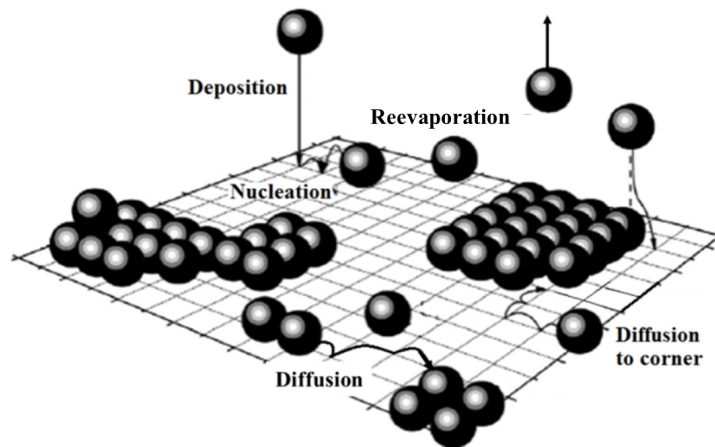


Figure II.1 - Atomistic processes of the epitaxial growth.

Based on thermodynamic grounds and taking in account the variations of surface and interface energies, three possible growth modes may be considered during epitaxial growth (Figure II.2):

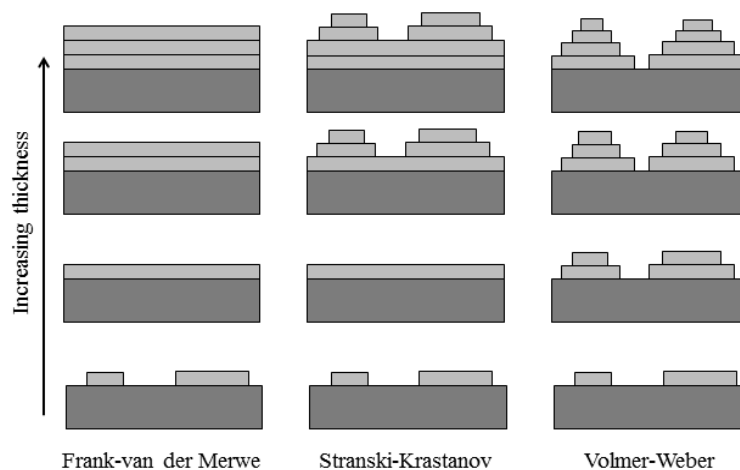


Figure II.2 - Three possible epitaxial growth modes during the deposition of film material on substrate.

- **Frank-van der Merwe mode** or 2D layer-by-layer growth: In this growth mode, a new layer is forming only after the completion of the underneath layer. It occurs when the wettability of the substrate by the film is high. The ideal layer-by-layer growth mode is difficult to be realized over a long distance. The deposited atoms are more strongly linked to the substrate than to each other.
- **Volmer-Weber mode** or 3D island growth: In that case, the bonding energy between film atoms is much stronger than between film atoms and substrate, the wettability of the the

substrate by the film is low. The Volmer-Weber growth evolves by coalescence of a large number of surface nuclei that grow bigger and spread during the growth. Thus, it may lead to a high mosaicity in the epitaxial film and a large roughness of the surface. Usually, continuation of the Volmer Weber growth mode will result in the columnar growth which forms needle-like structure on the substrate.

- **Stranski-Krastonov growth mode** or mixed growth: This growth mode is considered as an intermediate mode between the two previous growth modes. After forming an intermediate 2D wetting layer (few monolayers) on the substrate, 3D islands are formed on its top.

In the general case of heteroepitaxy, the lattice mismatch between film and substrate has to be taken in account: At the first steps of growth, the epitaxial film is growing pseudomorphically, adapting its lattice parameter to the substrate one. Accumulation of elastic strain energy occurs and increases with the deposited thickness. Beyond a certain critical thickness, relaxation of elastic strain energy can take place following two possible processes: plastic relaxation by formation of dislocations at the interface or elastic relaxation by formation of coherent 3D islands. Thus, the growth mode will greatly influence the crystalline structure of epitaxial films. Large lattice mismatch that leads to high elastic strain may give rise to various defects in the film, like crystallographic misorientation relative to the substrate, polycrystalline structure or even amorphous structure. Small lattice mismatch between film material and substrate is essential in the epitaxial growth to decrease interface strain and obtain high-quality crystalline film.

In some cases, the lattice mismatch accommodation can operate differently. Consider, for example materials having a similar cubic lattice structure and nearly close lattice constants, so that direct cube-on-cube growth mode is allowed during deposition, as illustrated in Figure II.3 (a). As an illustration, the lattice constant of SrTiO<sub>3</sub> (STO) cubic structure is 3.905 Å close to that of BaTiO<sub>3</sub> (BTO) ( $a = 3.992 \text{ \AA}$ ,  $c = 4.036 \text{ \AA}$ ). The heteroepitaxy of BTO on STO substrate follows the cube-on-cube growth mode due to the small lattice mismatch (~2.2%). In other cases where film and substrate have different lattice constants, a large lattice mismatch can be accommodated by re-orientating the crystalline structure. Crystalline silicon has a larger lattice constant (5.432 Å) than that of STO, but the heteroepitaxy of STO on Si is still possible because the lattice mismatch can decrease to 1.65% by rotating the STO unit cell 45° relative to the Si substrate (Figure II.3 (b)). Figure II.3 (c) illustrates another case corresponding to a pseudostructure. The example is the heteroepitaxy of SrRuO<sub>3</sub> (SRO), which has an orthorhombic structure with lattice constants  $a = 5.567 \text{ \AA}$ ,  $b = 5.530 \text{ \AA}$  and  $c = 7.845 \text{ \AA}$ , on STO substrate. The

crystalline structure of SRO can be considered as a pseudocubic unit cell with a lattice constant of 3.923 Å that is very close to that of STO substrate.

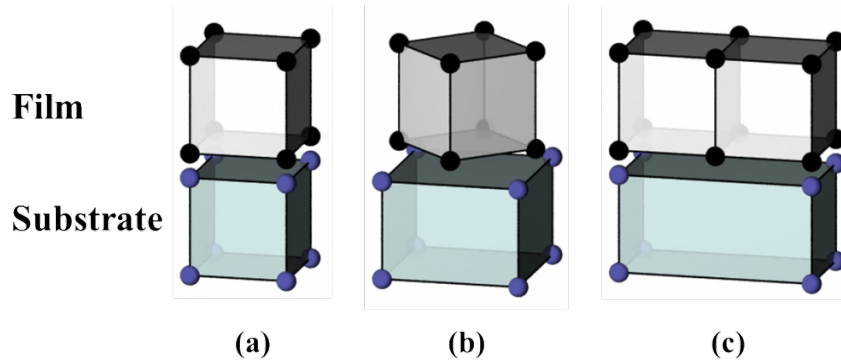


Figure II.3 - The arrangement of the unit cell of the film material on the substrate: (a) cube-on-cube mode, (b) rotation of film unit cell by 45°, and (c) pseudo-structure.

To resume, there will be a direct relationship between the growth mode and the film morphology, giving rise to different structural properties such as crystalline quality, surface roughness and interface abruptness in heterostructures, and thus modifying the physical properties.

### II.2.2) Molecular Beam Epitaxy

Since its invention in the late 1960s by J. R. Arthur and Alfred Y. Cho to realize the superlattice structure of GaAs and  $\text{Al}_x\text{Ga}_{1-x}\text{As}$  [6], MBE system has been widely used to deposit high-quality epitaxial film of various materials, such as functional oxides, III-V semiconductors, and even organic materials, in semiconductor manufacturing and research. Compared with other deposition technologies, MBE system has several advantages:

- An Ultra-High Vacuum (UHV) environment: The deposition process is typically carried on at  $10^{-10} \sim 10^{-9}$  Torr, providing a contamination-free environment for a high-quality epitaxial growth. The atomic species sublimated from effusion cells may directly arrive at sample surface without collision with the residual atoms in UHV, and therefore generate a so-called “molecular beam” between the cell aperture and the substrate.
- A precise control of the growth at monolayer scale and of the quality of surfaces and interfaces: Deposition speed in MBE system is relatively low ( $< 10$  nm/min), so that the layer-by-layer growth mode can be achieved. The deposition process can be easily controlled by switching mechanical shutters on the path of the molecular beams. Moreover,

the stoichiometry of the growing film can be easily controlled and tuned by changing the temperature of each effusion cell, enabling a precise control of the chemical composition of the film. Even superlattice structures can be elaborated by periodically switching the shutters.

- A compatibility with in-situ growth monitoring tools: Thanks to the UHV ambient, an *in-situ* monitoring of the growing surface is feasible by using Reflective High-Energy Electron Diffraction (RHEED), which has become a versatile tool in MBE system to characterize crystalline structure and growth mechanisms of epitaxial films.

Figure II.4 shows the Riber 2300 MBE system used at INL, which is dedicated to the deposition of functional oxides. This equipment consists of the different following parts:

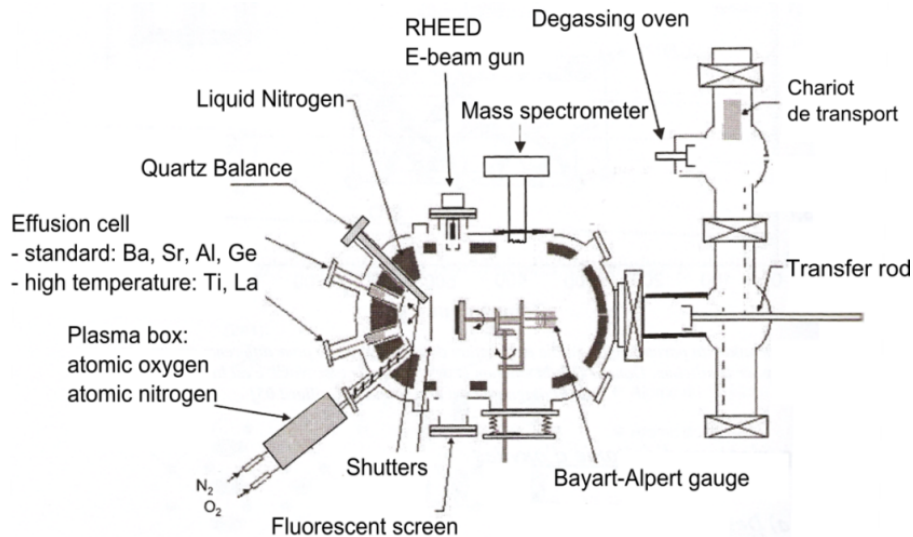


Figure II.4 - Schematic of a typical MBE system for oxide deposition.

- A sample introduction chamber equipped with an outgassing furnace and a transfer chamber: They serve as buffer chambers to prevent the contamination and keep the UHV when transferring the sample. A 2-inch molyblock is used as universal sample holder, which can be transferred using a cartridge and several magnetically-coupled canes between the chambers.
- An MBE growth chamber: It contains the main components for epitaxial deposition such as effusion cells, RHEED system, plasma generator and mass spectrometer, and an *in-situ* observation tool, RHEED equipment. The UHV in the growth chamber is maintained by a series of pumps, like mechanical pump, turbo pump, ionic pump and cryogenic pump.

During deposition, sample surface is directly exposed to the atomic beams. A main shutter above the sample surface and several shutters in front of each effusion cell aperture are switchable by using magnetically-coupled valves to control the deposition process. A proportional-integral-derivative controller is used to stabilize the substrate temperature and the temperature of each effusion cell. For the deposition of oxide or nitride films, the desired atmosphere can be introduced from an external gas source. The plasma can be generated when a high-energy atmosphere is desired.

RHEED system becomes an essential component in modern MBE system, since it allows the *in-situ* observation of the growing surface by the operator in order to monitor the deposition process. The system mainly consists of an electron beam gun and a fluorescence screen, as illustrated in Figure II.5. In this setup, the electron beam is generated by thermionic emission and emitted towards sample surface with an incident grazing angle of around  $1^{\circ}\sim 3^{\circ}$ . At such small incident angle, the penetration depth of the electron beam into the sample surface is limited within a few nanometers, so that RHEED can be considered as a surface-sensitive analytical tool. The electron beam diffracted from sample surface is directly visualized on the fluorescence screen. An external camera is often used to record the RHEED pattern for post-analysis.

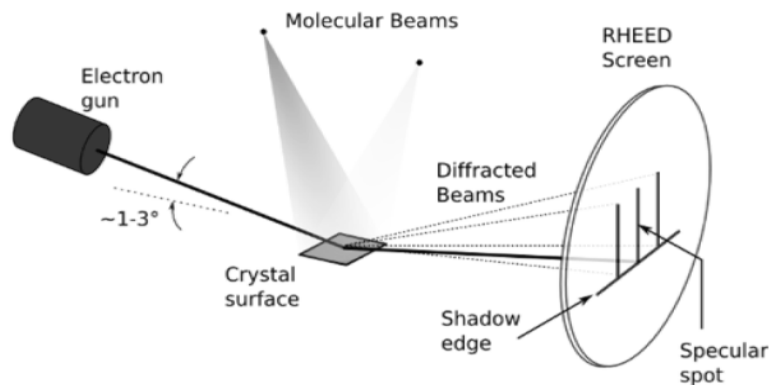
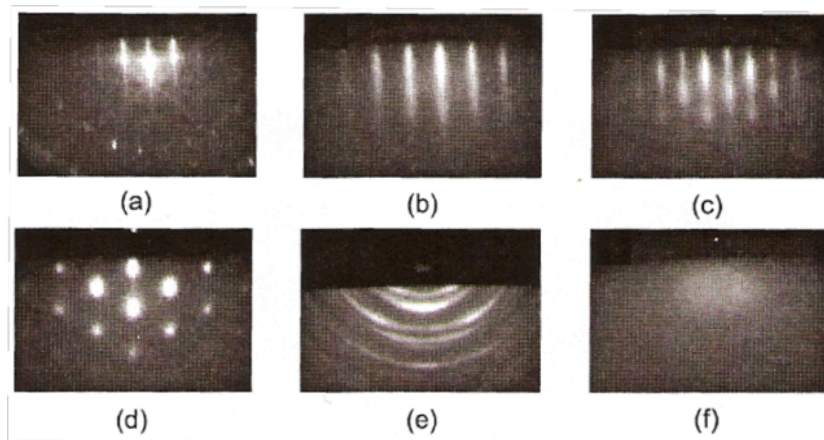


Figure II.5 - Schematics of the RHEED system in MBE growth chamber.

Several important information of the growing surface can be derived from analysis of RHEED patterns, like crystalline quality, lattice constants, surface roughness and growth mode. Similar to other diffraction techniques, RHEED pattern represents on the screen the Fourier transform of the sample crystalline structure in reciprocal space. Due to the limited penetration depth of the electron beam, the probed volume underneath the surface has actually a 2D geometry so that the usual diffraction spot degrade to diffraction rods. For an ideal surface with perfect-ordered atoms, a series of streaky lines is generated on RHEED pattern, which can be regarded as the intersection of those diffraction rods with the fluorescence screen (Figure II.6 (a)). For real

crystalline surfaces, diffused lines are obtained on RHEED pattern with lower contrast, indicating the deviation of crystalline lattice from the perfect one (Figure II.6 (b)). When the deposition follows 3D growth mode, RHEED pattern becomes spotty due to the fact that the incident electron beam is diffracted by the 3D structures of the rough surface. The RHEED pattern actually probes the 3D crystalline structure which shows the reciprocal spots on the screen. Polycrystalline surface gives rise to a series of concentric rings on RHEED pattern, since the crystalline domains are randomly distributed on the surface. Amorphous material often exhibits a diffused halo without any feature on RHEED pattern. Figure II.6 summarizes these six types of RHEED patterns which possibly happen during the growth of the film.



**Figure II.6 - Six types of RHEED patterns for (a) perfect crystalline surface, (b) real epitaxial surface, (c) rough surface, (d) 3D growth mode, (e) polycrystalline surface and (f) amorphous surface.**

In the particular case of epitaxial growth of STO buffer layer on Si substrate, RHEED pattern is also helpful to maintain the chemical stoichiometry of Sr and Ti by observing the surface reconstruction. Generally, when the epitaxial growth is out of the stoichiometry, the extra atoms steadily occupy the periodic minimal energy sites on the surface, forming additional features on RHEED pattern. In the case of a Sr-rich STO surface, each Sr atom will occupy a 2 unit cell along (110) direction on STO surface. The  $\times 2$  surface reconstruction appears between the main integral lines on RHEED pattern. When the surface is Ti rich, the  $\times 2$  surface reconstruction occurs along (100) direction on RHEED pattern as illustrated in Figure II.7. Therefore, by monitoring the RHEED pattern along (110) and (100) directions in real time during the deposition process, the chemical stoichiometry can be maintained by changing the deposition speed of either Sr or Ti effusion cell.

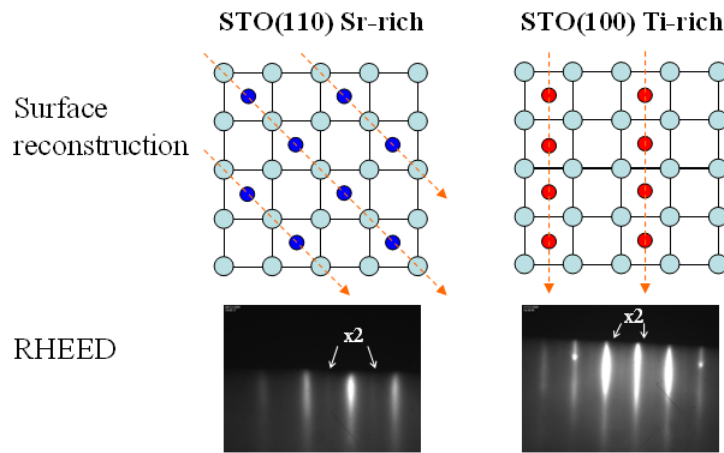


Figure II.7 - The  $\times 2$  reconstruction of STO surface in the case of Sr- and Ti-rich and the corresponding RHEED pattern.

### II.2.3) Pulsed Laser Deposition

PLD is a versatile deposition technology to grow high-quality thin film in semiconductor manufacturing [7, 8, 9]. During the deposition process, a succession of laser pulses heats, ionizes and evaporates the target material. A transient plasma plume is formed and rapidly expands onto the substrate surface. The atoms ablated from the target material arrive at the substrate surface through the plasma plume and then nucleate to form the thin film. This deposition technology by using laser pulse allows a stoichiometric transfer for a variety of materials, such as high-temperature superconductors [10], functional oxides [11, 12, 13] and nitrides [14, 15, 16], carbides [17, 18], metals [19, 20], and even polymers [21, 22, 23]. The high-power laser pulses used in the deposition favor the stoichiometric transfer of the target material onto the substrate surface. The stoichiometry of the film deposited by PLD is very close to that of the target material, and therefore it is possible to prepare stoichiometric films using a single alloy bulk material. Compared with the other deposition technologies, PLD system usually has a relatively simple configuration shown in Figure II.8 for the setup used in this thesis. The UHV is maintained in the growth chamber in the order of  $10^{-9}$  mbar. A KrF excimer laser (wavelength: 248 nm, pulse duration: 30 ns) is generated by an external laser system and focused through a series of optical lens on the surface of target material. For some PLD setups, an optical aperture is usually employed to define the cross-section of the laser beam.

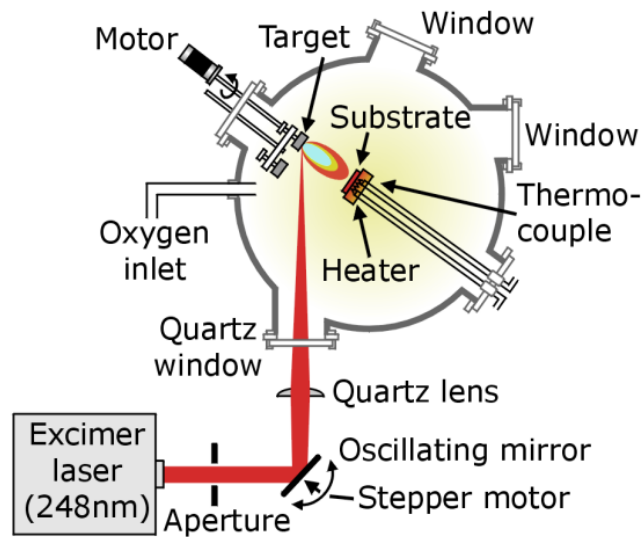


Figure II.8 - The configuration of a typical PLD system.

Several aspects that can influence the plasma plume, like laser energy, pulse duration, background pressure, target-substrate distance, also determine the crystalline quality of the deposited film. Hereafter, we will discuss those important parameters in details:

- **Substrate temperature:** Similar to other deposition technologies, substrate temperature is an essential parameter to control the crystalline structure and the quality of the film. A sufficient temperature is necessary to enhance the thermal diffusion of species and the crystallization process. The nucleation density usually decreases with increasing substrate temperature, leading to a more homogeneous thin film [24]. However, an overheating problem could also result in the deviation of the stoichiometry from that of target material, and therefore lead to undesired phase in the thin film.
- **Pulsed laser:** The laser energy used to ablate the target material is mainly determined by several aspects, like wavelength, energy flux, and pulse frequency. The optical index of the target material determines the ablation depth of the laser beam, usually ~20 nm. Different from other deposition technologies, within the duration of laser pulse, a large super-saturated flux of ablated atoms arrive at the substrate surface, causing a very large nucleation density. The high nucleation density on the surface can increase the roughness of the deposited film, and result in a reduced crystalline quality.
- **Atmosphere:** A reactive gas in the growth chamber is required when some materials are deposited, such as oxide and nitride. Taking the deposition of STO as an example, an

oxygen atmosphere can compensate an oxygen loss during the ablation process. An insufficient oxygen pressure could result in the formation of oxygen vacancies in STO thin film, degrading the electrical properties. On the other hand, high-pressure atmosphere could scatter and decelerate the ablated high-energy atoms, and therefore change the shape and the energy of the plasma plume. The high-energy plasma could re-sputter the deposited film, and consequently slow down the deposition speed and change the stoichiometry.

- **Target-substrate distance:** Usually, the substrate surface is mounted parallel to the surface of the target material, and faced at the center of the plasma plume. The target-substrate distance (typically 2 ~ 10 cm) is a key parameter that determines the activation energy and the flux of deposited atoms arriving at substrate surface. A larger distance can result in the lack of kinetic energy of the deposited atoms, and a smaller distance can cause a re-sputtering process. Besides, the homogeneity of the film, which is related to the distribution of the atom flux in the plasma plume, is also determined by the target-substrate distance.

#### **II.2.4) Sol-gel method**

Sol-gel method is a wet chemical deposition technology commonly used in thin film deposition and nanomaterial synthesis <sup>[25]</sup>. Comparing with other conventional processing methods for metallic oxide fabrication, like sintering of ceramics, pulling single crystals and drawing glass fibers, obviously, the sol-gel method has many advantages, especially for thin film fabrication, as follows:

- Good homogeneity. Since it is a liquid reaction processing, the diffusion rate of ions or molecules in a liquid is much faster than that in a solid.
- Ease of composition control and doping.
- Low sintering temperature.
- Large-area thin films. The spin-coating method is compatible with modern semiconductor fabrication to spread sol-gel solution on a large inch Si wafer, even for those coating on a surface with a complicated shape. The coating area is not limited by a vacuum chamber, such as vapor deposition or sputtering.
- Large possibility of microstructure control. Different microstructures of final products can be obtained by modifying the deposition conditions, like porous or dense, organic-inorganic hybrids, multi-layer structures, and nano-composites.
- Lower cost than other techniques.

## Chapter II - Epitaxial growth and characterization technologies

---

The term “sol-gel” explicitly concerns two chemical states during the process, namely *sol* and *gel*. Figure II.9 describes the sol-gel processing fabrication for metallic oxide thin film. The sol is a colloidal solution that consists of several starting materials in the form of submicron solid particles dispersed in the solvent as the precursor [26]. Generally, the sol particles may interact by van der Waals forces or hydrogen bonds. For most ferroelectric oxides, the starting material is usually organometallic compound, which undergoes hydrolysis and poly-condensation process at near room temperature to prepare the precursor solution. To spread the sol on the substrate for thin film deposition, several methods are available, like spin-coating, spraying, and dip-coating. Then, the sol film undergoes a series of thermal treatments to be solidified to form a crystalline oxide film on the substrate. During the solidification, the coated sol film is first dried to remove the solvent. The discrete colloidal particles precipitate to form the gel which is a cross-linked polymer network with abundance of pores. In most gel systems used for materials synthesis, the interactions are of a covalent nature and the gel process is irreversible. Then, the gel film is calcinated at an elevated temperature (350°C ~ 450°C). During the calcination, the pores in the film will shrink and the gel network will collapse, leading to smaller contact angle of the grains. Usually, the density of the gel increases with increasing the calcination temperature. At the same time, the organometallic compounds are decomposed by removing -OH and other functional groups. Only oxide material remains in the film after calcination to form a layer of amorphous material. A post thermal treatment at higher temperature (500°C ~ 800°C) is required to crystallize and enhance the crystalline phase of the film.

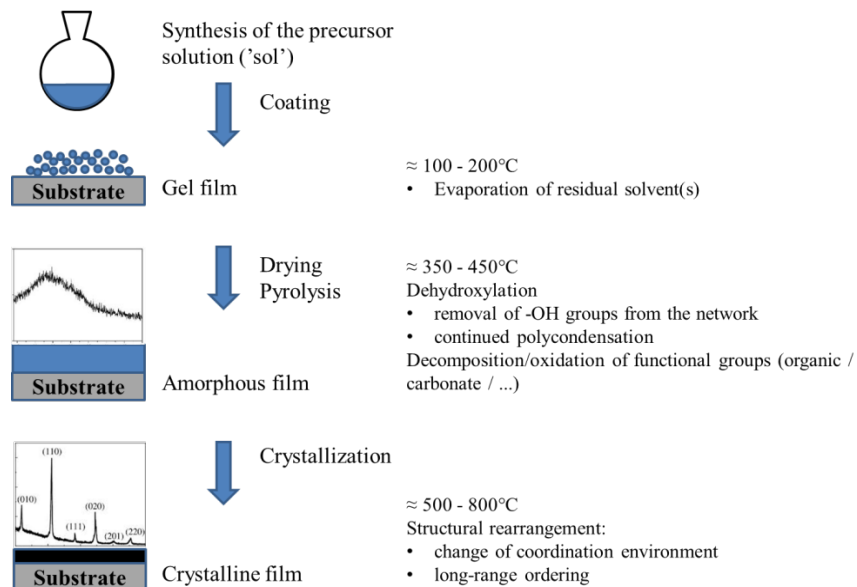


**Figure II.9 - The process of sol-gel deposition.**

For PZT material, the crystallization temperature of the thermodynamically stable perovskite phase is between 500°C and 700°C, usually via a transient non-ferroelectric pyrochlore-type phase, which is lead-deficient. The latter is stable between approximately 450°C and 550°C [27]. By Rapid Thermal Annealing over the temperature region of stability of the pyrochlore phase, the perovskite phase could be enhanced [28]. Extra lead organic compound in sol-gel solution could lower the perovskite crystallization temperature [29], and compensate the lead loss during thermal treatment. The crystallization temperature of the perovskite PZT also depends on the Zr/Ti ratio and is higher for Zr-rich PZT. The activation energy for the nucleation is larger than for the growth, in other words, nucleation is the rate-limiting step for the perovskite crystallization. The activation energy for nucleation is decreasing with increasing Ti-content in PZT [30, 31].

### **II.3) Characterization technologies**

#### **II.3.1) X-ray diffraction**

Crystalline structure of epitaxial thin films was analyzed by XRD technology. The configuration of the *Rigaku SmartLab* high-resolution diffractometer used in this thesis is illustrated in Figure II.10, which consists of several components like a microfocus rotating anode X-ray tube, a twin-crystal monochromator, a series of aperture slits, an X-ray detector and a mechanical rotational system. In X-ray tube, X-ray radiation is produced by the collision of high-velocity electron beam on a cathode target material, usually Cu. During the collision, most of the kinetic energy of electron beam is dissipated as heat, but around 1% of the energy is converted into X-ray radiation. A typical X-ray spectrum (Figure II.11) consists of a continuous background and a series of atomic emission lines which corresponds to the specific elements in the cathode. Table II.1 shows the wavelength of the atomic emission lines of several common cathode materials. Usually, the monochromator is required to single out the desired emission line, like Cu  $K_{\alpha 1}$ , from the continuous background as incident X-ray beam. A series of aperture slits are installed on the path of incident X-ray beam to define the divergence angle and the width of the incident beam. On the path of diffracted X-ray beam, the aperture slits determines the angular resolution. The attenuator in front of the X-ray detector is necessary to decrease the intensity of diffracted X-ray beam to the measurement limit of the detector. During the characterization, the intensity of diffracted X-ray beam is measured by X-ray detector while changing the angles in the rotational system according to the specific XRD mode. Finally, the intensity is recorded as a function of those angles.

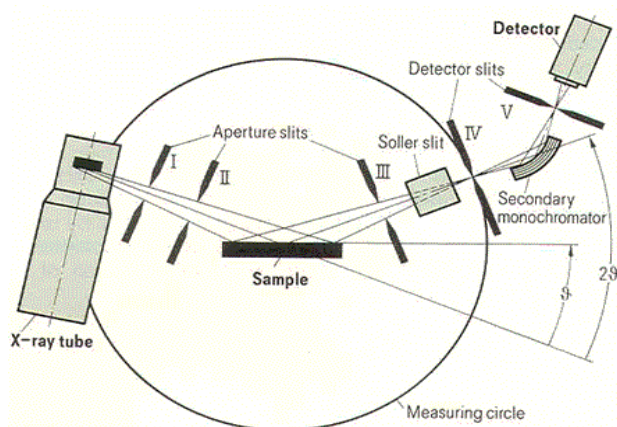


Figure II.10 - The configuration of Rigaku SmartLab high-resolution X-ray diffractometer.

Table II.1 - The wavelength of the characteristic emission lines for several common cathode materials.

Emission line	Cu (29#)	Mo (42#)	Fe (26#)	Co(27#)	Cr (24#)
$K_{\alpha 1}$ (Å)	1.54060	0.70930	1.93604	1.78897	2.28970
$K_{\alpha 2}$ (Å)	1.54439	0.71359	1.93998	1.79285	2.29361
$K_{\beta}$ (Å)	1.39222	0.63229	1.75661	1.62079	2.08487

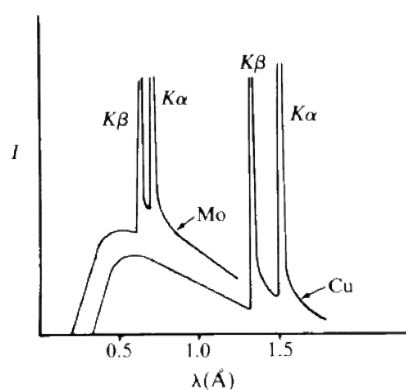


Figure II.11 - A typical X-ray spectrum generated by Mo and Cu cathode target.

In principle, XRD measurement uses the elastic scattering of X-ray photons by the core - electrons of the atoms to detect the crystalline structure of the material. In the elastic scattering, the wavelength of X-ray photon is maintained constant but the wave vector is changed. The X-ray beam diffracted by each atom in a periodic crystalline structure will interfere with each other, producing a structure-dependent intensity. Since the number of the unit cell is nearly infinite in the material, only in some particular conditions, the intensity of the interference is not equal to zero. Bragg's law defines the possible values of  $2\theta$  angle, namely the angle between the incident beam and the diffracted beam, at which such particular condition can be satisfied. In Bragg's law,

the crystalline structure is regarded as a stack of parallel diffracting planes (Figure II.12) and those possible  $2\theta$  angles are defined by the following equation:

$$2d \sin \theta = n\lambda \quad \text{Equ. II.1}$$

where  $d$  is the spacing between the parallel diffracting planes,  $\lambda$  is the wavelength of the X-ray, and  $n$  represents the diffraction order.

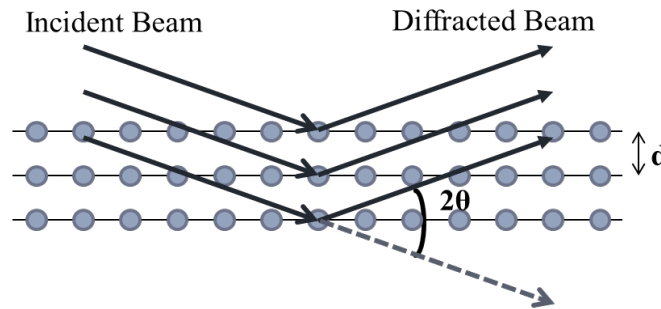


Figure II.12 - The illustration of Bragg's law.

Moreover, a more general law called “Laue equations” is available to describe the possible diffraction conditions that use the wave vector in the equation instead of the wavelength:

$$\Delta \vec{k} = \vec{k}_o - \vec{k}_i = \vec{G} \quad \text{Equ. II.2}$$

where  $\vec{k}_o$  and  $\vec{k}_i$  are the wave vector of the incident beam and the diffracted beam respectively,  $\Delta \vec{k}$  is the difference of  $\vec{k}_o$  and  $\vec{k}_i$  called “scattering vector”, and  $\vec{G}$  is a reciprocal space vector of the crystalline structure. The Bragg's law discussed above is thus the particular case in Laue equations, which regards the scattering vector as  $2\sin \theta / \lambda$ . In short, the possible diffractions only happen when the scattering vector is equal to a reciprocal space vector of sample's crystalline structure. Therefore, XRD characterization is actually equivalent to the detection of the reciprocal vector by rotating the scattering vector in reciprocal space. With *Rigaku* high-resolution XRD, several crystallographic angles in the rotational system can be changed, as illustrated in Figure II.13.

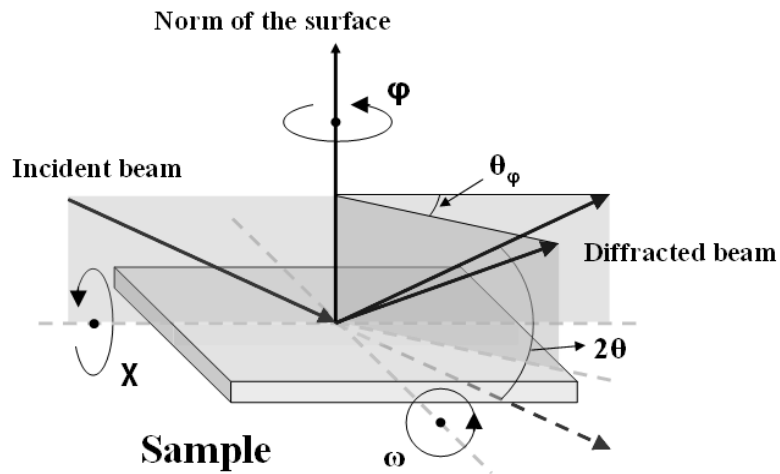


Figure II.13 - Several crystallographic angles changed in XRD measurement.

By combining the use of those crystallographic angles, structural characterization in diverse XRD modes can be realized. The corresponding analyzed region of various XRD modes in the reciprocal space is respectively presented in Figure II.14 by taking cubic crystalline structure as an example. The detail of each XRD mode will be discussed in details as follows:

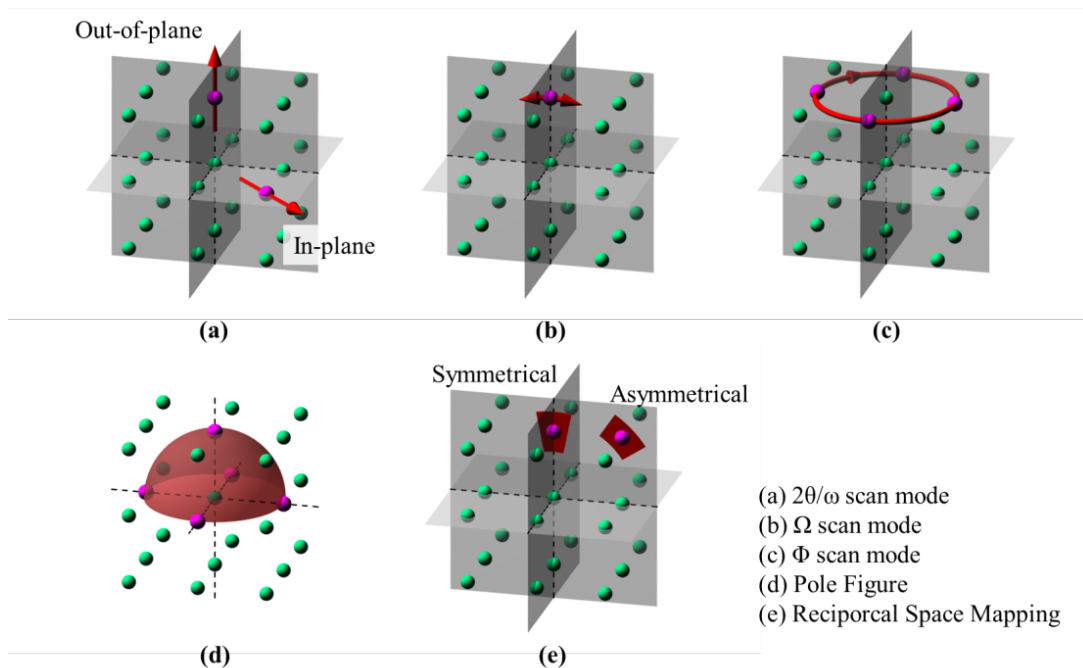


Figure II.14 - The analyzed region (in red) detected by various XRD modes in the reciprocal space. Taking cubic crystalline structure as an example.

- **$2\theta/\omega$  scan:** This mode simultaneously rotates  $2\theta$  and  $\omega$  angles while keeping  $\theta = \omega$ . During scanning, the scattering vector  $\Delta k$  is always along the normal direction of the film surface. So the reciprocal vector and the lattice constant in the out-of-plane direction are analyzed in this mode.
- **In-plane  $2\theta/\omega$  scan:** To measure the in-plane lattice constants,  $2\theta$  and  $\omega$  angles must be as small as possible while keeping sufficient intensity of diffracted X-ray for the detector. Instead of changing  $2\theta/\omega$  angle, this mode rotates  $\theta_\phi$  and  $\phi$  angles simultaneously. In addition, the initialization step to align the  $\phi$  angle along the scattering vector is required before the measurement.
- **$\Omega$  scan:** It is also called “rocking curve”, since the incident and diffracted beams simultaneously rotate in the same direction by changing  $\omega$  angle while keeping  $2\theta$  angle constant. It is primarily used to analyze the crystalline quality of the film in terms of mosaicity, curvature, misorientation, and inhomogeneity.
- **$\Phi$  scan:** This mode can analyze the orientation of the film crystalline structure. During the scan, the corresponding  $\chi$  angle of the detected crystalline plane, like (101), is fixed at a desired orientation, while  $\phi$  angle rotates from  $0^\circ$  to  $360^\circ$ . By this way, the symmetry of the crystalline plane around the normal to the surface is analyzed.
- **Pole Figure:** Pole figure can be regarded as a series of  $\Phi$  scans, which varies the  $\chi$  angle for each single scan. The analyzed region in the reciprocal space covers a semi-spherical surface, which has a fixed  $2\theta$  angle, namely a fixed length of scattering vector. In pole figure, more detailed information than the  $\Phi$  scan about the symmetry of the analyzed crystalline structure is visualized in the 2D image.
- **Reciprocal Space Mapping:** This mode takes a 2D snapshot of the selected region in the reciprocal space, which actually consists of a series of  $\Phi$  scans while varying the  $2\theta$  angle for each single scan. It provides the most complete amount of information about the texture, the crystalline quality, the internal strain, and the fine structure of the film crystal <sup>[32]</sup>.
- **X-Ray Reflectivity (XRR):** This mode does not detect any crystalline structure, but gives information on thickness, density and interface roughness of the different layers of a heterostructure. The rotational system in XRR measurement is similar to that of  $2\theta/\omega$  scan, but has a very small incident angle usually less than  $10^\circ$ . With such small incident angle, X-ray beam is partially reflected at the surface and different interfaces of a heterostructure. The interference of all the reflected X-ray beams gives rise to the outcoming X-ray beam,

where the reflectivity of the heterostructure is determined by the thickness, the electron density, and the roughness of each layer. By using Fourier transform or transfer-matrix method, the related parameters of each layer can be derived.

### **II.3.2) Transmission Electron Microscopy**

The first TEM setup was invented by Max Knoll and Ernst Ruska in 1931 as the extension of the optical microscopy, it utilizes high-speed electron beam instead of light to image the object. In TEM, the electrons are emitted either by thermionic or field electron emission, and then accelerated by high voltage (100 ~ 1000 kV) to a velocity approaching the speed of light ( $0.6c \sim 0.9c$ ). The associated de Broglie wavelength is much smaller ( $0.04 \sim 0.008 \text{ \AA}$ ) than that of the light and thus allows a sub-nanometric resolution. Such high resolution enables material imaging and structure determination at atomic level. Besides, due to the electric charge carried by the electron, the control of the electron beam, like focus and bending, is much easier than that of the light by using either electric field or magnetic field. Figure II.15 shows the schematic of a typical TEM column which mainly consists of several components, such as electron beam gun, two series of magnetic lenses as the ocular and objective lens, and the screen in the vacuum system. An energy dispersive spectrometer, which analyses the emitted X-ray associated with the interaction of the electrons and material sample to detect the chemical composition, is usually added to TEM setup nowadays.

Bright field mode is the most common mode of operation for TEM. In this mode, the contrast of TEM image is formed directly by the scattering and the absorption of electrons in the sample. The thicker part of the sample or the part with a higher atomic weight will appear dark, while the others will appear bright. Therefore, TEM contrast can distinguish any variation of the crystalline structure, like dislocations, grain boundaries and additional phases. The diffraction mode is another TEM mode used for the analysis of crystalline materials in which the electron beam undergoes Bragg scattering. By using an objective aperture, the desired Bragg diffraction can be selectively projected on the imaging screen, making this mode useful for the detection of crystalline structure. As an application, the crystalline orientation in layers of a heterostructure along the electron beam direction can be analyzed. In this thesis, TEM setup is mainly used to analyze crystalline structure, interfaces of heterostructure layers and other morphotropic structures in ferroelectric materials.

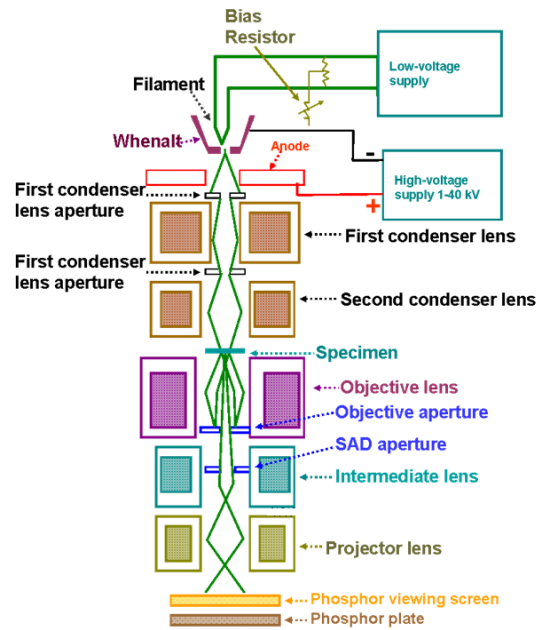


Figure II.15 - The schematic of a transmission electron microscope column.

### II.3.3) Electrical measurement

#### II.3.3.1) Impedance meter

The electrical properties of ferroelectric films were characterized by electrical impedance measurements using a *HP 4284A* impedance meter. The schematic of the equipment is shown in Figure II.16, and it can be simplified as an equivalent 4-point probes system. An ac voltage is used as the excitation signal, while dc voltage is applied as a bias. The complex voltage ( $U_{Lpot-Hpot}$ ) and current ( $I_{Lcur-Hcur}$ ) are measured by integrating the output signal during a given time constant. From the Ohm's law, the complex impedance ( $\tilde{Z}$ ) can be derived.

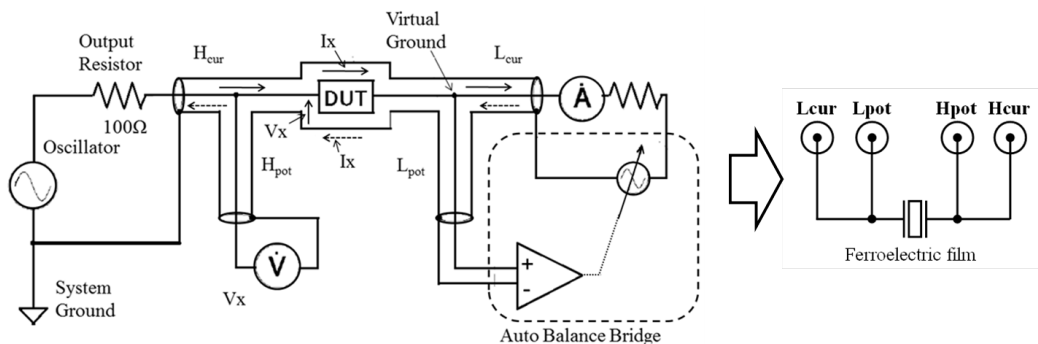


Figure II.16 - Principle of *HP 4284A* impedance meter and the equivalent circuit in the electrical characterization.

The electrical results can be analyzed according to two equivalent circuit models, namely the parallel circuit model and the series circuit model (Figure II.17). In the series circuit model, the real and imaginary parts of the impedance represent the resistance ( $R$ ) and the reactance ( $X$ ), respectively. In the parallel circuit model, the admittance ( $\tilde{Y}$ ), namely the inverse of the impedance, is used to represent the conductance ( $G$ ) and the susceptance ( $B$ ). Equation II.3 gives the real and the imaginary parts of the impedance and the admittance:

$$\text{Impedance in series circuit: } \tilde{Z} = \frac{\tilde{U}}{\tilde{I}} = R + jX = R_s - \frac{1}{2\pi f C_s} j \quad \text{Equ. II.3}$$

$$\text{Admittance in parallel circuit: } \tilde{Y} = \frac{\tilde{I}}{\tilde{U}} = G + jB = G - 2\pi f C_p j$$

where  $f$  is the frequency of the excitation ac signal,  $j$  is the imaginary unit,  $R_s$  and  $C_s$  are the resistance and the capacitance in series circuit,  $G$  and  $C_p$  are the conductance and the capacitance in parallel circuit. When small capacitance is measured, which implies that the effect of the parallel resistance ( $R_p$ ) has relatively more significance than that of series resistance ( $R_s$ ), the parallel circuit model ( $C_p$ - $G$ ) should be used. Otherwise, the series circuit model ( $C_s$ - $R_s$ ) should be used. For ferroelectric thin film capacitor whose capacitance is usually less than 1 nF, the  $C_p$ - $G$  parallel circuit model is often used in the electrical characterization.

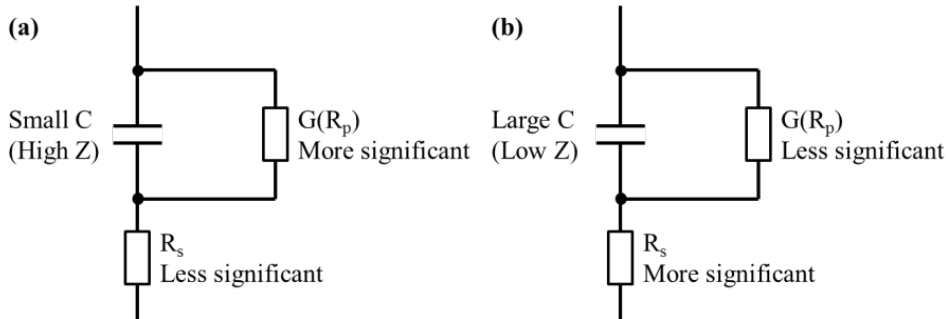


Figure II.17 - Two modes in the electrical characterization: (a)  $C_p$ - $G$  parallel mode, (b)  $C_s$ - $R_s$  series mode.

In addition, quality factor ( $Q$ ) and dissipation factor ( $D$ ), namely loss tangent, are often used to quantify the inherent dissipation in the ferroelectric film, which are defined as follows:

$$Q = \frac{1}{D} = \frac{|X|}{R} \text{ or } Q = \frac{1}{D} = \frac{|B|}{G} \quad \text{Equ. II.4}$$

In *HP 4284A*, three variables, namely dc bias, ac frequency and amplitude, can be swept during the measurement. In the following part, several commonly used modes in the electrical characterization will be addressed by taking  $C_p$ - $D$  mode as an example, namely capacitance and dielectric loss in parallel circuit:

**C<sub>p</sub>-D vs. dc bias** (or C-V measurement): A typical ferroelectric film often shows a butterfly-like hysteresis loop in C-V measurement (Figure II.18). The dielectric permittivity in ferroelectric film involves two contributions: 1) extension of the permanent polarization at high dc bias, and 2) domain wall movements at low dc bias. Usually, the latter one is more significant than the former one in electrical permittivity, leading to the rise of dielectric permittivity at low dc bias. The C-V curve often exhibits a slight asymmetry that is probably caused by the presence of internal fields, known as imprint effect.

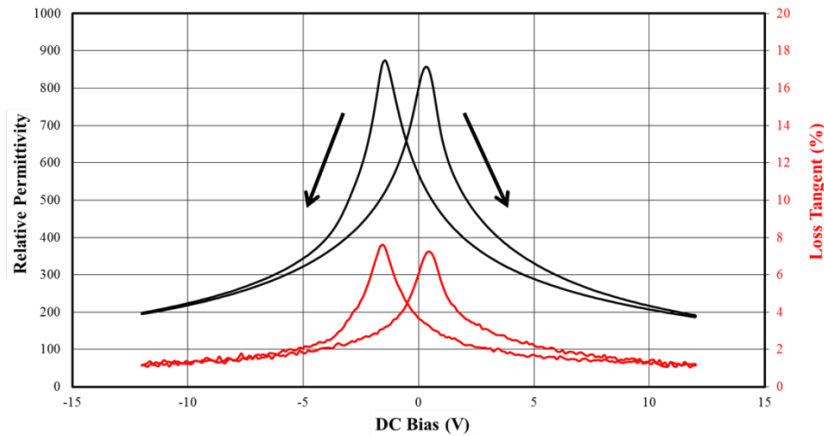


Figure II.18 – The electrical impedance of PZT ferroelectric film in C<sub>p</sub>-D mode by sweeping dc bias.

The tunability of ferroelectric films in dielectric permittivity is defined using Equation II.5:

$$\text{Tunability} = \frac{\varepsilon_r(0) - \varepsilon_r(E)}{\varepsilon_r(E)} \times 100 \quad \text{Equ. II.5}$$

where  $\varepsilon_r(0)$  and  $\varepsilon_r(E)$  are the dielectric permittivity at zero field and under applied bias field, respectively. The loss tangent (related to the leakage current) is also an important parameter of thin film ferroelectric capacitor since it degrades the charge retention. It is largely dependent on the structural and chemical quality of the ferroelectric film and of the film – electrode interfaces.

**C<sub>p</sub>-D vs. ac frequency:** The dielectric dispersion is essentially related to the separation of positive and negative charges which has various sources at different resonance frequency, such as ferroelectric domain walls movement, dipolar vibration, atomic movement, and separation of electrons and nuclei (Figure II.19). At high frequency, those having lower resonance frequency do not contribute to the permittivity due to the fact that the separation of the charges cannot follow the change of the alternative electric field. Debye model and its variants are commonly used to describe the dielectric dispersion by using the concept of ideal and non-interacting

electric dipoles. In Debye relaxation, the electric permittivity of a single electric dipole is represented as a function of the frequency of ac electric field by the following equations:

$$\hat{\epsilon}(\omega) = \epsilon_{\infty} + \frac{\Delta\epsilon}{1 + i\omega\tau} \quad \text{Equ. II.6}$$

where  $\epsilon_{\infty}$  is the permittivity at the high frequency limit,  $\Delta\epsilon = \epsilon_s - \epsilon_{\infty}$  where  $\epsilon_s$  is the static, low frequency permittivity,  $\omega$  is the angular frequency, and  $\tau$  is the characteristic relaxation time of the medium. The dielectric permittivity is a complex value of which the real and the imaginary parts are related to the stored energy and the dissipated energy in the electric dipole.

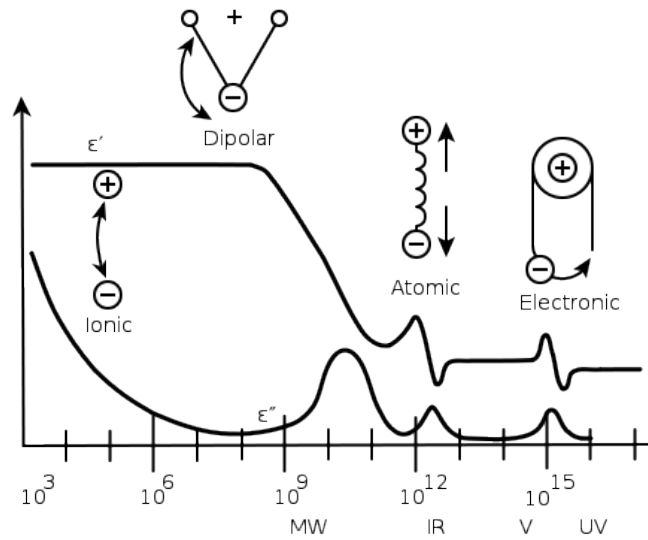


Figure II.19 - Dielectric permittivity ( $\epsilon'$  and  $\epsilon''$ ) spectrum over a wide range of frequencies.

**C<sub>p</sub>-D vs. ac amplitude:** It is also called “Rayleigh analysis” which was developed as an analogue approach as the Rayleigh law applied for ferromagnetic material <sup>[33,34]</sup>. In ferroelectric material, the dielectric or piezoelectric response includes both intrinsic and extrinsic contributions. The intrinsic response refers to the atomic lattice contribution at the unit cell level. The extrinsic response refers to the movement of domain walls <sup>[35]</sup>. The defects in the ferroelectric material act as the pinning centers to prevent the movement. In such a case, the potential energy becomes an irregular function of the domain wall position (Figure II.20). For small electric field, the movement of domain walls is confined between the large potential barriers, and thus is reversible near the equilibrium position. For large electric field, the domain wall is driven across the potential barrier, and thus the movement is an irreversible and lossy process.

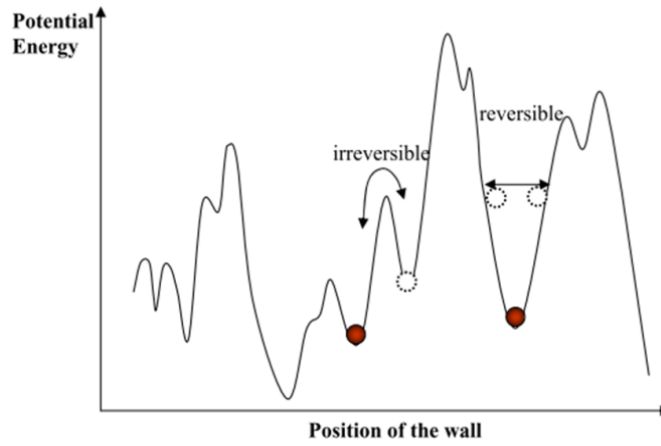


Figure II.20 - Potential of a domain wall in a medium with randomly distributed pinning centers.

Several characterization technologies are available to separate intrinsic and extrinsic contributions in ferroelectrics, like temperature dependence of the piezoelectric and dielectric properties <sup>[36]</sup>, the frequency dispersion, and also the Rayleigh analysis. The Rayleigh analysis is often performed under the sub-switching condition, namely the ac amplitude is lower than the coercitive electric field, to avoid the unexpected polarization switching. The field-dependent dielectric permittivity and polarization can be simply expressed as following:

$$\begin{aligned} \varepsilon_{33} &= \varepsilon_{init} + \alpha E_0 \\ P_3 &= \varepsilon_{init} E_0 + \alpha E_0^2 \end{aligned} \quad \text{Equ. II.7}$$

where  $\varepsilon_{init}$  is the initial dielectric permittivity caused by the intrinsic component and the reversible movement of domain walls, and  $\alpha$  is the Rayleigh coefficient which quantifies the field-dependent irreversible movement of domain walls <sup>[37]</sup>. These two parameters are found to be strongly dependent on various parameters, such as grain size, local fluctuation of chemical composition, crystalline structure of the material, nature of defects, external dc bias, history of the sample, and also aging conditions. Another version of Rayleigh Law introduces a threshold electric field ( $E_{th}$ ) into the equation <sup>[38]</sup>, namely the permittivity remains constant for  $E < E_{th}$  and then increases according to the following equation for  $E > E_{th}$ :

$$\varepsilon_{33} = \varepsilon_{init} + \alpha(E_0 - E_t) \quad \text{Equ. II.8}$$

This  $E_{th}$  value is often not easily determined since the increase of the permittivity can happen gradually, and therefore the selection of  $E_{th}$  value may become arbitrary. A 5% rise with respect to the low field value has been proposed as the reference for  $E_{th}$  <sup>[39]</sup>. Because the nonlinearities have been associated with interface pinning, the threshold field is considered as the measurement of the degree of pinning effect <sup>[40]</sup>. In addition, at higher fields beyond the Rayleigh region, the

onset of polarization switching changes the energy landscape of the system. The Rayleigh Law no longer applies and the field dependence becomes sub or super linear. In Figure II.21, the three regions in the field-dependent dielectric permittivity are schematically represented.

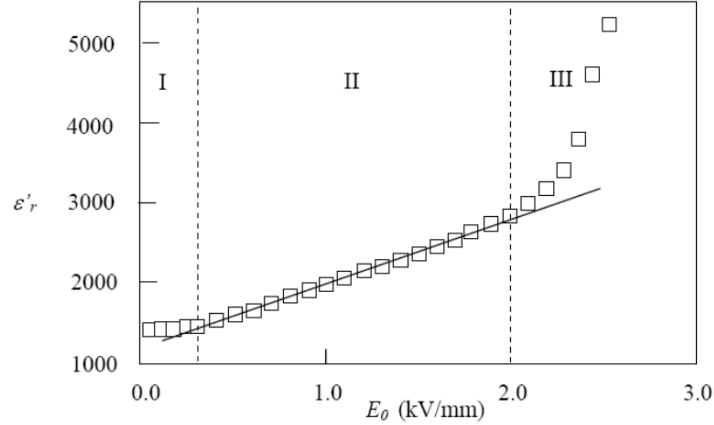


Figure II.21 - Schematic of the ac field dependence of dielectric permittivity <sup>[41]</sup> including 3 regions, namely the low field region (I), the Rayleigh region (II), and the high field region (III).

### II.3.3.2) Polarization vs. electric field

Two electronic circuits are commonly used to measure the polarization of ferroelectric film, namely Sawyer-Tower circuit <sup>[42]</sup> and virtual ground circuit. Figure II.22 exhibits the configuration of Sawyer-Tower circuit used in this thesis. On the oscilloscope, channel X ( $V_x$ ) displays the voltage of the applied ac signal and channel Y ( $V_y$ ) displays the voltage drop across the reference capacitor ( $C_{ref}$ ) which is proportional to the accumulated charge on the surface of ferroelectric film. The polarization and the applied electric field on the ferroelectric film can be derived by following equations:

$$P = \frac{Q}{S} = \frac{C_{ref} V_y}{S} \tag{Equ. II.9}$$

$$E = \frac{V_x - V_y}{d}$$

where  $S$  and  $d$  are the area and the thickness of the ferroelectric capacitor, respectively.

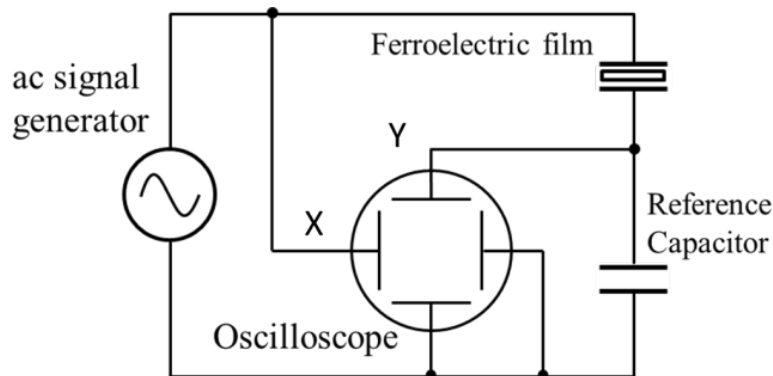


Figure II.22 - Illustration of the Sawyer-Tower circuit.

### II.3.4) Piezoresponse Force Microscopy

Piezoresponse Force Microscopy (PFM) is a versatile characterization technology for studying at a sub-micronic scale the piezoelectric properties of ferroelectric films. It is usually based on a modified Atomic Force Microscopy setup. Figure II.23 shows the main features of a typical PFM setup. By using a conductive tip, an electric field is directly applied at nanometric scale on the surface of a ferroelectric film. The induced displacement of the film surface is mechanically coupled with the PFM cantilever, and can be detected with a four - quadrant photodiode in the setup<sup>[43]</sup>. However, the static displacement induced by the applied electric field is too weak ( $\sim 100$  pm) to be easily detected because of the relatively large surface roughness. Increasing the imaging voltage is a way to increase the signal-to-noise ratio, but a high imaging voltage may possibly reverse the ferroelectric domains and make a non-destructive characterization impossible. Practically, a sinusoidal ac voltage is applied in PFM setup instead of a dc voltage. The amplitude of the applied ac voltage is usually smaller than the coercive voltage of the ferroelectric film to avoid the destruction of ferroelectric domains structure. Consequently, the local surface of a ferroelectric film vibrates at the same frequency as the applied ac voltage. A lock-in amplifier is used to extract the electrical signal associated with the vibration from an extremely noisy background by using the applied ac voltage as a reference. The amplitude and phase of the vibration are the final outputs at each pixel of the image while scanning the surface of the ferroelectric film.

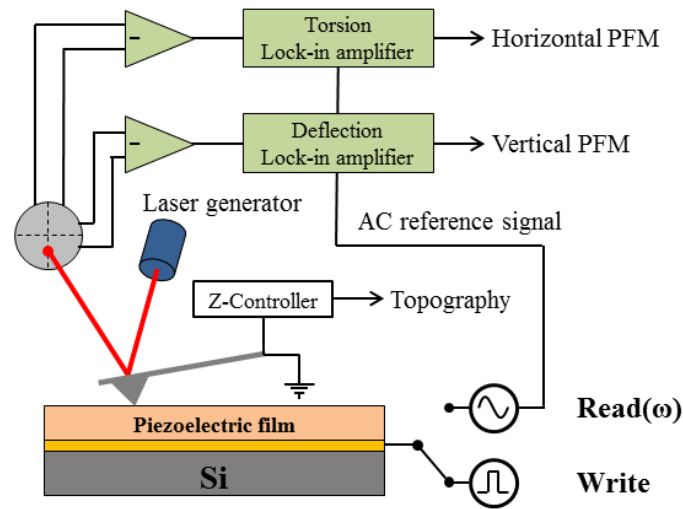


Figure II.23 - The principle of a typical PFM setup.

In ferroelectric films, the mechanical vibration induced by the applied ac voltage is mainly determined by the orientation and the strength of the permanent polarization under the PFM tip. According to the orientation of the permanent polarization, two effects may happen in the measurement. When the permanent polarization is along the normal of the film, local surface will contract or extend. The amplitude of the longitudinal vibration is related to  $d_{33}$  value. When the permanent polarization is parallel to the film surface, local surface will shear. The amplitude of transverse vibration is related to  $d_{14}$  and  $d_{25}$  values. By using vertical or lateral mode, PFM setup can individually detect these two types of vibrations (Figure II.24). For the arbitrary orientation, the vector of permanent polarization on the surface of ferroelectric film can be mapped if these 3 piezoelectric coefficients are measured. In addition, to quantify the piezoelectric coefficients, a reference material with a known piezoelectric coefficient, like quartz film, is often used to calibrate the proportionality constant between the output amplitude and the piezoelectric coefficient. Figure II.25 exhibits an example of an ideal surface of ferroelectric film, where the phase and the amplitude vary according to the ferroelectric domains under the PFM tip during the scan. For those two polarizations having opposite directions, the phase difference is  $180^\circ$ . The ferroelectric film vibrates in the opposite direction under the same ac electric field. When the PFM tip scans across the boundary of ferroelectric domains, the amplitude of the vibration decreases nearly to zero due to the opposite vibrations. Usually, there is a series of resonance frequencies determined by the whole system which consists of the PFM tip and the ferroelectric film in mechanical and electrical coupling. At such resonance frequency, the induced vibration by the applied ac voltage has the maximum amplitude; this could be utilized to obtain a higher signal-to-noise ratio. But at such resonance frequency, not only the piezoelectric coefficient but

also the structural parameters of the film will determine the mechanical vibration, like acoustic wave. So the resonance frequency should not be used to measure the piezoelectric coefficient.

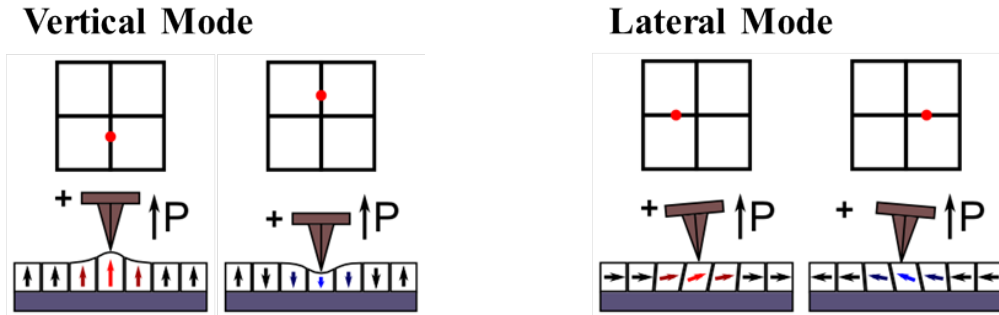


Figure II.24 –Two PFM modes: vertical and lateral mode.

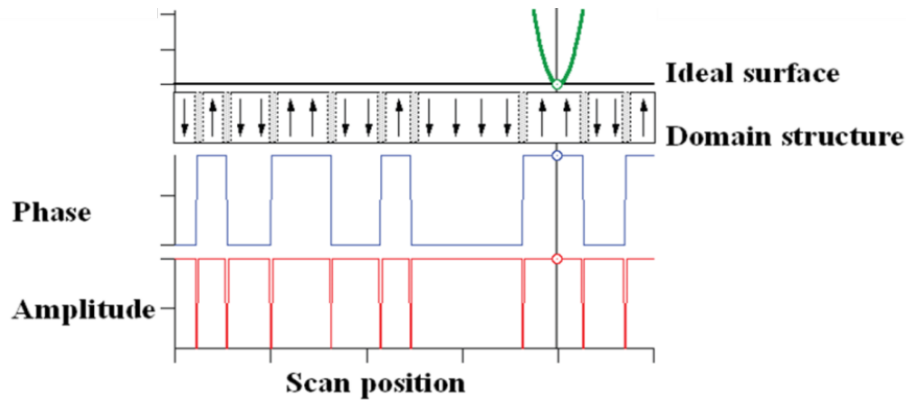


Figure II.25 - The influence of the orientation of the permanent polarization on the output amplitude and phase of lock-in amplifier in an ideal smooth ferroelectric film.

### II.3.5) Mechanical characterization

The mechanical performance of piezoelectric devices was characterized by *WYKO NT3300* Profiling System which can make non-contact distance variation and vibration measurements by using light interference. Two modes are available for this setup: Phase-Shift Interferometry (PSI) that uses a single wavelength of the light, and Vertical-Scanning Interferometry (VSI) that uses multiple wavelengths of the light. PSI mode is suitable for a continuous surface whose roughness is less than 1/4 wavelength (about 150 nm) and the resolution is about 0.1 nm. VSI mode is good for measuring the height variations as high as millimeter, but has a reduced resolution of about 10 - 30 nm. Here, PSI mode is used in the characterization of piezoelectric devices, like membrane and cantilever, since the actuated mechanical displacement is in agreement with the range and the resolution of this mode. The configuration of the profiling system is shown in Figure II.26.

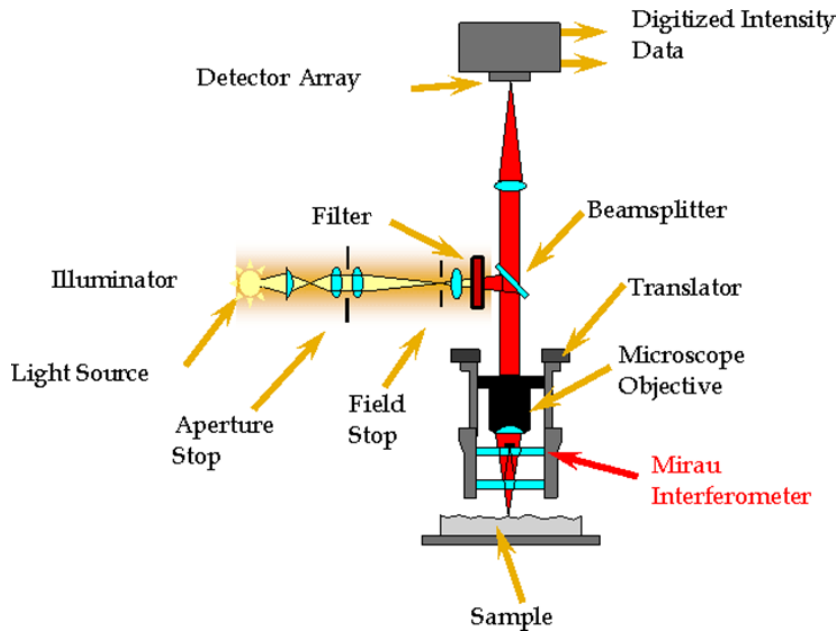


Figure II.26 - The configuration and the principle of WYKO NT3300 profiling system.

In WYKO NT3300 profiling system, a white light beam generated by the illuminator is filtered by a monochromator into single wavelength for PSI mode. A beam splitter is used to divide the light beam into two paths, in which one is focused on the sample surface for detection and another used as reference. During scanning on the sample surface, the optical path of the detection beam varies with the vertical profile of the surface at the focus of the light, so the phase changes. At Mirau interferometer, the detection beam reflected from the film surface interferes with the reference beam and thus the intensity changes according to the profile of the surface. The intensity at each pixel is converted to the vertical height to form the profile image of the sample surface. In this thesis, the profiling analysis was mainly used to measure the mechanical displacement of the piezoelectric devices as a function of the applied dc voltage. By using finite element method or analytic method, such function is modeled and the piezoelectric coefficients can be extracted.

#### II.4) Reference

- [1] C. V Falub, H. von Känel, F. Isa, R. Bergamaschini, A. Marzegalli, D. Chrastina, G. Isella, E. Müller, P. Niedermann, and L. Miglio, "Scaling hetero-epitaxy from layers to three-dimensional crystals.," *Science (New York, N.Y.)*, vol. 335, no. 6074, pp. 1330–4, Mar. 2012.

- [2] C. J. Sandroff, J. P. Harbison, R. Ramesh, M. J. Andrejco, M. S. Hegde, C. C. Chang, E. M. Vogel, and D. M. Hwang, "GaAs Clusters in the Quantum Size Regime: Growth on High Surface Area Silica by Molecular Beam Epitaxy.," *Science (New York, N.Y.)*, **vol. 245**, no. 4916, pp. 391–3, Jul. 1989.
- [3] Y. Qi, S. H. Rhim, G. F. Sun, M. Weinert, and L. Li, "Epitaxial Graphene on SiC(0001): More than Just Honeycombs," *Physical Review Letters*, **vol. 105**, no. 8, p. 085502, Aug. 2010.
- [4] X. Wu, M. Sprinkle, X. Li, F. Ming, C. Berger, and W. de Heer, "Epitaxial-Graphene/Graphene-Oxide Junction: An Essential Step towards Epitaxial Graphene Electronics," *Physical Review Letters*, **vol. 101**, no. 2, p. 026801, Jul. 2008.
- [5] S. Tomasulo, K. Nay Yaung, J. Simon, and M. L. Lee, "GaAsP solar cells on GaP substrates by molecular beam epitaxy," *Applied Physics Letters*, **vol. 101**, no. 3, p. 033911, 2012.
- [6] A. Y. Cho and J. R. Arthur, "Molecular beam epitaxy," *Progress in Solid State Chemistry*, **vol. 10**, pp. 157–191, Jan. 1975.
- [7] R. Singh and J. Narayan, "Pulsed-laser evaporation technique for deposition of thin films: Physics and theoretical model," *Physical Review B*, **vol. 41**, no. 13, pp. 8843–8859, May 1990.
- [8] J. T. Cheung and H. Sankur, "Growth of thin films by laser-induced evaporation," *Critical Reviews in Solid State and Materials Sciences*, **vol. 15**, no. 1, pp. 63–109, Jan. 1988.
- [9] D. H. Lowndes, D. B. Geohegan, A. A. Puretzky, D. P. Norton, and C. M. Rouleau, "Synthesis of Novel Thin-Film Materials by Pulsed Laser Deposition," *Science*, **vol. 273**, no. 5277, pp. 898–903, Aug. 1996.
- [10] D. Dijkkamp, T. Venkatesan, X. D. Wu, S. A. Shaheen, N. Jisrawi, Y. H. Min-Lee, W. L. McLean, and M. Croft, "Preparation of Y-Ba-Cu oxide superconductor thin films using pulsed laser evaporation from high T<sub>c</sub> bulk material," *Applied Physics Letters*, **vol. 51**, no. 8, p. 619, 1987.
- [11] V. Craciun, J. Elders, J. G. E. Gardeniers, and I. W. Boyd, "Characteristics of high quality ZnO thin films deposited by pulsed laser deposition," *Applied Physics Letters*, **vol. 65**, no. 23, p. 2963, 1994.
- [12] H. J. Wen, "Investigation of existing defects and defect generation in device-grade SiO<sub>2</sub> by ballistic electron emission spectroscopy," *Journal of Vacuum Science & Technology B: Microelectronics and Nanometer Structures*, **vol. 15**, no. 4, p. 1080, Jul. 1997.

- [13] J. S. Horwitz, K. S. Grabowski, D. B. Chrisey, and R. E. Leuchtner, "In situ deposition of epitaxial  $\text{PbZr}_x\text{Ti}_{1-x}\text{O}_3$  thin films by pulsed laser deposition," *Applied Physics Letters*, **vol. 59**, no. 13, p. 1565, 1991.
- [14] R. D. Vispute, J. Narayan, H. Wu, and K. Jagannadham, "Epitaxial growth of AlN thin films on silicon (111) substrates by pulsed laser deposition," *Journal of Applied Physics*, **vol. 77**, no. 9, p. 4724, 1995.
- [15] D. Feiler, R. S. Williams, A. A. Talin, H. Yoon, and M. S. Goorsky, "Pulsed laser deposition of epitaxial AlN, GaN, and InN thin films on sapphire(0001)," *Journal of Crystal Growth*, **vol. 171**, no. 1–2, pp. 12–20, Jan. 1997.
- [16] R. D. Vispute, V. Talyansky, R. P. Sharma, S. Choopun, M. Downes, T. Venkatesan, Y. X. Li, L. G. Salamanca-Riba, A. A. Iliadis, K. A. Jones, and J. McGarrity, "Advances in pulsed laser deposition of nitrides and their integration with oxides," *Applied Surface Science*, **vol. 127–129**, pp. 431–439, May 1998.
- [17] F. Santerre, M. A. El Khakani, M. Chaker, and J. P. Dodelet, "Properties of TiC thin films grown by pulsed laser deposition," *Applied Surface Science*, **vol. 148**, no. 1–2, pp. 24–33, Jun. 1999.
- [18] Y. H. Tang, T.-K. Sham, D. Yang, and L. Xue, "Preparation and characterization of pulsed laser deposition (PLD) SiC films," *Applied Surface Science*, **vol. 252**, no. 10, pp. 3386–3389, Mar. 2006.
- [19] J. G. Lunney, "Pulsed laser deposition of metal and metal multilayer films," *Applied Surface Science*, **vol. 86**, no. 1–4, pp. 79–85, Feb. 1995.
- [20] H. U. Krebs, M. Störmer, S. Fähler, O. Bremert, M. Hamp, A. Pundt, H. Teichler, W. Blum, and T. H. Metzger, "Structural properties of laser deposited metallic alloys and multilayers," *Applied Surface Science*, **vol. 109–110**, pp. 563–569, Feb. 1997.
- [21] S. G. Hansen and T. E. Robitaille, "Formation of polymer films by pulsed laser evaporation," *Applied Physics Letters*, **vol. 52**, no. 1, p. 81, 1988.
- [22] S. T. Li, E. Arenholz, J. Heitz, and D. Bäuerle, "Pulsed-laser deposition of crystalline Teflon (PTFE) films," *Applied Surface Science*, **vol. 125**, no. 1, pp. 17–22, Jan. 1998.
- [23] A. Piqué, R. C. Auyeung, J. Stepnowski, D. Weir, C. Arnold, R. McGill, and D. Chrisey, "Laser processing of polymer thin films for chemical sensor applications," *Surface and Coatings Technology*, **vol. 163–164**, pp. 293–299, Jan. 2003.

- [24] J. D. Ferguson, G. Arikan, D. S. Dale, A. R. Woll, and J. D. Brock, "Measurements of Surface Diffusivity and Coarsening during Pulsed Laser Deposition," *Physical Review Letters*, **vol. 103**, no. 25, p. 256103, Dec. 2009.
- [25] C. J. Brinker, A. J. Hurd, P. R. Schunk, G. C. Frye, and C. S. Ashley, "Review of sol-gel thin film formation," *Journal of Non-Crystalline Solids*, **vol. 147–148**, pp. 424–436, Jan. 1992.
- [26] J. T. Davis, E. K. Rideal, *Interfacial Phenomena* (Academic Press: New York, 1963).
- [27] A. H. Carim, B. A. Tuttle, D. H. Dougherty, and S. L. Martinez, "Microstructure of Solution-Processed Lead Zirconate Titanate (PZT) Thin Films," *Journal of the American Ceramic Society*, **vol. 74**, no. 6, pp. 1455–1458, Jun. 1991.
- [28] E. M. Griswold, L. Weaver, M. Sayer, and I. D. Calder, "Phase transformations in rapid thermal processed lead zirconate titanate," *Journal of Materials Research*, **vol. 10**, no. 12, pp. 3149–3159, Mar. 2011.
- [29] Suzuki H, Kondo Y, Kaneko S, and Hayashi T, *T MRS Jap* **24**, 39–42 (1999).
- [30] C. K. Kwok and S. B. Desu, "Low temperature perovskite formation of lead zirconate titanate thin films by a seeding process," *Journal of Materials Research*, **vol. 8**, no. 02, pp. 339–344, Jan. 2011.
- [31] Zelinski BJ, Brinker CJ, Clark DE, Ulrich DR (eds) *Better ceramics through chemistry IV*, vol. 180. Materials Research Society, Pittsburg, 663–668 (1990).
- [32] P. F. Fewster, "Reciprocal space mapping," *Critical Reviews in Solid State and Materials Sciences*, **vol. 22**, no. 2, pp. 69–110, Jun. 1997.
- [33] L. Rayleigh, *Philos. Mag.* **23**, 225 (1887).
- [34] L. Néel, "Théories des lois d'aimantation de Lord Rayleigh," *Cah. Phys.*, **vol. 12**, pp. 1-20, 1942.
- [35] Q. M. Zhang, H. Wang, N. Kim, and L. E. Cross, "Direct evaluation of domain-wall and intrinsic contributions to the dielectric and piezoelectric response and their temperature dependence on lead zirconate-titanate ceramics," *Journal of Applied Physics*, **vol. 75**, no. 1, p. 454, 1994.
- [36] F. Xu, S. Trolier-McKinstry, W. Ren, B. Xu, Z.-L. Xie, and K. J. Hemker, "Domain wall motion and its contribution to the dielectric and piezoelectric properties of lead zirconate titanate films," *Journal of Applied Physics*, **vol. 89**, no. 2, p. 1336, 2001.

- [37] R. E. Eitel, T. R. Shrout, and C. A. Randall, “Nonlinear contributions to the dielectric permittivity and converse piezoelectric coefficient in piezoelectric ceramics,” *Journal of Applied Physics*, **vol. 99**, no. 12, p. 124110, 2006.
- [38] D. A. Hall, “Rayleigh behaviour and the threshold field in ferroelectric ceramics,” *Ferroelectrics*, **vol. 223**, no. 1, pp. 319–328, Mar. 1999.
- [39] S. Li, W. Cao, and L. E. Cross, “The extrinsic nature of nonlinear behavior observed in lead zirconate titanate ferroelectric ceramic,” *Journal of Applied Physics*, **vol. 69**, no. 10, p. 7219, 1991.
- [40] H.-J. Hagemann, “Loss mechanisms and domain stabilisation in doped BaTiO<sub>3</sub>,” *Journal of Physics C: Solid State Physics*, **vol. 11**, no. 15, pp. 3333–3344, Aug. 1978.
- [41] D. A. Hall and P. J. Stevenson, “High field dielectric behaviour of ferroelectric ceramics,” *Ferroelectrics*, **vol. 228**, no. 1, pp. 139–158, May 1999.
- [42] C. Sawyer and C. Tower, “Rochelle Salt as a Dielectric,” *Physical Review*, **vol. 35**, no. 3, pp. 269–273, Feb. 1930.
- [43] O. Kolosov, A. Gruverman, J. Hatano, K. Takahashi, and H. Tokumoto, “Nanoscale Visualization and Control of Ferroelectric Domains by Atomic Force Microscopy,” *Physical Review Letters*, **vol. 74**, no. 21, pp. 4309–4312, May 1995.

**Chapter III - Integration of epitaxial PZT thin film on Si substrate**

---

---

<b>III.1) Introduction .....</b>	<b>78</b>
<b>III.2) Evaluation of SrTiO<sub>3</sub> film on Si(001) for the use of buffer layer .....</b>	<b>78</b>
III.2.1) Experimental details .....	78
III.2.1.1) Chemical treatment of Si(001) substrate .....	78
III.2.1.2) Passivation of Si(001) surface using Sr .....	80
III.2.1.3) Two-step growth method .....	81
III.2.2) Crystalline structure and surface topography of epitaxial SrTiO <sub>3</sub> film .....	83
III.2.3) Conclusion .....	84
<b>III.3) Sol-gel deposition of PZT film on SrTiO<sub>3</sub>/Si(001) .....</b>	<b>85</b>
III.3.1) Sol-gel deposition of PZT film .....	85
III.3.2) Influence of annealing temperature .....	86
III.3.2.1) Crystalline structure .....	87
III.3.2.2) Surface topography .....	90
III.3.2.3) Electrical characterization .....	90
III.3.3) Microscopic structure of PZT/SrTiO <sub>3</sub> /Si(001) stack .....	92
III.3.4) Chemical profile of PZT/SrTiO <sub>3</sub> /Si(001) stack .....	94
III.3.5) Conclusion .....	97
<b>III.4) Use of SrRuO<sub>3</sub> bottom electrode for integration of PZT on Si .....</b>	<b>97</b>
III.4.1) Introduction .....	97
III.4.2) Pulsed laser deposition of SrRuO <sub>3</sub> film on SrTiO <sub>3</sub> /Si(001) .....	99
III.4.3) Sol-gel deposition of PZT film on SrRuO <sub>3</sub> /SrTiO <sub>3</sub> /Si(001) .....	101
III.4.3.1) Crystalline structure .....	102
III.4.3.2) Microscopic structure .....	104
III.4.3.3) Electrical characterizations .....	107
III.4.3.4) Microscopic piezoelectric properties .....	112
<b>III.5) Conclusion .....</b>	<b>114</b>
<b>III.6) Reference .....</b>	<b>115</b>

### **III.1) Introduction**

In this chapter, we will present the strategies developed to realize the integration of epitaxial PZT(52:48) films on Si substrate. Integration of functional oxides on Si requires the use of buffer layer to transfer the crystalline structure from silicon to oxide <sup>[1,2]</sup>. Two fabrication procedures were employed which are alternatively based on Gd<sub>2</sub>O<sub>3</sub> or SrTiO<sub>3</sub> (STO) as the buffer layer. First, the use of Gd<sub>2</sub>O<sub>3</sub> layer on Si(111) substrate was attempted which, however, leads to a pyrochlore-containing PZT film due to the presence of large lattice mismatch. This experiment, lack of successful integration of epitaxial PZT films on Si, will be introduced in Appendix A. In the second alternative, STO buffer layer grown by Molecular Beam Epitaxy (MBE) on Si(001) substrate was employed. PZT films were mainly deposited by sol-gel method directly on STO buffer layer with or without SrRuO<sub>3</sub> (SRO) bottom electrode. The SRO layer was grown by Pulsed Laser Deposition (PLD) for electrical characterizations. Finally, the as-grown ferroelectric films will be characterized by X-Ray Diffraction (XRD) to verify the epitaxial structure. Atomic Force Microscopy (AFM) was used for surface topography and Transmission Electron Microscopy (TEM) was carried out for microstructure which was observed on Si(110) cross-section. Ferroelectric properties of the PZT films were then studied using either macroscopic electrical measurement or Piezoresponse Force Microscopy (PFM) for their local electromechanical behavior. And other characterizations performed on the PZT films were also introduced respectively in this chapter.

### **III.2) Evaluation of SrTiO<sub>3</sub> film on Si(001) for the use of buffer layer**

#### **III.2.1) Experimental details**

In this section, we mainly introduce the fabrication process for the epitaxial growth of STO film on Si(001) substrate which is another promising buffer layer for integration of functional materials on Si. The whole process can be divided into 3 steps. The first step involves the chemical treatment for a clean and atomically flat Si surface. Then, passivation of Si surface will be performed in MBE chamber to obtain an oxide-terminated and SiO<sub>2</sub>-free Si surface. Finally, the so-called two-step growth method was used in order to obtain substrate-like STO film on Si, which has been already well developed at INL institute.

##### **III.2.1.1) Chemical treatment of Si(001) substrate**

In the industry, buffered hydrofluoric acid (BHF) is widely used to remove the native SiO<sub>2</sub> layer for chemical treatment of Si surface <sup>[3]</sup>. HF selectively etches SiO<sub>2</sub> without attacking Si substrate, which takes the following chemical reaction:



where  $\text{H}_2[\text{SiF}_6]$  is water soluble. At INL, the treatment combines the use of BHF solution and ultraviolet (UV) ozone generator in order to form a protective contamination-free  $\text{SiO}_2$  layer on Si surface. Optimal treatment process has been already developed at INL institute as below:

1. First, Si substrate is processed by UV ozone generator for 20 min to bury a layer of pure  $\text{SiO}_2$  underneath the native  $\text{SiO}_2$  layer.
2. The entire  $\text{SiO}_2$  layer is removed by BHF etching for 30 sec. The Si substrate is then cleansed by deionized water (DI-water) for 90 sec to dilute the remnant BHF and dried in pure nitrogen flux.
3. Si substrate is again processed by UV ozone generator for 2 min. Finally, a layer of high-purity contamination-free  $\text{SiO}_2$  is formed which can protect the Si surface from atmosphere before being introduced into MBE chamber.

After chemical treatment, Si surface is covered by  $\sim 1\text{nm}$ -thick  $\text{SiO}_2$  layer and is prepared for the deposition of STO layer. Figure III.1 (a) shows the surface topography of the treated Si wafer, which was obtained by AFM setup in the air. Atomic steps are clearly observed with the terrace width of 150 nm and single-layer step height. In Figure III.1 (b), RHEED pattern was measured on the same Si surface after removal of  $\text{SiO}_2$  layer in the vacuum.  $\times 2$  reconstruction, which corresponds to the Si free surface, is clearly seen in the pattern along Si[110] azimuth. The reconstruction is generated due to the minimization of surface energy by forming the surface chemical bonds<sup>[4]</sup>. On Si(001) surface, the atoms yield a dimmer structure along Si[110] rows, leading to a doubling of the surface periodicity along the Si[110] direction<sup>[5]</sup>.

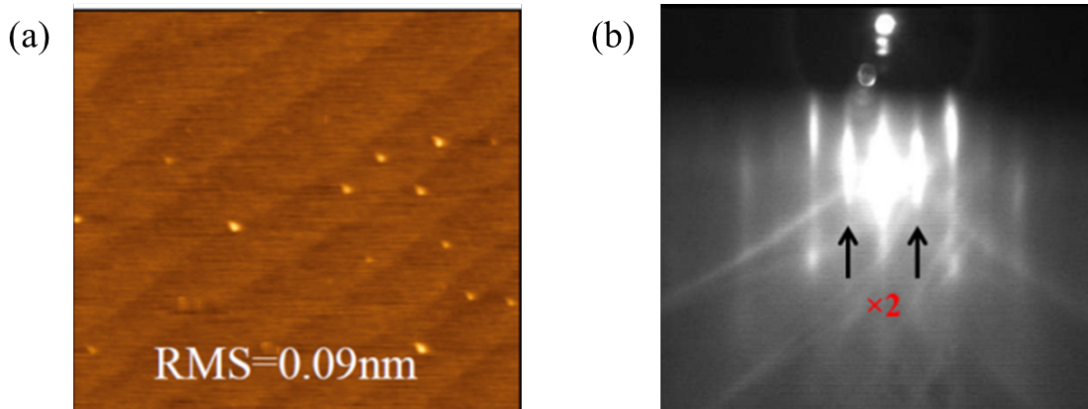


**Figure III.1 - Si(001) surface after chemical treatment: (a)  $1 \times 1 \mu\text{m}^2$  AFM surface topography measured in the air and (b) RHEED pattern with  $\times 2$  surface reconstruction measured in the vacuum along Si[110] azimuth.**

### III.2.1.2) Passivation of Si(001) surface using Sr

Passivation of Si(001) surface is a key process to provide an oxide-terminated and SiO<sub>2</sub>-free Si surface for subsequent deposition of STO film. Here, a Sr-assisted passivation process developed by Motorola labs<sup>[6]</sup> was used. The process is schematically shown in Figure III.2 and each step will be discussed in detail. Eventually, a SrO-terminated Si(001) surface is obtained.

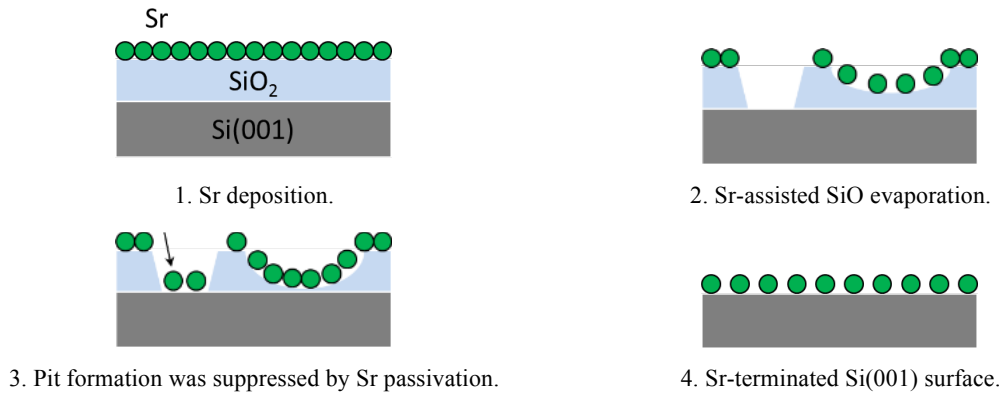


Figure III.2 - The mechanism of de-oxidation by using strontium (Ref. 6).

1. After chemical treatment, Si surface is covered by a 1nm-thick SiO<sub>2</sub> layer. Sr deposition is performed on this SiO<sub>2</sub>/Si(001) substrate in UHV at 600°C in order to cover 2 ML of Sr on the surface.
2. The substrate is then annealed at 750°C for 20 min to remove the SiO<sub>2</sub> layer. Under Sr catalysis, following chemical reactions promote the formation of volatile SiO gas:



3. Meanwhile, Sr atoms are partially evaporated during the annealing process until 1/6 - 1/3 ML of Sr remains on the Si surface. RHEED pattern of this sub-ML Sr will show  $\times 2$ ,  $\times 3$  and  $\times 6$  features along the Si[110] azimuth at 600°C, indicating a mixture of  $c(3\times 2)$  and  $c(6\times 2)$  phases of Sr/Si system on the Si surface (Figure III.3 (a)).
4. In order to obtain a 1/2 ML Sr coverage, deposition of additional Sr must be performed at 600°C to turn the RHEED pattern to the one that has only  $\times 2$  feature (Figure III.3 (b)). Finally, this 1/2 ML Sr is oxidized at approximately 400°C for 1 min to form 1/2 ML SrO on the Si surface. During the oxidation, such  $\times 2$  feature of the RHEED pattern remains stable and the oxygen pressure should be as low as  $5\times 10^{-8}$  Torr in order to avoid the formation of silicate.

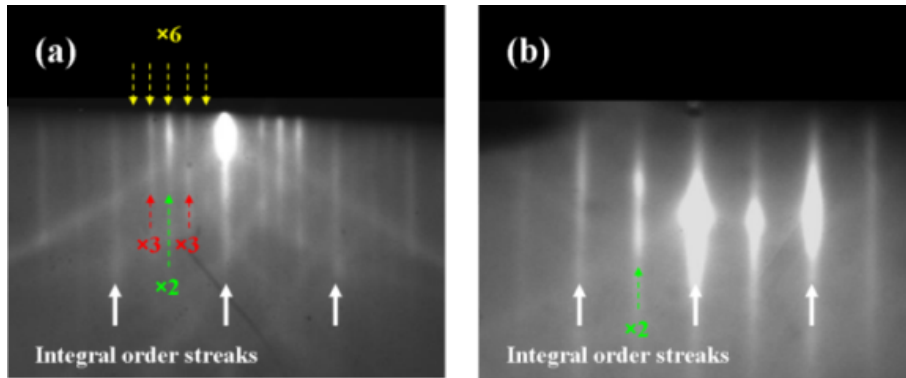


Figure III.3 - Evolution of the RHEED pattern on the Sr/Si system along the Si[110] azimuth from (a) 1/6 - 1/3 ML to (b) 1/2 ML Sr coverage on the surface.

### III.2.1.3) Two-step growth method

Several aspects must be considered for deposition of STO film on Si(001) substrate, especially like lattice mismatch and interface energy. As discussed in Chapter II, small lattice mismatch can be achieved between STO and Si if STO unit cell rotates by  $45^\circ$  around Si[001] axis (Figure III.4 (a)). Besides, the systematic study in Ref. 7 gives the surface energies for SrO-terminated STO surface ( $0.801 \text{ J/m}^2$ ), Si surface ( $1.7 \text{ J/m}^2$ ), and STO/Si interface ( $0.574 \text{ J/m}^2$ ), implying that  $\gamma_{\text{Si}} > \gamma_{\text{STO}} + \gamma_{\text{interface}}$ , namely STO can wet Si surface. Therefore, 2D growth mode is theoretically available for the epitaxial growth of STO on Si. Moreover, it was experimentally confirmed that the STO film can keep stable on Si surface up to the temperature of 1000 K [8]. Figure III.4 (b) illustrates such atomistic model for the epitaxial growth of STO film on SrO-passivated Si(001) surface.

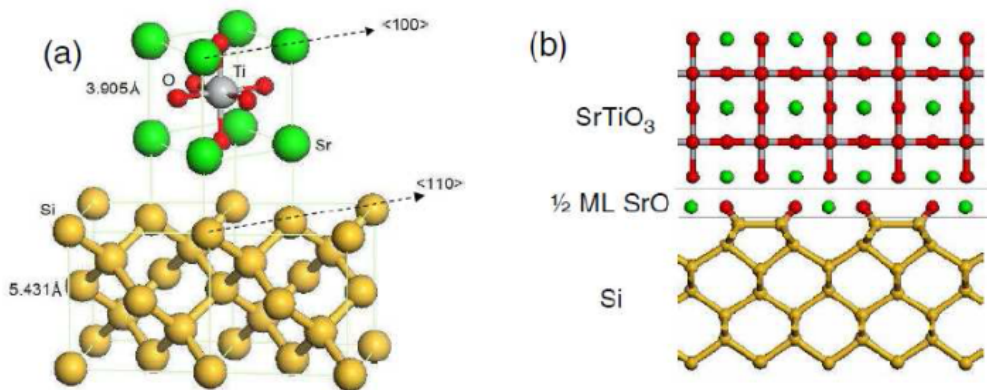


Figure III.4 - The atomistic model of (a) the epitaxial relationship between STO and Si(001) substrate and (b) the epitaxial growth of STO on 1/2 ML SrO covered Si substrate.

At INL, the pioneer work of STO epitaxy on STO or Si substrate using our oxide MBE system has been well established [9, 10, 11]. The growth window for STO homoepitaxy and heteroepitaxy on Si was successfully identified, which is helpful to optimize the growth condition from thermo-kinetic aspect. Figure III.5 shows such thermo-kinetic diagram in oxygen pressure and substrate temperature for STO/Si(001) system. In the homoepitaxy, substrate temperature could span a large range from 250°C to 750°C. In the whole temperature range, RHEED pattern always shows streaky feature, indicating a well-crystallized STO film. Besides, when the growth temperature is lower than 450°C, Bragg spots appear in the pattern suggesting a 3D growth mode. Oxygen pressure can be as high as the upper limit of our MBE system ( $1 \times 10^{-5}$  Torr) while the streaky RHEED pattern is still observed. In the limit of growth rate of our MBE system (1~3 ML/min), STO film always shows a good crystalline structure in the homoepitaxy.

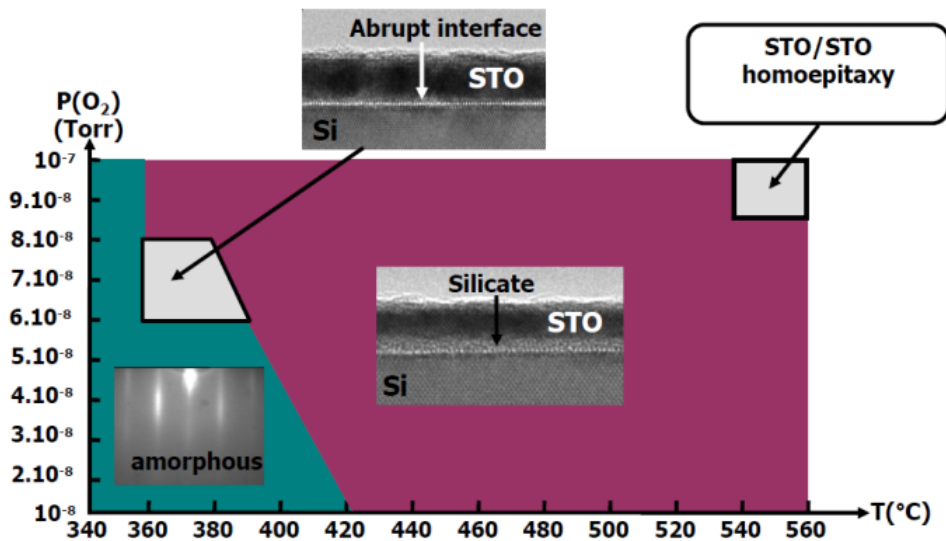


Figure III.5 - The thermo-kinetic diagram of STO/Si(001) system in oxygen pressure and substrate temperature. The inset images are the RHEED pattern and the TEM images.

For STO heteroepitaxy on Si, initial stage must be carefully optimized in order to transfer the crystalline structure from SrO/Si to STO with a well-defined STO/Si interface. Once a certain thick STO film (~10 ML) is grown, the subsequent growth can turn to the homoepitaxial one since the effect of STO/Si interface becomes negligible. Therefore, two-step growth method has been proposed by taking the advantage of both epitaxial growth windows. In the initial stage, first 2 ML STO requires low oxygen pressure ( $5 \times 10^{-8}$  Torr) and low substrate temperature (360°C) to avoid degradation of STO/Si interface. This 2 ML STO usually exhibits an amorphous feature on RHEED pattern which will turn to the streaky feature with growing. After that, oxygen pressure can be set up to  $1 \times 10^{-6}$  Torr while keeping the substrate temperature. The low substrate

temperature ensures an atomically abrupt STO/Si interface by preventing the formation of amorphous silicate layer at the interface [12, 13]. The high oxygen pressure at this stage enhances the stoichiometry, hindering the formation of oxygen vacancies that lead to a degradation of electrical properties. Once 10 ML STO is deposited, annealing process at 600°C is performed in UHV to enhance the crystallization of STO film. In the following growth, the condition can turn to the homoepitaxial one, where the optimal substrate temperature is 600°C and the optimal oxygen pressure is  $1 \times 10^{-6}$  Torr. When the desired thickness is achieved, the sample should be cooled in oxygen down to room temperature in order to prevent the formation of oxygen vacancies.

Figure III.6 shows the RHEED patterns of a 56ML-thick STO film along Si[100] and Si[110] azimuths, respectively. The streaky lines and the high contrast in the pattern reveal a well-defined 2D growth mode, i.e. good crystalline quality and high surface smoothness. Since the Sr/Ti ratio is at the good stoichiometry, no additional feature, like  $\times 2$  surface reconstruction, is observed on both patterns. Additional characterizations on this STO film will be introduced in the following section to examine the usefulness as the buffer layer.

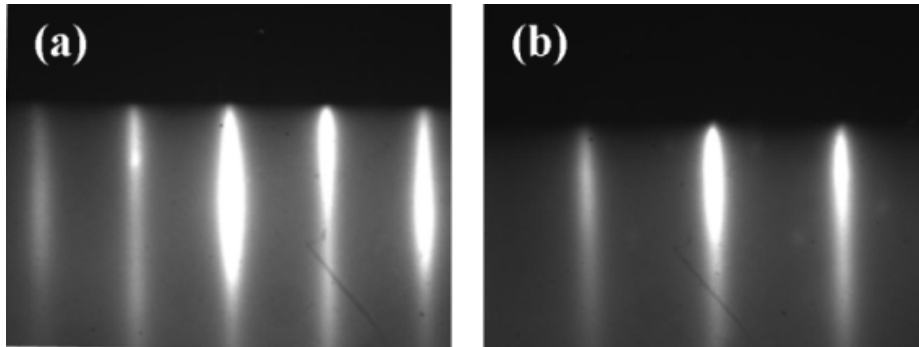


Figure III.6 - RHEED patterns of a 56ML-thick STO film on Si(001) along (a) Si[100] and (b) Si[110] azimuths.

### III.2.2) Crystalline structure and topography of epitaxial SrTiO<sub>3</sub> film

Crystalline structure of the STO film deposited by two-step growth method was characterized by XRD. Figure III.7 shows the out-of-plane  $2\theta/\omega$  XRD for a 6nm-thick STO film on Si(001) substrate. The sharp and intense peak at  $2\theta = 69.13^\circ$  is Si(004) Bragg peak. STO(002) Bragg peak at  $2\theta = 46.65^\circ$  shows an outspread peak with the Pendellösung fringes, which is due to the small thickness and the extremely smooth surface of the STO film. STO lattice constants derived from out-of-plane and in-plane (not shown)  $2\theta/\omega$  XRD are  $c = 3.96 \text{ \AA}$  and  $a = 3.89 \text{ \AA}$ . Compared with those of bulk STO (cubic lattice with  $a = 3.905 \text{ \AA}$ ), this 6nm-thick STO film

undergoes a compressive stress due to the smaller lattice constant of the Si substrate ( $a/\sqrt{2} = 3.840 \text{ \AA}$ ). In principle, STO film can regain its bulk lattice constant at the thicknesses above the order of 30 ML, namely above 12 nm<sup>[14]</sup>. Moreover, the inset image in Figure III.7 exhibits the  $\Phi$  scan XRD on STO{202} and Si{404} Bragg peaks. Both Bragg peaks having a 4-fold rotational symmetry demonstrate that the STO film is single crystal with tetragonal structure on Si substrate. The angle between two Bragg peaks is  $45^\circ$ , caused by the rotation of STO unit cell around Si[001] axis. Therefore, the crystalline relationship of STO/Si is [100] STO (001) // [110] Si (001). In addition, an extremely smooth STO surface with step-and-terrace structure was observed by AFM (Figure III.8). In average, the surface structure has a terrace width of 240 nm and a unit cell height of STO lattice, i.e. 0.4 nm, along <100> on the surface.

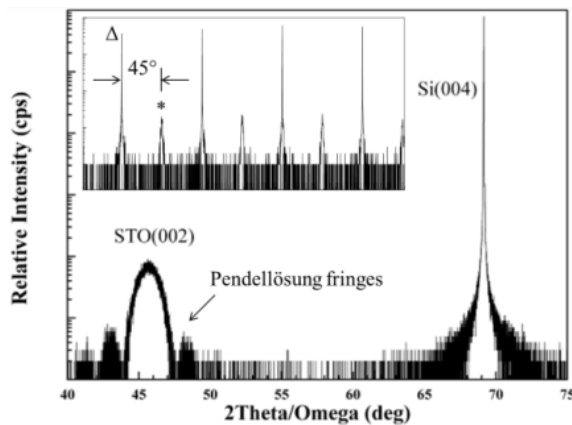


Figure III.7 - Out-of-plane  $2\theta/\omega$  XRD on STO/Si(001). The inset image shows the  $\Phi$  scan on STO(202) (\*) and Si(404) ( $\Delta$ ).

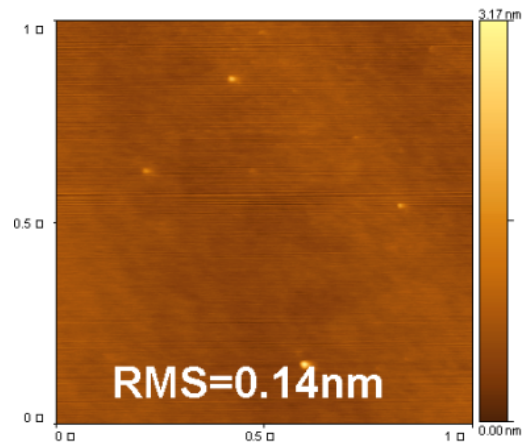


Figure III.8 - Surface topography of the as-grown STO film within  $1 \times 1 \mu\text{m}^2$  area.

### III.2.3) Conclusion

The epitaxial growth of STO film on Si(001) developed by Motorola Lab was successfully realized in our oxide MBE system. The epitaxial STO film exhibits a single crystalline structure in the form of perovskite lattice with an abrupt and commensurate oxide/Si interface. The film quality of the as-prepared STO film approaches that of the bulk counterpart thanks to the well-established two-step method. Various characterizations confirm that such STO-terminated Si(001) substrate can act as an excellent oxide template for the subsequent deposition of functional materials. In the following, we will perform sol-gel deposition of PZT film on this STO/Si(001) substrate to obtain integration of ferroelectric thin film on Si.

### **III.3) Sol-gel deposition of PZT film on SrTiO<sub>3</sub>/Si(001)**

#### **III.3.1) Sol-gel deposition of PZT film**

At LETI, sol-gel deposition of functional oxide films has been employed for a long time due to its simplicity and compatibility to modern cleanroom technologies. Therefore, it was used in this thesis to grow ferroelectric films on STO/Si(001) substrate. For PZT deposition, the sol-gel precursor solution from Mitsubishi Chemical Inc. mainly consists of several organometallic compounds, like lead acetate (Pb(CH<sub>3</sub>COO)<sub>2</sub>), zirconium tetra-n-butoxide (Zr(OC<sub>4</sub>H<sub>9</sub>)<sub>4</sub>), and titanium tetra-iso-propoxide (Ti(OCH(CH<sub>3</sub>)<sub>2</sub>)<sub>4</sub>), as the starting materials which are dissolved into the isopropanol alcohol ((CH<sub>3</sub>)<sub>2</sub>CHOH). This precursor solution is one of the acetic acid based sol-gel solutions which were invented at Queen's University in 1988 [15]. The acetic acid sol-gel solution rests with the property of acetic acid to slow the hydrolysis and the condensation reaction of transition metal alkoxides by forming more stable metal alkoxo-acetylates [16]. Chemical composition of the solution is identical to the stoichiometry of the final PZT film except that extra 10 wt% Pb is intentionally added to redeem the loss during thermal treatment, namely Pb:Zr:Ti = 100:52:48 with 10 wt% Pb for the PZT film at MPB. Figure III.9 shows the whole sol-gel deposition process employed in this thesis [17].

To spread PZT precursor solution on STO/Si substrate, spin-coating is employed [18]. At the rotation speed of 1500 rpm for 20 sec, 70nm-thick PZT film can be obtained on a 2-inch Si wafer by one spin-coating. Then, the coated sol film is dried at 130°C for 150 sec to evaporate the solvent and calcined at 350°C in the air for 150 sec. Low-temperature calcination is found mandatory before high-temperature annealing in order to yield a smooth surface without hillocks [19, 20]. After calcination, high-temperature annealing process is carried out in a RTA furnace to crystallize the amorphous PZT film. The advantage of RTA in the area of ferroelectric films is the short duration, which can largely reduce the time-temperature pyrochlore phase and enhance the formation of perovskite phase [21]. In addition, oxide films treated by RTA have a better surface morphology and serious out-diffusion is efficiently prevented. The latter one is of particular importance when considering integration of ferroelectric films with other semiconductor devices [22]. In this thesis, RTA was performed for 1 min in pure oxygen flux (100 sccm). At such short duration, the loss of volatile PbO is largely depressed [23]. Figure III.10 shows the variation of the preset temperature used for 650°C RTA, where the heating rate is around 14°C/s and the sample is cooled in the protection of oxygen flux.

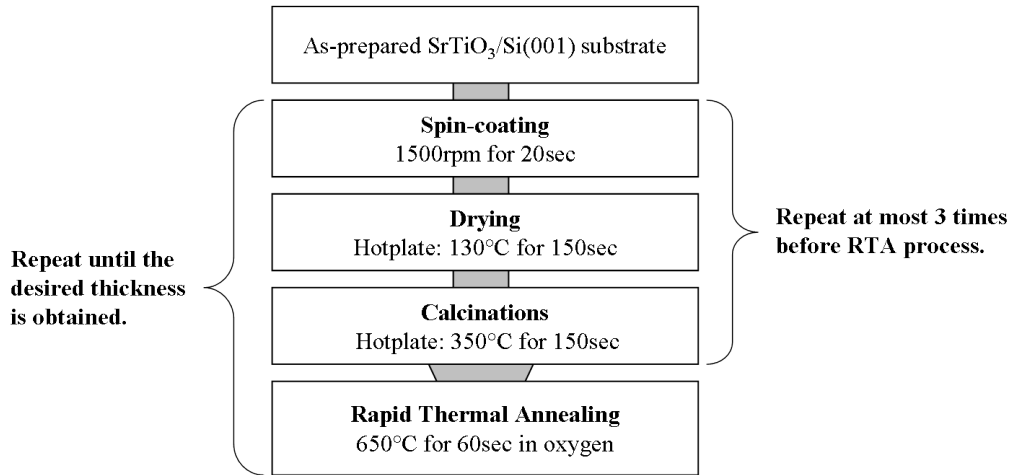


Figure III.9 - Sol-gel deposition process used in this thesis for epitaxy of PZT films on STO/Si.

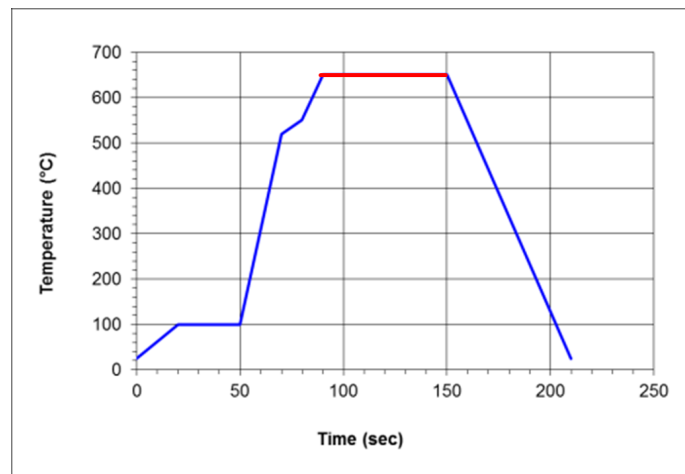


Figure III.10 - Variation of the preset temperature used for RTA annealing for 1 min at 650°C. The annealing period is indicated in red.

### III.3.2) Influence of annealing temperature

As discussed in Section III.4.1, RTA annealing temperature, i.e. the driving force for crystallization of the amorphous PZT film, must be carefully optimized to obtain high-quality crystalline PZT film. During the annealing, various film defects are possibly formed, like Pb deficiency, pyrochlore phase, and crystalline mis-orientation, which are closely related to the annealing temperature [24, 25]. In this section, the influence of RTA temperature on epitaxial PZT(52:48) film will be studied at 650°C and 700°C for comparison. Both temperatures are often used [26] and 700°C is used at LETI for PZT deposition on Pt/Si substrate. The two PZT films were deposited on STO/Si(001) by performing one spin-coating and the thickness of the STO

buffer layer is about 6 nm. PZT film thickness is measured by X-Ray Reflectivity (XRR) and both are about 70 nm. In the following, we will present the comparison between 650°C and 700°C PZT samples from their crystalline structure and electrical properties. Finally, we conclude that the PZT film annealed at 650°C, i.e. standard RTA temperature, has better film quality and will be exerted more characterizations.

### III.3.2.1) Crystalline structure

Out-of-plane  $2\theta/\omega$  XRD was performed on both PZT films annealed at 650°C and 700°C to measure the crystalline structure (Figure III.11). No metastable pyrochlore phase is detected in both PZT films by checking the Bragg angles in Table III.1 [27]. Therefore, 650°C is sufficiently high to crystallize pure perovskite PZT phase. Only (00l) Bragg peaks are detected for PZT and STO, indicating a unique crystalline orientation normal to the film surface. Fine crystalline structures are derived from the Gaussian fit of PZT(002) Bragg peak. Within, 650°C PZT film consists of two PZT phases, of which the one with larger c-axis lattice constant (4.071 Å) dominates the film, i.e. 90.76% in the peak area, and the remnant has a smaller c-axis lattice constant (4.005 Å). For 700°C PZT film, two PZT phases have the same c-axis lattice constant (4.031 Å) but different peak width. From XRD database (ICSD 90478), lattice constants of the bulk PZT(52:48) are known as  $c = 4.110$  Å and  $a = 4.055$  Å, which are indicated in the figure for a- and c-domains. Compared with the bulk one, smaller c-axis lattice constant in the PZT films indicates a tensile stress. In principle, tensile stress often develops in PZT film as residual stress after the cooling process in RTA treatment due to the fact that the thermal expansion coefficient of PZT film ( $\sim 10^{-5} \text{ K}^{-1}$ ) is larger than that of Si substrate ( $2.6 \times 10^{-6} \text{ K}^{-1}$ ) [28]. To relieve such stress, either strained PZT film occurs leading to large out-of-plane lattice constant or a-domain structure is formed [29]. Thus, segregation of two PZT phase occurs in 650°C PZT film and, on the contrary, RTA treatment at an elevated temperature for 700°C PZT film results in large volume of a-domains. This a-domain orientation leads to a reduction in the ferroelectric properties of thin film, provided that non-180° motions are minimized [30]. Moreover, the rocking curve of PZT(002) Bragg peak reveals a quite different film quality between two PZT films, where the FWHM values are 0.87° and 2.64° for 650°C and 700°C PZT film. Obviously, the PZT film annealed at the standard RTA temperature has superior film quality compared with the one annealed at an elevated temperature.

**Table III.1 - XRD data for PZT pyrochlore phase.**

<i>hkl</i>	111	311	222	400	331	511	440	622	444	800
<i>d<sub>hkl</sub></i> (Å)	6.04	3.16	3.02	2.62	2.40	2.02	1.85	1.58	1.51	1.31
<i>2θ<sub>hkl</sub></i> (°)	14.65	28.22	29.55	34.20	37.44	44.83	49.21	58.36	61.34	72.03

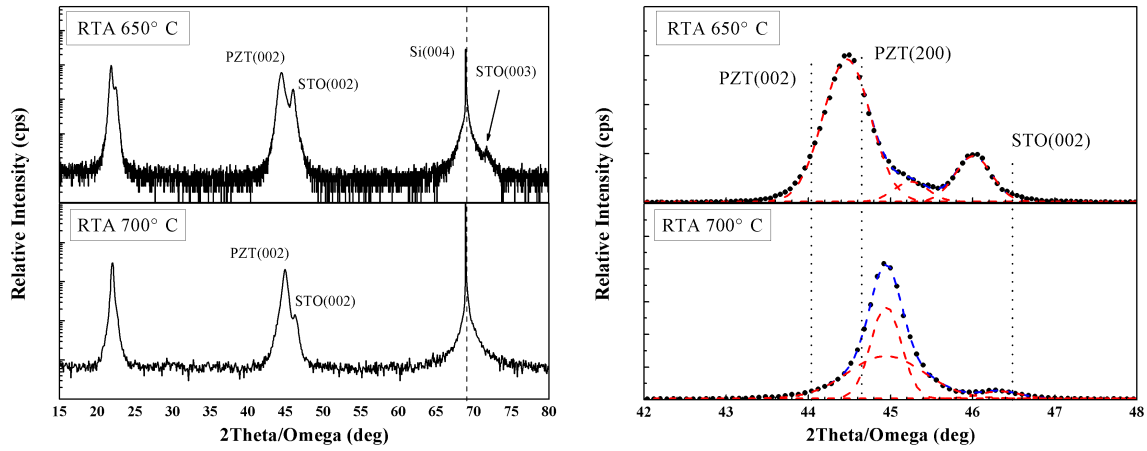


Figure III.11 - Out-of-plane  $2\theta/\omega$  XRD on 650°C and 700°C annealed PZT films on STO/Si(001). The right image shows the Gaussian fit on PZT(002) Bragg peak with indication of the bulk counterparts.

Furthermore, in order to confirm the epitaxial growth of the PZT films,  $\Phi$  scan XRD was performed on PZT{202} and Si{404} Bragg peaks. In Figure III.12, 4-fold rotational symmetry is observed on those Bragg peaks for both 650°C and 700°C PZT films. Angular difference of 45° between PZT{202} and Si{404} Bragg peaks is caused by the rotation of PZT lattice along the Si[001] axis. This rotation reduces the lattice mismatch of PZT and STO so that the preliminary of epitaxial growth can be satisfied. In conclusion, the relationship of the crystalline orientations in PZT/STO/Si(001) heterostructure is derived as [100] PZT (001) // [100] STO (001) // [110] Si (001) for both PZT samples.

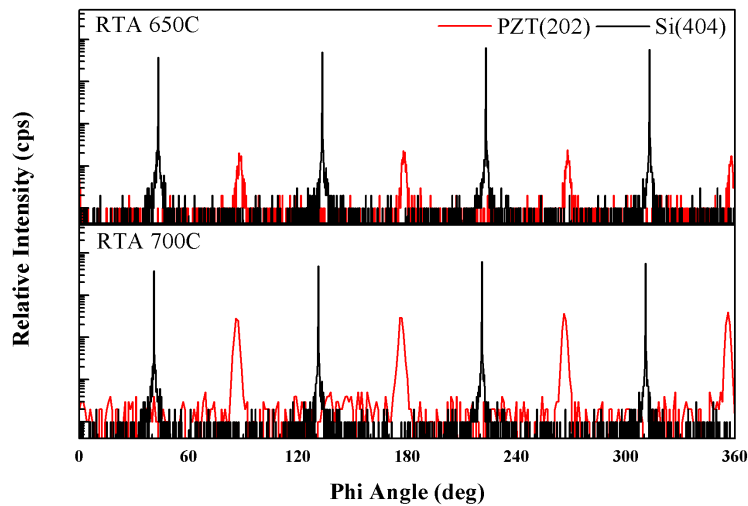


Figure III.12 -  $\Phi$  scan XRD on PZT{202} and Si{404} Bragg peaks for both 650°C and 700°C PZT films.

### Chapter III - Integration of epitaxial PZT thin film on Si substrate

Since 650°C RTA treatment gives rise to better film quality, more XRD measurements were performed on 650°C PZT film. Figure III.13 shows the XRD pole figures on PZT{002}, PZT{202}, and Si{404} Bragg peaks, which span from 0° to 90° in  $\chi$  angle and from 0° to 360° in  $\Phi$  angle. Except for (001)-oriented perovskite PZT lattice, no additional PZT phase and preferred crystalline orientation is observed in the pole figures. It indicates that the PZT film grown by sol-gel method with 650°C RTA temperature is a pure single crystalline perovskite PZT phase on STO/Si(001) substrate. It is consistent with the result as obtained in the  $\Phi$  scan XRD.

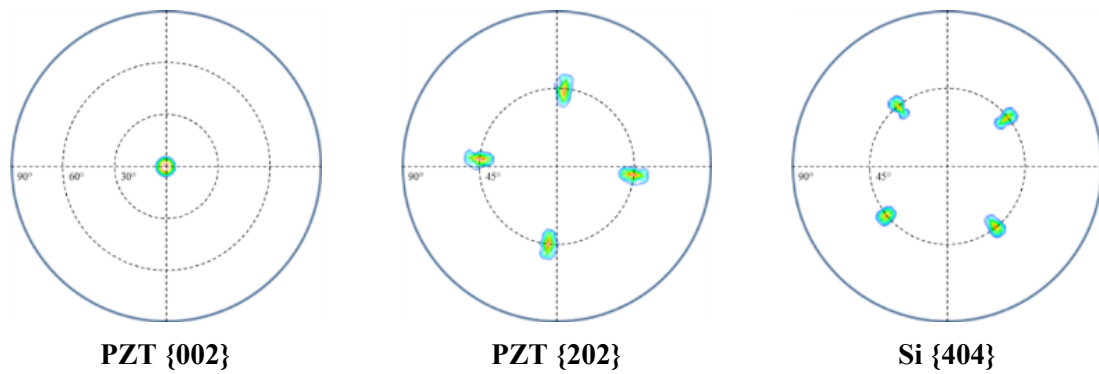


Figure III.13 - XRD pole figures on PZT{002}, PZT{202} and PZT{404} Bragg peaks for 650°C PZT film.

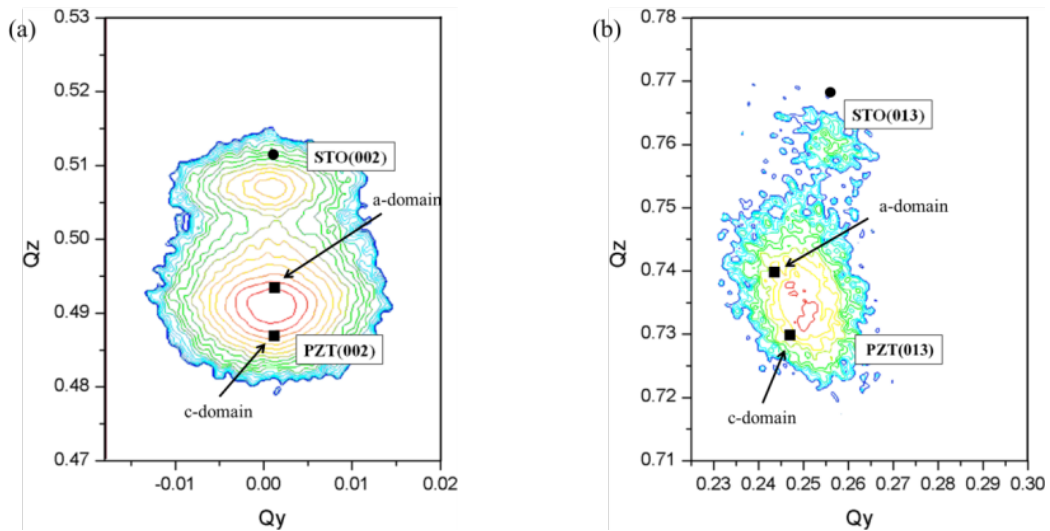


Figure III.14 - Reciprocal space mapping on (a) PZT(002) and (b) PZT(013) Bragg spots for 650°C PZT film.

Texture structure of 650°C PZT film was studied by Reciprocal Space Mapping (RSM) around PZT(002) and PZT(013) Bragg spots, as shown in Figure III.14. For PZT(002), the Bragg spot locates between c- and a-domain, similar to the result of  $2\theta/\omega$  scan XRD, indicating that the

PZT film undergoes a tensile stress. STO(002) Bragg spot shows a smaller  $Q_z$  value than that of the bulk one, which is mainly due to the clamping effect of Si substrate whose lattice constant is smaller than that of STO. In addition, the PZT(013) Bragg spot with an ellipse-like shape suggests a homogeneous PZT crystalline structure close to c-domain PZT structure. Such result is in agreement with the  $2\theta/\omega$  scan XRD where the PZT structure with larger c-axis lattice constant is dominant in the film.

### III.3.2.2) Surface Topography

Surface topography was measured by VEECO Dimension 3100 AFM setup in tapping mode. In Figure III.15, both 650°C and 700°C PZT samples show a quite smooth surface within the area of  $1 \times 1 \mu\text{m}^2$ . Large amount of nano-scale hillocks are observed in random distribution on the surface of 650°C PZT film. On the contrary, no additional feature can be seen on the surface of 700°C PZT film. The RMS values of the surface roughness derived from the  $5 \times 5 \mu\text{m}^2$  AFM topography is 0.80 nm for 650°C PZT film and 1.36 nm for 700°C PZT film, demonstrating a large topographic fluctuation on the surface of 700°C PZT film.

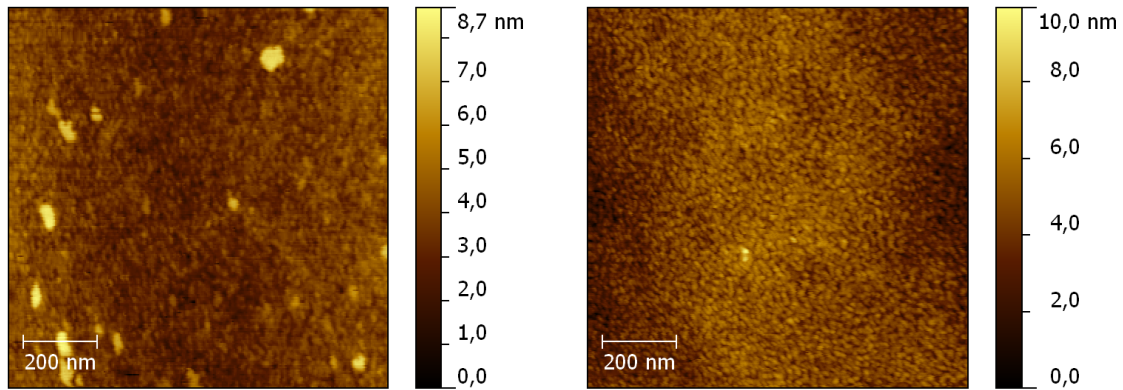


Figure III.15 - Surface topography of PZT films on STO/Si annealed at 650°C (left) and 700°C (right).

### III.3.2.3) Electrical characterization

To measure the electrical properties of PZT/STO/Si, Au/Ni top electrode was deposited by e-beam evaporator and patterned by lift-off method. Ni layer between Au and PZT acts as an adhesive layer to enhance the electrical contact. The final Au/Ni top electrode is about  $90 \times 90 \mu\text{m}^2$  large and 250 nm thick, where the Ni layer is about 3 nm thick. Electrical impedance of the Au/Ni/PZT/STO/Si capacitor was measured by HP Agilent 4284A impedance meter, where the top electrode was applied by detection voltage and the p-type Si substrate was virtually grounded. Before the measurement, poling process was performed on PZT films at 8 V for 1 min. In Figure

III.16, the capacitance of the stack is shown as the function of applied dc bias which was measured in  $C_p$ -G mode using 0.1V ac voltage. For both PZT samples, the capacitance shows a larger value at negative dc bias than that at positive dc bias, similar to a typical n-MOS capacitor. High depletion region is observed at positive dc bias for both PZT samples. Relative permittivity derived at -6 V is 44.27 for 650°C PZT film and 79.06 for 700°C PZT film, smaller than that of a typical PZT (300~3850) and STO (300). Small dielectric permittivity is mainly due to the appearance of  $\text{SiO}_2$  layer at STO/Si interface (see the TEM image in Figure III.18), which is formed during the thermal treatment of sol-gel deposition. The interfacial  $\text{SiO}_2$  layer which has a small relative permittivity (usually  $\sim 3.9$ ) will take the most applied voltage drop in the heterostructure and, therefore, leads to a small permittivity measured in the C-V curve.

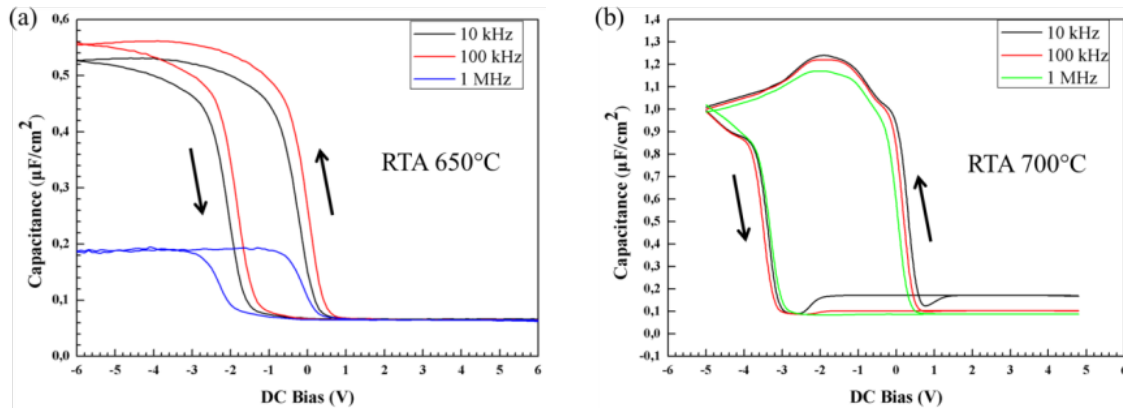


Figure III.16 - The capacitance of Au/Ni/PZT/STO/Si stack at 10 kHz, 100 kHz, and 1 MHz for the PZT films annealed at 650°C (a) and 700°C (b), respectively.

Moreover, all the C-V hysteric loops at various frequencies show an anti-clockwise direction. Since the ferroelectrically-inactive layer takes the most applied voltage, the contribution of the ferroelectric PZT layer to the hysteric loop is nearly negligible than that of STO and  $\text{SiO}_2$  layers. Therefore, the heterostructure of our PZT films can be regarded as a typical n-MOS capacitor. Charge transport in the n-MOS capacitor allows charge injection from either side of the electrical contacts, leading to the clockwise C-V hysteric loop if charge injection takes place from Si substrate or the anti-clockwise hysteric C-V loop if charge injection takes place from top electrode (Figure III.17) <sup>[31]</sup>. On the contrary, the metal-ferroelectric-silicon (MFS) heterostructure always shows the clockwise C-V hysteric loop if the oxide charge is negligible. As a result, two hysteric loops add up to a combined C-V curve which could change the clockwise hysteresis, that is the characteristic of ferroelectric material, to an anti-clockwise one. In our PZT films, the charge injection is likely attributed to the high-density oxygen vacancies which are generated due to the insufficient oxygen ambient ( $< 10^{-6}$  torr) in MBE system during

STO deposition. Therefore, the large charge injection leads to the anti-clockwise hysteresis loop in the C-V measurement for both 650°C and 700°C PZT films.

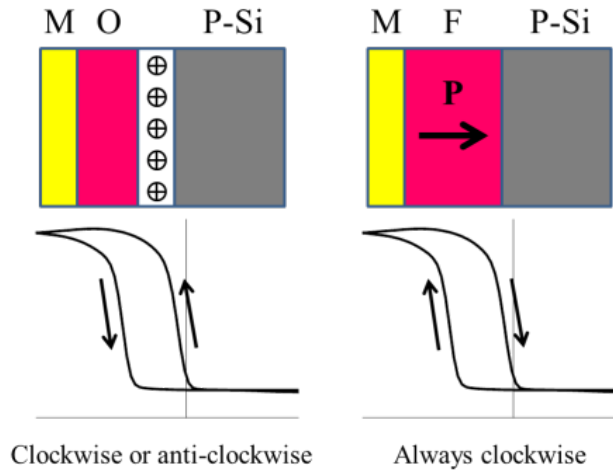


Figure III.17 - Clockwise and anti-clockwise C-V hysteresis loop for an n-MOS capacitor and clockwise C-V hysteresis loop for an MFS capacitor.

### III.3.3) Microscopic structure of PZT/SrTiO<sub>3</sub>/Si(001) stack

TEM measurement was used to study the microstructure of PZT/STO/Si heterostructure, which was performed on the PZT film annealed at 650°C along the Si(110) cross section. Figure III.18 shows the TEM images at the magnification of 50k and 150k. Each layer in the heterostructure is clearly identified due to the abrupt interfaces. The layer thickness is 70 nm for PZT, 14.7 nm for STO, and 5 nm for SiO<sub>2</sub>, respectively. Amorphous SiO<sub>2</sub> layer forms between STO and Si due to the RTA treatment at 650°C in pure oxygen. Epitaxial growth of PZT film was not degraded by the formation of SiO<sub>2</sub> layer thanks to the stable STO buffer layer. In addition, subgrain structure is observed in both PZT and STO layers, which contributes to the fluctuation of the contrast in the images. The formation of subgrain structure is a typical microstructural response to the elastic stress, relating to the progressive mis-orientation until large-angle grain boundaries are formed<sup>[32]</sup>. In our PZT films, elastic stress mainly originates due to the lattice mismatch and the thermal treatment. The rotation of the subgrain structure is limited within small angle, demonstrating that the stress is relatively small and, therefore, the single crystalline structure of the PZT film is still not interrupted. Average size of the subgrain is about 45×35 nm<sup>2</sup> for PZT film and 13×10 nm<sup>2</sup> for STO film. From the side of Si substrate to PZT top surface, density of the subgrains gradually decreases and the size increases. It is likely caused by the relaxation process of the elastic stress. Similar subgrain structure was also observed in the

*Chapter III - Integration of epitaxial PZT thin film on Si substrate*

epitaxial STO film in Ref. 33, which was considered as an alternative structure of a- and c-domains.

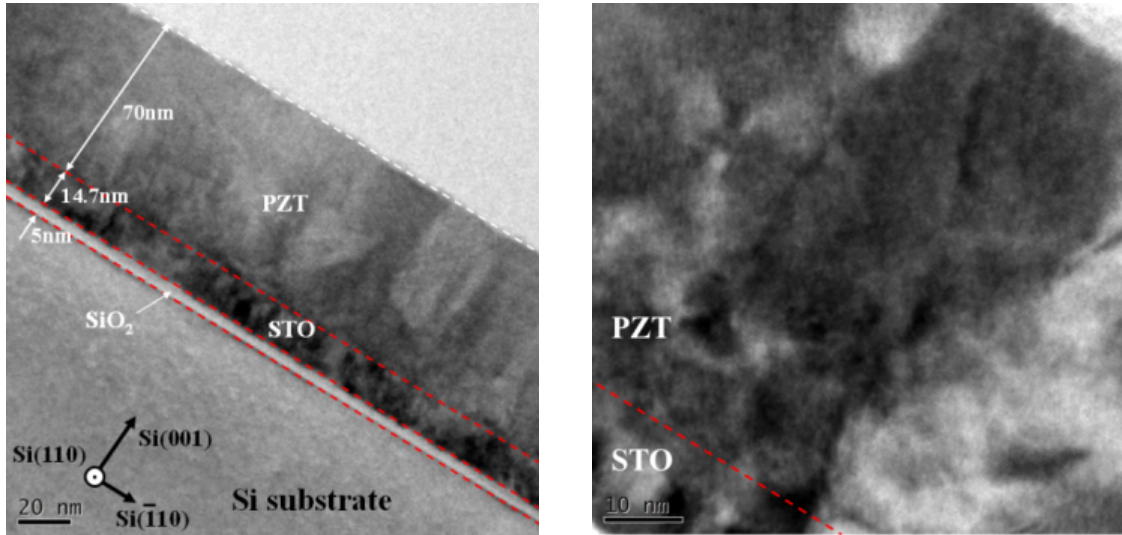


Figure III.18 - TEM images of PZT/STO/Si(001) heterostructure at the magnification of 50k (left) and 150k (right) along Si(110) cross section.

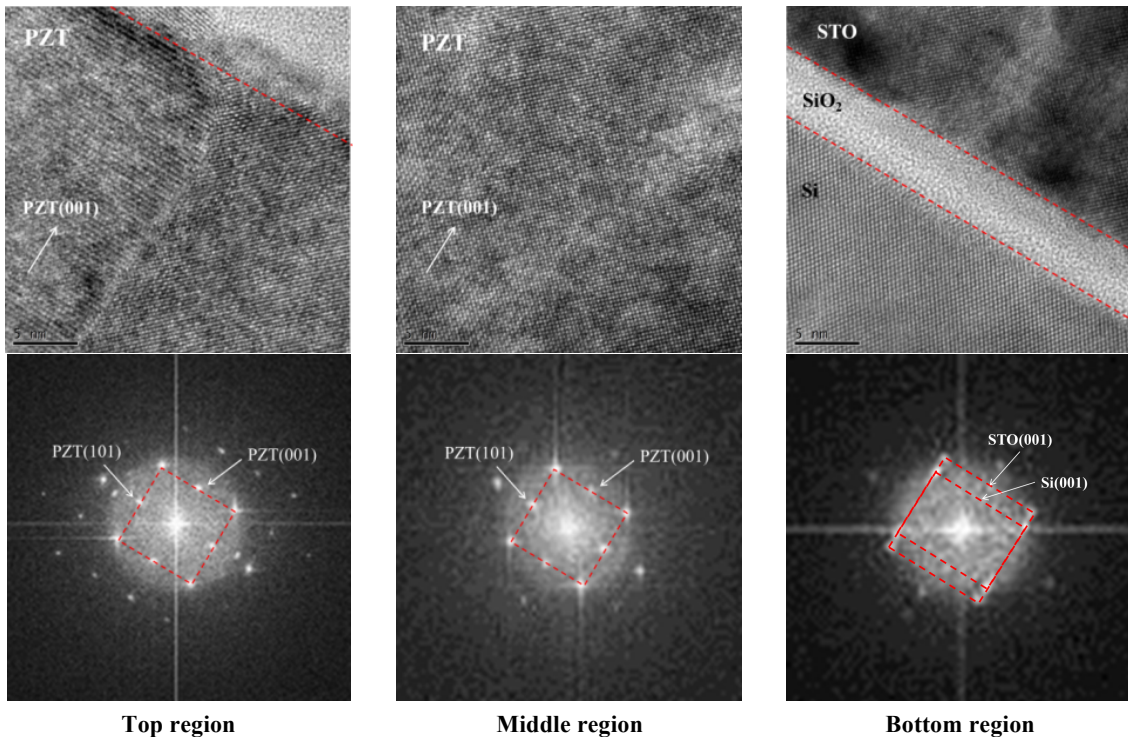


Figure III.19 - HR-TEM images of PZT/STO/Si(001) heterostructure at the magnification of 400k and the corresponding Fourier transform, which are taken in different film depth.

Figure III.19 shows the high-resolution TEM (HR-TEM) images at the magnification of 400k on the same PZT specimen. Three HR-TEM images were respectively taken at different film depth from the top surface to the STO/Si interface. Near the top surface, a subgrain boundary is clearly seen separating two regions which are visualized as different lattice planes. However, the Fourier Transform (FT) image reveals a pure perovskite PZT phase in the reciprocal space. In the middle region of the PZT layer, both HR-TEM and FT images show a pure single crystalline structure. Lattice constants derived from the reciprocal spots of the FT image are 4.091 Å for c-axis and 4.068 Å for a-axis, larger than those from XRD measurement. The larger lattice constants can be attributed to the fact that the sample specimen prepared for TEM measurement was intentionally thinned at submicron thickness for TEM observation, leading to the structural relaxation of the film. Again, the TEM image near STO/Si interface clearly shows a 5nm-thick amorphous SiO<sub>2</sub> layer between STO and Si substrate. In the bottom region, no additional TEM contrast contributes to the Si crystalline lattice, suggesting that the diffusion of metallic atoms, like Pb from PZT layer, is efficiently prevented by STO buffer layer. The corresponding FT image shows two different reciprocal lattices which are related to the Si and STO crystalline structures.

#### **III.3.4) Chemical profile of PZT/SrTiO<sub>3</sub>/Si(001) stack**

Sol-gel PZT film usually presents an inhomogeneous chemical profile along the film depth after high-temperature annealing process, namely at the phase transformation from amorphous metallic oxide phase to perovskite phase<sup>[34]</sup>. The formation of compositional gradient is mainly due to the fact that Ti-rich compositions nucleate and grow more easily, leading to higher Ti content towards the substrate and higher Zr content towards the film surface<sup>[35]</sup>. Figure III.20 shows such formation during crystallization process. Since the sol-gel solutions are mixed at molecular level, the homogeneity of the initial gel film is still maintained after calcination at 350°C<sup>[36]</sup>. The in-plane lattice constant of PbTiO<sub>3</sub> is 3.95 Å, and for PbZrO<sub>3</sub> the lattice constants are  $a_0 = 5.87$  Å,  $c_0 = 4.10$  Å<sup>[37]</sup>. Therefore, the formation of PbZrO<sub>3</sub>, having a larger lattice mismatch with STO template (3.905 Å), is preferred in the bulk of the film rather than at PZT/STO interface. On the other hand, the phase transformation to perovskite is more exothermic with increasing Ti concentration, namely more energetically preferred<sup>[14]</sup>. Thus, the initial stage of crystallization is dominated by Ti-rich composition, and consequently Zr content is generally enriched in the remnant gel film. Moreover, the diffusion in the amorphous film is larger than that in the crystalline film where it is practically zero for the cations due to the low annealing temperature (i.e. 650°C) as compared to the temperature at which the cations start to migrate (above 850°C)<sup>[38]</sup>. Eventually, the compositional gradient of Ti and Zr is formed in the PZT film after full crystallization.

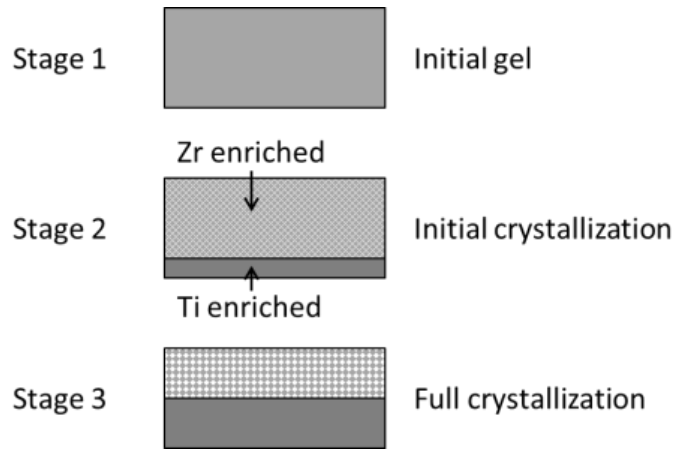


Figure III.20 - Formation of gradient PZT film during crystallization process.

Thick PZT film, which is prepared by multiply annealing process, often shows an oscillating chemical profile (Figure III.21) [39]. At MPB, PZT film has the maximum piezoelectric properties and small deviation away from the nominal chemical composition in local film can lead to the dramatic degradation of the properties for the whole PZT film [40]. On the other hand, the loss of volatile Pb, which happens by evaporation into the air or diffusion into the substrate during the thermal treatment, can bring about the deficiency of Pb in PZT film. Although extra Pb is often added into the sol-gel solution, gradient Pb content, which can result in unwanted PZT phase, can also deteriorate the electrical properties of the PZT film [41].

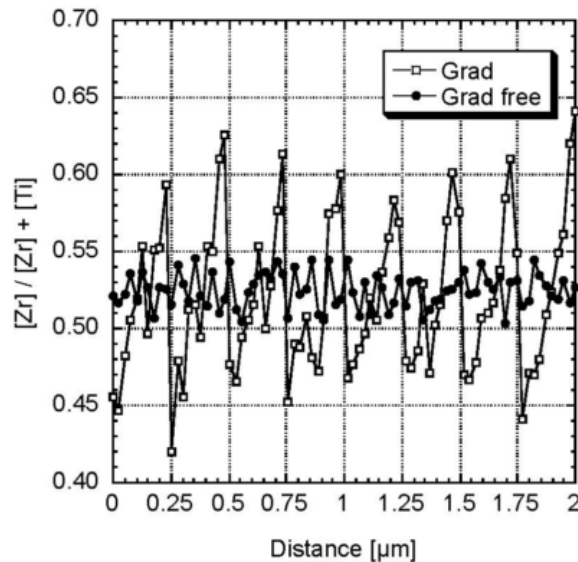


Figure III.21 - Zr content within a 2 $\mu\text{m}$ -thick PZT film measured as a function of the distance to the bottom electrode. Open squares: standard film with 53/47 solutions; filled circles: film with optimized Zr/Ti.

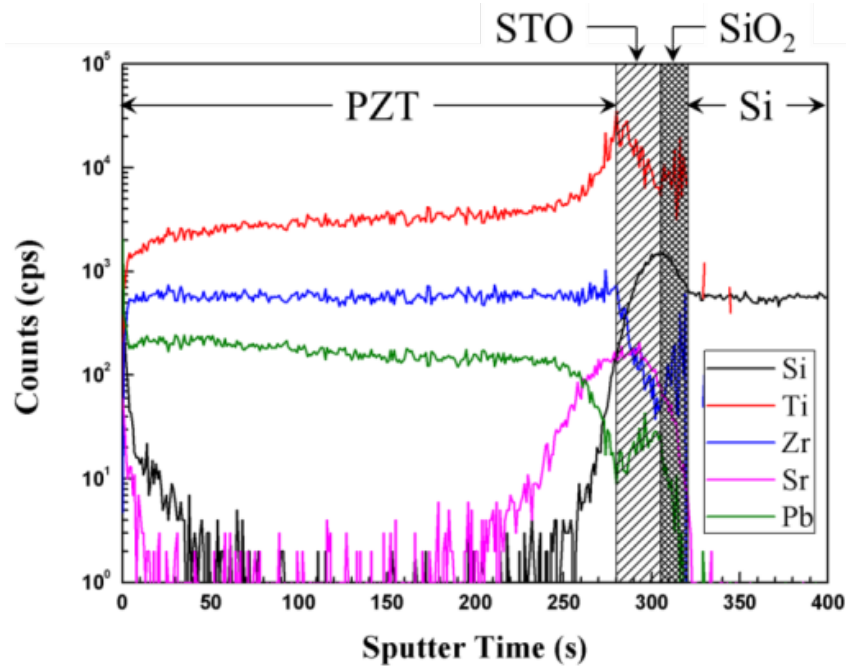


Figure III.22 - Chemical profile of the epitaxial PZT film on STO/Si(001) substrate measured by SIMS.

To analyze the chemical profile of our PZT film, Secondary Ion Mass Spectrometry (SIMS) was performed on the PZT film annealed at 650°C, where STO buffer layer is 13 nm and PZT layer which was fabricated by performing 3 cycles of spin-coating, drying and calcination before RTA is 250 nm. Time-of-flight SIMS depth profiling was measured with following conditions:

- Analysis gun: 25 keV  $\sim 1.8$  pA  $\text{Bi}^+$ ; raster size  $90 \times 90 \mu\text{m}^2$
- Sputter gun: 2 keV 180 nA  $\text{Cs}^+$ ; raster size  $300 \times 300 \mu\text{m}^2$

Figure III.22 shows such depth-dependent chemical profile in epitaxial PZT sample, where the abscissa is the sputtering time in second, with zero indicating the film outer surface, and the ordinate is referred to the elemental concentration in counts per second. Although the absolute concentration is not easily obtained from the counts, SIMS is sensitive to the variation of the elemental concentration and, therefore, each layer can be identified. In the figure, higher Ti content is observed near the side of Si substrate and lower Ti content is near the side of film surface, which is consistent with the result in Ref. 42. Diffusion of Sr from STO buffer layer to PZT film is clearly shown as an exponential decrease of Sr content in PZT film. Extra PZT phase is possibly formed near the interface, which is observed in Ref. 43, 44 near PZT/Pt interface. On the contrary, Zr content remains almost constant in the PZT film, leading to the change of Zr/Ti ratio, where the larger Zr/Ti ratio ( $> 52/48$ ) near the film surface could form rhombohedral phase and the smaller Zr/Ti ratio ( $< 52/48$ ) near the substrate could form tetragonal phase. Pb content

slightly decreases towards the substrate and dramatically drops off at the interface. Pb segregation in PZT film is caused by the lead diffusion to the surface, which is a result of oxidation of the Pb or kinetic demixing, both of which are favored by oxygen deficiency during thermal annealing [45]. Although few amount of Si is detected in the oxide layers, STO buffer layer acts as an excellent barrier which prevents the diffusion of all the metallic elements into the Si substrate. It's believed that this temperature-dependent diffusion process deteriorates PZT film quality and also electrical properties, making 650°C superior to the higher annealing temperature.

### **III.3.5) Conclusion**

In this section, sol-gel deposition of PZT film was performed on STO/Si(001) template and followed by a RTA process at 650°C and 700°C. The experiment proves that 650°C RTA temperature is sufficiently high to complete the crystallization of the deposited PZT film while 700°C RTA temperature could deteriorate the film quality due to the overheating. Both XRD and TEM measurements confirm an epitaxial single crystalline PZT film with no pyrochlore phase on STO/Si(001) substrate. It is concluded that crystalline orientation of the as-prepared PZT/STO/Si stack follows the relationship of [100] PZT (001) // [100] STO (001) // [110] Si (001). However, due to the lack of a bottom electrode with low resistivity and Ohmic contact in the PZT capacitor, ferroelectric properties cannot be properly measured. Thus, in the next section we will introduce a conductive SRO layer in the stack and then characterize epitaxial PZT film based on this bottom electrode.

## **III.4) Use of SrRuO<sub>3</sub> bottom electrode for integration of PZT on Si**

### **III.4.1) Introduction**

As discussed in Section III.4, doped-Si substrate cannot play the role of bottom electrode to apply the actuation voltage on PZT film, as it will result in the most voltage drop on ferroelectrically-inactive layers. Thus, an additional conductive layer on STO/Si(001) must be considered, which should have high conductivity and also structural and chemical compatibility with STO-terminated Si substrate and PZT layer. In this thesis work, SRO film grown by PLD is used for this purpose. SRO has been proven to be a promising bottom electrode [46] for preparing various technically important oxides, such as superconducting [47], ferroelectric [48] and high dielectric-constant materials [49]. SRO is a ternary transition metal oxide, having good electrical conductivity (~280  $\mu\Omega\cdot\text{cm}$  for single crystal) and GdFeO<sub>3</sub>-type orthorhombic structure (space group *Pbnm*) with lattice constants of  $a_0 = 5.57 \text{ \AA}$ ,  $b_0 = 5.53 \text{ \AA}$ , and  $c_0 = 7.85 \text{ \AA}$  [50]. SRO unit cell can be regarded as a slightly distorted tetragonal structure (Figure III.23) with lattice constants of

Chapter III - Integration of epitaxial PZT thin film on Si substrate

$a_t = 3.93 \text{ \AA}$ ,  $c_t = 7.85 \text{ \AA}$  and  $\gamma = 89.6^\circ$ . Small lattice mismatch allows the deposition of SRO on various substrates, such as STO [51, 52], LaAlO<sub>3</sub> [53, 54], MgO [55], and Si with yttria-stabilized zirconia as buffer layer [56]. Besides, the lattice mismatch of SRO and PZT on the {001} surface is fairly small (-2.7%). Moreover, SRO is chemically stable up to 1200 K in either oxidizing or inert gas atmospheres [57].

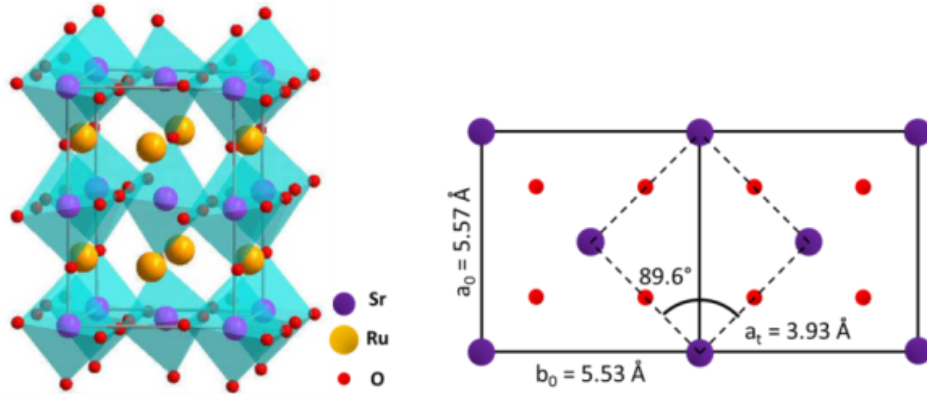


Figure III.23 - The crystalline structure of SrRuO<sub>3</sub> and the reduced pseudo-cubic structure.

In principle, when SRO is deposited on exact (001) STO substrate, the film can grow epitaxially with its (001), (110), or (1-10) planes parallel to the (001) STO surface, leading to six possible domain orientations (Figure III.24) [58]. In order to prepare epitaxial single-domain SRO film on STO, a vicinal STO (001) substrate is used with a large miscut angle and a miscut direction close to the [010] axis [59, 60]. The constriction from high-density atomic steps on the miscut STO surface facilitates the epitaxy of SRO with only one single domain [61].

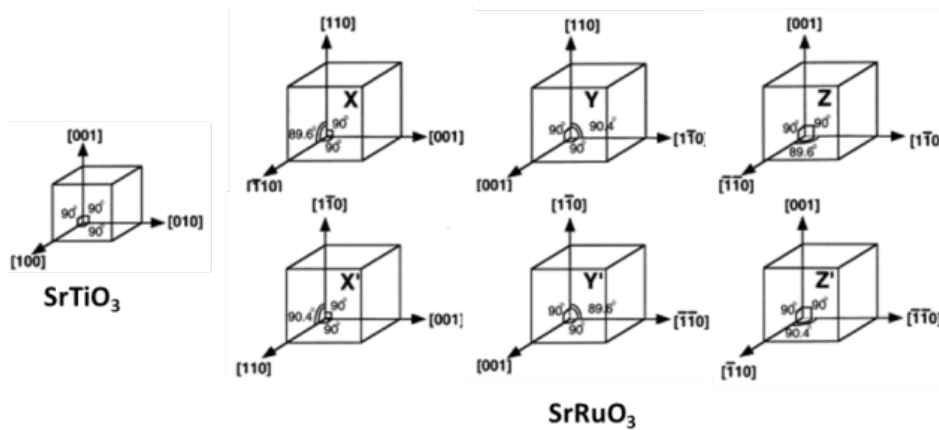


Figure III.24 - Schematic diagram presenting six possible domain orientations of SRO on STO (001) substrate.

### III.4.2) Pulsed laser deposition of SrRuO<sub>3</sub> film on SrTiO<sub>3</sub>/Si(001)

The PLD setup used to grow SRO film on STO/Si in this thesis has been introduced in Chapter 2. The optimal growth condition has been well developed at the National Institute of Materials Physics (NIMP) in Bucharest Romania. STO/Si substrate is first cleansed by acetone and ethanol, and then dried in nitrogen flux to remove the surface contamination. KrF excimer laser at the wavelength of 248 nm is used to ablate SRO target. During the deposition, STO/Si substrate is mounted at the center of the plasma plume with a substrate-target distance of 6 cm. Energy density of the laser is about 2 J/cm<sup>2</sup>, and the pulse frequency is 5 Hz. In the optimal condition, substrate temperature is 700°C and oxygen pressure is about 0.133 mbar. The nominal deposition rate under this condition is about 25 nm/2000 pulses. In Table III.2, all the parameters used in PLD deposition of SRO film are summarized.

**Table III.2 - Optimal growth condition for PLD deposition of SRO film on STO/Si(001) substrate.**

Laser wavelength:	248 nm	Substrate temperature:	700 °C
Pulse frequency:	5 Hz	Oxygen pressure:	0.133 mbar
Energy density:	2 J/cm <sup>2</sup>	Deposition rate:	25 nm / 2000 pulses
Substrate-target distance:	6 cm		

Electrical resistivity of the as-grown SRO film<sup>[62]</sup> was measured by 4-point probes method, as shown in Figure III.25. Linear relationship of the applied current and the measured voltage is observed in the whole range of measurement from 1 μA to 3 mA, corresponding to the voltage from 0.46 mV to 1.6 V. Within this range, electrical resistivity remains constant at 408.8 μΩ•cm. Compared with the SRO film deposited on STO substrate in Ref. 63 with a resistivity of 650 μΩ•cm, our SRO film on STO/Si obviously gives a smaller electrical resistivity. In the reference, the lowest resistivity (< 200 μΩ•cm) was found at the substrate temperature of 775°C. However, at such substrate temperature the film surface has a relatively larger roughness than that at 700°C, making it inappropriate for the use of bottom electrode.

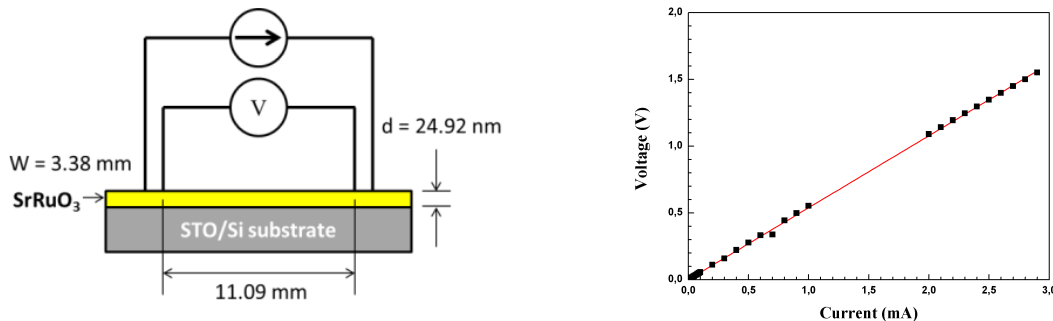


**Figure III.25 - 4-point probes method (left) and I-V characteristic of the as-grown SRO film on STO/Si (right).**

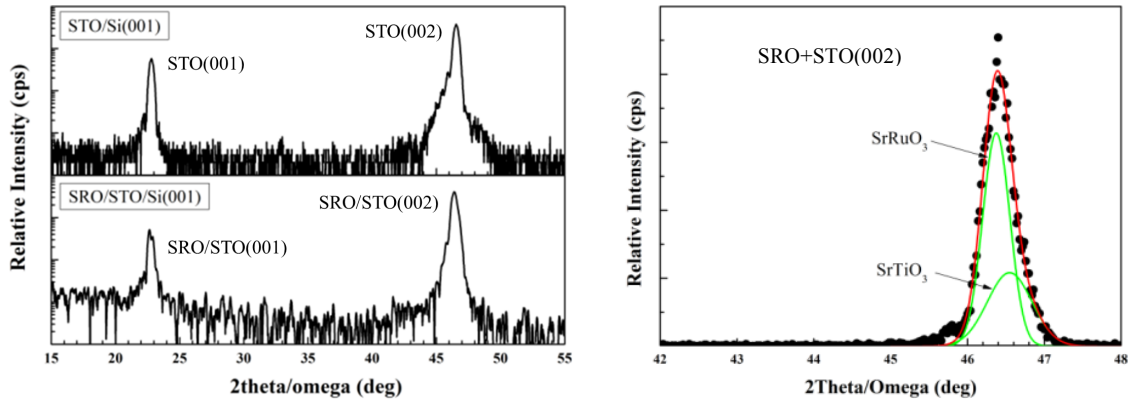


Figure III.26 - Out-of-plane  $2\theta/\omega$  XRD of SRO/STO/Si(001) stack and STO/Si(001) substrate (left) and the Gaussian fit on SRO+STO(002) Bragg peak.

In Figure III.26, SRO film grown on STO/Si(001) and its substrate was measured by out-of-plane  $2\theta/\omega$  XRD, where the SRO and STO Bragg peaks are superposed due to the similar lattice constant. The measurement indicates that the SRO film is epitaxially grown on STO/Si(001) substrate. Out-of-plane lattice constant derived from the Gaussian fit of SRO+STO(002) Bragg peak is  $3.913 \text{ \AA}$  for 22.9nm-thick SRO layer and  $3.899 \text{ \AA}$  for 22.6nm-thick STO layer. Compared with the bulk lattice constant ( $c_t/2 = 3.925 \text{ \AA}$ ), SRO crystalline structure at such thickness is nearly fully relieved. In Figure III.27, AFM topography reveals a quite smooth SRO film surface with the RMS value of the roughness about 0.49 nm. Large amount of sub-micron grains forms on the film surface with an average size of around 150 nm.

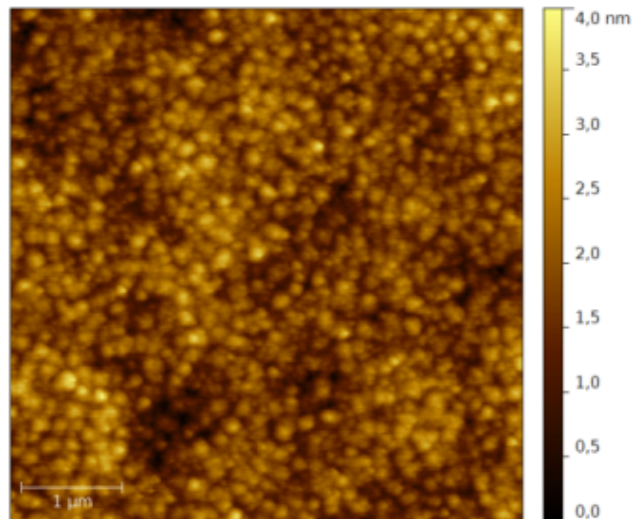


Figure III.27 -  $5 \times 5 \mu\text{m}^2$  AFM surface topography of the as-grown SRO film deposited on STO/Si(001) substrate.

In conclusion, our SRO film deposited by PLD on STO/Si(001) substrate exhibits an epitaxial single crystalline structure with high film quality. Electrical measurement shows that the conductivity of the SRO film is as low as few hundreds  $\mu\Omega\cdot\text{cm}$  and is nearly constant in the whole range of the measurement. AFM topography reveals a quite smooth surface of the film. Therefore, our SRO film could be an appropriate bottom electrode to substitute doped-Si substrate for integration of epitaxial PZT films on STO/Si substrate. In the following, we will present the sol-gel deposition of PZT film on this SRO/STO/Si(001) substrate.

### **III.4.3) Sol-gel deposition of PZT film on SrRuO<sub>3</sub>/SrTiO<sub>3</sub>/Si(001)**

Based on SRO bottom electrode, sol-gel deposition of PZT(52:48) films on STO/Si(001) substrate was processed in this section with the same recipe as we used for 650°C PZT in Section III.3.1. Compared with doped-Si, actuation voltage is directly applied on PZT layer through SRO bottom electrode so that ferroelectric properties could be reproduced in the electrical measurement. From crystallographic perspective, STO buffer layer is essential to the whole epitaxial heterostructure, such as its crystalline structure and thickness, and therefore could affect the properties of the PZT film. On the other hand, ferroelectric film usually has degraded electrical properties than the intrinsic properties of the bulk one, where the formation of tensile residual stress and ferroelectric dead layer acts an important role<sup>[64, 65]</sup>. Tensile stress develops on cooling through the Curie point resulting in a-axis domains<sup>[66, 67]</sup> and ferroelectric dead layer with low permittivity and inactive piezoelectric response often occurs near the ferroelectrics/electrode interface<sup>[68]</sup>. By increasing the film thickness, residual stress can be structurally released<sup>[69]</sup> and the effect of dead layer can be largely reduced. Therefore, ferroelectric films are often grown up to  $\mu\text{m}$  thickness in order to approach the intrinsic properties and achieve the large actuation force and deflection for MEMS applications<sup>[70]</sup>.

In this section, effects of STO buffer layer and PZT film thickness will be studied. Three PZT samples were deposited by sol-gel method on SRO/STO/Si(001) substrate. In Sample A and B, PZT film was fabricated based on different quality of STO buffer layer, where the STO layer of Sample A is epitaxial single crystal with good quality and the STO layer of Sample B has inferior crystalline quality with small amount of (101)-oriented crystalline structure. Here, crystalline quality is defined by the FWHM value of the rocking curve on STO(002) Bragg peak. Besides, 1.26 $\mu\text{m}$ -thick PZT film was grown on SRO/STO/Si(001) substrate for Sample C. In sol-gel method, each cycle of spin-coating, drying and calcinations was repeated 3 times before one RTA annealing, as described in Figure III.9. RTA annealing was processed 1 time for the 250nm-thick PZT films of Sample A and B and 5 times for the 1.26 $\mu\text{m}$ -thick PZT film of Sample C. Table III.3 summarizes all the parameters of the heterostructure for 3 PZT samples. In the

following, we will present various characterizations on those 3 PZT samples, i.e. crystalline and microscopic structure, electrical measurement, and piezoelectric response.

**Table III.3 - The parameters of the PZT/SRO/STO/Si(001) heterostructure for PZT samples.**

Heterostructure	Sample A	Sample B	Sample C
PZT(52:48)	250 nm	250 nm	1.26 $\mu\text{m}$
SrRuO <sub>3</sub>	22.9 nm	21.0 nm	20.0 nm
SrTiO <sub>3</sub>	22.6 nm	11.1 nm	21.0 nm
	FWHM(STO(002)) = 0.45°	FWHM(STO(002)) = 1.44°	FWHM(STO(002)) = 0.90°
Si(001) substrate	---	---	---

### III.4.3.1) Crystalline structure

In Figure III.28, out-of-plane  $2\theta/\omega$  XRD is measured on 3 PZT samples where the PZT/SRO/STO/Si stack and the SRO/STO/Si substrate are indicated in black and red, respectively. The measurement demonstrates a pure perovskite PZT phase in all the samples which are free of pyrochlore phase and have only PZT(00 $l$ ) crystalline orientation normal to the film surface. Interestingly, the PZT film of Sample B grown on a STO buffer layer with small amount of (101)-oriented structure still shows a single crystalline structure.  $\Phi$  scan XRD on PZT{202} and Si{404} Bragg peaks (not shown) confirms that all the PZT films are epitaxially grown on SRO/STO/Si(001) substrate with crystalline orientation of [100] PZT (001) // [100] SRO (001) // [100] STO (001) // [110] Si (001). Furthermore, fine crystalline structure of epitaxial PZT films can be derived by fitting the PZT(002) Bragg peak with multiply Gaussian functions, shown in the right image of Figure III.28. For Sample A, PZT film consists of two phases where the one with larger c-axis lattice constant dominates the film. On the contrary, Sample B consists of only one PZT phase that has the similar lattice constant as the dominant phase of Sample A. The difference of Sample A and B in crystalline structure could be attributed to the crystalline quality of the PZT film. The film quality is defined as the FWHM value of the rocking curve of PZT(002) Bragg peak, giving a value of 0.32° for Sample A and 1.13° for Sample B. The inferior PZT quality of Sample B is epitaxially originated from its STO buffer layer which has a large FWHM value. Thus, the inferior film quality likely provides a mechanism for structural relaxation, leading to a uniform PZT lattice constant in Sample B, while segregation of PZT lattice constant occurs in Sample A where large residual stress forms due to the lack of relaxation mechanism. Three PZT phases are found in Sample C, which is likely caused by the multiply RTA processes during the sol-gel deposition of  $\mu\text{m}$ -thick PZT film. Since the PZT film was grown in layer-by-layer mode, each PZT sublayer undergoes different times of thermal treatment, thus leading to the segregation of PZT lattice constant in Sample C. An intermediate

FWHM value of  $0.67^\circ$  is measured for Sample C. Besides, the fitting result of the PZT(002) and STO(002) Bragg peaks by multiply Gaussian functions is summarized in Table III.4.

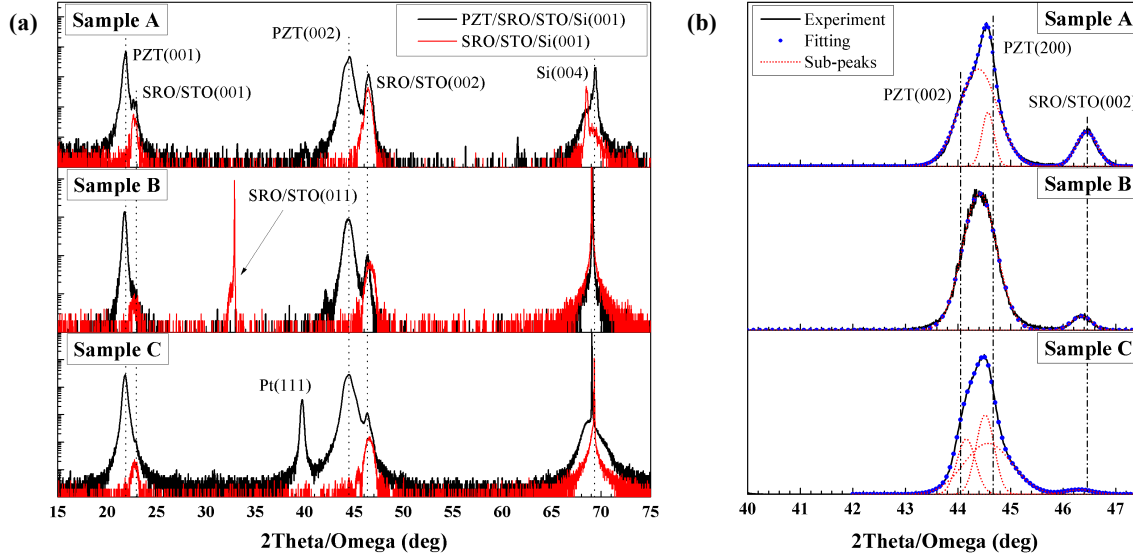


Figure III.28 - (a) Out-of-plane  $2\theta/\omega$  XRD of PZT/SRO/STO/Si stack (black) and SRO/STO/Si substrate (red) and (b) the Gaussian fit on PZT(002) Bragg peak.

Table III.4 - The fitting result of PZT(002) and STO(002) Bragg peak by multiply Gaussian functions

	Sample A	Sample B	Sample C
PZT film	$c_1 = 4.078 \text{ \AA}$	$c = 4.076 \text{ \AA}$ FWHM = $1.13^\circ$	$c_1 = 4.098 \text{ \AA}$
	$c_2 = 4.062 \text{ \AA}$		$c_2 = 4.067 \text{ \AA}$
	FWHM = $0.32^\circ$		$c_3 = 4.062 \text{ \AA}$ FWHM = $0.32^\circ$
STO buffer layer	$c = 3.907 \text{ \AA}$ FWHM = $0.45^\circ$	$c = 3.915 \text{ \AA}$ FWHM = $1.44^\circ$	$c = 3.915 \text{ \AA}$ FWHM = $0.90^\circ$

More XRD measurement was performed on Sample A and B for comparison of different STO film quality. In Figure III.29, RSM patterns measured on PZT(013) and SRO/STO(013) Bragg spots show more details about crystalline texture. Both PZT samples consist of similar reciprocal pattern where the PZT(013) Bragg spot locates between a- and c-domains of the bulk material. Compared with Sample A, PZT(013) Bragg spot of Sample B has an ellipse-like shape indicating a more homogeneous crystalline structure in the PZT film. On the contrary, PZT(013) Bragg spot of Sample A can be decomposed into two overlapping PZT phases, which agrees with the fitting result of the out-of-plane  $2\theta/\omega$  XRD. Moreover, XRD pole figures in Figure III.30 directly evidence an epitaxial single crystalline PZT film on SRO/STO/Si(001) for both PZT

samples with crystalline orientation of (100) PZT [001] // (100) SRO [001] // (100) STO [001] // (110) Si [001].

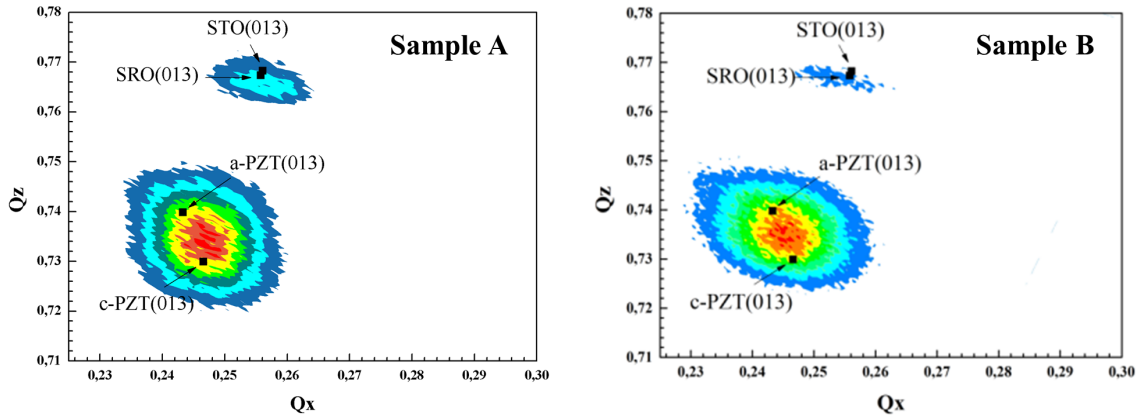


Figure III.29 - RSM measurement on the PZT(013) and SRO/STO(013) Bragg spots of Sample A and B. The corresponding Bragg spots of the bulk materials are indicated.

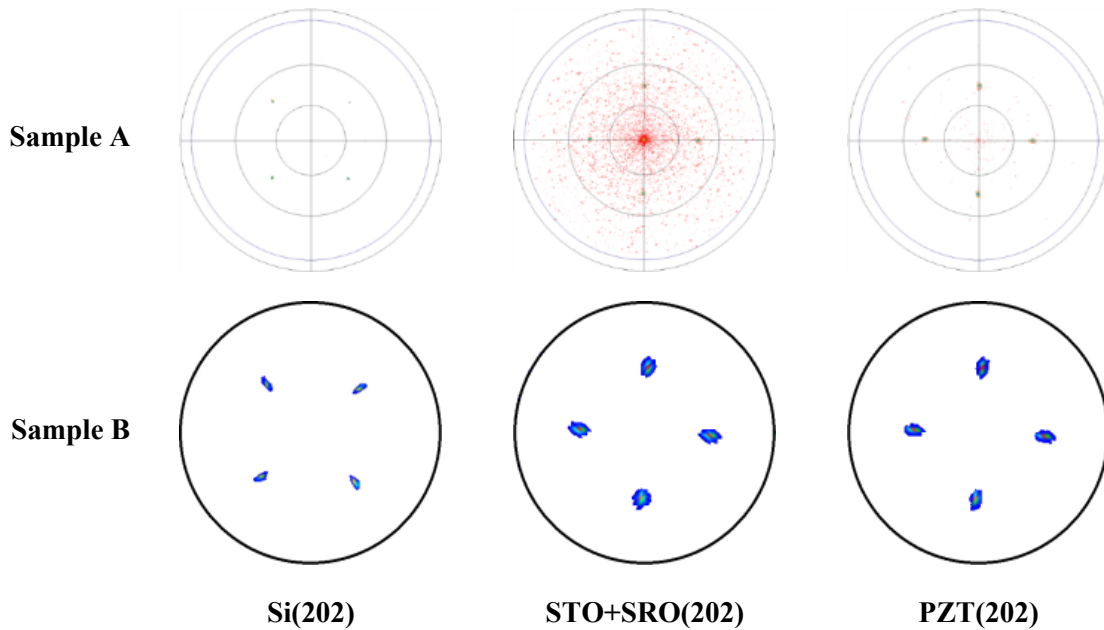


Figure III.30 - XRD pole figures of Sample A and B on Si{202}, SRO/STO{202}, and PZT{202} Bragg spots.

### III.4.3.2) Microscopic structure

Microscopic structure of PZT/SRO/STO/Si(001) was mainly observed by TEM on Sample C to study the  $\mu\text{m}$ -thick PZT film. The measurement was performed on a nm-thick specimen of Sample C along Si(110) cross section. In Figure III.31, a bright-field TEM image at the magnification of 4k is shown across the whole stack. Sample C totally consists of 15 PZT layers

### *Chapter III - Integration of epitaxial PZT thin film on Si substrate*

---

and each 3 layers were annealed by RTA after coating, leading to the formation of 5 RTA layers. Those RTA layers are clearly identified by the interfaces in TEM image. The thickness of each RTA layer from the substrate to the top surface is about 0.24  $\mu\text{m}$ , 0.24  $\mu\text{m}$ , 0.23  $\mu\text{m}$ , 0.27  $\mu\text{m}$ , and 0.28  $\mu\text{m}$ , respectively. The overall thickness of the PZT film is about 1.26  $\mu\text{m}$ . No pyrochlore phase is observed in all the PZT layers, which often appears as amorphous contrast in TEM image. Pore structure is formed in the 2<sup>nd</sup> RTA layer, whose average size is about 60 nm. It is assumed that those pores were formed due to a fast densification of the sublayer surface that prevents the evaporation of inner organic substances and forms bubbles [71]. Besides, fluctuation of the TEM contrast in the PZT film is mainly caused by the small tilt of the crystalline orientation. Since the PZT film is epitaxially grown on the substrate, such fluctuation likely results from the small-angle subgrain structure of the film. From substrate to the top surface, these subgrains slightly tilt with increase of the film thickness, leading that the TEM contrast gradually transforms from dark to bright. The tilt of the subgrains is a mechanism to relieve the residual stress which is thermally generated during RTA process by clamping effect of the Si substrate and is a thickness-dependent effect.

In addition, HR-TEM images at the magnification of 200k exhibit two regions near the Si substrate and within the PZT film of Sample C (Figure III.32). In the left image, flat and continuous interfaces with commensurate crystalline structure are clearly seen without any interfacial defects between each oxide layer. Similar to our PZT/STO/Si(001) sample, a 4.3nm-thick layer of amorphous SiO<sub>2</sub> forms between STO and Si due to the thermal treatment. The image also reveals a pure crystalline structure in the Si substrate, demonstrating that no lead is diffused into the Si substrate to form lead silicate. Besides, all the oxide films appear to be crystallized in perovskite structure with continuous crystalline lattice. FT image (at the corner of the image) evidences only one reciprocal lattice for all the oxide layers, implying that all the oxide layers near the substrate undergo an elastic stress and, therefore, have similar lattice constants. Moreover, the right image shows a continuous single crystalline structure of the PZT film, which is also confirmed by the single reciprocal lattice in the FT image (at the corner of the image). A pore with bright TEM contrast is found on the right part of the image, which corresponds to the porous structure in the second PZT sublayer in Figure III.31. The bright contrast is due to the small thickness of the pore compared with the other region, where the single crystalline structure is not interrupted in the pore and is continuous with the same lattice constants.

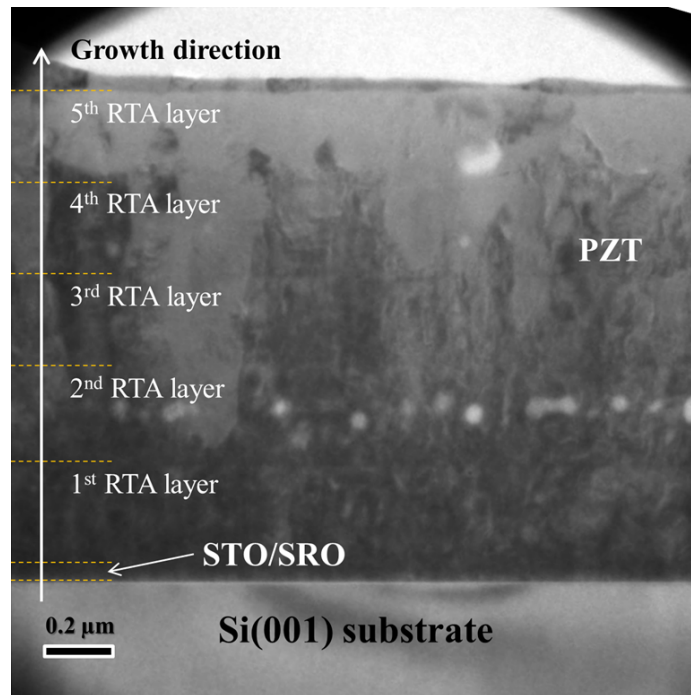


Figure III.31 - TEM image of Sample C at the magnification of 4k on Si(110) cross section.

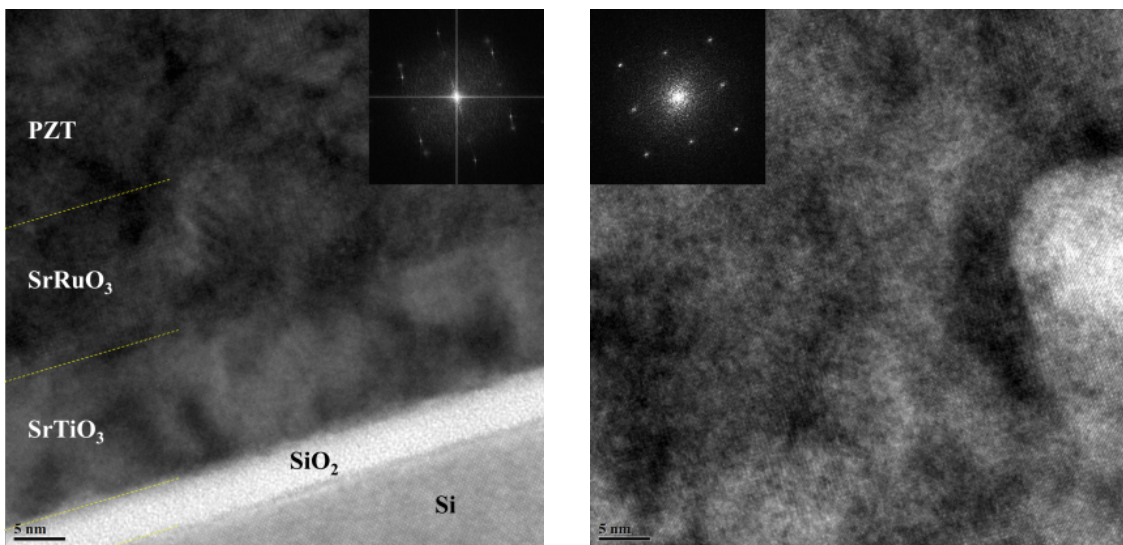


Figure III.32 - TEM images of PZT/SRO/STO/Si(001) at 200k magnification on Si(110) cross section at the regions near the Si substrate (left) and within the epitaxial PZT film (right).

### III.4.3.3) Electrical characterizations

To measure the electrical properties, Ru top electrode was deposited by rf sputtering on PZT films and then patterned by chemical etching to form Ru/PZT/SRO capacitors with the size of  $90 \times 90 \mu\text{m}^2$ . The thickness of Ru top electrode is about 100 nm. In the measurement circuits, detection voltage was applied across the Ru top electrode and the SRO bottom electrode and the latter was virtually grounded.

#### a. Impedance vs. dc bias

In Figure III.33, the electrical impedance as the function of dc bias, i.e. C-V curve, is shown for all the 3 PZT films which were measured in  $C_p$ -D mode using 0.1 V ac voltage at 100 kHz. For all the C-V curves, the expected butterfly shape induced by the polarization reversal can be clearly observed. Significant difference is observed in dielectric permittivity and loss between these 3 PZT samples which are 956 and 8.5% for Sample A, 1326 and 10.2% for Sample B, 1390 and 8.4% for Sample C at their maxima. At the maxima, the electrical permittivity and loss are mainly contributed from the domain wall movement and maximized due to the most randomly distributed ferroelectric domains at such dc bias<sup>[72]</sup>. The coercive electric field of the PZT films can be measured as the half value between the two maxima<sup>[73]</sup>, which is 28.8 kV/cm for Sample A, 28.8 kV/cm for Sample B, and 20.6 kV/cm for Sample C. Such coercive voltage is nearly independent on the range of the measurement and the ac frequency. Moreover, the saturation dielectric permittivity and loss at the high dc bias gradually increase from Sample A (269 and 1.7%) and B (379 and 2.3%) to Sample C (519 and 2.9%).

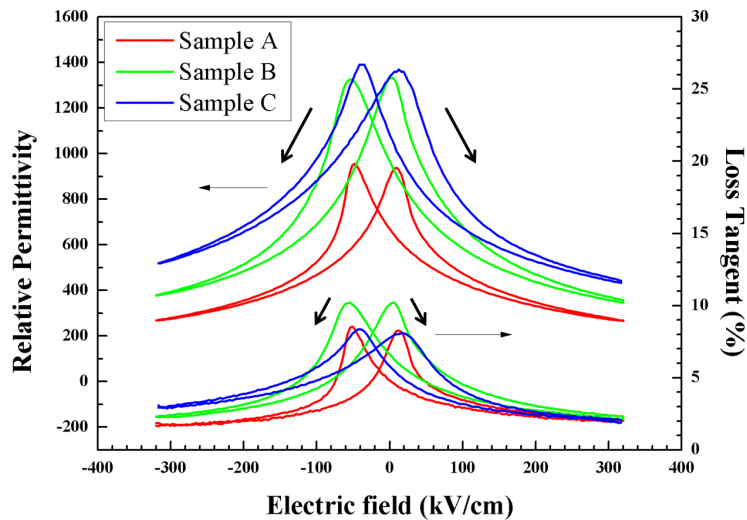
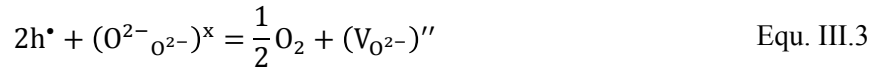


Figure III.33 - Electrical impedance of Ru/PZT/SRO capacitors at 100 kHz as the function of dc bias.

### *Chapter III - Integration of epitaxial PZT thin film on Si substrate*

---

In our PZT films, crystalline quality and film thickness could attribute to the distinct electrical impedance among the 3 PZT samples. The PZT film of Sample A with small film thickness and small FWHM value, i.e. good crystalline quality, undergoes a large residual stress due to the thermal treatment and the clamping effect of the Si substrate. The residual stress in the PZT film leads to the structural constraint on the reversal of the ferroelectric domains causing smaller dielectric permittivity. On the contrary, the inferior crystalline quality in Sample B and the large PZT film thickness in Sample C could provide additional mechanisms to release such residual stress, approach the properties of the bulk material, and thus strengthen the ferroelectric response to the applied ac electric field <sup>[74]</sup>. At the same time, domain wall movement increases the energy dissipation in the polarization reversal, leading to the larger dielectric loss in Sample B and C. Besides, the film thickness likely has the strong effect on the electrical impedance that Sample C has the largest dielectric permittivity in the whole range of the measurement and the smallest coercive electric field. Moreover, all the C-V curves are not symmetrical about zero dc bias but shift to the negative electric field, indicating that the spontaneous polarization towards the substrate is energetically favorable, which is known as the imprint effect. The imprint effect can be induced by various mechanisms <sup>[75, 76, 77, 78]</sup> and is mainly related to the formation of oxygen vacancies for PZT capacitors <sup>[79]</sup>. In our case, Ru top electrode provides a reducing ambience and leads to the formation of oxygen vacancies near the Ru/PZT interface in the PZT film <sup>[80]</sup> by following chemical reaction <sup>[81]</sup>:



where the equation takes the Kröger-Vink notation <sup>[82]</sup>. The loss of volatile PbO during thermal annealing also creates oxygen vacancies by the Schottky reaction near the top surface <sup>[83]</sup>.

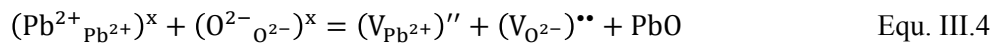


Figure III.34 schematically shows the influence of those oxygen vacancies on the preferred polarization orientation <sup>[84]</sup>. For symmetrical oxygen octahedron, the potential energy profile of the  $Ti^{4+}$  ion has two equally weighted potential minima located at the top and the bottom of the central plane. The octahedron distorted by the oxygen vacancy and the dangled bonds require additional energy  $2\Delta H_{pl}$  for  $Ti^{4+}$  located at the bottom minimum site to displace to the upper one. Therefore, the polarization directing from the center of oxygen octahedron to the  $Ti^{4+}$  ion energy-preferably orientates from the higher density of oxygen vacancies to the lower one, namely from Ru top electrode to SRO bottom electrode. Furthermore, the imprint effect in our PZT films can be also attributed to the asymmetrical materials and their growth conditions used for the top and bottom electrodes, i.e. Ru/PZT and SRO/PZT interfaces <sup>[85]</sup>, especially for Sample C in which

each PZT sublayer and electrode/PZT interface was processed by different times of RTA annealing.

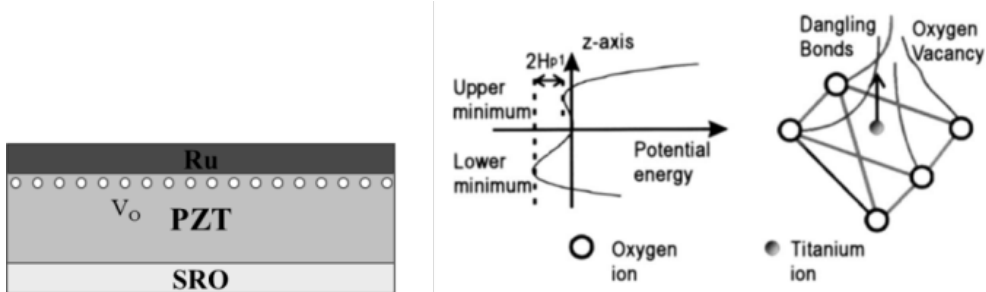


Figure III.34 - The influence of oxygen vacancies on the preferred orientation of spontaneous polarization.

### b. Impedance vs. ac frequency

Electrical impedance as the function of ac frequency, also known as dielectric dispersion, was measured from 1 kHz to 1 MHz on all the PZT samples (Figure III.35). Although similar tendencies of dielectric permittivity and loss are observed, their values vary between the 3 PZT samples in the whole range of frequency values. Both values increase from Sample A, B to Sample C, in agreement with the result of the C-V measurement, which can be also attributed to the variance of the crystalline quality and the film thickness. In principle, dielectric dispersion of a perovskite film has certain characteristic features which allow interpretation of the measured values on the assumption of the intrinsic properties, the grain boundary, the film thickness, the buffer layer and series resistance associated with the electrodes<sup>[86]</sup>. For the range of kHz - MHz, no bulk relaxation mechanisms can result in a dielectric dispersion and, thus, their characteristics are mainly affected by the processing condition of the top and bottom electrodes, the size of the capacitors, and the film thickness<sup>[87]</sup>.

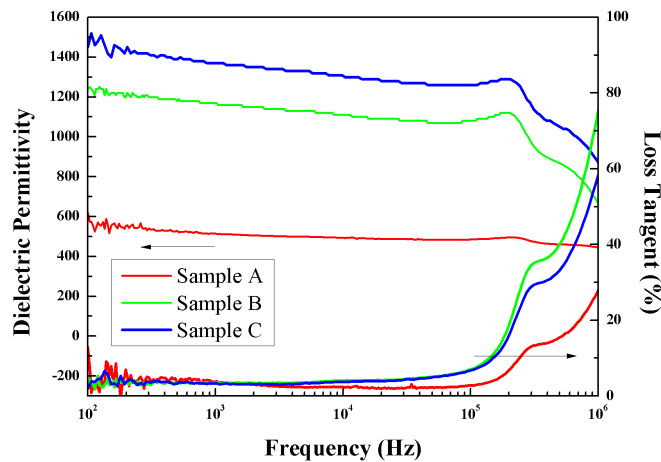


Figure III.35 - Electrical impedance of sample-A and sample-B as a function of ac frequency.

c. Polarization vs. electric field

Electric-field-induced polarization, i.e. P-E loop, was measured by Sawyer-Tower circuit in which a sinusoidal ac voltage at 500 Hz was applied on Ru top electrode and a 23 nF capacitor was used as the reference capacitor. In Figure III.36, all the P-E loops exhibit typical ferroelectric hysteresis induced by the ac electric field on the PZT films. For comparison, the P-E loops of Sample A and B are not as distinct as their electrical impedance in the C-V measurement. The similarity indicates that the difference of the dielectric response affected by the effect of STO buffer layer between Sample A and B is not obvious under the large ac voltage in the P-E measurement than that under the small ac voltage in the C-V measurement. Besides, the P-E loop of Sample C has the thinnest shape, which is likely attributed to the effect of the film thickness. To summarize, the remnant polarization and the coercive electric field, which takes the average of negative and positive values, i.e.  $E_c = (E_c^+ + E_c^-)/2$ , are  $14.50 \mu\text{C}/\text{cm}^2$  and  $70.0 \text{ kV}/\text{cm}$  for Sample A,  $17.89 \mu\text{C}/\text{cm}^2$  and  $76.1 \text{ kV}/\text{cm}$  for Sample B,  $24.60 \mu\text{C}/\text{cm}^2$  and  $45.5 \text{ kV}/\text{cm}$  for Sample C. Moreover, the P-E loops of Sample A and B slightly shift to the negative electric field due to the imprint effect of the PZT film, as we discussed in the C-V measurement.

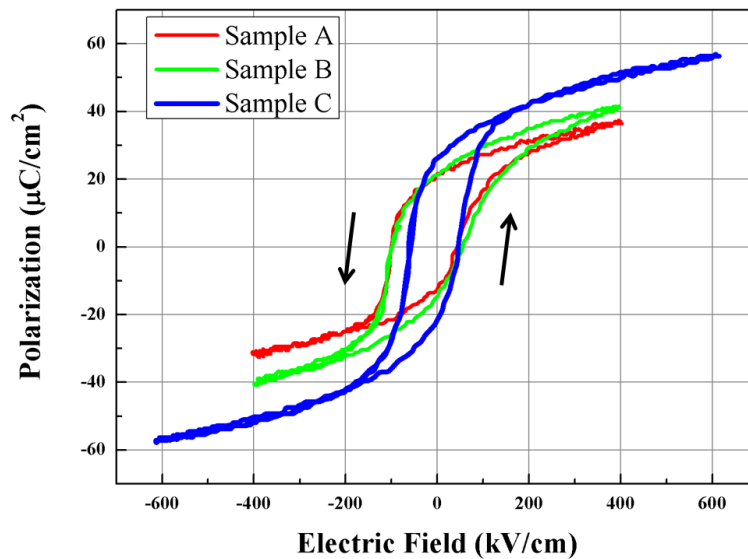


Figure III.36 - Polarization as a function of applied electric field for Ru/PZT/SRO capacitors.

Generally, thickness-dependent P-E loop can be attributed to a number of factors, where foremost of these are the role of residual stress and interface layers with the properties that differ from the interior of the PZT film <sup>[88]</sup>. Sample A and B with small PZT thickness are likely affected by the clamping effect of Si substrate and the interface layers. Increase of the film thickness can release the residual stress and reduce the contribution of the interface layers,

causing that the electrical properties approach to its bulk counterparts. Thus, the small coercive electric field and the large remnant and saturation polarization of Sample C are due to the large PZT film thickness. Sample B has a slightly larger saturation polarization than that of Sample A, which is possibly caused by the inferior film quality in Sample B. Moreover, compared with C-V measurement the coercive electric field derived from P-E loop nearly doubles for all the PZT samples. The doubling of the coercive electric field is attributed to the fact that the P-E loop is acquired at a certain frequency and the C-V curve is a quasistatic measurement, i.e. the dc bias is swept at few millivolts/second (equivalent to mHz in frequency) with a negligible ac detection voltage<sup>[89]</sup>.

**d. Leakage current vs. dc voltage**

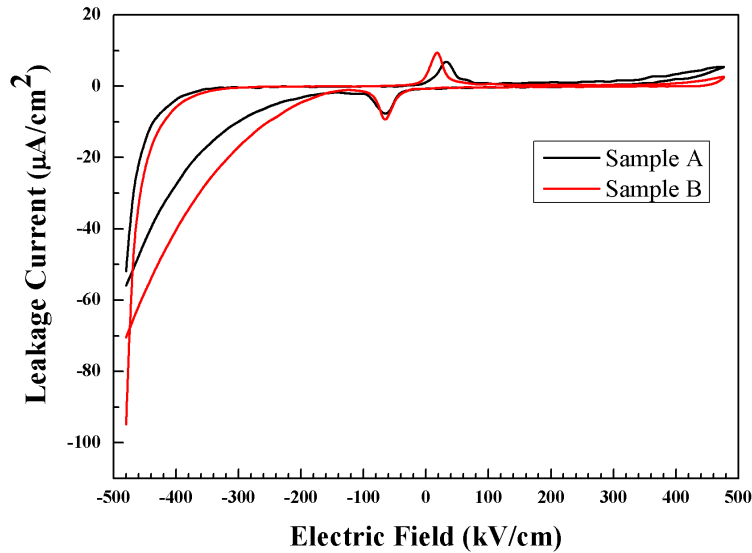


Figure III.37 - Leakage current density as the function of dc voltage measured on Sample A and B.

I-V characteristics are studied between Sample A and B showing little difference in the leakage current in Figure III.37. For both PZT samples, the leakage current density is less than  $100\mu\text{A}/\text{cm}^2$  within  $\pm 12$  V. Two local maxima of the current density occur near the zero dc voltage due to the polarization reversal, in agreement with the coercive voltage in the C-V measurement. Compared with polycrystalline film, epitaxial PZT film with enhanced crystalline quality has a larger leakage current density at the same dc voltage<sup>[90]</sup>. Small leakage current in polycrystalline PZT film is attributed to the structural defects, especially grain boundaries, which affect the charge transport by either trapping (lower concentration) or scattering the carriers (lower mobility)<sup>[91]</sup>. The non-symmetry of the I-V curves at high voltage likely originates from the use of different top and bottom electrode materials. The negative dc bias corresponds to the

electron injection from Ru top electrode to PZT film. It can be assumed that the combination of the injected electrons with the high-density oxygen vacancies at Ru/PZT interface contributes to the larger leakage current at negative dc bias. Besides, the breakdown voltage was measured by applying an increasing dc voltage until the leakage current suddenly reaches to the compliance current of the equipment. The positive and negative breakdown voltages are averaged, giving the value of 702kV/cm for Sample A and 682kV/cm for Sample B, respectively.

#### **III.4.3.4) Local electromechanical properties**

Local electromechanical properties of Sample A and B at microscopic scale were measured by PFM at NIMP institute to study the effect of STO buffer layer. The PFM setup is based on a modified VEECO Dimension 3100A AFM setup with a dual-frequency resonance-tracking lock-in amplifier. The PFM cantilever used to apply detection voltage on the local PZT surface is coated by conductive diamond, which has a resonance frequency at 75 kHz and a force constant at 2.8 N/m. In Figure III.38, surface topography is measured for both PZT samples where Sample A has a relatively rough surface and Sample B consists of high-density hillocks on the surface. To measure ferroelectric hysteresis loop, cantilever tip was fixed on the sample surface while applying the detection voltage. PFM field-off mode was used in the measurement, namely the piezoresponse of the film is read after removal of dc bias at each step. The use of field-off mode is mainly to reduce the capacitance signal of the PZT film on the output and, therefore, is likely affected by the back-switching effect <sup>[92]</sup>. In Figure III.38, such hysteresis loops, presented by the phase component, are clearly observed for both PZT samples. Sample A shows a rectangular shape with abrupt switching feature and, on the contrary, Sample B gives a gradual switching feature. Generally, several factors are concerned with polarization reversal as the function of dc bias, such as domain nucleation at critical dc bias, domain growth after nucleation, and pinning effect <sup>[93]</sup>. The abrupt switching feature in Sample A manifests a uniform critical dc bias, i.e. coercive voltage, in the PZT film. Due to the high film quality with less pinning centers in Sample A, ferroelectric domains switched by dc bias grow rapidly, leading to a complete domain switching in a transient time constant across the whole PZT film. On the contrary, the pinning centers in the PZT film of Sample B due to the inferior film quality largely distribute the critical dc bias in the film and, therefore, the switching process of the polarizations occurs gradually in a large range of dc bias.

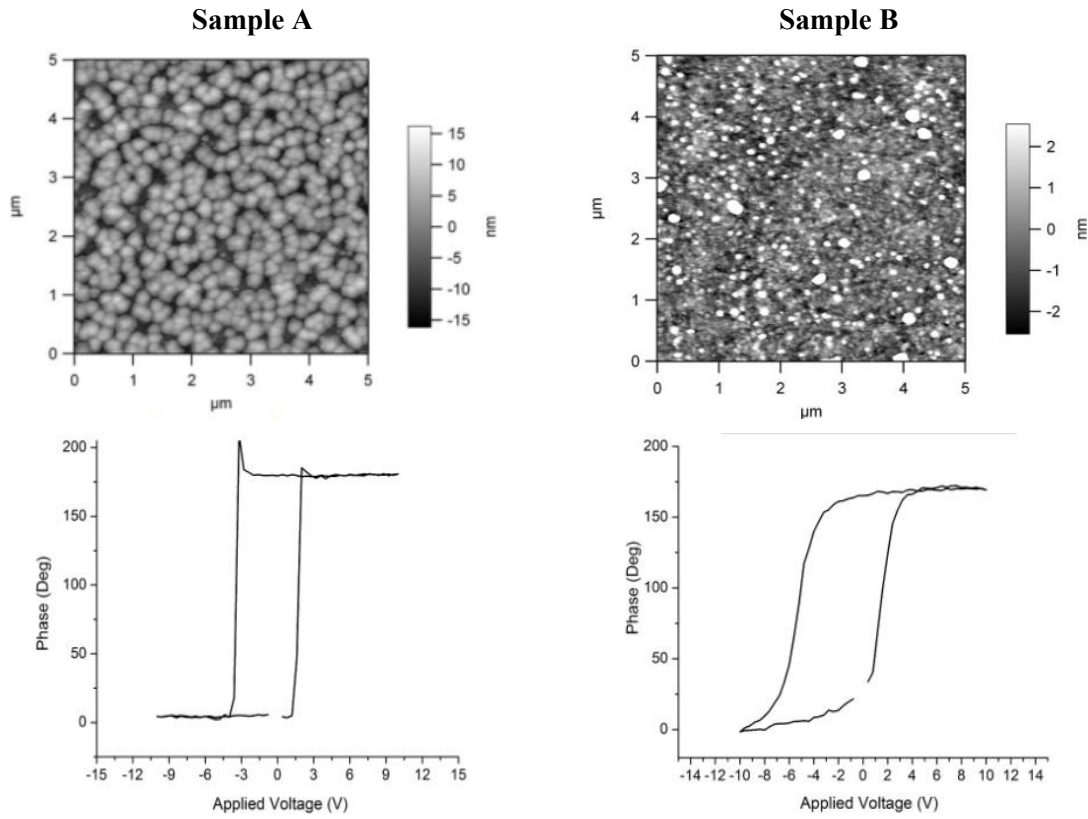
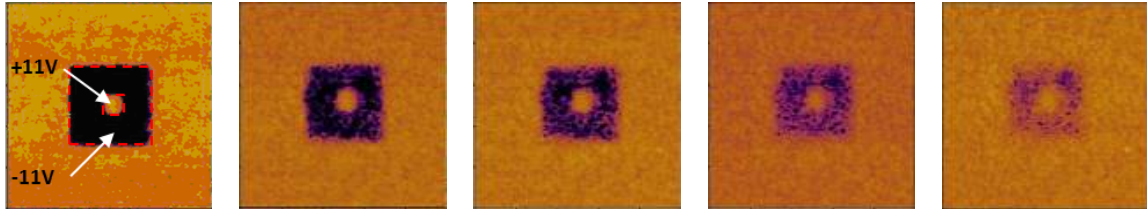


Figure III.38 - Surface topography and hysteresis loop measured on Sample A and B.

Memory effect of ferroelectric film is essentially important for the application of Fe-FET devices [94]. The retention property describes such effect of the film, which can retain a given level of electric signal in the electrical dipole after a given time period from the write operation. It is usually defined by the remnant polarization stored in the ferroelectric film, such as  $R = \left[ 1 - \frac{\Delta P_r}{P_r(0)} \right] \times 100$ , where  $\Delta P_r$  is the decrease of the remnant polarization due to depoling effect and  $P_r(0)$  is the remnant polarization at time zero [95]. By PFM setup, retention property can be studied by periodically reading the artificial ferroelectric domains which were intentionally created by dc voltage in the film. Figure III.39 shows such time-dependent artificial ferroelectric domain for both PZT samples each 30 min within 2 hours. Here, the phase component of PFM output is taken for the images. The bright region in the artificial ferroelectric domain corresponds to +11V writing voltage, which has the similar feature as the unpoled region. It indicates that the spontaneous polarization in both PZT samples holds the energetically-preferred orientation towards the substrate, which is in agreement with the imprint effect as we concluded from the macroscopic electrical measurement. With increase of the duration, two PZT samples exhibit distinct behavior in the retention property. Sample-A shows a volatile ferroelectric domain whose

spontaneous polarization in the dark region gradually switches back to the energy-preferred direction, namely, towards the Si substrate. On the contrary, sample-B shows a nearly constant PFM image in the whole duration, demonstrating a good resistance to the back-switching mechanism. In principle, the back switching effect can be attributed to the thermodynamic instability which is caused by electrostatic or elastic energy from built-in electric fields<sup>[96]</sup> and strain<sup>[97]</sup>. The better resistance to such instability in sample-B can be attributed to the high-density pinning centers, such as dislocations, formed in the PZT film. On the other hand, the formation of dislocations effectively decreases the thermal stress which is regarded as the driving force in the back-switching process. However, for sample-A where the dislocation is insufficient to release the thermal stress, large driving force combined with the lack of pinning centers is the cause for the back switching effect with increase of the time.

**Sample A**



**Sample B**

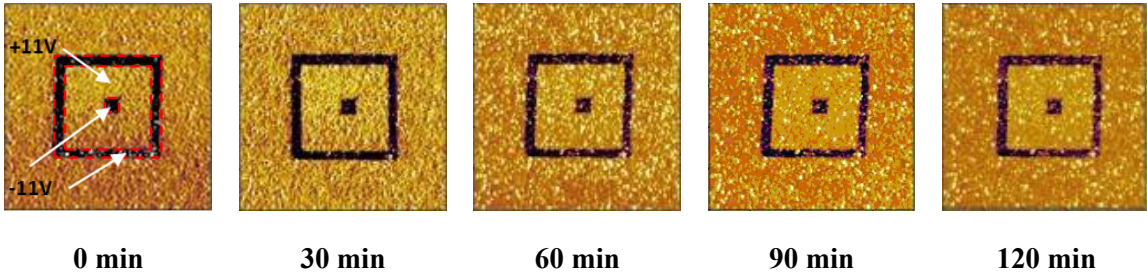


**Figure III.39 - Time evolution of the artificial ferroelectric domain created on Sample A and B within 2 hours.**

**III.5) Conclusion**

In this chapter, we introduced the fabrication process and the characterizations to integrate epitaxial PZT films on STO/Si(001) substrate. Epitaxial growth of STO film on Si(001) is successfully realized by effusion cell in our MBE system, providing an excellent oxide/Si substrate for the subsequent growth of PZT film. Then, epitaxial PZT film was grown by sol-gel method on STO/Si(001) thank to the small lattice mismatch between PZT and STO. In addition, SRO film was deposited by PLD on STO/Si(001) for the use of bottom electrode due to its high conductivity and similar perovskite structure with most functional oxides. The as-prepared

PZT/SRO/STO/Si(001) heterostructure was verified as epitaxial growth with the crystalline orientation as (100) PZT [001] // (100) SRO [001] // (100) STO [001] // (110) Si [001]. Finally, both macro- and microscopic electrical measurements exhibit good ferroelectric and piezoelectric response in the epitaxial PZT film. Successful integration of epitaxial PZT film on Si substrate using oxide buffer layer and bottom electrode definitely provides a new approach for various applications. In Chapter 5, we will introduce the microfabrication process using standard cleanroom technologies on this epitaxial PZT film to realize simple piezoelectric devices.

### **III.6) References**

- 
- [1] C. J. Först, C. R. Ashman, K. Schwarz, and P. E. Blöchl, "The interface between silicon and a high-k oxide.," *Nature*, **vol. 427**, no. 6969, pp. 53–6, Jan. 2004.
- [2] H. J. Osten, D. Kühne, A. Laha, M. Czernohorsky, E. Bugiel, and A. Fissel, "Integration of functional epitaxial oxides into silicon: From high-K application to nanostructures," *Journal of Vacuum Science & Technology B: Microelectronics and Nanometer Structures*, **vol. 25**, no. 3, p. 1039, 2007.
- [3] H. Proksche, "The Influence of NH<sub>4</sub>F on the Etch Rates of Undoped SiO<sub>2</sub> in Buffered Oxide Etch," *Journal of The Electrochemical Society*, **vol. 139**, no. 2, p. 521, 1992.
- [4] F. Liu, M. Hohage, M.G. Lagally, *Encyclopedia of Applied Physics*, Wiley-VCH Verlag GmbH, London, p.321 (1999).
- [5] R. Tromp, R. Hamers, and J. Demuth, "Si(001) Dimer Structure Observed with Scanning Tunneling Microscopy," *Physical Review Letters*, **vol. 55**, no. 12, pp. 1303–1306, Sep. 1985.
- [6] Y. Wei, X. Hu, Y. Liang, D. C. Jordan, B. Craigo, R. Droopad, Z. Yu, A. Demkov, J. L. Edwards, and W. J. Ooms, "Mechanism of cleaning Si(100) surface using Sr or SrO for the growth of crystalline SrTiO<sub>3</sub> films," *Journal of Vacuum Science & Technology B: Microelectronics and Nanometer Structures*, **vol. 20**, no. 4, p. 1402, 2002.
- [7] X. Zhang, A. Demkov, H. Li, X. Hu, Y. Wei, and J. Kulik, "Atomic and electronic structure of the Si/SrTiO<sub>3</sub> interface," *Physical Review B*, **vol. 68**, no. 12, p. 125323, Sep. 2003.
- [8] D. G. Schlom and J. H. Haeni, "A Thermodynamic Approach to Selecting Alternative Gate Dielectrics," *MRS Bulletin*, **vol. 27**, no. 03, pp. 198–204, Jan. 2011.
- [9] G. Delhaye, C. Merckling, M. El-Kazzi, G. Saint-Girons, M. Gendry, Y. Robach, G. Hollinger, L. Largeau, and G. Patriarche, "Structural properties of epitaxial SrTiO<sub>3</sub> thin films

- grown by molecular beam epitaxy on Si(001),” *Journal of Applied Physics*, **vol. 100**, no. 12, p. 124109, 2006.
- [10] G. Delhayé, M. El Kazzi, M. Gendry, G. Hollinger, and Y. Robach, “Hetero-epitaxy of SrTiO<sub>3</sub> on Si and control of the interface,” *Thin Solid Films*, **vol. 515**, no. 16, pp. 6332–6336, Jun. 2007.
- [11] G. Niu, W. W. Peng, G. Saint-Girons, J. Penuelas, P. Roy, J. B. Brubach, J.-L. Maurice, G. Hollinger, and B. Vilquin, “Direct epitaxial growth of SrTiO<sub>3</sub> on Si (001): Interface, crystallization and IR evidence of phase transition,” *Thin Solid Films*, **vol. 519**, no. 17, pp. 5722–5725, Jun. 2011.
- [12] G. J. Norga, C. Marchiori, C. Rossel, A. Guiller, J. P. Locquet, H. Siegwart, D. Caimi, J. Fompeyrine, J. W. Seo, and C. Dieker, “Solid phase epitaxy of SrTiO<sub>3</sub> on (Ba,Sr)O/Si(100): The relationship between oxygen stoichiometry and interface stability,” *Journal of Applied Physics*, **vol. 99**, no. 8, p. 084102, 2006.
- [13] X. Hu, H. Li, Y. Liang, Y. Wei, Z. Yu, D. Marshall, J. Edwards, R. Droopad, X. Zhang, A. A. Demkov, K. Moore, and J. Kulik, “The interface of epitaxial SrTiO<sub>3</sub> on silicon: in situ and ex situ studies,” *Applied Physics Letters*, **vol. 82**, no. 2, p. 203, 2003.
- [14] G. Niu, G. Saint-Girons, B. Vilquin, G. Delhayé, J.-L. Maurice, C. Botella, Y. Robach, and G. Hollinger, “Molecular beam epitaxy of SrTiO<sub>3</sub> on Si (001): Early stages of the growth and strain relaxation,” *Applied Physics Letters*, **vol. 95**, no. 6, p. 062902, 2009.
- [15] G. Yi, Z. Wu, and M. Sayer, “Preparation of Pb(Zr,Ti)O<sub>3</sub> thin films by sol gel processing: Electrical, optical, and electro-optic properties,” *Journal of Applied Physics*, **vol. 64**, no. 5, p. 2717, 1988.
- [16] J. Livage, M. Henry, and C. Sanchez, “Sol-gel chemistry of transition metal oxides,” *Progress in Solid State Chemistry*, **vol. 18**, no. 4, pp. 259–341, Jan. 1988.
- [17] Guanghua Yi, “Sol-Gel Processing of PZT Films”, PhD Thesis, Queen's University.
- [18] G. A. C. M. Spierings, M. J. E. Ulenaers, G. L. M. Kampschöer, H. A. M. van Hal, and P. K. Larsen, “Preparation and ferroelectric properties of PbZr<sub>0.53</sub>Ti<sub>0.47</sub>O<sub>3</sub> thin films by spin coating and metalorganic decomposition,” *Journal of Applied Physics*, **vol. 70**, no. 4, p. 2290, 1991.
- [19] S. S. Dana, K. F. Etzold, and J. Clabes, “Crystallization of sol-gel derived lead zirconate titanate thin films,” *Journal of Applied Physics*, **vol. 69**, no. 8, p. 4398, 1991.

- [20] Chang Jung Kim, Dae Sung Yoon, Zhong-Tao Jiang, Kwangsoo No, "Investigation of the drying temperature dependence of the orientation in sol-gel processed PZT thin films", *Journal of Materials Science*, **vol. 32**, no. 5, p. 1213, 1997.
- [21] K. R. Udayakumar, J. Chen, V. Kumar, S. B. Krupanidhi, and L. E. Cross, Proceedings of the 7th IEEE International Symposium on Application of Ferroelectrics, June 6-8, 1990, Urbana Champaign, IL, pp. 744-746.
- [22] J. Chen, K. R. Udayakumar, K. G. Brooks, and L. E. Cross, "Rapid thermal annealing of sol-gel derived lead zirconate titanate thin films," *Journal of Applied Physics*, **vol. 71**, no. 9, p. 4465, 1992.
- [23] E. Sato, Y. Huang, M. Kosec, A. Bell, and N. Setter, "Lead loss, preferred orientation, and the dielectric properties of sol-gel prepared lead titanate thin films," *Applied Physics Letters*, **vol. 65**, no. 21, p. 2678, 1994.
- [24] G. Velu, D. Remiens, and B. Thierry, "Ferroelectric properties of PZT thin films prepared by sputtering with stoichiometric single oxide target: Comparison between conventional and rapid thermal annealing," *Journal of the European Ceramic Society*, **vol. 17**, no. 14, pp. 1749-1755, Jan. 1997.
- [25] R. Thomas, S. Mochizuki, T. Mihara, and T. Ishida, "Effect of substrate temperature on the crystallization of Pb(Zr,Ti)O<sub>3</sub> films on Pt/Ti/Si substrates prepared by radio frequency magnetron sputtering with a stoichiometric oxide target," *Materials Science and Engineering: B*, **vol. 95**, no. 1, pp. 36-42, Jul. 2002.
- [26] T.-L. Ren, T.-Q. Shao, W.-Q. Zhang, C.-X. Li, J.-S. Liu, L.-T. Liu, J. Zhu, and Z.-J. Li, "Fabrication and properties of silicon-based PZT thin films for MFSFET applications," *Microelectronic Engineering*, **vol. 66**, no. 1-4, pp. 554-560, Apr. 2003.
- [27] C. K. Kwok and S. B. Desu, "Pyrochlore to perovskite phase transformation in sol-gel derived lead-zirconate-titanate thin films," *Applied Physics Letters*, **vol. 60**, no. 12, p. 1430, 1992.
- [28] G. A. C. M. Spierings, G. J. M. Dormans, W. G. J. Moors, M. J. E. Ulenaers, and P. K. Larsen, "Stresses in Pt/Pb(Zr,Ti)O<sub>3</sub>/Pt thin-film stacks for integrated ferroelectric capacitors," *Journal of Applied Physics*, **vol. 78**, no. 3, p. 1926, 1995.
- [29] B. A. Tuttle, T. J. Garino, J. A. Voigt, T. J. Headley, D. Dimos, and M. O. Eatough, Science and Technology of Electroceramic Thin Films: Proceedings of the NATO Advanced Workshop,

1994, Villa Del Mare, Italy, edited by O. Auciello and R. Waser (Kluwer Academic Publishers, New York, 1995), p.117.

[30] F. Xu, S. Trolier-McKinstry, W. Ren, B. Xu, Z.-L. Xie, and K. J. Hemker, "Domain wall motion and its contribution to the dielectric and piezoelectric properties of lead zirconate titanate films," *Journal of Applied Physics*, **vol. 89**, no. 2, p. 1336, 2001.

[31] M. Takata *et. al*, Fundamental Characteristics of New Non-Volatile Memory with Extremely High Density Metal Quantum Dots, ECS International Semiconductor Technology Conference, (2002).

[32] J.L. Urai, W.D. Means, and G.S. Lister, *Dynamic recrystallization of minerals*, Geophys. Monogr., Am. Geophys. Union (1986).

[33] G. Niu, J. Penuelas, L. Largeau, B. Vilquin, J. L. Maurice, C. Botella, G. Hollinger, and G. Saint-Girons, "Evidence for the formation of two phases during the growth of SrTiO<sub>3</sub> on silicon," *Physical Review B*, **vol. 83**, no. 5, p. 054105, Feb. 2011.

[34] F. Calame and P. Muralt, "Gradient free sol-gel Pb(ZrxTi1-x)O<sub>3</sub> thin films," in *2007 Sixteenth IEEE International Symposium on the Applications of Ferroelectric*, 80–82 (2007).

[35] P. Muralt, "Texture control and seeded nucleation of nanosize structures of ferroelectric thin films," *Journal of Applied Physics*, **vol. 100**, no. 5, p. 051605, 2006.

[36] A. Etin, G. E. Shter, S. Baltianski, G. S. Grader, and G. M. Reisner, *Journal of the American Ceramic Society*, **vol. 89**, no. 8, pp. 2387–2393, Aug. 2006.

[37] B. Jaffe, W. R. Cook, and H. Jaffe, *Piezoelectric Ceramics*, 1st edition, Academic Press Inc, London, U.K., 1971.

[38] Florian CALAME (2008), *PZT Thin Film Growth and Chemical Composition Control on Flat and Novel Three-Dimensional Micromachined Structures for MEMS Devices*, Dissertation, Ecole Polytechnique Fédérale de Lausanne, (Thesis N° 3820 (2007))

[39] F. Calame and P. Muralt, "Growth and properties of gradient free sol-gel lead zirconate titanate thin films," *Applied Physics Letters*, **vol. 90**, no. 6, p. 062907, 2007.

[40] P. Muralt, *IEEE transactions on ultrasonics, ferroelectrics, and frequency control* **47**, 903–15 (2000).

[41] Y. L. Tu and S. J. Milne, "Characterization of single layer PZT (53/47) films prepared from an air-stable sol-gel route," *Journal of Materials Research*, **vol. 10**, no. 12, pp. 3222–3231, Mar. 2011.

- [42] F. Calame and P. Muralt, "Growth and properties of gradient free sol-gel lead zirconate titanate thin films," *Applied Physics Letters*, **vol. 90**, no. 6, p. 062907, 2007.
- [43] S. Habouti, A. Lahmar, M. Dietze, C.-H. Solterbeck, V. Zaporozhchenko, and M. Es-Souni, "Substrate heterostructure effects on interface composition, microstructure development and functional properties of PZT thin films," *Acta Materialia*, **vol. 57**, no. 7, pp. 2328–2338, Apr. 2009.
- [44] L. Fè, G. J. Norga, D. J. Wouters, H. E. Maes, and G. Maes, "Chemical structure evolution and orientation selection in sol-gel-prepared ferroelectric  $\text{Pb}(\text{Zr,Ti})\text{O}_3$  thin films," *Journal of Materials Research*, **vol. 16**, no. 09, pp. 2499–2504, Jan. 2011.
- [45] B. E. Watts, F. Leccabue, G. Bocelli, G. Padeletti, S. Kaciulis, and L. Pandolfi, "Lead enrichment at the surface of lead zirconate titanate thin films," *Journal of the European Ceramic Society*, **vol. 25**, no. 12, pp. 2495–2498, Jan. 2005.
- [46] A. Galdi, P. Orgiani, L. Maritato, and L. Méchin, "Correlation between structural properties and resistivity critical behavior in  $\text{SrRuO}_3$  thin films," *J. Phys. Condens. Matter*, **vol. 24**, no. 43, p. 435603, Oct. 2012.
- [47] Q. X. Jia, S. R. Foltyn, P. N. Arendt, J. R. Groves, T. G. Holesinger, M. E. Hawley, and P. Lu, "Role of  $\text{SrRuO}_3$  buffer layers on the superconducting properties of  $\text{YBa}_2\text{Cu}_3\text{O}_7$  films grown on polycrystalline metal alloy using a biaxially oriented  $\text{MgO}$  template," *Applied Physics Letters*, **vol. 81**, no. 24, p. 4571, 2002.
- [48] O. Trithaveesak, J. Schubert, and C. Buchal, "Ferroelectric properties of epitaxial  $\text{BaTiO}_3$  thin films and heterostructures on different substrates," *Journal of Applied Physics*, **vol. 98**, no. 11, p. 114101, 2005.
- [49] R. J. Bouchard and J. L. Gillson, "Electrical properties of  $\text{CaRuO}_3$  and  $\text{SrRuO}_3$  single crystals," *Materials Research Bulletin*, **vol. 7**, no. 9, pp. 873–878, Sep. 1972.
- [50] C. W. Jones, P. D. Battle, P. Lightfoot, and W. T. A. Harrison, "The structure of  $\text{SrRuO}_3$  by time-of-flight neutron powder diffraction," *Acta Crystallographica Section C Crystal Structure Communications*, **vol. 45**, no. 3, pp. 365–367, Mar. 1989.
- [51] C. B. Eom, R. B. Van Dover, J. M. Phillips, D. J. Werder, J. H. Marshall, C. H. Chen, R. J. Cava, R. M. Fleming, and D. K. Fork, "Fabrication and properties of epitaxial ferroelectric heterostructures with ( $\text{SrRuO}_3$ ) isotropic metallic oxide electrodes," *Applied Physics Letters*, **vol. 63**, no. 18, p. 2570, 1993.

- [52] C. B. Eom, R. J. Cava, R. M. Fleming, J. M. Phillips, R. B. Vandover, J. H. Marshall, J. W. Hsu, J. J. Krajewski, and W. F. Peck, "Single-Crystal Epitaxial Thin Films of the Isotropic Metallic Oxides  $\text{Sr}_{1-x}\text{Ca}_x\text{RuO}_3$  ( $0 \leq x \leq 1$ ).," *Science (New York, N.Y.)*, **vol. 258**, no. 5089, pp. 1766–9, Dec. 1992.
- [53] Q. X. Jia, X. D. Wu, S. R. Foltyn, and P. Tiwari, "Structural and electrical properties of  $\text{Ba}_{0.5}\text{Sr}_{0.5}\text{TiO}_3$  thin films with conductive  $\text{SrRuO}_3$  bottom electrodes," *Applied Physics Letters*, **vol. 66**, no. 17, p. 2197, 1995.
- [54] X. D. Wu, S. R. Foltyn, R. C. Dye, Y. Coulter, and R. E. Muenchausen, "Properties of epitaxial  $\text{SrRuO}_3$  thin films," *Applied Physics Letters*, **vol. 62**, no. 19, p. 2434, 1993.
- [55] P. Tiwari, X. D. Wu, S. R. Foltyn, M. Q. Le, I. H. Campbell, R. C. Dye, and R. E. Muenchausen, "Epitaxial  $\text{YBa}_2\text{Cu}_3\text{O}_{7-\delta}$  thin films on  $\text{SrRuO}_3/\text{Pt}/\text{MgO}$ ," *Applied Physics Letters*, **vol. 64**, no. 5, p. 634, 1994.
- [56] S. Y. Hou, J. Kwo, R. K. Watts, J.-Y. Cheng, and D. K. Fork, "Structure and properties of epitaxial  $\text{Ba}_{0.5}\text{Sr}_{0.5}\text{TiO}_3/\text{SrRuO}_3/\text{ZrO}_2$  heterostructure on Si grown by off-axis sputtering," *Applied Physics Letters*, **vol. 67**, no. 10, p. 1387, 1995.
- [57] W. Bensch, "Structure and thermochemical reactivity of  $\text{CaRuO}_3$  and  $\text{SrRuO}_3$ ," *Solid State Ionics*, **vol. 43**, pp. 171–177, Nov. 1990.
- [58] J. C. Jiang, W. Tian, X. Pan, Q. Gan, and C. B. Eom, "Effects of miscut of the  $\text{SrTiO}_3$  substrate on microstructures of the epitaxial  $\text{SrRuO}_3$  thin films," *Materials Science and Engineering: B*, **vol. 56**, no. 2–3, pp. 152–157, Nov. 1998.
- [59] Q. Gan, R. A. Rao, and C. B. Eom, "Control of the growth and domain structure of epitaxial  $\text{SrRuO}_3$  thin films by vicinal (001)  $\text{SrTiO}_3$  substrates," *Applied Physics Letters*, **vol. 70**, no. 15, p. 1962, 1997.
- [60] D. Estève, T. Maroutian, V. Pillard, and P. Lecoeur, "Step velocity tuning of  $\text{SrRuO}_3$  step flow growth on  $\text{SrTiO}_3$ ," *Phys. Rev. B*, **vol. 83**, no. 19, p. 193401, May 2011.
- [61] D. Esteve, T. Maroutian, V. Pillard, G. Agnus, and P. Lecoeur, "Study of 2D growth stability of  $\text{SrRuO}_3$  on  $\text{SrTiO}_3$ ," *J. Phys. Conf. Ser.*, **vol. 303**, p. 012060, Jul. 2011.
- [62] C. Jorel, H. Colder, A. Galdi, and L. Méchin, "Epitaxial PZT thin films on YSZ-buffered Si (001) substrates for piezoelectric MEMS or NEMS applications," *IOP Conf. Ser. Mater. Sci. Eng.*, **vol. 41**, p. 012012, Dec. 2012.

- [63] N. D. Zakharov, K. M. Satyalakshmi, G. Koren, and D. Hesse, "Substrate temperature dependence of structure and resistivity of SrRuO<sub>3</sub> thin films grown by pulsed laser deposition on (100) SrTiO<sub>3</sub>," *Journal of Materials Research*, **vol. 14**, no. 11, pp. 4385–4394, Jan. 2011.
- [64] M. Dekkers, M. D. Nguyen, R. Steenwelle, P. M. te Riele, D. H. A. Blank, and G. Rijnders, "Ferroelectric properties of epitaxial Pb(Zr,Ti)O<sub>3</sub> thin films on silicon by control of crystal orientation," *Applied Physics Letters*, **vol. 95**, no. 1, p. 012902, 2009.
- [65] D. Isarakorn, A. Sambri, P. Janphuang, D. Briand, S. Gariglio, J.-M. Triscone, F. Guy, J. W. Reiner, C. H. Ahn, and N. F. de Rooij, "Epitaxial piezoelectric MEMS on silicon," *Journal of Micromechanics and Microengineering*, **vol. 20**, no. 5, p. 055008, May 2010.
- [66] K. R. Udayakumar, P. J. Schuele, J. Chen, S. B. Krupanidhi, and L. E. Cross, "Thickness-dependent electrical characteristics of lead zirconate titanate thin films," *Journal of Applied Physics*, **vol. 77**, no. 8, p. 3981, 1995.
- [67] L. Lian and N. R. Sottos, "Effects of thickness on the piezoelectric and dielectric properties of lead zirconate titanate thin films," *Journal of Applied Physics*, **vol. 87**, no. 8, p. 3941, 2000.
- [68] Y. Bastani, T. Schmitz-Kempen, A. Roelofs, and N. Bassiri-Gharb, "Critical thickness for extrinsic contributions to the dielectric and piezoelectric response in lead zirconate titanate ultrathin films," *Journal of Applied Physics*, **vol. 109**, no. 1, p. 014115, 2011.
- [69] S. S. Sengupta, S. M. Park, D. a. Payne, and L. H. Allen, "Origins and evolution of stress development in sol-gel derived thin layers and multideposited coatings of lead titanate," *Journal of Applied Physics*, **vol. 83**, no. 4, p. 2291, 1998.
- [70] D. L. Polla, "Microelectromechanical systems based on ferroelectric thin films," *Microelectronic Engineering*, **vol. 29**, no. 1–4, pp. 51–58, Dec. 1995.
- [71] K. Miyazawa, "Structure and expected piezoelectric properties of sol-gel derived multilayer PZT films," *Solid State Ionics*, **vol. 108**, no. 1–4, pp. 85–90, May 1998.
- [72] P. Khaenamkaew, S. Muensit, I. K. Bdikin, and a. L. Kholkin, "Effect of Zr/Ti ratio on the microstructure and ferroelectric properties of lead zirconate titanate thin films," *Materials Chemistry and Physics*, **vol. 102**, no. 2–3, pp. 159–164, Apr. 2007.
- [73] L. Pintilie, M. Lisca, and M. Alexe, "Polarization reversal and capacitance-voltage characteristic of epitaxial Pb(Zr,Ti)O<sub>3</sub> layers," *Applied Physics Letters*, **vol. 86**, no. 19, p. 192902, 2005.

- [74] D. M. Kim, C. B. Eom, V. Nagarajan, J. Ouyang, R. Ramesh, V. Vaithyanathan, and D. G. Schlom, "Thickness dependence of structural and piezoelectric properties of epitaxial  $\text{Pb}(\text{Zr}_{0.52}\text{Ti}_{0.48})\text{O}_3$  films on Si and  $\text{SrTiO}_3$  substrates," *Applied Physics Letters*, **vol. 88**, no. 14, p. 142904, 2006.
- [75] W. L. Warren, B. A. Tuttle, D. Dimos, G. E. Pike, H. N. Al-Shareef, R. Ramesh, J. T. Evans, and J. Jr, "Imprint in Ferroelectric Capacitors," *Japanese Journal of Applied Physics*, **vol. 35**, no. Part 1, No. 2B, pp. 1521–1524, Feb. 1996.
- [76] K. Abe and S. Komatsu, "Ferroelectric properties in epitaxially grown  $\text{Ba}_x\text{Sr}_{1-x}\text{TiO}_3$  thin films," *Journal of Applied Physics*, **vol. 77**, no. 12, p. 6461, 1995.
- [77] W. Liu, J. Ko, and W. Zhu, "Asymmetric switching behavior of  $\text{Ni}/\text{Pb}_{1.1}(\text{Zr}_{0.3}\text{Ti}_{0.7})\text{O}_3/\text{Pt}$  thin films," *Materials Letters*, **vol. 49**, no. 2, pp. 122–126, Jun. 2001.
- [78] T. Lü and W. Cao, "Influence of imperfect surface on properties of ferroelectric thin film," *Microelectronic Engineering*, **vol. 66**, no. 1–4, pp. 818–824, Apr. 2003.
- [79] C. Park and D. Chadi, "Microscopic study of oxygen-vacancy defects in ferroelectric perovskites," *Physical Review B*, **vol. 57**, no. 22, pp. R13961–R13964, Jun. 1998.
- [80] R. Ramesh, H. Gilchrist, T. Sands, V. G. Keramidas, R. Haakenaasen, and D. K. Fork, "Ferroelectric La-Sr-Co-O/Pb-Zr-Ti-O/La-Sr-Co-O heterostructures on silicon via template growth," *Applied Physics Letters*, **vol. 63**, no. 26, p. 3592, 1993.
- [81] M. V. Raymond and D. M. Smyth, "Defect chemistry and transport properties of  $\text{Pb}(\text{Zr}_{1/2}\text{Ti}_{1/2})\text{O}_3$ ," *Integrated Ferroelectrics*, **vol. 4**, no. 2, pp. 145–154, Mar. 1994.
- [82] F. A. Kröger and H. J. Vink, in *Solid State Physics—Advances in Research and Applications*, edited by F. Seitz and T. Turnbull Academic, New York, 1957, **Vol. 3**, pp. 307–435.
- [83] R. L. Holman, "Intrinsic nonstoichiometry in the lead zirconate-lead titanate system determined by Knudsen effusion," *Journal of Applied Physics*, **vol. 44**, no. 12, p. 5227, 1973.
- [84] V. C. Lo, "Modeling the role of oxygen vacancy on ferroelectric properties in thin films," *Journal of Applied Physics*, **vol. 92**, no. 11, p. 6778, 2002.
- [85] L. Pintilie, M. Lisca, M. Alexe, CAS Proc., **vol. 2**, IEEE Catalog No: 04TH8748, Sinaia, Romania, 2004, p. 415.
- [86] M. Sayer, A. Mansingh, A. K. Arora, and A. Lo, "Dielectric response of ferroelectric thin films on non-metallic electrodes," *Integrated Ferroelectrics*, **vol. 1**, no. 1, pp. 129–146, Apr. 1992.

- [87] V. Chivukula, J. Ilowski, I. Emesh, D. McDonald, P. Leung, and M. Sayer, "Dielectric properties of ferroelectric thin films in the frequency range of mHz-GHz," *Integrated Ferroelectrics*, **vol. 10**, no. 1–4, pp. 247–255, Oct. 1995.
- [88] K. R. Udayakumar, P. J. Schuele, J. Chen, S. B. Krupanidhi, and L. E. Cross, "Thickness-dependent electrical characteristics of lead zirconate titanate thin films," *Journal of Applied Physics*, **vol. 77**, no. 8, p. 3981, 1995.
- [89] L. Pintilie, M. Lisca, and M. Alexe, "Polarization reversal and capacitance-voltage characteristic of epitaxial Pb(Zr,Ti)O<sub>3</sub> layers," *Applied Physics Letters*, **vol. 86**, no. 19, p. 192902, 2005.
- [90] R. Moazzami, C. Hu, and W. H. Shepherd, "Electrical characteristics of ferroelectric PZT thin films for DRAM applications," *IEEE Transactions on Electron Devices*, **vol. 39**, no. 9, pp. 2044–2049, 1992.
- [91] L. Pintilie, I. Vrejoiu, D. Hesse, G. LeRhun, and M. Alexe, "Ferroelectric polarization-leakage current relation in high quality epitaxial Pb(Zr,Ti)O<sub>3</sub> films," *Physical Review B*, **vol. 75**, no. 10, p. 104103, Mar. 2007.
- [92] A. Gruverman, "Principles and Applications of Piezoresponse Force Microscopy", CNMS Workshop on Piezoresponse Force Microscopy, Oak Ridge National Laboratory (2007).
- [93] S. Kalinin, E. Karapetian, and M. Kachanov, "Nanoelectromechanics of piezoresponse force microscopy," *Physical Review B*, **vol. 70**, no. 18, p. 184101, Nov. 2004.
- [94] G. A. Salvatore, L. Lattanzio, D. Bouvet, I. Stolichnov, N. Setter, and A. M. Ionescu, "Ferroelectric transistors with improved characteristics at high temperature," *Applied Physics Letters*, **vol. 97**, no. 5, p. 053503, 2010.
- [95] B. S. Sharma, S. F. Vogel, and P. I. Prentky, "Retention in thin ferroelectric films," *Ferroelectrics*, **vol. 5**, no. 1, pp. 69–75, Jan. 1973.
- [96] R. R. Mehta, "Depolarization fields in thin ferroelectric films," *Journal of Applied Physics*, **vol. 44**, no. 8, p. 3379, 1973.
- [97] M. Cruz, Y. Chu, J. Zhang, P. Yang, F. Zavaliche, Q. He, P. Shafer, L. Chen, and R. Ramesh, "Strain Control of Domain-Wall Stability in Epitaxial BiFeO<sub>3</sub> (110) Films," *Physical Review Letters*, **vol. 99**, no. 21, p. 217601, Nov. 2007.

*Chapter III - Integration of epitaxial PZT thin film on Si substrate*

---

---

**Chapter IV - Integration of epitaxial PMN-PT films on Si substrate**

---

---

<b>IV.1) Introduction .....</b>	<b>126</b>	
IV.1.1) Relaxor ferroelectrics .....	126	
IV.1.2) PMN-PT solid solution .....	127	
<b>IV.2) Sol-gel deposition of PMN-PT films on SrTiO<sub>3</sub>/Si(001) .....</b>	<b>130</b>	
IV.2.1) Introduction .....	130	
IV.2.2) Sol-gel deposition of PMN-PT films .....	131	
IV.2.3) Crystalline structure and surface topography .....	132	
IV.2.4) Microstructure of epitaxial PMN-PT films .....		
1	3	4
IV.2.5) Phase transition studied by infrared transmission .....	136	
<b>IV.3) Use of SrRuO<sub>3</sub> as bottom electrode for integration of PMN-PT on Si..</b>	<b>139</b>	
IV.3.1) Structural characterization by XRD .....	139	
IV.3.2) Electrical properties .....	140	
<b>IV.4) Conclusion .....</b>	<b>142</b>	
<b>IV.5) Reference .....</b>	<b>143</b>	

## IV.1) Introduction

### IV.1.1) Relaxor ferroelectrics

Relaxor ferroelectrics with anomalous properties have dramatically promoted piezoelectric performance over ordinary ferroelectric materials. For example, compared with  $\text{Pb}(\text{Zr}_x\text{Ti}_{1-x})\text{O}_3$  (PZT),  $\text{Pb}(\text{Mg}_{1/3}\text{Nb}_{2/3})\text{O}_3\text{-PbTiO}_3$  (PMN-PT), one of the lead-based relaxor ferroelectrics, shows dielectric permittivity that can be 10 to 20 times and piezoelectric coefficients that can be 5 to 10 times larger than those of bulk PZT ceramics. Besides, it has a large electromechanical coupling coefficient of  $k_{33} \sim 0.9$  [1]. Thus, relaxor ferroelectrics could provide superior properties which make them attractive for various high technological applications. These applications involve ferroelectric hysteresis (for non-volatile memories), high permittivity (for capacitors [2, 3]), high piezoelectric effects (for sensors, actuators [4], resonant wave devices [5], and energy harvester [6, 7]), high pyroelectric coefficients (for infrared detectors [8], micro-cooler [9]), strong electro-optic effects (for optical switches [10]) and anomalous temperature coefficients of the resistivity (for overload protection circuits [11]). Compared with Debye-like ferroelectrics, they are featured by diffuse frequency-dependent permittivity maximum with a broad relaxation spectrum and other anomalous temperature-dependent electrical properties [12]. (1) In normal ferroelectrics, dielectric susceptibility shows a Curie-Weiss law behavior at the transition temperature ( $T_c$ ), whereas in relaxor ferroelectrics at the transition temperature ( $T_m$ ) the peak must have a divergence but it is broad and rounded. (2) In relaxor ferroelectrics, there is a strong frequency dependence in the peak position,  $T_m$  as a function of  $\chi'(T)$ . (3) The polarization in normal ferroelectrics goes to zero at  $T_c$  and in relaxor ferroelectrics the polarization extends well beyond  $T_m$ . In Figure IV.1, different properties of normal and relaxor ferroelectrics are summarized for comparison, mainly from electric-field-induced or temperature-dependent polarization, and temperature-dependent dielectric permittivity. The principal mechanism leading to the anomalous properties of the relaxor ferroelectric is the formation of polar nanoclusters in the disordered matrix of the materials, which will develop into macroscopic ferroelectric domains in normal ferroelectric materials. In the following, we will mainly discuss such physical background for relaxor ferroelectrics.

In principle, the mechanism leading to the diversity of the dielectrics can be attributed to the so-called correlation length ( $r_c$ ) which is a temperature-dependent quantity relating to the dipole-dipole interactions [13]. For normal dielectrics, the correlation length is as small as lattice constant, where the dipole polarizes only the region in its immediate vicinity. Thus, normal dielectrics behave like an isolated dipole which can be pictured by Debye equation or its variants [14, 15, 16, 17]. In highly polarizable dielectrics, the presence of a dipolar entity can induce dipoles

within a large correlation length, where the dipolar motion is correlated, leading to the formation of a polar nano-region. In Figure IV.2, the comparison in microstructure is schematically drawn between ordinary and ferroelectric dielectrics [18]. Further, the physical picture of ferroelectricity in Figure IV.2 (b) can be divided into two classes according to  $r_c$  and the mean separation between dipoles ( $r_{ij}$ ) [19]. For those ferroelectrics where  $r_c < r_{ij}$ , spatial randomness of the uncorrelated polar regions suppresses ferroelectric order and a dipolar glass-like (or relaxor) state occurs at low temperature due to some correlations among the nano-regions, i.e. identified as relaxor ferroelectrics. On the contrary, since  $r_c > r_{ij}$  (Figure IV.2 (b)), normal ferroelectrics can undergo a phase transition into ferroelectric order accompanied with spontaneous polarization.

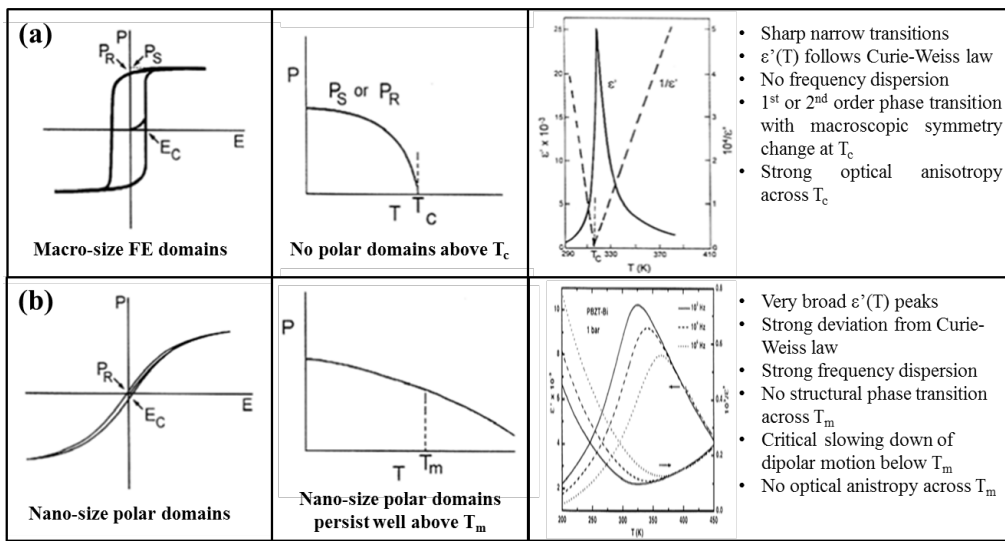


Figure IV.1 - Comparison between normal (a) and relaxor (b) ferroelectrics.

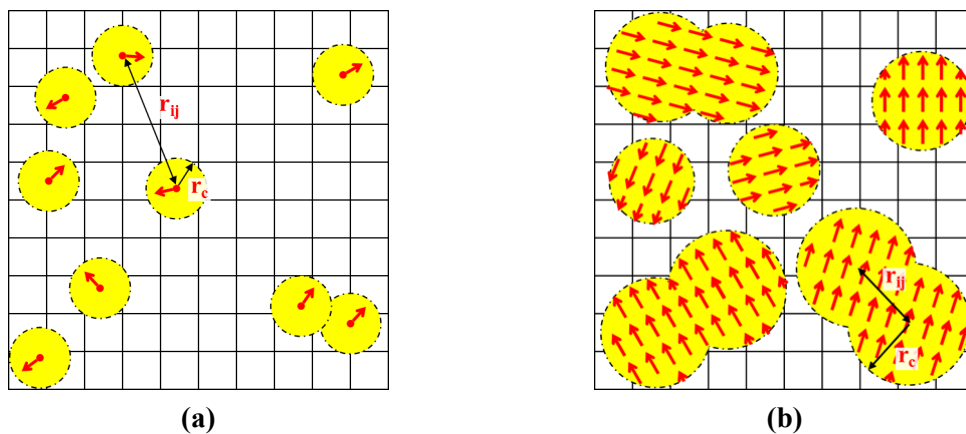


Figure IV.2 - Domain structure of a dipolar entity in a normal dielectric host lattice (a) and in a soft FE mode lattice (b).

With the help of the physical model discussed above, different electrical properties between normal and relaxor ferroelectrics can be understood. First, remnant polarization is small in relaxor ferroelectrics due to the lack of dipole interaction and, therefore, coercive electric field also decreases. With decrease of  $r_c$ , e.g. caused by increase of the temperature, the hysteresis loop of relaxor ferroelectrics approaches that of ordinary dielectrics, i.e. a slim loop, especially for the extreme case where  $r_{ij} \gg r_c$ . This temperature-dependent correlation length will give the phase diagram in Figure IV.3, where  $N^*$  is a characteristic quantity of the relaxor material separating dipolar glass and normal ferroelectrics according to  $r_c$ . Besides, similar to its analogs, i.e. glass materials, relaxor ferroelectrics have not first-order ferroelectric phase transition, like normal ferroelectrics, which will undergo a smooth decrease of field-induced polarization through the so-called dynamic transition temperature ( $T_m$ ). The polarization retains a finite value to rather high temperature due to the fact that nano-size polar domains persist above  $T_m$ . Here, the temperature at which the nano-size polar domains come into existence is called Burns temperature ( $T_d$ ). On the other hand, relaxor ferroelectrics naturally exhibit a diffuse phase transition and strong frequency dispersion in the peak temperature ( $T_m$ ) and the magnitude of permittivity below  $T_m$ . Frequency dispersion in the relaxors is associated with the large distribution in the size of the polar region which is possibly caused by the compositional fluctuations in the materials.

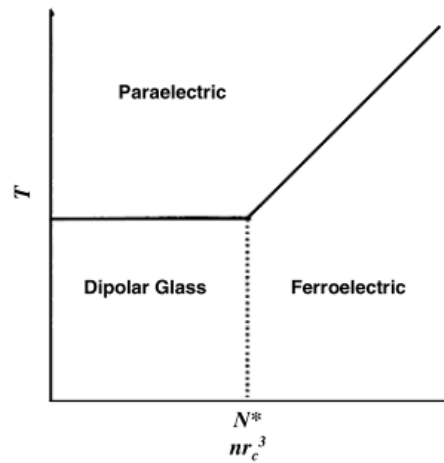


Figure IV.3 - Schematic temperature–dipolar phase diagram showing the relationships between the dipolar glass, ferroelectric and paraelectric phase.

#### IV.1.2) PMN-PT solid solution

$\text{Pb}(\text{Mg}_{1/3}\text{Nb}_{2/3})\text{O}_3$  (PMN) and its derivative PMN-PT are the most extensively studied relaxor ferroelectrics [20, 21, 22] and, therefore, in this chapter we will try to achieve the epitaxial growth of PMN-PT films on Si(001) substrate using  $\text{SrTiO}_3$  (STO) buffer layer. Generally, the

strategy of manufacturing relaxor ferroelectrics is to incorporate ferroelectrically-active materials into dielectric host material in order to introduce dipolar defects. Typical examples include the most commonly used relaxors, such as lead magnesium niobate (i.e. PMN) <sup>[23]</sup>, lead magnesium niobate-lead titanate (i.e. PMN-PT) <sup>[24]</sup>, lead lanthanum zirconate titanate where the La atoms substitute and occupy the site of Pb <sup>[25]</sup>. PMN is a Pb-containing relaxor ferroelectric and has a chemical formula like  $Pb(B'_x B''_{1-x})O_3$ , where B' is the ferroelectrically-inactive cation and B'' is the ferroelectrically-active cation. The 1:2 atomic ratio of B' and B'' in PMN provides the mechanism to form compositional fluctuations away from complete B ordering, leading to the formation of polar region. On the contrary, for those materials, like  $Pb(Sc_{1/2}Ta_{1/2})O_3$ ,  $Pb(Mg_{1/2}W_{1/2})O_3$ , and  $Pb(Yb_{1/2}Nb_{1/2})O_3$  with 1:1 atomic ratio of B' and B'', complete ordering is possible and the relaxor transition is eventually replaced by a normal ferroelectric transition <sup>[26]</sup>. In PMN, two distinct types of ordered domains are identified existing in nanoscale region <sup>[12]</sup>. One type is formed due to the chemical order of 1:1 atomic ratio between B' and B'' caused by compositional fluctuations. Such B':B''=1:1 ordered domains are embedded into the disordered matrix to retain the charge balance, and cannot develop to long-range order. Previous research results show that ordered domains appear in PMN with a size less than 5 nm and a volume fraction less than 30% <sup>[27, 28]</sup>. They also show that another type of ordered domains has local rhombohedral symmetry (*R3m*) with a size less than 10 nm, which is formed by atomic shifts along {111} direction. These atomic shifts nucleate in the cubic matrix on cooling through  $T_d$  and are correlated to form polar nano-regions which give PMN its ferroelectric behavior. The volume and the number of polar nano-regions increase with decrease of the temperature. However, growth of polar nano-regions is inhibited by the chemical order and never coarsens into large domains. Due to the presence of polar nano-regions, PMN shows a broad maximum of dielectric permittivity near 265 K with a huge value ( $\sim 10^4$  at 1 kHz) and other anomalous properties (huge dielectric permittivity  $\sim 10^4$ , giant electrocaloric <sup>[29]</sup> and piezoelectric <sup>[30]</sup> coefficients) useful for various applications. Its electrical properties can be tuned by doping normal ferroelectric materials  $PbTiO_3$  (PT) to enhance the interaction between polar nano-regions. Figure IV.4 shows the phase diagram of PMN solid solution with PT <sup>[31]</sup>, where a morphotropic phase boundary at  $X = 0.3 \sim 0.35$  exists, separating rhombohedral phase (relaxor ferroelectrics) and tetragonal phases (normal ferroelectrics). It is noteworthy that in the region where  $X < 0.3$ , PMN-PT phase undergoes a rhombohedral structure in the nano-regions whose longest body diagonal randomly distributes along eight {111} directions leading to a pseudocubic crystalline structure in the macroscopic measurement, like X-Ray Diffraction (XRD). Dielectric constant increased with Mg and Nb concentration, reaching a maximum at 0.9PMN-0.1PT, with loss tangent values below 0.03. For 0.9PMN-0.1PT at room temperature, the pseudocubic lattice constant is  $4.029 \text{ \AA}$  <sup>[32]</sup>.

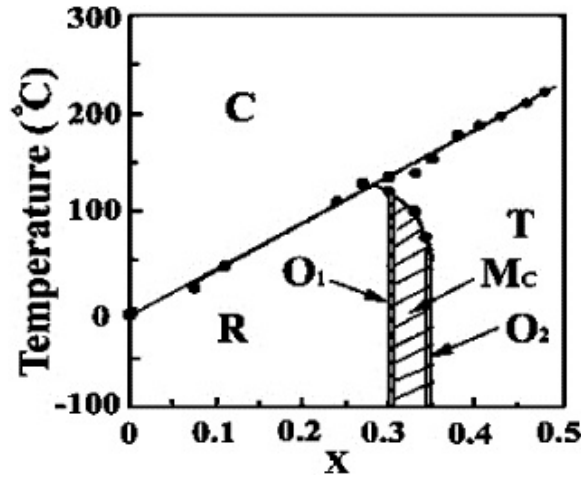


Figure IV.4 - Phase diagram of PMN-PT solid solution ( $X$  is the concentration of PT). C, R, T, M, and O refer to cubic, rhombohedral, tetragonal, monoclinic, and orthorhombic phase regions, respectively.

## IV.2) Sol-gel deposition of PMN-PT films on SrTiO<sub>3</sub>/Si(001)

### IV.2.1) Introduction

Since PMN was first synthesized by Smolenskii and Agranovskaya in the late 1950s<sup>[33]</sup>, various technologies have been developed to deposit PMN and PMN-PT thin films, such as Pulsed Laser Deposition (PLD)<sup>[34]</sup>, sol-gel deposition<sup>[35]</sup>, radio frequency magnetron sputtering<sup>[36]</sup>, Metal Organic Vapor Phase Epitaxy<sup>[37]</sup>. Among those, sol-gel deposition is a competitive one due to its large homogeneity, good stoichiometry, low cost, and compatibility with modern IC fabrication process<sup>[38]</sup>. To meet the system-on-chip requirement, the imperative consideration is to integrate PMN-PT films on Si wafer. The main challenge for the fabrication is the formation of pyrochlore-free PMN-PT<sup>[39,40]</sup>. PMN-PT tends to form a pyrochlore phase under relatively high annealing temperature ( $\sim 850^\circ\text{C}$ ) due to the enhanced interaction of  $\text{Pb}^{2+}$  with  $\text{Nb}^{5+}$ <sup>[41]</sup> and, thus, appropriate selection of annealing temperature should be considered while keeping a complete crystallization. Low reaction temperature to form perovskite PMN-PT can be achieved by adding extra PbO or MgO into the starting materials<sup>[42,43]</sup> and, simultaneously, additional PbO can compensate the loss during thermal annealing. Fan *et al* found that excessive lead can help to eliminate the unwanted pyrochlore phase in sol-gel deposition<sup>[44]</sup>. Another strategy to enhance the relaxor properties of PMN-PT films is derived from the fact that the relaxor properties essentially relates with Mg-O-Nb bonds. The *so-called* columbite method was developed in which Mg-Nb-containing compound is first prepared before reacting with Pb-containing compound to form PMN-PT<sup>[23,45]</sup>. This B-site precursor method was largely extended to the perovskite formation of other relaxor ferroelectrics by Lee *et al*<sup>[46,47]</sup>. Moreover, for sol-

gel method modified precursor solution is often used, in which either new raw materials and solvent are prepared [48, 49, 50, 51] or chemical additives, like catalyst, are involved to promote the formation of perovskite phase, yield a smooth surface, and densify the thin film [52]. For the substrate, platinized Si surface is commonly used in the industry for its good metallic properties and high oxidation resistance. But little success has been achieved in obtaining high quality PMN-PT films due to the formation of pyrochlore phase [53, 54]. Another possibility is a CeO<sub>2</sub>/YSZ terminated Si substrate [55, 56]. However, high fabrication temperature of PMN-PT using PLD prevents its integration with standard IC process. Thus, seeding layer is necessarily inserted between PMN-PT and the substrate to ameliorate the interface and improve the perovskite formation, like PbO [40], PZT [57] and PT [32]. Besides, the effect of seeding layer combined with thermal treatment could influence the crystalline orientation and the textured structure of the film [36, 58]. Researchers found that piezoelectric coefficients and other electrical properties of PMN-PT films are strongly influenced by the c-axis crystalline orientation, i.e. either c-{100} or c-{111} PMN-PT, where c-{100} PMN-PT usually shows better performance [38, 59]. Therefore, for Si monolithic integration, seeding layer on Si surface turns to be a preliminary requirement for high-quality PMN-PT thin films.

Recently, use of STO as buffer layer on Si for the growth of functional materials, like InP [60], PZT [61, 62], has attracted increasing attentions for scientific interests and industrial applications. Having the commensurate crystalline structure with PMN-PT [63, 64], STO is supposed to be an excellent template on Si substrate to avoid the problems mentioned above and yield single crystalline films. On the other hand, epitaxial single crystal oxides have been proven possessing enhanced electrical performance and properties compared to their polycrystalline counterpart [65, 30]. In this section, we tried to deposit 0.9PMN-0.1PT films using sol-gel method on STO-terminated Si(001) substrate to obtain single crystal PMN-PT films. Then, SRO layer was added into the stack as bottom electrode, which allows us to perform electrical measurements on PMN-PT films.

#### **IV.2.2) Sol-gel deposition of PMN-PT films**

PMN-PT films were deposited on STO-terminated Si(001) substrate using the similar sol-gel process as we employed for PZT deposition (Figure IV.5). PMN-PT precursor solution mainly consists of several metalorganic compounds which are dissolved in 1-butanol (C<sub>4</sub>H<sub>10</sub>O) solvent, such as lead acetate trihydrate (Pb(CH<sub>3</sub>COO)<sub>2</sub>·3H<sub>2</sub>O), magnesium acetate tetrahydrate (Mg(CH<sub>3</sub>COO)<sub>2</sub>·4H<sub>2</sub>O), niobium pentaethoxide (Nb<sub>2</sub>(OC<sub>2</sub>H<sub>5</sub>)<sub>10</sub>), and titanium tetra-isopropoxide (Ti{OCH(CH<sub>3</sub>)<sub>2</sub>}<sub>4</sub>). Except for extra 10wt% Pb, atomic ratio of Pb:Mg:Nb:Ti is chosen as 100:30:60:10 for 0.9PMN-0.1PT solid solution due to its high dielectric constant and

outstanding electrostriction coefficients near room temperature<sup>[66]</sup>. Extra lead is added in order to compensate the loss during thermal treatment. During the fabrication, STO/Si substrate was first cleaned by acetone and ethanol and then dried by nitrogen flux. Spin-coating process at 1500 rpm for 20 sec was performed to spread the solution onto STO/Si substrate. Coated sol film was then dried at 130°C for 150 seconds and pyrolyzed at 350°C for 150 seconds in air. Finally, the pyrolyzed film was annealed at 650°C for 1 min in pure oxygen flux by Rapid Thermal Annealing (RTA). The thickness of *as-grown* PMN-PT film by 1 spin-coating was around 90 nm, larger than that of PZT film (70 nm) for the same fabrication condition. The larger thickness of the PMN-PT film can be attributed to the high viscosity of the sol-gel solution than that of the PZT one.

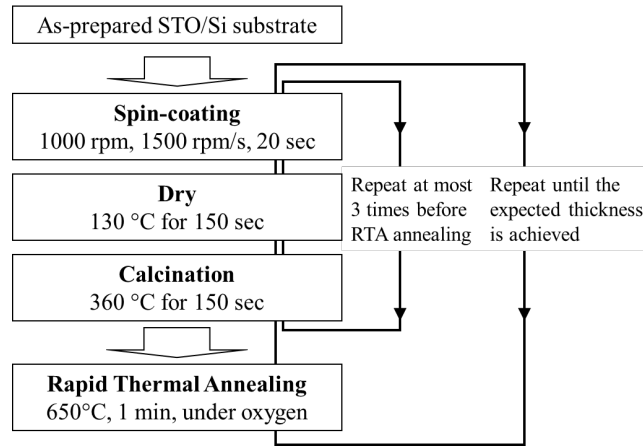


Figure IV.5 - Sol-gel fabrication process used in this thesis to grow PMN-PT films on STO/Si(001) substrate.

### IV.2.3) Crystalline structure and surface topography

Figure IV.6 shows the out-of-plane  $2\theta/\omega$  XRD on PMN-PT(90 nm)/STO(34 nm)/Si(001) stack from  $2\theta = 40^\circ$  to  $75^\circ$ . Only (00 $l$ ) Bragg reflections with sharp peak for PMN-PT and STO layers are observed, indicating that the PMN-PT film is epitaxially grown on STO/Si(001) substrate without pyrochlore phase and other preferential crystallographic orientations. Gaussian fit on the (002) peaks shows that the c-axis lattice constant is 4.016 Å for PMN-PT and 3.896 Å for STO. The in-plane  $2\theta/\omega$  XRD (not shown) shows an a-axis lattice constant of 4.064 Å for PMN-PT and 4.026 Å for STO. Compared with the bulk PMN-PT ( $c = 4.029$  Å), our epitaxial PMN-PT film undergoes a tensile stress which is likely induced by the thermal treatment. Besides, small FWHM value ( $\sim 0.52^\circ$ ) of the rocking curve on PMN-PT (002) Bragg peak attests for a high-quality epitaxial thin film. XRD pole figure was performed on PMN-PT{202} and Si{202} Bragg peaks (the inset images in Figure IV.6), showing a 4-folded central symmetry for both PMN-PT and Si. This indicates a uniform crystalline orientation of PMN-PT on Si(001)

substrate, which is coherent with the result of the  $2\theta/\omega$  XRD. The pole figure of PMN-PT{202} rotates by  $45^\circ$  relatively to that of Si{202}, which is required by the nature of epitaxy to decrease the lattice mismatch between PMN-PT and Si. Therefore, the relationship of crystallographic orientations in the heterostructure is deduced as  $[110]$  PMN-PT (001) //  $[110]$  STO (001) //  $[100]$  Si (001).

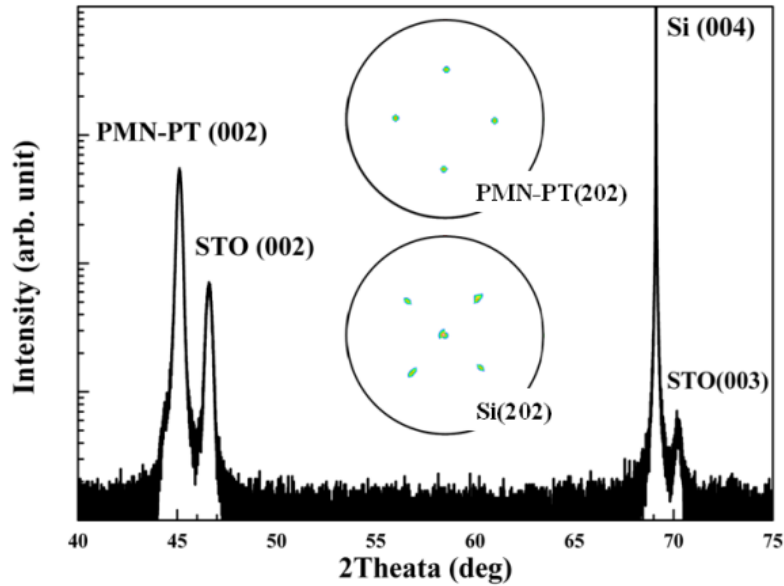


Figure IV.6 -  $2\theta/\omega$  XRD measurement on PMN-PT/STO/Si(001) stack. The inset shows the pole figure characterization on PMN-PT{202} and Si{202}.

In Figure IV.7, the detailed crystalline structure of the PMN-PT film is measured by Reciprocal Space Mapping from  $2\theta = 42^\circ$  to  $70^\circ$  with the  $\Omega$  range of  $\pm 3.5^\circ$ . The range of the mapping spans from PMN-PT(002) to STO(003) peaks, visualizing a symmetrical pattern about the normal direction of the film surface. Similar to the result of the  $2\theta/\omega$  XRD, no other preferential crystalline orientation and meta-phase is observed. The in-plane mapping on PMN-PT(110) in Figure IV.7 (b) shows a reciprocal spot with circular symmetry, indicating a pure perovskite phase with single crystalline structure in the PMN-PT film.

Surface topography at nanoscale was observed by Atomic Force Microscopy (AFM) on the PMN-PT film, as shown in Figure IV.8 on an image of  $5 \times 5 \mu\text{m}^2$  area. The surface roughness was estimated through its root-mean-square value equal to 2.9 nm for this image size. The surface can be described as formed by nano-scaled island-like specks of average size 100 nm. No clear evidence of crystalline grain boundaries and surface defects was observed.

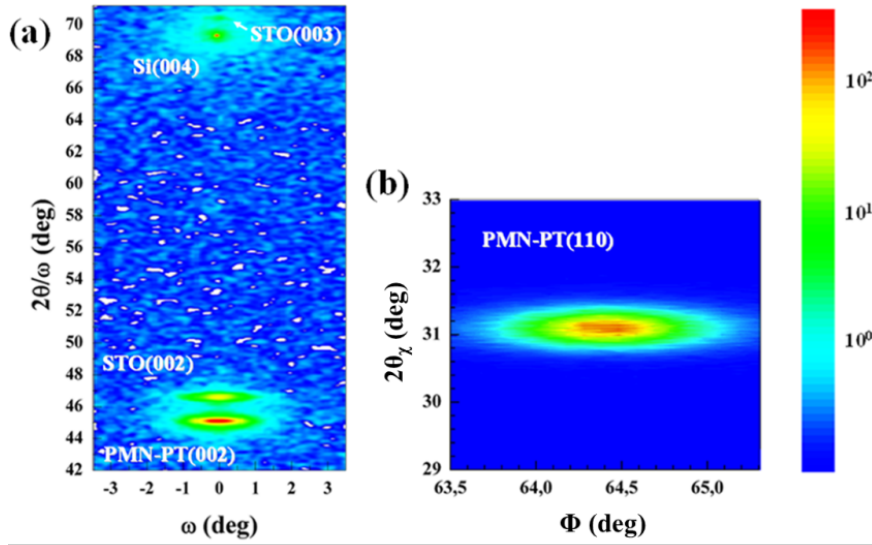


Figure IV.7 - XRD reciprocal space mapping on PMN-PT/STO/Si. (a) The out-of-plane direction ranged from  $2\theta=42^\circ$  to  $70^\circ$  with  $\Omega$  range of  $\pm 3.5^\circ$  and (b) The in-plane region around PMN-PT(110) Bragg spot.

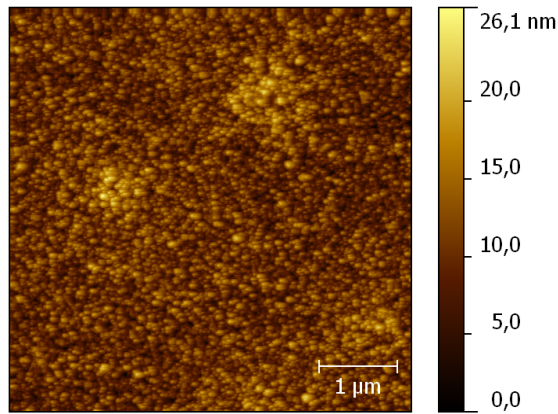


Figure IV.8 - Surface topography of as-grown PMN-PT film within  $5 \times 5 \mu\text{m}^2$  area.

#### IV.2.4) Microstructure of epitaxial PMN-PT film

High-Resolution Transmission Electron Microscopy (HR-TEM) characterization was carried out on PMN-PT/STO/Si(001) stack from Si(110) cross-section for observing its microscopic structure. Figure IV.9 shows two TEM images at the magnifications of 20k and 200k, respectively. Similar to PZT samples, a 5.7nm-thick  $\text{SiO}_2$  layer is formed between STO and Si layers due to oxidation during the thermal treatment of PMN-PT film. The thickness of PMN-PT film is about 90.6 nm, and that of STO is about 34.1 nm. Si substrate shows no additional feature on the background contrast of its lattice matrix, indicating that the diffusion of

metals into Si substrate is negligible owing to STO buffer layer. The fluctuation of TEM contrast in PMN-PT and STO mainly results from the subgrains, whose average size is about 107 nm for PMN-PT layer and 20 nm for STO layer. The smoothness of PMN-PT surface is disturbed near the subgrain boundaries, which can be also observed in the AFM topography as the surface specks. The inset image of Figure IV.9 (a) shows the electron diffraction of the whole stack. Ignoring Si substrate, only one set of reciprocal lattice is observed for PMN-PT or STO. Moreover, the circular symmetry of PMN-PT(002) spot with no splitting indicates that the whole observed PMN-PT layer is single crystalline. In addition to the fundamental perovskite reflections, no extra reciprocal spot appears at the  $\{h+1/2, k+1/2, l+1/2\}$  positions which would arise from chemical ordering of the B cations. It indicates that the epitaxial PMN-PT film has no trace of the ordered domains, like the Mg:Nb = 1:1 nano-cluster, at room temperature. The presence of the subgrains in the PMN-PT film with tiny tilt angle has no effect on the TEM image and does not interrupt the continuity of the crystalline lattice but still contributes to the spread width of rocking curve, i.e. mosaicity of the thin film. TEM image in Figure IV.9 (b) at the magnification of 200k reveals a commensurate PMN-PT/STO interface. Misfit dislocations and lattice deformation of PMN-PT are not observed in the image. The inset image shows the Fourier transform from the selective PMN-PT layer. The uniformity of the PMN-PT reciprocal lattice again confirms a single crystalline structure. The lattice constants derived from the electron diffraction are  $a = 4.01 \text{ \AA}$ ,  $c = 4.04 \text{ \AA}$  for PMN-PT and  $a = 3.89 \text{ \AA}$ ,  $c = 3.91 \text{ \AA}$  for STO. Since both PMN-PT and STO films recover their bulk lattice constants, it is believed that the discrepancy of the lattice constant between TEM and XRD results is attributed to the thinning process during TEM cross-section preparation<sup>[67]</sup>.

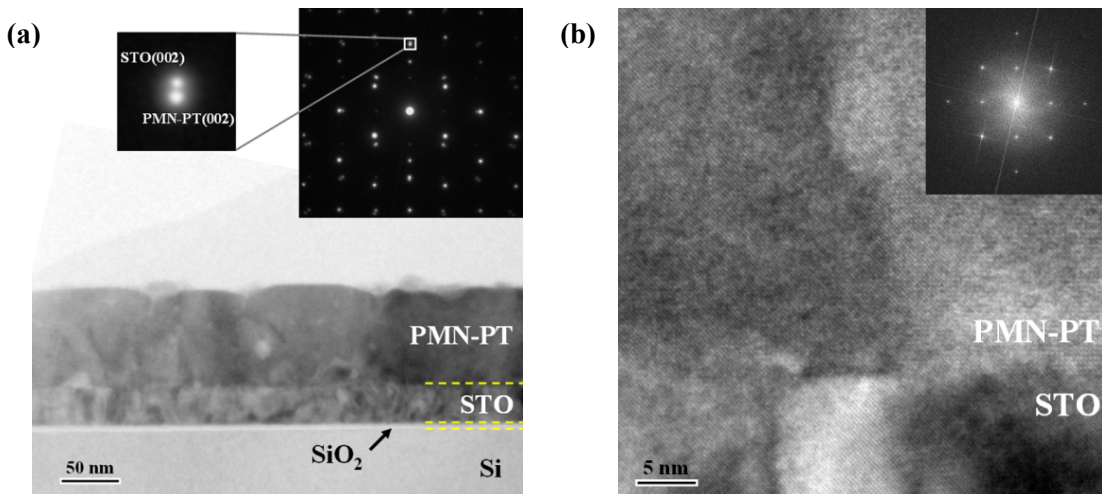


Figure IV.9 - TEM images of the PMN-PT/STO/Si(001) stack on Si(110) cross-section with the magnification of (a)  $\times 20k$  and (b)  $\times 200k$ . Image (c), the Fourier transform from (a), shows single crystalline in reciprocal space. Image (d) shows the TEM diffraction on the whole stack.

#### IV.2.5) Phase transition studied by infrared transmission

Lattice dynamics of our epitaxial PMN-PT film was studied by infrared transmission spectroscopy at varying temperature. Infrared spectrum is widely used to measure structural or molecular characteristics of the material since the electrical interaction between the characteristic phonon in the sample material and the incident infrared photon gives rise to the resonance frequency in the absorbance<sup>[68, 69]</sup>. This experiment was performed at AILES (Advanced Infrared Line Exploited for Spectroscopy) infrared beamline in SOLEIL synchrotron using a Bruker E55 Fourier transform spectrometer with resolution of 1 cm<sup>-1</sup> and a liquid N<sub>2</sub> cooled bolometer that covers the 20 - 1000 cm<sup>-1</sup> spectral region. PMN-PT film grown on STO-Si template and the STO-Si template itself were characterized at various temperatures by IR transmission since silicon is transparent in the IR wavelength range. Figure IV.10 shows the infrared transmission spectra of an epitaxial 90nm-thick 0.9PMN-0.1PT film grown on STO/Si(001) substrate at the selected temperatures from 5 K to 385 K. Contribution of the STO/Si substrate to the infrared transmittance, which was also measured, is retracted from the PMN-PT/STO/Si result. The measurement spans from 20 cm<sup>-1</sup> to 700 cm<sup>-1</sup> in wavenumber with normal specular transmission through the flat planar film surface, i.e. along Si(001) direction. In principle, infrared transmittance can be transformed to the linear absorption coefficient ( $\alpha$ ) which is an intrinsic parameter of the material and relates to the complex dielectric permittivity ( $\varepsilon = \varepsilon' - i\varepsilon''$ ). In all cases, the complex permittivity can be obtained in a standard way by the Kramers–Kronig analysis of broad-enough frequency range of infrared spectrum<sup>[70]</sup>. In practice, a more accurate and convenient method is to use simple physically acceptable models for the dielectric function  $\varepsilon(\omega)$  and fit them directly to the infrared spectrum. The so-called Drude-Lorentz model and its derivatives were proposed to express the dielectric function as the sum of damped quasi-harmonic oscillators in the following form<sup>[71]</sup>.

$$\varepsilon(\omega) = \varepsilon' - i\varepsilon'' = \varepsilon_{\infty} + \sum_i \frac{\omega_{pi}^2}{\omega_{0i}^2 - \omega^2 + i\gamma_i\omega} \quad \text{Equ. IV.1}$$

where  $\omega_{pi}$ ,  $\omega_{0i}$  and  $\gamma_i$  denote the plasma frequency, the transverse optical (TO) eigenfrequency and the line width (scattering rate) of the  $i$ -th Lorentz oscillator.  $\varepsilon_{\infty}$  is the high-frequency dielectric constant representing the contribution of all oscillators at very high frequencies. For our PMN-PT film, the fitting result of Drude-Lorentz model using least-square method are shown in Figure IV.10 (solid lines) and the experimental spectra are shown by circular dots. Moreover, Figure IV.11 exhibits the complex dielectric permittivity deduced from the best fitting of the results.

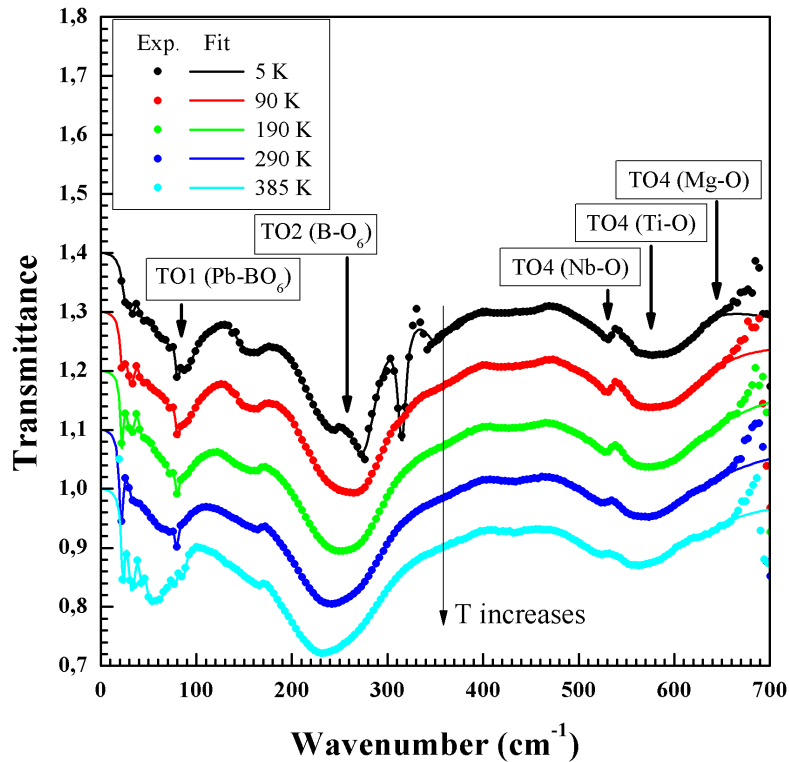


Figure IV.10 - Infrared transmission spectra of the epitaxial 90nm-thick 0.9PMN-0.1PT film at selected temperatures from 5 K to 385 K. The experimental data is shown by circular dots and the fitting result is shown by solid lines. The spectra are shifted in y-axis for better visualization. Characteristic regions are indicated with the related chemical bond, where the B site represents the Nb or Ti atom. The peak around 320  $\text{cm}^{-1}$  on the measurement performed at 5K is due to the presence of dopants inside the silicon (vibration signature).

According to group analysis, there are three active infrared bands for a simple perovskite structure  $\text{ABO}_3$  ( $Pm3m$ ), i.e. (i) Last mode: A-cation oscillation against  $\text{BO}_6$ -octahedra framework (TO1)<sup>[72]</sup>, (ii) Slater mode: mutual B- $\text{O}_6$  oscillations<sup>[73]</sup>, (iii) Axe mode: the bending of the  $\text{O}_6$  octahedra (TO4)<sup>[74]</sup>. An additional fourth mode is related to B'-B'' vibrations for ordered  $\text{A}(\text{B}'_{1/2}\text{B}''_{1/2})\text{O}_3$  ( $\text{Fm}\bar{3}\text{m}$ )<sup>[75]</sup>. Compared with PMN at room temperature<sup>[76]</sup>, admixture of 10% PT in our epitaxial 0.9PMN-0.1PT film result in an increase in the TO1 ( $55 \text{ cm}^{-1} \sim 71 \text{ cm}^{-1}$ ) and TO2 ( $216 \text{ cm}^{-1} \sim 238 \text{ cm}^{-1}$ ) frequencies and decrease in the TO4 ( $569 \text{ cm}^{-1} \sim 561 \text{ cm}^{-1}$ ) frequency at the same temperature. Temperature-dependent frequency shift of TO1 band is clearly seen from  $90.0 \text{ cm}^{-1}$  at 5 K to  $52.6 \text{ cm}^{-1}$  at 385 K, indicating a ferroelectric soft mode towards the Burns temperature ( $T_d$ ) from the lowest temperature. The relevant softening temperature should be much higher than the ferroelectric transition temperature<sup>[77]</sup>, namely around  $T_d$  where the polar nano-regions begin to appear<sup>[78]</sup>. Beside, an underdamped band with sharp peak permanently occurs at  $79.4 \text{ cm}^{-1}$  at all the temperatures. In TO2 mode, the bands slightly shift to

the lower frequency towards the high temperature suggesting an increase of the interatomic bond length, i.e. thermal expansion. Three peaks at  $275\text{ cm}^{-1}$ ,  $316\text{ cm}^{-1}$ ,  $343\text{ cm}^{-1}$  have pronounced intensity in the 5 K spectrum, which gradually decrease with increase of the temperature and become negligible above 70 K. Related to the B'-B'' vibrations, they are specific for the ordered structure in the PMN-PT film and give a measure of the overall degree of order (including short range order) [75]. In the disordered sample at elevated temperature, this mode becomes weaker and broader. Since the ferroelectric soft mode always happens, the appearance of these three peaks likely indicates a local ferroelectric transition at 70K. At high frequency from  $470\text{ cm}^{-1}$  to  $700\text{ cm}^{-1}$ , the band is associated to (Nb-O), (Ti-O), and (Mg-O) TO4 stretching modes in the PMN-PT structure [79]. Moreover, the presence of some additional weak infrared modes, essentially at  $157\text{ cm}^{-1}$  and  $430\text{ cm}^{-1}$ , which slowly disappear upon heating might be connected with the appearance of 3 different atoms in the B sites or the polar clusters in the paraelectric phase [80].

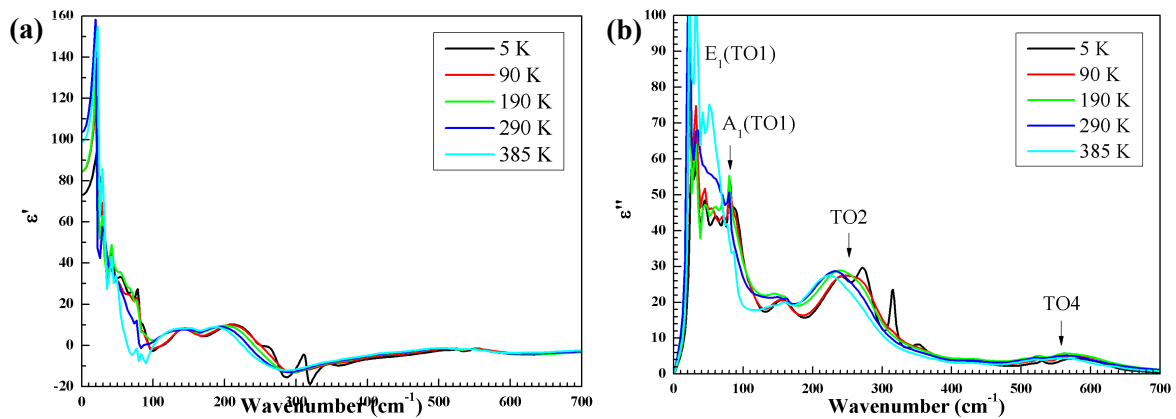


Figure IV.11 - Dielectric permittivity and loss spectra of epitaxial 0.9PMN-0.1PT film obtained from the fits of infrared transmittance in Figure IV.10 using Drude-Lorentz model.

Real dielectric permittivity ( $\epsilon'$ ) in Figure IV.11 (a) shows a strong dispersion. The static permittivity, i.e.  $\epsilon'$  at  $0\text{ cm}^{-1}$ , is about 100 for 0.9PMN-0.1PT, which is much lower than the experimental value of the bulk counterpart ( $10^3 \sim 10^4$ ). Low static permittivity is possibly attributed to the absence of an additional dispersion below the phonon range, which comes from fluctuations of polar nanoregions [81]. On the other hand, the residual stress of the PMN-PT thin film could be another source to the decrease of the low static permittivity. Again, the mode in the  $270\text{-}350\text{ cm}^{-1}$  range correlates a high-degree ordered structure in the PMN-PT film below 70K. In Figure IV.11 (b), TO1 mode is split into  $A_1$  and  $E$  symmetry for rhombohedral phase. The dielectric loss ( $\epsilon''$ ) clearly shows a decrease of  $A_1(\text{TO1})$  frequency towards the high temperature, indicating a ferroelectric soft mode.

### IV.3) Use of SrRuO<sub>3</sub> as bottom electrode for integration of PMN-PT on Si

To study the electrical properties, epitaxial PMN-PT film was grown on STO/Si(001) using PLD deposited SRO as bottom electrode. 270nm-thick PMN-PT film was obtained by performing 3 cycles of spin-coating, drying, and calcination as we used in Section IV.2.2. RTA was performed after these 3 cycles to crystallize the amorphous PMN-PT film. In the following, we present the crystalline and electrical properties of the PMN-PT(270 nm)/SRO(21.0 nm)/STO(12.1 nm)/Si(001) stack.

#### IV.3.1) Structural characterization by XRD

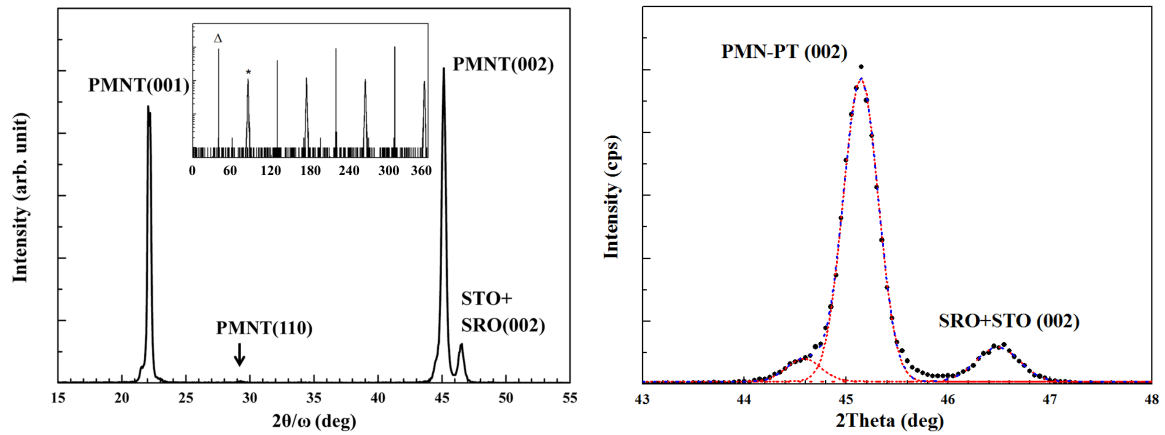


Figure IV.12 - Out-of-plane  $2\theta/\omega$  XRD of the as-grown PMN-PT film on SRO/STO/Si(001) substrate. The inset in the left image is the  $\phi$  scan XRD on PMN-PT{202} (\*) and Si{404} ( $\Delta$ ), respectively. The right image shows the Gaussian fit on PMN-PT (002) and SRO/STO(002) Bragg peaks.

In Figure IV.12, out-of-plane  $2\theta/\omega$  XRD shows that the epitaxial PMN-PT film has only (001) crystalline orientation normal to the film surface with a very slight trace of PMN-PT(110) domain in the film. Epitaxy of the PMN-PT film on SRO/STO/Si(001) is confirmed by  $\Phi$  scan XRD (inset image). The relationship of the crystalline orientations derived from the  $\Phi$  scan XRD is  $[110]$  PMN-PT (001) //  $[110]$  SRO (001) //  $[110]$  STO (001) //  $[100]$  Si (001) for PMN-PT/SRO/STO/Si(001) heterostructure. Gaussian fit of PMN-PT(002) Bragg peak exhibits two PMN-PT phases in the film, where the c-axis lattice constants are 4.062 Å and 4.014 Å. The latter one with smaller c-axis lattice constant takes the most volume of the film. Compared with the 90nm-thick film on STO/Si, this 270nm-thick PMN-PT film likely involves phase segregation along the film thickness. It is assumed that the part near the substrate is constrained by the tensile stress due to the thermal treatment, leading to a smaller c-axis lattice constant, and the part near the top surface has a larger c-axis lattice constant due to the relaxation of the tensile stress. On the

contrary, only one lattice constant (4.016 Å) appears in the 90nm-thick PMN-PT film, which is similar to that of the part near the substrate in the 270nm-thick PMN-PT film. Thus, the tetragonality of the PMN-PT crystalline lattice is enhanced with increase of the film thickness. In addition, the crystalline structure of the SRO/STO film having the c-axis lattice constant of 3.904 Å is fully relieved on Si substrate.

### IV.3.2) Electrical measurement

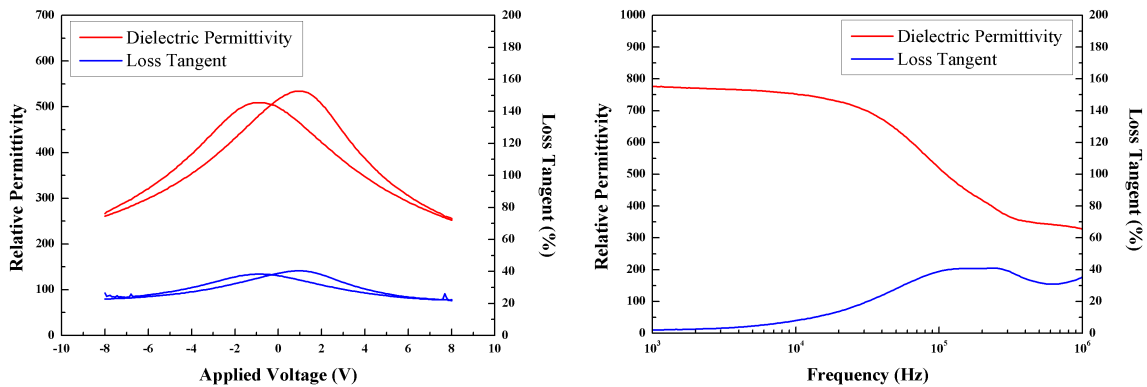


Figure IV.13 – Electrical impedance of Ru/PMN-PT/SRO/STO/Si capacitor as a function of dc bias at 100 kHz (left) and ac frequency (right), which is measured in C<sub>p</sub>-D mode.

Electrical measurements were performed on the Ru/PMN-PT/SRO/STO/Si stack using a thin-film capacitor with a size of 100×100 μm<sup>2</sup> and a PMN-PT film thickness of 270 nm at room temperature. In Figure IV.13, dielectric permittivity and loss of the PMN-PT films are shown as a function of dc bias at 100 kHz and ac frequency, where the measurement was carried out in C<sub>p</sub>-D mode. In the C-V curve, butterfly-like hysteresis loop is clearly observed, indicating a typical ferroelectric behavior. Compared with the bulk counterpart, PMN-PT thin film capacitor exhibits a low dielectric permittivity (< 800) in the whole range of either dc bias or ac frequency. The degraded dielectric permittivity of the thin relaxor ferroelectrics film is likely attributed to the impact of the residual stress which is developed due to thermal treatment and lattice mismatch [82]. Between PMN-PT films of 90 nm and 270 nm thickness, a tensile stress is developed in the film and gradually relaxed with increase of the film thickness. On the other hand, the average mismatch stress could be transformed into a non-uniform (chemically disordered) stress when the film is cooled down through the phase transition, and thus impacts the relaxor properties of the PMN-PT film. The amplitude of such non-uniform stress can be related to the peak spreading of the rocking curve and increases with decrease of the film thickness. The larger amplitude of the non-uniform stress corresponds to larger film stiffness which is proportional to the relative permittivity of the clamped film. Thus, it is possible to explain the low dielectric permittivity of

our 270nm-thick epitaxial PMN-PT thin film. Moreover, decrease of dielectric permittivity with increase of ac frequency is observed in C-f measurement. It is likely due to the small resonance frequency of this non-uniform state which contributes less to the dielectric response at high frequency. Large dielectric loss of the PMN-PT film (~40%) is measured at high frequency. Except for the contribution of film defects, like oxygen vacancies, Pb deficiency, etc., such non-uniform state with large film stiffness possibly leads to the high energy dissipation during the polarization reversal at high frequencies.

Figure IV.14 shows the electric-field-induced polarization of the epitaxial PMN-PT film measured using Sawyer-Tower circuit at 500 Hz. Generally, slim hysteresis loop indicates relaxor-like behavior since no preferentially oriented polarization occurs at zero electric field while the wide one indicates ferroelectric-like behavior<sup>[83]</sup>. For the hysteresis loop with small opening in the figure, our epitaxial PMN-PT film likely acts as a one between a pure relaxor and a normal ferroelectrics. The loop widening could be related to the presence of the self-polarization<sup>[84]</sup>. The origin of the self-polarization could be related to the inhomogeneous distribution of space charges through the film, charge concentration at the film-electrode interface, or internal fields which is caused by Schottky barrier at the film-electrode interface<sup>[85]</sup>. Thus, the charge gradient induced in the film could result in preferentially-oriented polar nano-regions which would give rise to the ferroelectric effect. Moreover, the non-negligible leakage current in the measurement probably also attributes to the widened hysteresis loop.

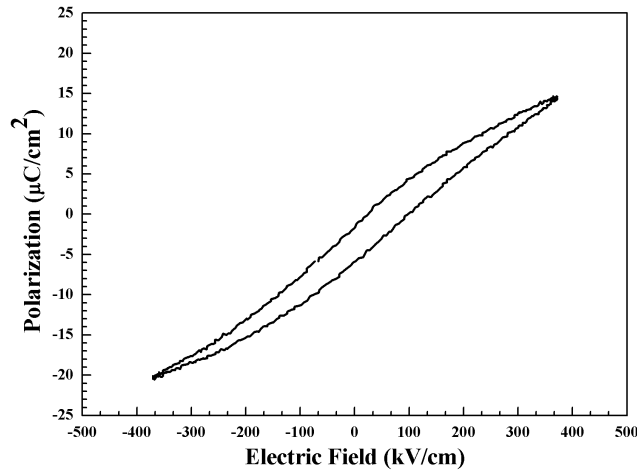


Figure IV.14 - Polarization hysteresis loop measured at 500 Hz for the epitaxial PMN-PT film.

Moreover, temperature-dependent dielectric permittivity  $\epsilon(T)$  was measured from 5 K to 450 K at 1 kHz, 10 kHz, and 100 kHz (Figure IV.15). The epitaxial PMN-PT film has no feature of relaxor ferroelectrics which clearly show a diffused frequency-dependent  $T_m$  and only a slow

transition of dielectric permittivity occurs in a large range of temperature. This is possibly coherent with the ferroelectric soft mode observed in the infrared transmission on the thinner PMN-PT film. Another phenomenon related to the appearance of the local ferroelectric transition likely does not affect the dielectric permittivity or slightly relates with the inflection point of the permittivity function at around 70 K.

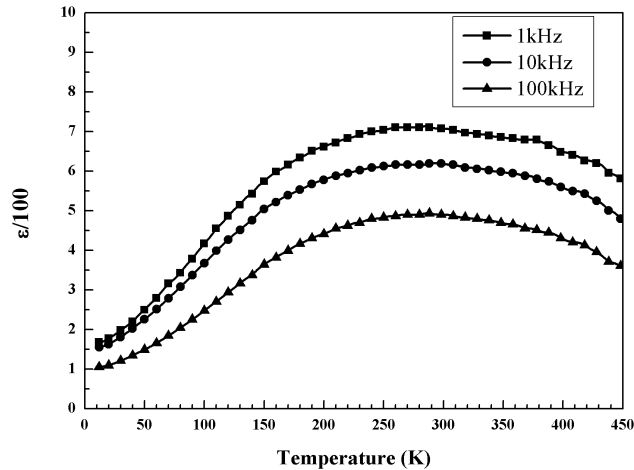


Figure IV.15 - Temperature-dependent dielectric permittivity measured at different ac frequency.

#### IV.4) Conclusion

Although it is difficult to achieve sol-gel deposition of a pure perovskite PMN-PT film on Si due to its complex chemical composition, our strategy using STO buffer layer and SRO bottom electrode successfully attains a single crystalline 0.9PMN-0.1PT film without pyrochlore phase on Si(001) substrate. XRD characterization confirms an epitaxial PMN-PT film on either STO/Si(001) or SRO/STO/Si(001) substrate, which undergoes an in-plane tensile stress and thus has a smaller c-axis lattice constant compared to the bulk one. No TEM evidence supports the presence of any superlattice structure, i.e. chemical ordering structure, in the 90nm-thick PMN-PT film at room temperature. However, temperature-dependent infrared transmission shows a clear softening process towards the high temperature in the 5 K ~ 385 K range and a local ferroelectric transition occur at around 70 K. No feature of relaxor ferroelectrics is observed in the temperature-dependent electrical measurement. Since large tensile stress occurs in the epitaxial single crystal PMN-PT film caused by the clamping effect of Si substrate, the effect of elastic stress is likely responsible for the anomalous behavior and should extract profound experimental researches on those phenomena. In addition, based on our tentative experiments in this thesis, further optimization and characterizations are still required to enhance the film quality of sol-gel PMN-PT film and perform systematical study on the variety of the effects. The similar

research performed on single crystal PMN-PT, polycrystalline PMN-PT film, or the film based on oxide substrates should be carefully studied for single crystalline PMN-PT film on Si substrate, such as strain effect <sup>[81, 86]</sup>, morphotropic boundary <sup>[87]</sup>, chemical composition <sup>[88]</sup>, bottom electrode <sup>[89]</sup>, and so on. Especially for sol-gel deposition, chemical profile and homogeneity of the epitaxial film are closely related to the growth condition, which thus influences various characteristics of the PMN-PT film. Moreover, single crystalline PMN-PT film grown on Si needs to be extensively developed and studied for diverse electronic devices. New applications might be discovered due to its high electrical performance and anomalous microscopic structure.

#### **IV.5) Reference**

- 
- [1] S.-E. Park and T. R. Shrout, "Ultrahigh strain and piezoelectric behavior in relaxor based ferroelectric single crystals," *Journal of Applied Physics*, **vol. 82**, no. 4, p. 1804, 1997.
- [2] N. Ortega, A. Kumar, J. F. Scott, D. B. Chrisey, M. Tomazawa, S. Kumari, D. G. B. Diestra, and R. S. Katiyar, "Relaxor-ferroelectric superlattices: high energy density capacitors.," *Journal of physics. Condensed matter : an Institute of Physics journal*, **vol. 24**, no. 44, p. 445901, Nov. 2012.
- [3] U. Syamaprasad and A. Nair, "Multilayer capacitor ceramics in the PMN-PT-BT system: effect of MgO and 4PbO·B<sub>2</sub>O<sub>3</sub> additions," *Journal of Materials Science: Materials in Electronics*, **vol. 8**, pp. 199–205, 1997.
- [4] F. Y. Lee, S. Goljahi, I. M. McKinley, C. S. Lynch, and L. Pilon, "Pyroelectric waste heat energy harvesting using relaxor ferroelectric 8/65/35 PLZT and the Olsen cycle," *Smart Materials and Structures*, **vol. 21**, no. 2, p. 025021, Feb. 2012.
- [5] Q. Zhang, J. Zhai, and L. B. Kong, "Relaxor Ferroelectric Materials for Microwave Tunable Applications," *Journal of Advanced Dielectrics*, **vol. 02**, no. 01, p. 1230002, Jan. 2012.
- [6] Q.-M. Wang, "Piezoelectric Energy Harvesting using Single Crystal Pb(Mg<sub>1/3</sub>Nb<sub>2/3</sub>)O<sub>3</sub>-xPbTiO<sub>3</sub> (PMN-PT) Device," *Journal of Intelligent Material Systems and Structures*, **vol. 20**, no. 5, pp. 559–568, Nov. 2008.
- [7] A. Mathers, K. Moon, and J. Yi, "A vibration-based PMN-PT energy harvester," *Sensors Journal, IEEE*, **vol. 9**, no. 7, pp. 731–739, 2009.

- [8] S. E. Aleksandrov, G. a. Gavrilov, a. a. Kapralov, E. P. Smirnova, G. Y. Sotnikova, and a. V. Sotnikov, "Relaxer ferroelectrics as promising materials for IR detectors," *Technical Physics*, **vol. 49**, no. 9, pp. 1176–1180, Sep. 2004.
- [9] L. Shaobo and L. Yanqiu, "Research on the electrocaloric effect of PMN/PT solid solution for ferroelectrics MEMS microcooler," *Materials Science and Engineering: B*, **vol. 113**, no. 1, pp. 46–49, Oct. 2004.
- [10] PhD Thesis: D. Jeong, "Electro-optical properties in relaxor ferroelectric materials and the device applications," Pennsylvania State University, 2004.
- [11] Stuart T. Smith, Shane C. Woody, Richard M. Seugling, "Closed loop control systems employing relaxor ferroelectric actuators," U.S. Patent 6 707 230, Mar 16, 2004.
- [12] I. W. Chen, "Structural origin of relaxor ferroelectrics—revisited," *Journal of Physics and Chemistry of Solids*, **vol. 61**, no. 2, pp. 197–208, Feb. 2000.
- [13] L. E. Cross, "Relaxor ferroelectrics," *Ferroelectrics*, **vol. 76**, no. 1, pp. 241–267, Dec. 1987.
- [14] P. Debye, *Ver. Deut. Phys. Gesell.* **vol. 15**, pp. 777; reprinted 1954 in collected papers of Peter J.W. Debye Interscience, New York.
- [15] S. Havriliak and S. Negami, "A complex plane representation of dielectric and mechanical relaxation processes in some polymers," *Polymer*, **vol. 8**, pp. 161–210, Jan. 1967.
- [16] K. S. Cole and R. H. Cole, "Dispersion and Absorption in Dielectrics I. Alternating Current Characteristics," *The Journal of Chemical Physics*, **vol. 9**, no. 4, p. 341, 1941.
- [17] K. S. Cole, "Dispersion and Absorption in Dielectrics II. Direct Current Characteristics," *The Journal of Chemical Physics*, **vol. 10**, no. 2, p. 98, 1942.
- [18] G. A. Samara, "The relaxational properties of compositionally disordered ABO<sub>3</sub> perovskites," *Journal of Physics: Condensed Matter*, **vol. 15**, no. 9, pp. R367–R411, Mar. 2003.
- [19] B. Vugmeister and M. Glinchuk, "Dipole glass and ferroelectricity in random-site electric dipole systems," *Reviews of Modern Physics*, **vol. 62**, no. 4, pp. 993–1026, Oct. 1990.
- [20] H. Fu and R. Cohen, "Polarization rotation mechanism for ultrahigh electromechanical response in single-crystal piezoelectrics," *Nature*, **vol. 403**, no. 6767, pp. 281–3, Jan. 2000.
- [21] S. Mischenko, Q. Zhang, R. W. Whatmore, J. F. Scott, and N. D. Mathur, "Giant electrocaloric effect in the thin film relaxor ferroelectric 0.9Pb(Mg<sub>1/3</sub>Nb<sub>2/3</sub>)O<sub>3</sub>-0.1PbTiO<sub>3</sub> near room temperature," *Applied Physics Letters*, **vol. 89**, no. 24, p. 242912, 2006.

- [22] Z. Kutnjak, J. Petzelt, and R. Blinc, "The giant electromechanical response in ferroelectric relaxors as a critical phenomenon.," *Nature*, **vol. 441**, no. 7096, pp. 956–9, Jun. 2006.
- [23] S. L. Swartz and T. R. Shrout, "Fabrication of perovskite lead magnesium niobate," *Materials Research Bulletin*, **vol. 17**, no. 10, pp. 1245–1250, Oct. 1982.
- [24] K. R. Udayakumar, J. Chen, V. Kumar, S. B. Krupanidhi, and L. E. Cross, "Fabrication and characterization of PMN-PT thin films," in *[Proceedings] 1990 IEEE 7th International Symposium on Applications of Ferroelectrics*, pp. 744–746.
- [25] M. Ishida, H. Matsunami, and T. Tanaka, "Preparation and properties of ferroelectric PLZT thin films by rf sputtering," *Journal of Applied Physics*, **vol. 48**, no. 3, p. 951, 1977.
- [26] C. I-Wei, L. Ping, and W. Ying, "Structural origin of relaxor perovskites," *Journal of Physics and Chemistry of Solids*, **vol. 57**, no. 10, pp. 1525–1536, Oct. 1996.
- [27] J. Chen, H. M. Chan, and M. P. Harmer, "Ordering Structure and Dielectric Properties of Undoped and La/Na-Doped  $\text{Pb}(\text{Mg}_{1/3}\text{Nb}_{2/3})\text{O}_3$ ," *Journal of the American Ceramic Society*, **vol. 72**, no. 4, pp. 593–598, Apr. 1989.
- [28] A. D. Hilton, D. J. Barber, C. A. Randall, and T. R. Shrout, "On short range ordering in the perovskite lead magnesium niobate," *Journal of Materials Science*, **vol. 25**, no. 8, pp. 3461–3466, Aug. 1990.
- [29] D. Saranya, A. R. Chaudhuri, J. Parui, and S. B. Krupanidhi, "Electrocaloric effect of PMN-PT thin films near morphotropic phase boundary," *Bulletin of Materials Science*, **vol. 32**, no. 3, pp. 259–262, Aug. 2009.
- [30] S. H. Baek, J. Park, D. M. Kim, V. A. Aksyuk, R. R. Das, S. D. Bu, D. A. Felker, J. Lettieri, V. Vaithyanathan, S. S. N. Bharadwaja, N. Bassiri-Gharb, Y. B. Chen, H. P. Sun, C. M. Folkman, H. W. Jang, D. J. Kreft, S. K. Streiffer, R. Ramesh, X. Q. Pan, S. Trolier-McKinstry, D. G. Schlom, M. S. Rzechowski, R. H. Blick, and C. B. Eom, "Giant piezoelectricity on Si for hyperactive MEMS.," *Science (New York, N.Y.)*, **vol. 334**, no. 6058, pp. 958–61, Nov. 2011.
- [31] Y. Guo, H. Luo, D. Ling, H. Xu, T. He, and Z. Yin, "The phase transition sequence and the location of the morphotropic phase boundary region in  $(1-x)[\text{Pb}(\text{Mg}_{1/3}\text{Nb}_{2/3})\text{O}_3]-x\text{PbTiO}_3$  single crystal," *Journal of Physics: Condensed Matter*, **vol. 15**, no. 2, pp. L77–L82, Jan. 2003.
- [32] L. F. Francis and D. A. Payne, "Thin-Layer Dielectrics in the  $\text{Pb}[(\text{Mg}_{1/3}\text{Nb}_{2/3})_{1-x}\text{Ti}_x]\text{O}_3$  System," *J. Am. Ceram. Soc.*, **vol. 74**, **no. 12**, pp. 3000–3010, Dec. 1991.
- [33] G.A. Smolenskii and A.I. Agranovskaya, *Sov. Phys. Tech. Phys.* 3, 1380 (1958).

- [34] C. Tantigate, J. Lee, and a. Safari, "Processing and properties of  $\text{Pb}(\text{Mg}_{1/3}\text{Nb}_{2/3})\text{O}_3$ - $\text{PbTiO}_3$  thin films by pulsed laser deposition," *Applied Physics Letters*, **vol. 66**, no. 13, p. 1611, 1995.
- [35] K. Babooram, H. Tailor, and Z.-G. Ye, "Phase formation and dielectric properties of  $0.9\text{Pb}(\text{Mg}_{1/3}\text{Nb}_{2/3})\text{O}_3$ - $0.1\text{PbTiO}_3$  ceramics prepared by a new sol-gel method," *Ceramics International*, **vol. 30**, no. 7, pp. 1411-1417, Jan. 2004.
- [36] W. Z. Li, J. M. Xue, Z. H. Zhou, J. Wang, H. Zhu, and J. M. Miao, " $0.67\text{Pb}(\text{Mg}_{1/3}\text{Nb}_{2/3})\text{O}_3$ - $0.33\text{PbTiO}_3$  thin films derived from RF magnetron sputtering," *Ceramics International*, **vol. 30**, no. 7, pp. 1539-1542, Jan. 2004.
- [37] S. Lee, M. C. Custodio, H. Lim, R. Feigelson, J.-P. Maria, and S. Trolier-McKinstry, "Growth and characterization of  $\text{Pb}(\text{Mg}_{1/3}\text{Nb}_{2/3})\text{O}_3$  and  $\text{Pb}(\text{Mg}_{1/3}\text{Nb}_{2/3})\text{O}_3$ - $\text{PbTiO}_3$  thin films using solid source MOCVD techniques," *Journal of Crystal Growth*, **vol. 226**, no. 2-3, pp. 247-253, Jun. 2001.
- [38] F. Wang and S. Leppävuori, "Properties of epitaxial ferroelectric  $\text{PbZr}_{0.56}\text{Ti}_{0.44}\text{O}_3$  heterostructures with  $\text{La}_{0.5}\text{Sr}_{0.5}\text{CoO}_3$  metallic oxide electrodes," *Journal of Applied Physics*, **vol. 82**, no. 3, p. 1293, 1997.
- [39] M. Lejeune and J. Boilot, "Influence of ceramic processing on dielectric properties of perovskite type compound," *Ceramics International*, **vol. 9**, no. 4, pp. 119-122, Oct. 1983.
- [40] H.-C. Wang and W. A. Schulze, "The Role of Excess Magnesium Oxide or Lead Oxide in Determining the Microstructure and Properties of Lead Magnesium Niobate," *Journal of the American Ceramic Society*, **vol. 73**, no. 4, pp. 825-832, Apr. 1990.
- [41] W. Gong, J.-F. Li, X. Chu, and L. Li, "Texture Control of Sol-Gel Derived  $\text{Pb}(\text{Mg}_{1/3}\text{Nb}_{2/3})\text{O}_3$ - $\text{PbTiO}_3$  Thin Films Using Seeding Layer," *Journal of the American Ceramic Society*, **vol. 87**, no. 6, pp. 1031-1034, Jun. 2004.
- [42] J. P. Guha, D. J. Hong, and H. U. Anderson, "Effect of Excess PbO on the Sintering Characteristics and Dielectric Properties of  $\text{Pb}(\text{Mg}_{1/3}\text{Nb}_{2/3})\text{O}_3$ - $\text{PbTiO}_3$ -Based Ceramics," *Journal of the American Ceramic Society*, **vol. 71**, no. 3, pp. C-152-C-154, Mar. 1988.
- [43] D. H. Kang and K. H. Yoon, "Dielectric properties due to excess PbO and MgO in lead magnesium niobate ceramics," *Ferroelectrics*, **vol. 87**, no. 1, pp. 255-264, Nov. 1988.
- [44] H. Fan, G.-T. Park, J.-J. Choi, and H.-E. Kim, "Preparation and Characterization of Sol-Gel-Derived Lead Magnesium Niobium Titanate Thin Films with Pure Perovskite Phase and Lead

- Oxide Cover Coat,” *Journal of the American Ceramic Society*, **vol. 85**, no. 8, pp. 2001–2004, Aug. 2002.
- [45] S. L. Swartz, T. R. Shrout, W. a. Schulze, and L. E. Cross, “Dielectric Properties of Lead-Magnesium Niobate Ceramics,” *Journal of the American Ceramic Society*, **vol. 67**, no. 5, pp. 311–314, May 1984.
- [46] B.-H. Lee, N.-K. Kim, J.-J. Kim, and S.-H. Cho, “Perovskite formation sequence by B-site precursor method and dielectric properties of PFW-PFN ceramics,” *Ferroelectrics*, **vol. 211**, no. 1, pp. 233–247, Jan. 1998.
- [47] B.-H. Lee, N.-K. Kim, and B.-O. Park, “Perovskite formation and dielectric characteristics of PFW<sub>0.2</sub>•PFT<sub>0.8-x</sub>•PFN<sub>x</sub> system ceramics,” *Ferroelectrics*, **vol. 227**, no. 1, pp. 87–96, Apr. 1999.
- [48] M. Feng, W. Wang, H. Ke, J. C. Rao, and Y. Zhou, “Highly (111)-oriented and pyrochlore-free PMN–PT thin films derived from a modified sol–gel process,” *Journal of Alloys and Compounds*, **vol. 495**, no. 1, pp. 154–157, Apr. 2010.
- [49] M. L. Calzada, M. Algueró, J. Ricote, a. Santos, and L. Pardo, “Preliminary results on sol-gel processing of <100> oriented Pb(Mg<sub>1/3</sub>Nb<sub>2/3</sub>)O<sub>3</sub>-PbTiO<sub>3</sub> thin films using diol-based solutions,” *Journal of Sol-Gel Science and Technology*, **vol. 42**, no. 3, pp. 331–336, Oct. 2006.
- [50] Y. Takahashi, Y. Matsuoka, K. Yamaguchi, M. Matsuki, and K. Kobayashi, “Dip coating of PT, PZ and PZT films using an alkoxide-diethanolamine method,” *Journal of Materials Science*, **vol. 25**, no. 9, pp. 3960–3964, Sep. 1990.
- [51] N. Tohge, S. Takahashi, and T. Minami, “Preparation of PbZrO<sub>3</sub>-PbTiO<sub>3</sub> Ferroelectric Thin Films by the Sol-Gel Process,” *Journal of the American Ceramic Society*, **vol. 74**, no. 1, pp. 67–71, Jan. 1991.
- [52] L. G. Hubert-Pfalzgraf, “Some trends in the design of homo- and heterometallic molecular precursors of high-tech oxides,” *Inorganic Chemistry Communications*, **vol. 6**, no. 1, pp. 102–120, Jan. 2003.
- [53] J. H. Lee, Y. J. Oh, T. Y. Kim, M. R. Choi, and W. Jo, “Piezoelectric and electromechanical properties of relaxor ferroelectric Pb(Mg<sub>1/3</sub>Nb<sub>2/3</sub>)O<sub>3</sub>(65%)-PbTiO<sub>3</sub>(35%) thin films observed by scanning force microscopy.,” *Ultramicroscopy*, **vol. 107**, no. 10–11, pp. 954–7, Oct. 2007.
- [54] P. Kumar, R. K. Patel, C. Prakash, and T. C. Goel, “Effect of substrates on phase formation in PMN-PT 68/32 thin films by sol–gel process,” *Materials Chemistry and Physics*, **vol. 110**, no. 1, pp. 7–10, Jul. 2008.

- [55] N. Wakiya, K. Shinozaki, and N. Mizutani, "Preparation of heteroepitaxial  $\text{Pb}(\text{Mg}_{1/3}\text{Nb}_{2/3})\text{O}_3$  (PMN) thin film by pulsed laser deposition on Si(001) substrate using  $\text{La}_{0.5}\text{Sr}_{0.5}\text{CoO}_3$  (LSCO)/ $\text{CeO}_2$ /YSZ triple buffer," *Thin Solid Films*, **vol. 384**, no. 2, pp. 189–194, Mar. 2001.
- [56] J. Jiang, H.-H. Hwang, W.-J. Lee, and S.-G. Yoon, "Microstructural and electrical properties of  $0.65\text{Pb}(\text{Mg}_{1/3}\text{Nb}_{2/3})\text{O}_3$ – $0.35\text{PbTiO}_3$  (PMN–PT) epitaxial films grown on Si substrates," *Sensors and Actuators B: Chemical*, **vol. 155**, no. 2, pp. 854–858, Jul. 2011.
- [57] T. M. Correia, J. S. Young, R. W. Whatmore, J. F. Scott, N. D. Mathur, and Q. Zhang, "Investigation of the electrocaloric effect in a  $\text{Pb}(\text{Mg}_{1/3}\text{Nb}_{2/3})\text{O}_3$ – $\text{PbTiO}_3$  relaxor thin film," *Applied Physics Letters*, **vol. 95**, no. 18, p. 182904, 2009.
- [58] J. H. Park, F. Xu, and S. Trolier-McKinstry, "Dielectric and piezoelectric properties of sol–gel derived lead magnesium niobium titanate films with different textures," *Journal of Applied Physics*, **vol. 89**, no. 1, p. 568, 2001.
- [59] J.-P. Maria, Ph.D. thesis, The Pennsylvania State University, 1998.
- [60] B. Gobaut, J. Penuelas, J. Cheng, A. Chettaoui, L. Largeau, G. Hollinger, and G. Saint-Girons, "Direct growth of InAsP/InP quantum well heterostructures on Si using crystalline  $\text{SrTiO}_3$ /Si templates," *Applied Physics Letters*, **vol. 97**, no. 20, p. 201908, 2010.
- [61] A. Lin, X. Hong, V. Wood, a. a. Verevkin, C. H. Ahn, R. a. McKee, F. J. Walker, and E. D. Specht, "Epitaxial growth of  $\text{Pb}(\text{Zr}_{0.2}\text{Ti}_{0.8})\text{O}_3$  on Si and its nanoscale piezoelectric properties," *Applied Physics Letters*, **vol. 78**, no. 14, p. 2034, 2001.
- [62] A. A. Talin, S. M. Smith, S. Voight, J. Finder, K. Eisenbeiser, D. Penunuri, Z. Yu, P. Fejes, T. Eschrich, J. Curless, D. Convey, and a. Hooper, "Epitaxial  $\text{PbZr}_{0.52}\text{Ti}_{0.48}\text{O}_3$  films on  $\text{SrTiO}_3$ /(001)Si substrates deposited by sol–gel method," *Applied Physics Letters*, **vol. 81**, no. 6, p. 1062, 2002.
- [63] R. McKee, F. Walker, and M. Chisholm, "Crystalline Oxides on Silicon: The First Five Monolayers," *Physical Review Letters*, **vol. 81**, no. 14, pp. 3014–3017, Oct. 1998.
- [64] J. W. Reiner, A. M. Kolpak, Y. Segal, K. F. Garrity, S. Ismail-Beigi, C. H. Ahn, and F. J. Walker, "Crystalline oxides on silicon.," *Advanced materials (Deerfield Beach, Fla.)*, **vol. 22**, no. 26–27, pp. 2919–38, Jul. 2010.
- [65] J. Ouyang, S. Y. Yang, L. Chen, R. Ramesh, and a. L. Roytburd, "Orientation dependence of the converse piezoelectric constants for epitaxial single domain ferroelectric films," *Applied Physics Letters*, **vol. 85**, no. 2, p. 278, 2004.

- [66] J.-G. Baek, T. Isobe, and M. Senna, "Synthesis of Pyrochlore-Free  $0.9\text{Pb}(\text{Mg}_{1/3}\text{Nb}_{2/3})\text{O}_3$ - $0.1\text{PbTiO}_3$  Ceramics via a Soft Mechanochemical Route," *Journal of the American Ceramic Society*, **vol. 80**, no. 4, pp. 973–981, Jan. 2005.
- [67] N. Salah, S. S. Habib, Z. H. Khan, A. Memic, A. Azam, E. Alarfaj, N. Zahed, and S. Al-Hamed, "High-energy ball milling technique for ZnO nanoparticles as antibacterial material," *Int. J. Nanomedicine*, **vol. 6**, pp. 863–9, Jan. 2011.
- [68] D. E. Bugay, "Characterization of the solid-state: spectroscopic techniques," *Advanced Drug Delivery Reviews*, **vol. 48**, no. 1, pp. 43–65, May 2001.
- [69] E. B. Wilson, J. C. Decius, and P. C. Cross, *Molecular Vibrations: The Theory of Infrared and Raman Vibrational Spectra*. Courier Dover Publications, 1955.
- [70] G. Andermann, A. Caron, and D. A. Dows, "Kramers-Kronig Dispersion Analysis of Infrared Reflectance Bands," *Journal of the Optical Society of America*, **vol. 55**, no. 10, p. 1210, Oct. 1965.
- [71] J. Petzelt, G. V. Kozlov, and A. A. Volkov, "Dielectric spectroscopy of paraelectric soft modes," *Ferroelectrics*, **vol. 73**, no. 1, pp. 101–123, Jun. 1987.
- [72] J. Last, "Infrared-Absorption Studies on Barium Titanate and Related Materials," *Physical Review*, **vol. 105**, no. 6, pp. 1740–1750, Mar. 1957.
- [73] J. Slater, "The Lorentz Correction in Barium Titanate," *Physical Review*, **vol. 78**, no. 6, pp. 748–761, Jun. 1950.
- [74] J. Axe, "Apparent Ionic Charges and Vibrational Eigenmodes of  $\text{BaTiO}_3$  and Other Perovskites," *Physical Review*, **vol. 157**, no. 2, pp. 429–435, May 1967.
- [75] M. E. Lines and A. M. Glass, *Principles and Applications of Ferroelectrics and Related Materials* (Clarendon, Oxford, 1977).
- [76] I. M. Reaney, J. Petzelt, V. V. Voitsekhovskii, F. Chu, and N. Setter, "B-site order and infrared reflectivity in  $\text{A}(\text{B}'\text{B}'')\text{O}_3$  complex perovskite ceramics," *Journal of Applied Physics*, **vol. 76**, no. 4, p. 2086, 1994.
- [77] S. Kamba, E. Buixaderas, J. Petzelt, J. Fousek, J. Nosek, and P. Bridenbaugh, "Infrared and Raman spectroscopy of  $[\text{Pb}(\text{Zn}_{1/3}\text{Nb}_{2/3})\text{O}_3]_{0.92}$ - $[\text{PbTiO}_3]_{0.08}$  and  $[\text{Pb}(\text{Mg}_{1/3}\text{Nb}_{2/3})\text{O}_3]_{0.71}$ - $[\text{PbTiO}_3]_{0.29}$  single crystals," *Journal of Applied Physics*, **vol. 93**, no. 2, p. 933, 2003.
- [78] G. Burns and F. Dacol, "Crystalline ferroelectrics with glassy polarization behavior," *Physical Review B*, **vol. 28**, no. 5, pp. 2527–2530, Sep. 1983.

- [79] E. B. Araújo, C. a. Guarany, K. Yukimitu, J. C. S. Moraes, and a. C. Hernandez, “Structural Phase Transition Studies on PMN-0.35PT using Infrared Spectroscopy,” *Ferroelectrics*, **vol. 369**, no. 1, pp. 35–42, Oct. 2008.
- [80] S. Kamba, D. Nuzhnyy, S. Veljko, V. Bovtun, J. Petzelt, Y. L. Wang, N. Setter, J. Levoska, M. Tyunina, J. Macutkevic, and J. Banys, “Dielectric relaxation and polar phonon softening in relaxor ferroelectric  $\text{PbMg}_{1/3}\text{Ta}_{2/3}\text{O}_3$ ,” *Journal of Applied Physics*, **vol. 102**, no. 7, p. 074106, 2007.
- [81] V. Bovtun, J. Petzelt, V. Porokhonsky, S. Kamba, and Y. Yakimenko, “Structure of the dielectric spectrum of relaxor ferroelectrics,” *Journal of the European Ceramic Society*, **vol. 21**, no. 10–11, pp. 1307–1311, Jan. 2001.
- [82] V. Nagarajan, C. S. Ganpule, B. Nagaraj, S. Aggarwal, S. P. Alpay, a. L. Roytburd, E. D. Williams, and R. Ramesh, “Effect of mechanical constraint on the dielectric and piezoelectric behavior of epitaxial  $\text{Pb}(\text{Mg}_{1/3}\text{Nb}_{2/3})\text{O}_3(90\%)\text{--PbTiO}_3(10\%)$  relaxor thin films,” *Applied Physics Letters*, **vol. 75**, no. 26, p. 4183, 1999.
- [83] Z. Kighelman, D. Damjanovic, a. Seifert, L. Sagalowicz, and N. Setter, “Relaxor behavior and electro-mechanical properties of  $\text{Pb}(\text{Mg}_{1/3}\text{Nb}_{2/3})\text{O}_3$  thin films,” *Applied Physics Letters*, **vol. 73**, no. 16, p. 2281, 1998.
- [84] Z. Kighelman, D. Damjanovic, and N. Setter, “Electromechanical properties and self-polarization in relaxor  $\text{Pb}(\text{Mg}_{1/3}\text{Nb}_{2/3})\text{O}_3$  thin films,” *Journal of Applied Physics*, **vol. 89**, no. 2, p. 1393, 2001.
- [85] A. L. Kholkin, K. G. Brooks, D. V Taylor, S. Hiboux, and N. Setter, “Self-polarization effect in  $\text{Pb}(\text{Zr,Ti})\text{O}_3$  thin films,” *Integrated Ferroelectrics*, **vol. 22**, no. 1–4, pp. 525–533, Mar. 1998.
- [86] R. Zheng, Y. Wang, H. Chan, C. Choy, and H. Luo, “Determination of the strain dependence of resistance in  $\text{La}_{0.7}\text{Sr}_{0.3}\text{MnO}_3\text{PMN-PT}$  using the converse piezoelectric effect,” *Physical Review B*, **vol. 75**, no. 21, p. 212102, Jun. 2007.
- [87] J. Ho, K. Liu, and I. Lin, “Study of ferroelectricity in the PMN-PT system near the morphotropic phase boundary,” *Journal of materials science*, **vol. 28**, pp. 4497–4502, 1993.
- [88] J. Wang, K. H. Wong, C. L. Choy, and H. L. W. Chan, “Composition control and electrical properties of PMN-PT thin films around the morphotropic boundary,” *Applied Physics A: Materials Science & Processing*, **vol. 79**, no. 3, pp. 551–556, Aug. 2004.

[89] M. Detalle, G. Wang, D. Rémiens, P. Ruterana, P. Roussel, and B. Dkhil, “Comparison of structural and electrical properties of PMN-PT films deposited on Si with different bottom electrodes,” *J. Cryst. Growth*, **vol. 305**, no. 1, pp. 137–143, Jul. 2007.



**Chapter V - Microfabrication and characterization of piezoelectric devices**

---

---

<b>V.1) Introduction .....</b>	<b>154</b>
<b>V.2) Microfabrication process .....</b>	<b>155</b>
V.2.1) Piezoelectric membrane .....	155
V.2.2) Piezoelectric cantilever .....	159
<b>V.3) Finite Element Method and analytic model .....</b>	<b>162</b>
V.3.1) Introduction .....	162
V.3.1.1) Finite Element Method .....	162
V.3.1.2) Analytic model .....	163
V.3.2) Characterization on piezoelectric membrane .....	165
V.3.3) Characterization on piezoelectric cantilever .....	167
<b>V.4) Conclusion .....</b>	<b>169</b>
<b>V.5) Reference .....</b>	<b>169</b>

## V.1) Introduction

MEMS microfabrication is not a completely new technology but based on a package of available cleanroom facilities which have been already developed for a long time in IC industry <sup>[1]</sup>. Except for that, additional technologies for MEMS manufacture must take diverse materials, like PZT, AlN, Ni, Fe, Co <sup>[2]</sup>, into consideration for various MEMS devices, which are more than the conventional materials used for IC manufacture, such as Si, SiO<sub>2</sub>, Si<sub>3</sub>N<sub>4</sub>, Al. On the other hand, various mechanical structures in MEMS devices need special fabrication process to satisfy different application-specific purpose. Similar to IC, MEMS manufactures handling the tiny dimension in massive production are also based on photolithography technology with a series of photomasks <sup>[3,4]</sup>. Table V.1 summarizes various cleanroom technologies used in IC and MEMS manufacture for comparison.

**Table V.1 - List of various cleanroom technologies for IC and MEMS microfabrication**

IC fabrication	MEMS fabrication
Thermal oxidation <sup>[5]</sup>	Surface micromachining <sup>[15]</sup>
Dopant diffusion <sup>[6]</sup>	Bulk micromachining <sup>[16]</sup> : Deep Reactive Ion Etching (DRIE) <sup>[17, 18]</sup>
Ion implantation <sup>[7]</sup>	Substrate bonding <sup>[19]</sup> : fusion bonding <sup>[20]</sup> , anodic bonding <sup>[21]</sup> , eutectic bonding <sup>[22]</sup> , solder bonding <sup>[23]</sup> , thermal compression <sup>[24]</sup>
Chemical vapor deposition <sup>[8]</sup>	Non-silicon microfabrication: LIGA <sup>[25]</sup> , SU-8 <sup>[26]</sup> and plastic molding <sup>[27]</sup> .
Evaporation <sup>[9]</sup>	Low-stress LPCVD <sup>[28]</sup>
Sputtering <sup>[10]</sup>	Batch micro-assembly <sup>[29]</sup> and monolithic integration <sup>[30]</sup>
Wet etching <sup>[11]</sup>	
Plasma etching <sup>[12]</sup>	
Reactive-ion etching <sup>[13]</sup>	
Ion milling <sup>[14]</sup>	

In this chapter, microfabrication will be performed on single crystal PZT films grown on Si substrate to realize piezoelectric membrane and cantilever. Both structures, already successfully realized at LETI with polycrystalline PZT <sup>[31, 32]</sup>, are the most commonly used mechanical structures in MEMS devices. In our case, piezoelectric membrane structures were fabricated starting with PZT stack having no bottom electrode. Membrane can be also fabricated when the bottom electrode is included in the initial stack. During the microfabrication, Si substrate was etched out from backside to access the bottom surface of the piezoelectric film and then followed by the deposition of metallic electrode. Microfabrication of piezoelectric membrane only requires PZT/STO/Si starting stack which is relatively simple for film deposition. On the contrary, cantilever fabrication requires as-prepared bottom electrode in the starting stack which increases the complicity of the deposition process. However, with bottom electrode, time-consuming backside etching of Si substrate can be avoided. Here, SOI (silicon on insulator) substrate is used

to define the cantilever thickness by preserving the SOI Si layer during the etching. But the presence of the buried SiO<sub>2</sub> layer could modify the optimal condition for deposition of those functional films on SOI substrate. In this thesis, PZT films deposited on SRO/STO/SOI substrate will be used for cantilever microfabrication. Furthermore, based on those two different mechanical structures, various measurements will be carried out to characterize the piezoelectric performance of the PZT films at device level. Using computational analysis, piezoelectric coefficients can be finally extracted from the measurement.

## V.2) Microfabrication process for membrane and cantilever

### V.2.1) Piezoelectric membrane

Piezoelectric membrane is designed to have large lateral dimension to enhance mechanical deflection at low actuation voltage. In this thesis, piezoelectric membrane has the lateral dimension of 400×400 μm<sup>2</sup> so that use of plastic photomask is possible manageable. The plastic photomask has sufficient resolution (minimum linewidth: 50 μm) in this case and can largely reduce the design duration. Photomask layout was designed using the software - CleWin. In CleWin, multiply photomask layers are visualized in superimposed view and the pattern geometry is represented by the vectors. Figure V.1 shows part of the photomask, including three individual layers colored in red for released membrane, green for top electrode, and blue for electrical contact. Two types of piezoelectric membrane can be identified on the photomask, where the one with double top electrodes can act as a piezoelectric signal filter (referred as Capa2) and another one with single top electrode is a normal capacitor (referred as Capa1). The cross pattern is designed for the alignment of multiply photomask layers. The right image in Figure V.1 exhibits the starting stack for the microfabrication, i.e. PZT/STO/Si, where the thicknesses are 250 nm, 17.5 nm, and 300 μm for PZT film, STO film, and Si substrate, respectively. Moreover, Figure V.2 schematically presents the whole microfabrication process, which can be divided into five main steps. Each step will be discussed in the following:

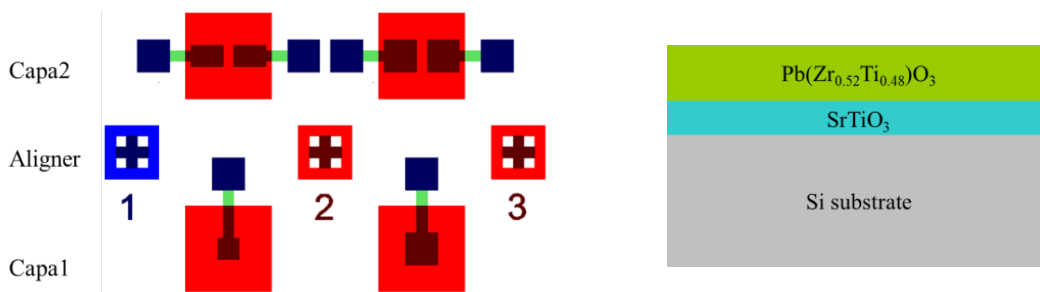


Figure V.1 - Plastic photomask for piezoelectric membrane microfabrication and the starting stack.

**1. Surface preparation.** Before microfabrication, Si wafer was cleansed by acetone and ethanol, and then dried in nitrogen flux to remove the contaminations.

**2. Top electrode.** Ru top electrode was fabricated by etching the coated Ru layer on PZT film. Ru electrode was used due to the fact that the PZT film with Ru electrode was found to have better resistance to fatigue problem compared with that of Pt top electrode<sup>[33]</sup>. 100nm-thick Ru top electrode was first deposited by rf sputtering on a cleansed PZT surface. Then, positive photoresist AZ1314 was spin-coated to obtain a 1.2 $\mu$ m-thick film on Ru top electrode. With the photomask, the coated photoresist was exposed under the radiation of ultraviolet light for lithography. Additional part of Ru top electrode was finally removed by wet etching, where the water-based solution with sodium hypochlorite (NaClO) was used.

**3. SiO<sub>2</sub> elastic layer.** To compensate residual stress and enhance mechanical deflection, SiO<sub>2</sub> elastic layer is usually added into the stack because of its compressive thermal stress<sup>[34]</sup> and simple fabrication process. SiO<sub>2</sub> deposition was carried out in a PE-CVD setup (Plasma-Enhanced Chemical Vapor Deposition) by decomposing TEOS (Si(OC<sub>2</sub>H<sub>5</sub>)<sub>4</sub>) at 650°C, where the following reaction occurs<sup>[35]</sup>:



Then, lithography was performed on the deposited SiO<sub>2</sub> layer which will be selectively etched to expose Ru top electrode for electrical contact. The etchant is buffered-HF solution.

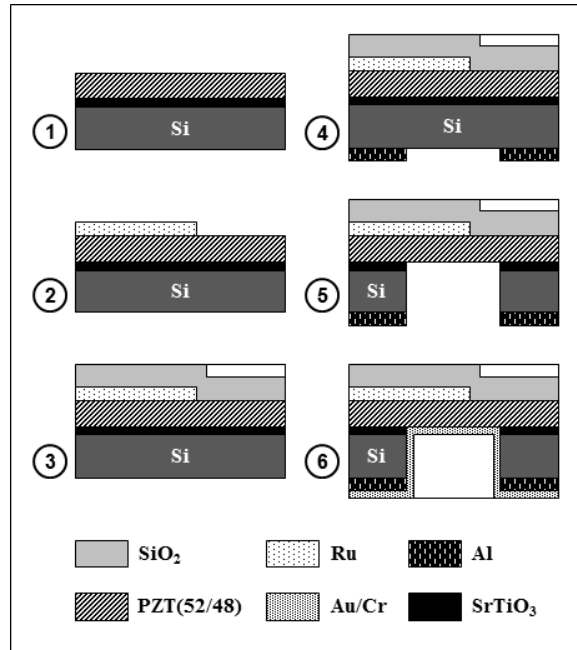


Figure V.2 - Schematics of the fabrication process for piezoelectric membrane.

**4. Deposition of Al layer.** A metallic hard mask was required for back etching of Si substrate, since the common polymer photoresist cannot persist with the plasma damage during the etching. Here, we use Al for hard mask because of its easy etching process. Al layer was first deposited on the back surface of Si wafer by PVD (Physical Vapor Deposition) and then the lithography was performed. Extra part of the Al layer was removed by wet etching, where the etching solution consists of phosphoric, acetic, and nitric acids, known as PAN etch.

**5. Back etching of Si substrate.** Si substrate was etched out by DRIE and RIE from backside in order to expose the back surface of the piezoelectric film for depositing bottom electrode. DRIE having a fast etching speed ( $\sim 1 \mu\text{m}/\text{min}$ ) is used to remove most of Si substrate and then followed by RIE to remove the remnant Si. DRIE technology is widely used in MEMS manufacture, high-density capacitors [36], and TSV (Through Silicon Via) [37] in advanced 3D wafer level packaging, due to its ability to form the structure with high-aspect ratios [38]. The dominant technology for high-rate DRIE is known as the Bosch process which alternatively repeats the following two modes to achieve nearly vertical structures (Figure V.3):

- Passivation on the bottom and the newly-exposed sidewall of the trench. For Si,  $\text{C}_4\text{F}_8$  is often used to yield a Teflon-like substance in the plasma during typically 10 seconds on Si.
- Plasma etching by  $\text{SF}_6$  for Si. This process is a nearly anisotropic etching, where the ionized atoms attack the wafer from a nearly vertical direction under electric field. The etching first removes the polymer deposited on the bottom of the trench during passivation and then continues to remove the silicon isotropically. This process does not etch the polymer on the sidewall since the etching of the polymer requires both radicals and ions.

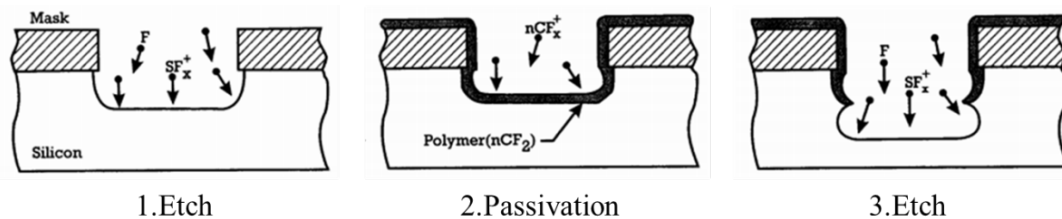
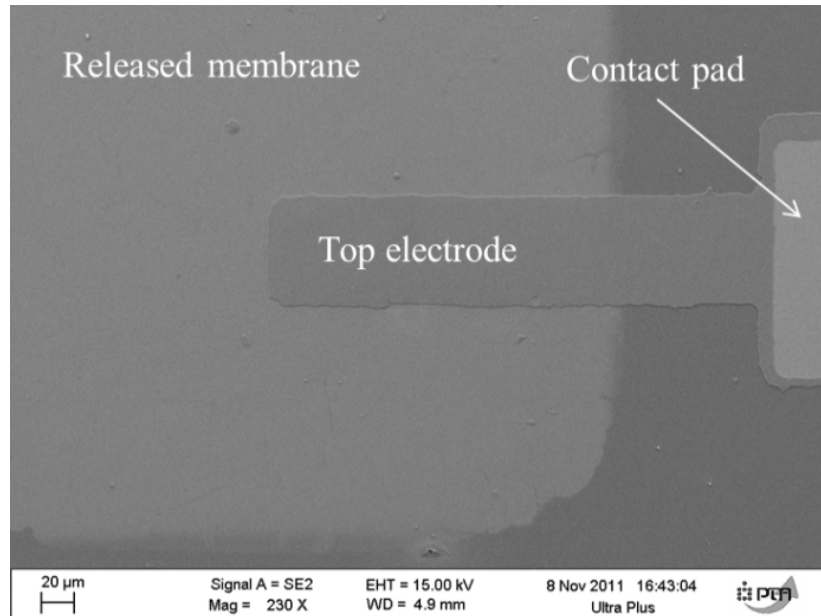


Figure V.3 - The Bosch process for etching a silicon trench by DRIE.

A single DRIE cycle will remove 0.5 to 1  $\mu\text{m}$  silicon and the cycle is repeated until the structure has been etched. Finally, to avoid plasma damage of DRIE on PZT film, remnant 5 $\mu\text{m}$ -thick Si substrate was etched by RIE using  $\text{CHF}_3/\text{O}_2$  etchant.

**6. Bottom electrode.** After back-etching of Si substrate, deposition of Au and Cr was performed to get electrical contact with the back surface of the piezoelectric membrane. Thickness of Au

and Cr are 100 nm and 10 nm, where the Cr layer is used to enhance the adhesion of Au with PZT film. In order to obtain a continuous bottom electrode fully covering the sidewall and the back surface of the piezoelectric membrane, both e-beam evaporation and rf sputtering technologies are necessarily required. For e-beam evaporation, substrate is usually tilted to expose the sidewall under vapour flux, however, which will draw a shadow on the opposite sidewall leading to the discontinuity of the deposited bottom electrode. For rf sputtering, high-energy plasma could damage the PZT film and argon atom is also possibly implanted, although it has a better step coverage than e-beam evaporation. Therefore, the strategy is to perform e-beam evaporation first to protect the membrane from the plasma damage and then use rf sputtering to fully cover the shadowed region.



**Figure V.4 - SEM image on a piezoelectric membrane.**

SEM image (Scanning Electron Microscopy) of the piezoelectric membrane taken from the top view is shown in Figure V.4. Released membrane is clearly seen with bright contrast, which is slightly different from designed rectangular pattern and shows a rounded rectangular geometry. This is mainly caused by the different etching speed of DRIE back-etching of Si substrate at the corner and the edge of the trench. In DRIE, the plasma ions accelerated by the electric field do not form a straight beam but an angularly scattered cone. This will decrease the etching speed at the corner compared with that at the edge, leading to concave bottom geometry after the etching. Thus, compromise between continuation of etching to obtain a well-defined geometry and protection of PZT film from plasma damage must be made.

### V.2.2) Piezoelectric cantilever

Chrome-coated hard photomask for piezoelectric cantilever fabrication was already designed and used at LETI. The patterns of the photomask are schematically shown in Figure V.5, including two individual layers for electrodes (green) and etched trench (grey) respectively. To define the thickness of the cantilever, the strategy is to use a SOI wafer where the SOI Si and the BOX (buried oxide) SiO<sub>2</sub> are preserved to form the structural layer of the cantilever, while the bulk Si substrate is partially etched to release the cantilever. On the photomask, both bottom and top electrodes are designed on the top surface of the PZT film, where the bottom electrode takes the big capacitor for electrical contact. Nevertheless, since the SRO layer is fully spread on the wafer, bottom electrode can be realized by contacting the SRO layer from the edge of the wafer, usually by silver paste. The fabrication differs from that of piezoelectric membrane, since SOI wafer and SRO bottom electrode are used in the starting stack. Note however that SOI wafer can also be used for piezoelectric membrane realization. It allows avoiding the deposition of elastic membrane. Instead of back etching of Si substrate as we did for piezoelectric membrane, the presence of SRO bottom electrode can help to avoid such time-consuming process and the same photomask is possibly used for all the etching processes. In Figure V.6, the microfabrication process for realizing piezoelectric cantilever on PZT/SRO/STO/SOI starting stack is schematically shown. The thickness is 250 nm for PZT, 20 nm for SRO, 24 nm for STO, 5 μm for SOI Si, and 500 nm for BOX SiO<sub>2</sub>. In the following, we will discuss each step in details.

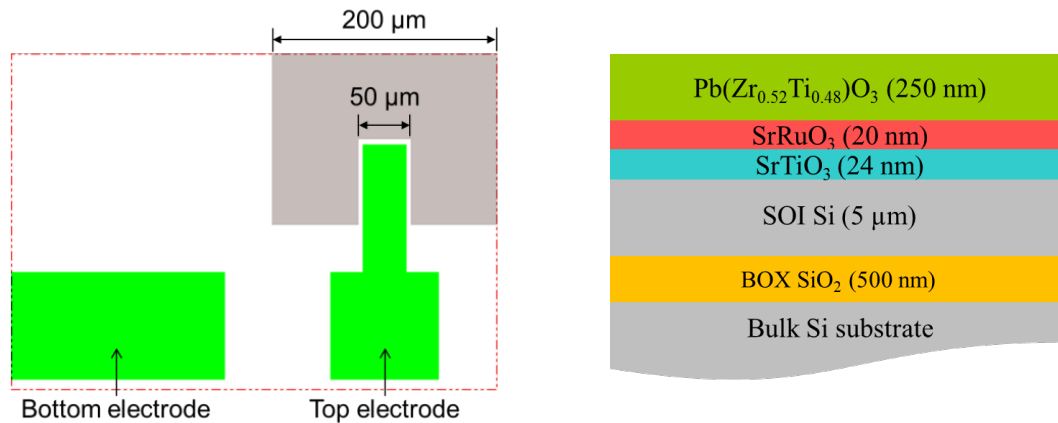


Figure V.5 - Schematically showing the patterns of the hard photomask for piezoelectric cantilever and the starting stack of the heterostructure (not to scale) for the fabrication.

**1. Surface preparation.** Before microfabrication, the substrate is cleansed by acetone and ethanol, and then dried in nitrogen flux to remove the contaminations.

**2. Top electrode.** Similar to piezoelectric membrane, 100nm-thick Ru top electrode was realized by patterning the coated Ru film on PZT layer. Besides, without the elastic layer, like SiO<sub>2</sub> for piezoelectric membrane, the whole surface of Ru top electrode can be electrically contacted by the testing probe.

**3. Etching of PZT layer.** PZT layer was patterned by chemical etching where the etchant solution consists of HF, HCl, DI-water with the atomic ratio of 5:9:200. The stop layer is SrRuO<sub>3</sub>. The etching process takes the following chemical reaction:

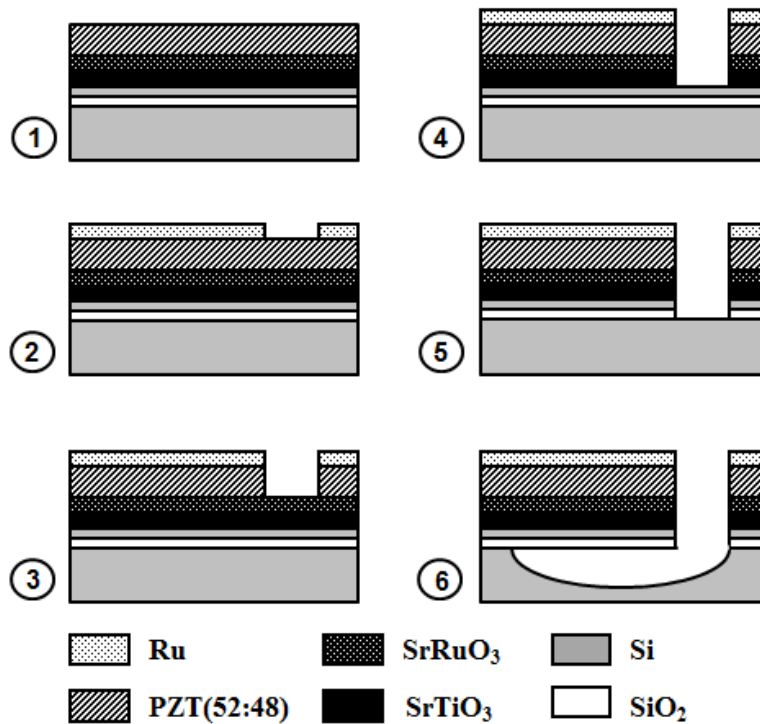
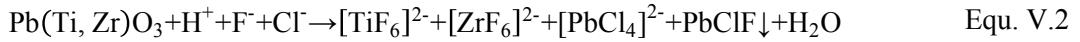


Figure V.6 - Schematics of the microfabrication process for piezoelectric membrane.

In addition, the photoresist used in the etching of PZT layer will be reused in the subsequent steps, including IBE (Ion Beam Etching) etching of SRO/STO, DRIE etching of SOI Si, and plasma etching of bulk Si substrate. Therefore, the photoresist is required to be chemically and mechanically robust enough for those processes. AZ 4562 photoresist is selected for this purpose and 6.2µm-thick film can be coated at 4000 rpm. To enhance the robustness of the photoresist, post-bake at 110°C was performed for 1 min. Finally, reflow process was carried out at 180°C for 15 min to avoid thermal softening and rounding which will form resist walls after IBE step.

**3. Etching of SRO/STO layer.** Since both SRO and STO have small thickness around 20 nm, IBE can be a convenient way to etch these layers. The etching process is monitored by mass spectrometry on the metallic elements, like Sr, Ru and Ti, where the signal of atom counts is used to determine the end of the etching process. In addition, due to the high energy of the ion beam during IBE etching, temperature increases rapidly within few minutes, leading to thermal decomposition of the photoresist. Therefore, cooling system is required in the IBE setup to avoid burning of the photoresist.

**4 & 5. Etching of SOI Si and BOX SiO<sub>2</sub>.** DRIE is selected in this case to perform highly anisotropic etching to remove additional SOI Si for a steep-sided trench. After etching, passivation of SOI Si layer is required at the end of DRIE using C<sub>4</sub>F<sub>8</sub> for 1 min. A Teflon-like passivation layer is formed to protect the SOI Si layer from the attack of the following XeF<sub>2</sub> etching. Finally, the etching of 500nm-thick BOX SiO<sub>2</sub> layer was achieved by RIE using the source gas of CHF<sub>3</sub>/SF<sub>6</sub>.

**6. Etching of bulk Si substrate to release the cantilever.** 50µm-thick Si was then etched from the substrate by a plasmaless and room-temperature process using XeF<sub>2</sub> as the source gas. XeF<sub>2</sub> gas isotropically etches Si without affecting most other materials, like oxides, resists, aluminum, gold, and most nitride films<sup>[39]</sup>, which is typically used to release non-silicon structures for MEMS microfabrication<sup>[40]</sup>. Other advantages include its fast etching rate and prevention of stiction between the structure being released and the substrate. In the process, the etching takes the following chemical reaction:



Finally, the coated photoresist will be stripped from the top surface. However, such microfabrication process described above draws many technical problems. Figure V.7 (a) exhibits an SEM image of a piezoelectric cantilever from the top view, where the photoresist was not completely stripped from the wafer. With many cracks observed on the surface, the photoresist seems to be burned and becomes sticky on the PZT layer. Another failure clearly demonstrated in Figure V.7 (b) is that the SOI Si under the photomask is partially removed and the gap forms between PZT/SRO/STO and BOX SiO<sub>2</sub>. Since the observed BOX SiO<sub>2</sub> layer is well defined by the photomask, we conclude that the missing SOI Si was removed during XeF<sub>2</sub> etching process due to the instable passivation layer deposited at the end of the DRIE process of the SOI Si etching. Therefore, the real film stack has the heterostructure of photoresist/Ru/PZT/SRO/STO/partial-SOI-Si/BOX-SiO<sub>2</sub>.

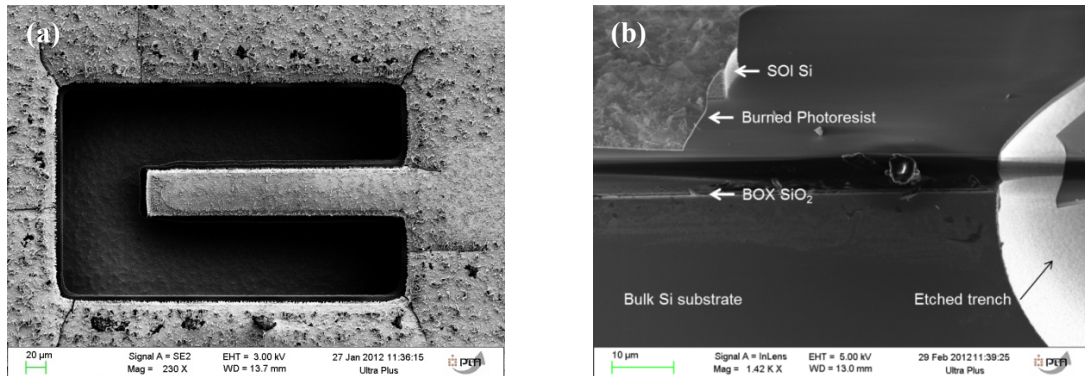


Figure V.7 - SEM images of the piezoelectric cantilever.

### V.3) Finite Element Method and analytic Model

#### V.3.1) Introduction

##### V.3.1.1) Finite Element Method

To extract piezoelectric coefficients from MEMS device, Finite Element Method (FEM) was used to simulate the mechanical displacement at a given dc voltage. The principle of FEM method can be found in the appendix of this chapter. Material model and boundary condition must be first identified for a well-defined FEM problem. Figure V.8 schematically shows a 2D FEM model (cross-section) as an example of simulation of a piezoelectric cantilever. In this case, use of 2D FEM model is available due to the planar stacks of the cantilever and the homogeneous vertical electric field. Two different physical materials are concerned in this model, i.e. linear elastic material and piezoelectric material. The former one involves all the materials expect for PZT layer, which requires only two parameters, i.e. Young's modulus and Poisson's ratio. More complicated elasticity matrix is needed if the material is not isotropically homogeneous. Additional parameters are needed for piezoelectric material, i.e. PZT, like piezoelectric coefficients and electrical permittivity, to respond to the applied voltage. Since the longitudinal expansion is negligible in this case, only the transverse piezoelectric coefficient ( $d_{31}$ ) is set in the coupling matrix. For boundary conditions, mechanical one should define the free boundaries and the fixed constraints, which are marked in blue and red respectively in the figure. On the other hand, electrical boundary condition should define the zero charged surfaces and the applied dc voltage around the PZT layer. Here, we define the applied voltage on the top surface and the grounded voltage on the bottom surface. Except for those two surfaces, the other surfaces of the PZT layer are zero charged to satisfy the electrical neutrality.



Figure V.8 - The planar stack of the piezoelectric cantilever. The mechanical free boundaries and fixed constraints are labeled in blue and red respectively.

The geometry of this model is meshed by mapped rectangles since the cross section of the cantilever takes rectangular shape (Figure V.9). Compared with free triangles, such meshing method can effectively reduce the number of the elements and the calculation errors in this case. For a given  $d_{31}$ , the ratio of the cantilever deflection and the applied voltage, i.e. sensitivity, can be derived from post-processing. Thus, the sensitivity as a function of  $d_{31}$  can be plotted by sweeping  $d_{31}$  value and the piezoelectric coefficients can be extracted by fitting the experimental result.

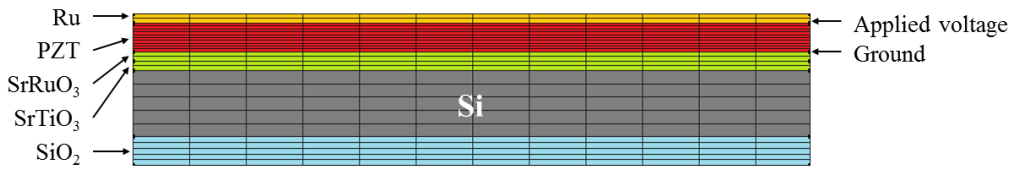


Figure V.9 - The mesh of the piezoelectric cantilever using mapped rectangles.

### V.3.1.2) Analytic model

Since piezoelectric cantilever usually takes a relatively simple form that consists of a stack of parallel layers (Figure V.10), such problem can be completely resolved by an analytic method<sup>[41]</sup>. In the stack, neighboring layers are mechanically coupled and the voltage is applied on the opposite surfaces of the ferroelectric layer. In Figure V.10, the stacked layers are denoted by  $i$  and the thickness is defined as  $t_i$ .  $h_i$  is defined as the distance from the top surface of layer  $i$  to the bottom of the cantilever. The normal direction of the stack is denoted as z-axis. The analytical model used in this thesis for piezoelectric cantilever takes several effects into consideration, such as residual stress, piezoelectricity, and thermal expansion. In the following, we will show the mathematical derivation of such model and give the function of the cantilever deflection at the end.

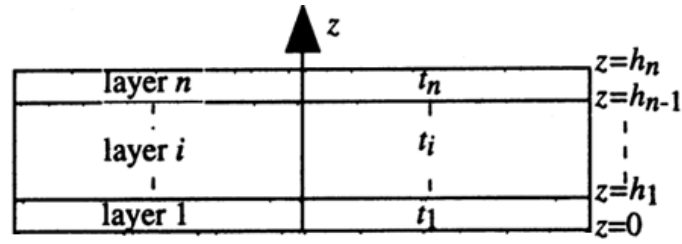


Figure V.10 - Schematics showing a multilayer structure in the cantilever.

In the model, the strain distributed in the multilayers can be decomposed into a uniform component ( $c$ ) and a bending component. Uniform strain is a homogenous component applying on the entire cantilever, which only induces the change of the length. Bending component is purely caused by the difference of the strain between the layers, leading to the bending of the cantilever with a bending axis whose length is unchanged. Hence, the total strain in the stack can be formulated as:

$$\varepsilon = c + \frac{z - t_b}{r} \quad (\text{for } 0 \leq z \leq h_n) \quad \text{Equ. V.4}$$

where  $z = t_b$  indicates the location of the bending axis and  $r$  is the radius of curvature of the stack. The normal stresses in the layers are related to the strains induced by various effects and defined by the following equation:

$$\sigma_i = E_i \left( \varepsilon - \frac{d_i V_i}{t_i} - \alpha_i \Delta T_i \right) - \bar{\sigma}_i \quad (\text{for } 0 \leq z \leq h_n) \quad \text{Equ. V.5}$$

where  $E_i$  is the Young's modulus,  $d_i$  is the in-plane piezoelectric coefficient ( $d_{31}$ ),  $V_i$  is the voltage across the piezoelectric film,  $t_i$  is the thickness,  $\alpha_i$  is the thermal expansion coefficient,  $\Delta T$  is the temperature difference, and  $\bar{\sigma}_i$  is the residual stress. In Eq. 5.5, the strain distribution in the stack is defined by three parameters, i.e.  $c$ ,  $t_b$ , and  $r$ . Those three parameters can be determined by the following boundary conditions:

**1. The resultant force due to the uniform strain component is zero.**

$$\sum_{i=1}^n \sigma_i t_i = \sum_{i=1}^n \left[ E_i \left( \varepsilon - \frac{d_i V_i}{t_i} - \alpha_i \Delta T_i \right) - \bar{\sigma}_i \right] t_i = 0 \quad \text{Equ. V.6}$$

Hence, the uniform strain component can be determined, such that

$$c = \frac{\sum_{i=1}^n (E_i t_i \alpha_i \Delta T_i - E_i d_i V_i + \bar{\sigma}_i t_i)}{\sum_{i=1}^n E_i t_i} \quad \text{Equ. V.7}$$

**2. The resultant force due to the bending strain component is zero.**

$$\sum_{i=1}^n \int_{h_{i-1}}^{h_i} \frac{E_i(z - t_b)}{r} dz = 0 \quad \text{Equ. V.8}$$

Hence, the position of the bending axis can be determined, such that

$$t_b = \frac{\sum_{i=1}^n E_i t_i (2h_{i-1} + t_i)}{2 \cdot \sum_{i=1}^n E_i t_i} \quad \text{Equ. V.9}$$

**3. The sum of the bending moment with respect to the bending axis ( $z = t_b$ ) is zero.**

$$\sum_{i=1}^n \int_{h_{i-1}}^{h_i} \sigma_i(z - t_b) dz = 0 \quad \text{Equ. V.10}$$

Hence, the curvature can be determined by Eqs. 5.7, 5.10, 5.12 and 5.13, such that

$$\frac{1}{r} = \frac{\sum_1^n E_i t_i (2h_{i-1} + t_i) \left( c - \alpha_i \Delta T + \frac{d_i V_i}{t_i} + \frac{\bar{\sigma}_i}{E_i} \right)}{\sum_1^n E_i t_i \left( 6h_{i-1}^2 + 6h_{i-1} t_i + 2t_i^2 - 3t_b (2h_{i-1} + t_i) \right)} \quad \text{Equ. V.11}$$

After the curvature ( $r$ ) is known from Equ. V.11, the small mechanical deflection at the end point of an L-length cantilever can be simply given by the following equation:

$$d = \frac{L^2}{2r} \quad \text{Equ. V.12}$$

### V.3.2) Characterization on piezoelectric membrane

Piezoelectric response at a given dc voltage was measured by interferometer for both membrane and cantilever. The principles of the interferometry and the setup used in this thesis have been introduced in Section II.3.5. During the measurement, dc voltage was swept while the topography of the piezoelectric device was measured and recorded at each voltage step. Figure V.11 (a) shows the topographic image of a Capal-typed piezoelectric membrane which was captured by the interferometer at zero dc voltage. By taking the mechanical deflection of a point on membrane surface as a function of dc voltage, hysteresis loop was drawn in Figure V.11 (b). The detected point on the membrane surface is indicated in the inset image. The appearance of such hysteresis loop demonstrates that the membrane was well actuated by the applied dc voltage through the piezoelectric effect of the PZT film. The slope of the linear part in the hysteresis loop is measured about  $1.95 \times 10^{-2} \mu\text{m/V}$ .

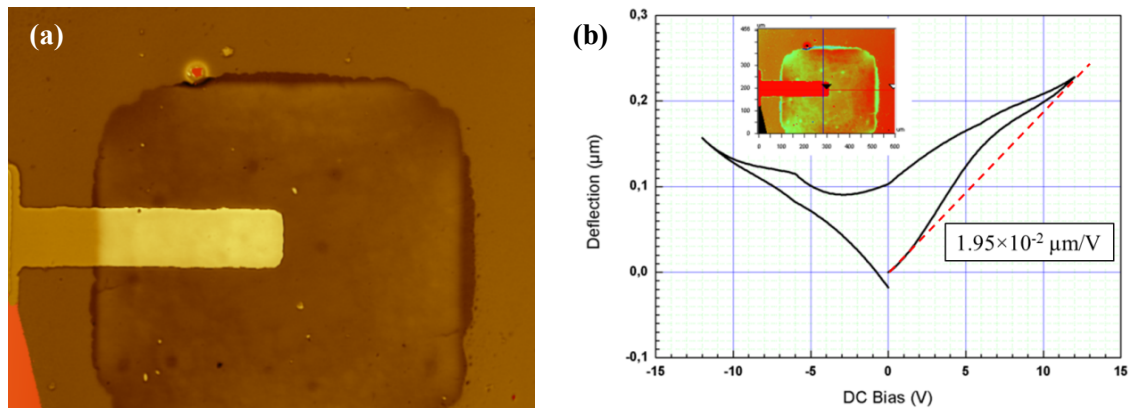


**Figure V.11 - (a) topography of a piezoelectric membrane captured by interferometer at zero dc voltage and (b) hysteresis loop of the mechanical deflection as a function of a point detected on membrane surface.**

On the other hand, Capa2-typed piezoelectric membrane with two top electrodes was measured by the electronic circuit in Figure V.12 (a), where one top electrode is fed by ac voltage and the other one is connected with oscilloscope. The SRO bottom electrode is grounded together with the electronic equipment. Therefore, the mechanical vibration actuated by ac voltage can propagate and induce the voltage on the other top electrode through piezoelectric effect. Figure V.12 (b) and (c) exhibit such open-circuit voltage generated by the piezoelectric membrane where the actuation ac voltage is sinuous and rectangular at 50 kHz. For sinuous ac voltage, the open-circuit voltage shows an asymmetrical output at its positive and negative parts, which can be attributed to the asymmetrical stack of the piezoelectric membrane. Delay is observed in the output voltage due to the finite-velocity propagation of the acoustic wave in the PZT film. For rectangular ac voltage, the electrical pulse induces a transient increase of the open-circuit voltage, which decreases exponentially after the switch of the sign of the input voltage. In this measurement, both direct and converse piezoelectric effects are necessary to transduce the ac voltage from one top electrode to the other and, therefore, the result further confirms the piezoelectricity of the epitaxial PZT film in the membrane.

In conclusion, piezoelectric membrane was successfully fabricated based on epi-PZT/STO/Si stack. Due to the lack of bottom electrode, Si substrate was etched out in order to access the bottom surface of the PZT film. Metallic bottom electrode was then deposited from backside of the stack. SEM image shows a rounded rectangular membrane slightly different from the designed pattern. The electrical measurement confirmed a piezoelectric response of the membrane structure.

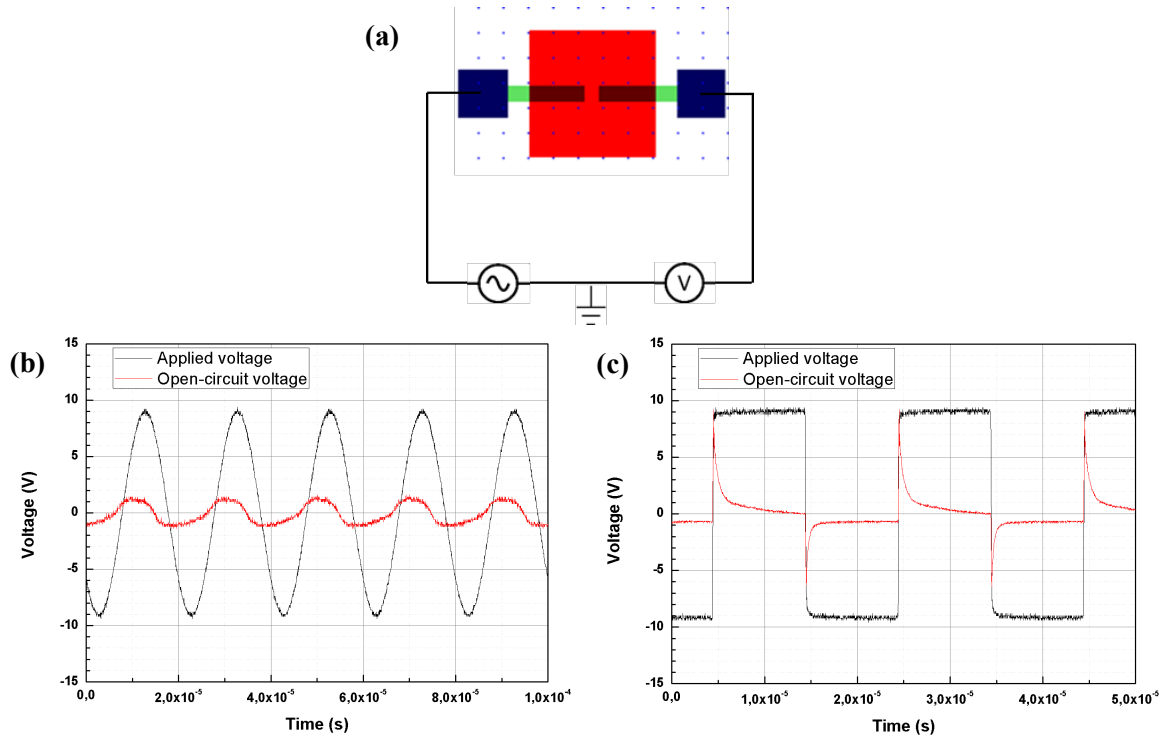


Figure V.12 - Electrical measurement of a Capa2-typed piezoelectric membrane: (a) schematics of the electronic circuit and the display on oscilloscope for (b) sinuous input and (c) pulsed input.

### V.3.3) Characterization on piezoelectric cantilever

A piezoelectric cantilever with a nominal length of  $140\ \mu\text{m}$  was measured by interferometry. Figure V.13 shows the profile along the length of the cantilever under a sweeping dc voltage between  $+8\ \text{V}$  and  $-8\ \text{V}$ . Undercut of  $20\ \mu\text{m}$  is observed due to the isotropic  $\text{XeF}_2$  etching process and therefore the real length of the cantilever is  $160\ \mu\text{m}$ . The right image in Figure V.13 clearly shows a hysteresis loop of the mechanical deflection actuated by the dc voltage at the point  $126\ \mu\text{m}$ -away from the clamp. The slope of the linear part of the hysteresis loop is  $0.28\ \mu\text{m}/\text{V}$ , which corresponds to  $0.413\ \mu\text{m}/\text{V}$  for the end point at the cantilever.

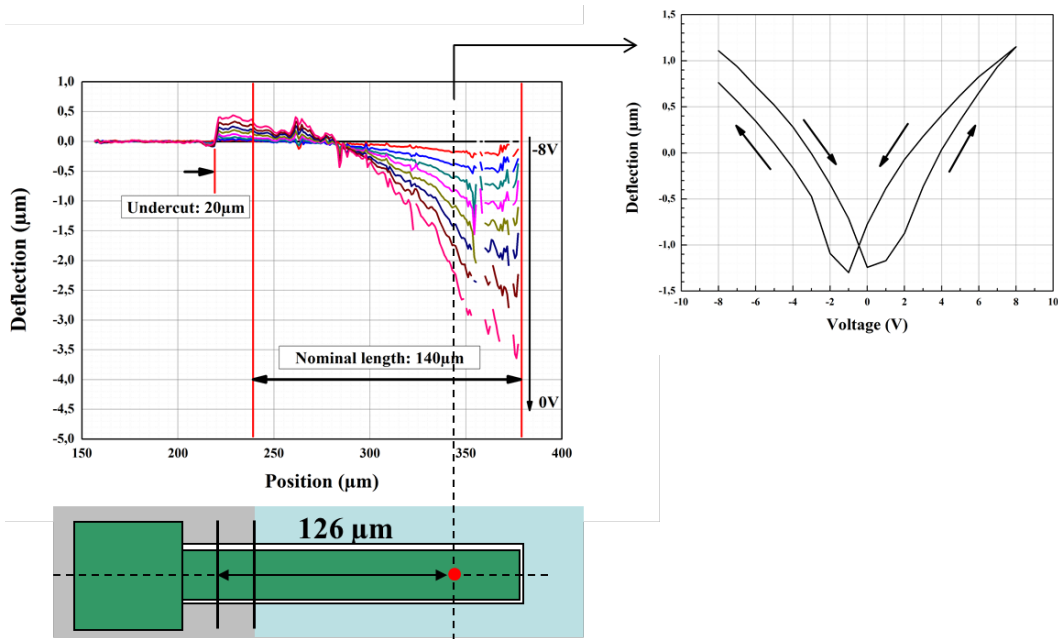


Figure V.13 - Characterization on the deflection of piezoelectric cantilever under a sweeping dc voltage, where the hysteresis loop was measured at the point 126 $\mu\text{m}$ -away from the clamp (indicated by red point).

For analytic modeling, Table V.2 summarizes all the useful parameters, i.e. the thickness and the young's modulus of each layer, where the young's modulus of SrRuO<sub>3</sub> and SrTiO<sub>3</sub> are taken from Ref. <sup>42</sup>. We set the young's modulus ( $E$ ) and the piezoelectric coefficient ( $d_{31}$ ) of PZT film as the variable of the deflection of the cantilever. Since the deflection is a linear function of  $E$  and  $d_{31}$ , the other effects, like residual stress and thermal expansion, can be ignored if relative deflection is taken into the calculation. Since part of SOI Si is unpredictably etched, we simply give the piezoelectric coefficient ( $d_{31}$ ) derived from analytic method for two types of stack, i.e. with or without SOI-Si/BOX-SiO<sub>2</sub>, with Young's modulus of 180 GPa for sol-gel PZT film <sup>[43, 44]</sup>. For the full stack with SOI-Si/BOX-SiO<sub>2</sub>, piezoelectric coefficient of PZT film is 198 pm/V and, on the contrary, for the stack with fully-etched SOI Si the value is quite small (4.17 pm/V).

Table V.2 - The parameters used in the model of piezoelectric cantilever.

	Thickness	Young's Modulus (GPa)
<b>Ru</b>	100 nm	447
<b>PZT</b>	250 nm	180
<b>SrRuO<sub>3</sub></b>	20 nm	164
<b>SrTiO<sub>3</sub></b>	24 nm	284
<b>SOI Si</b>	5 $\mu\text{m}$	170
<b>BOX SiO<sub>2</sub></b>	500 nm	70

#### V.4) Conclusion

In this chapter, based on single crystal epitaxial PZT films, we presented the cleanroom microfabrication processes dedicated to membrane and cantilever structures, respectively, and the characterizations to study their electromechanical performance. Microfabrication of membranes works well using PZT/STO/Si starting stack. However, microfabrication of cantilevers based on PZT/SRO/STO/SOI-Si starting stack drew many technical problems, such as burning of photoresist, unwanted etching of SOI Si. Those problems resulted in dysfunction of the piezoelectric cantilevers. For both structures, characterization of interferometry, which measures the mechanical deflection of the piezoelectric devices under a given dc voltage, clearly shows a piezoelectric response with hysteresis loop. Simulation by FEM and analytic method has been performed but precise piezoelectric coefficients are still impossible to be extracted due to various problems. Eventually, such microfabrication process should be optimized in the future, especially for cantilever structure, to avoid those technical problems mentioned above in order to extract the precise effective piezoelectric coefficients from simulation.

#### V.5) Reference

- 
- [1] Mohamed Gad-el-Hak, 2010, *MEMS: Design and Fabrication*, CRC Press, p. I-1 - I-5.
- [2] D. Niarchos, "Magnetic MEMS: key issues and some applications," *Sensors and Actuators A: Physical*, **vol. 109**, no. 1–2, pp. 166–173, Dec. 2003.
- [3] H. Miyajima and M. Mehregany, "High-aspect-ratio photolithography for MEMS applications," *Journal of Microelectromechanical Systems*, **vol. 4**, no. 4, pp. 220–229, 1995.
- [4] N. Harned, "Ultralight lithography [IC manufacture]," *IEEE Spectrum*, **vol. 36**, no. 7, pp. 35–40, Jul. 1999.
- [5] E. A. Irene, "Silicon oxidation studies: A revised model for thermal oxidation," *Journal of Applied Physics*, **vol. 54**, no. 9, p. 5416, 1983.
- [6] P. M. Fahey, P. B. Griffin, and J. D. Plummer, "Point defects and dopant diffusion in silicon," *Reviews of Modern Physics*, **vol. 61**, no. 2, pp. 289–384, Apr. 1989.
- [7] J. R. Conrad, J. L. Radtke, R. a. Dodd, F. J. Worzala, and N. C. Tran, "Plasma source ion-implantation technique for surface modification of materials," *Journal of Applied Physics*, **vol. 62**, no. 11, p. 4591, 1987.
- [8] K. Choy, "Chemical vapour deposition of coatings," *Progress in Materials Science*, **vol. 48**, no. 2, pp. 57–170, 2003.

- [9] Y. Xu, C. H. Lei, B. Ma, H. Evans, H. Efstathiadis, R. Manisha, M. Massey, U. Balachandran, and R. Bhattacharya, "Growth of textured MgO through e-beam evaporation and inclined substrate deposition," *Superconductor Science and Technology*, **vol. 19**, no. 8, pp. 835–843, Aug. 2006.
- [10] J.-C. Pivin, "An overview of ion sputtering physics and practical implications," *Journal of Materials Science*, **vol. 18**, no. 5, pp. 1267–1290, May 1983.
- [11] D. R. Turner, "On the Mechanism of Chemically Etching Germanium and Silicon," *Journal of The Electrochemical Society*, **vol. 107**, no. 10, p. 810, 1960.
- [12] M. Armacost, P. D. Hoh, R. Wise, W. Yan, J. J. Brown, J. H. Keller, G. A. Kaplita, S. D. Halle, K. P. Muller, M. D. Naeem, S. Srinivasan, H. Y. Ng, M. Gutsche, A. Gutmann, and B. Spuler, "Plasma-etching processes for ULSI semiconductor circuits," *IBM Journal of Research and Development*, **vol. 43**, no. 1.2, pp. 39–72, Jan. 1999.
- [13] H. Jansen, H. Gardeniers, M. de Boer, M. Elwenspoek, and J. Fluitman, "A survey on the reactive ion etching of silicon in microtechnology," *Journal of Micromechanics and Microengineering*, **vol. 6**, no. 1, pp. 14–28, Mar. 1996.
- [14] M. J. Vasile, "Microfabrication by ion milling: The lathe technique," *Journal of Vacuum Science & Technology B: Microelectronics and Nanometer Structures*, **vol. 12**, no. 4, p. 2388, Jul. 1994.
- [15] J. M. Bustillo, R. T. Howe, R. S. Muller, "Surface micromachining for micro-electromechanical systems," *Proceedings of the IEEE*, **vol. 86**, no. 8, pp. 1552–1574, 1998.
- [16] G. T. A. Kovacs, N. I. Maluf, and K. E. Petersen, "Bulk micromachining of silicon," *Proceedings of the IEEE*, **vol. 86**, no. 8, pp. 1536–1551, 1998.
- [17] F. Laermer and A. Urban, "Challenges, developments and applications of silicon deep reactive ion etching," *Microelectronic Engineering*, **vol. 67–68**, no. 4, pp. 349–355, Jun. 2003.
- [18] M. Hecke and W. K. Schomburg, "Review on micro molding of thermoplastic polymers," *Journal of Micromechanics and Microengineering*, **vol. 14**, no. 3, pp. R1–R14, Mar. 2004.
- [19] U. Gösele and Q.-Y. Tong, "SEMICONDUCTOR WAFER BONDING," *Annual Review of Materials Science*, **vol. 28**, no. 1, pp. 215–241, Aug. 1998.
- [20] P. W. Barth, "Silicon fusion bonding for fabrication of sensors, actuators and microstructures," *Sensors and Actuators A: Physical*, **vol. 23**, no. 1–3, pp. 919–926, Apr. 1990.

- [21] M. Nese and A. Hanneborg, "Anodic bonding of silicon to silicon wafers coated with aluminium, silicon oxide, polysilicon or silicon nitride," *Sensors and Actuators A: Physical*, **vol. 37–38**, pp. 61–67, Jun. 1993.
- [22] F. Mei, J. Jiang, and W. J. Meng, "Eutectic bonding of Al-based high aspect ratio microscale structures," *Microsystem Technologies*, **vol. 13**, no. 7, pp. 723–730, Jan. 2007.
- [23] J. F. Kuhmann, A. Preuss, B. Adolphi, K. Maly, T. Wirth, W. Oesterle, W. Pittroff, G. Weyer, and M. Fanciulli, "Oxidation and reduction kinetics of eutectic SnPb, InSn, and AuSn: a knowledge base for fluxless solder bonding applications," *IEEE Transactions on Components, Packaging, and Manufacturing Technology: Part C*, **vol. 21**, no. 2, pp. 134–141, Apr. 1998.
- [24] R. D. Black, S. D. Arthur, R. S. Gilmore, N. Lewis, E. L. Hall, and R. D. Lillquist, "Silicon and silicon dioxide thermal bonding for silicon-on-insulator applications," *Journal of Applied Physics*, **vol. 63**, no. 8, p. 2773, 1988.
- [25] C. Wenzel, A. Jahn, and D. Zeidler, "UV-LIGA: a promising and low-cost variant for microsystem technology," in *1998 Conference on Optoelectronic and Microelectronic Materials and Devices. Proceedings (Cat. No.98EX140)*, pp. 380–383.
- [26] C.-H. Lin, G.-B. Lee, B.-W. Chang, and G.-L. Chang, "A new fabrication process for ultra-thick microfluidic microstructures utilizing SU-8 photoresist," *Journal of Micromechanics and Microengineering*, **vol. 12**, no. 5, pp. 590–597, Sep. 2002.
- [27] J. Fahrenberg, W. Bier, D. Maas, W. Menz, R. Ruprecht, and W. K. Schomburg, "A microvalve system fabricated by thermoplastic molding," *Journal of Micromechanics and Microengineering*, **vol. 5**, no. 2, pp. 169–171, Jun. 1995.
- [28] T. I. Kamins, "Structure and Properties of LPCVD Silicon Films," *Journal of The Electrochemical Society*, **vol. 127**, no. 3, p. 686, 1980.
- [29] H. Van Brussel, J. Peirs, D. Reynaerts, A. Delchambre, G. Reinhart, N. Roth, M. Weck, and E. Zussman, "Assembly of Microsystems," *CIRP Annals - Manufacturing Technology*, **vol. 49**, no. 2, pp. 451–472, Jan. 2000.
- [30] J. H. Smith, S. Montague, J. J. Sniegowski, J. R. Murray, and P. J. McWhorter, "Embedded micromechanical devices for the monolithic integration of MEMS with CMOS," in *Proceedings of International Electron Devices Meeting*, pp. 609–612.

- [31] M. Cuffe, E. Defay, G. Le Rhun, P. Rey, F. Perruchot, A. Suhm, and M. Aïd, "Integrated metallic gauge in a piezoelectric cantilever," *Sensors Actuators A Phys.*, **vol. 172**, no. 1, pp. 148–153, Dec. 2011.
- [32] F. Casset, M. Cuffe, E. Defay, G. Le Rhun, A. Suhm, P. Ancey, and A. Devos, "Piezoelectric membrane actuator design," in *2011 12th Intl. Conf. on Thermal, Mechanical & Multi-Physics Simulation and Experiments in Microelectronics and Microsystems*, 2011, pp. 1/5–5/5.
- [33] S. D. Bernstein, T. Y. Wong, Y. Kisler, and R. W. Tustison, "Fatigue of ferroelectric  $\text{PbZr}_x\text{Ti}_y\text{O}_3$  capacitors with Ru and  $\text{RuO}_x$  electrodes," *Journal of Materials Research*, **vol. 8**, no. 1, pp. 12–13, Jan. 1993.
- [34] A. Tarraf, J. Daleiden, S. Irmer, D. Prasai, and H. Hillmer, "Stress investigation of PECVD dielectric layers for advanced optical MEMS," *Journal of Micromechanics and Microengineering*, **vol. 14**, no. 3, pp. 317–323, Mar. 2004.
- [35] S. K. Ray, C. K. Maiti, S. K. Lahiri, and N. B. Chakrabarti, "TEOS-based PECVD of silicon dioxide for VLSI applications," *Advanced Materials for Optics and Electronics*, **vol. 6**, no. 2, pp. 73–82, Mar. 1996.
- [36] J. H. Klootwijk, K. B. Jinesh, W. Dekkers, J. F. Verhoeven, F. C. van den Heuvel, H.-D. Kim, D. Blin, M. A. Verheijen, R. G. R. Weemaes, M. Kaiser, J. J. M. Ruigrok, and F. Roozeboom, "Ultrahigh Capacitance Density for Multiple ALD-Grown MIM Capacitor Stacks in 3-D Silicon," *IEEE Electron Device Letters*, **vol. 29**, no. 7, pp. 740–742, Jul. 2008.
- [37] K. Takahashi and M. Sekiguchi, "Through Silicon Via and 3-D Wafer/Chip Stacking Technology," in *2006 Symposium on VLSI Circuits, 2006. Digest of Technical Papers.*, pp. 89–92.
- [38] F. Laermer and A. Urban, "Challenges, developments and applications of silicon deep reactive ion etching," *Microelectronic Engineering*, **vol. 67–68**, no. 4, pp. 349–355, Jun. 2003.
- [39] F. I. Chang, R. Yeh, G. Lin, P. B. Chu, E. G. Hoffman, E. J. Kruglick, K. S. J. Pister, and M. H. Hecht, "Gas-phase silicon micromachining with xenon difluoride," 1995, pp. 117–128.
- [40] P. B. Chu, J. T. Chen, R. Yeh, G. Lin, J. C. P. Huang, B. A. Warneke, and S. J. Pister, "Controlled pulse-etching with xenon difluoride," in *Proceedings of International Solid State Sensors and Actuators Conference (Transducers '97)*, **vol. 1**, pp. 665–668.
- [41] C. H. Hsueh, "Thermal stresses in elastic multilayer systems," *Thin Solid Films*, **vol. 418**, no. 2, pp. 182–188, Oct. 2002.

- [42] S. H. Baek, J. Park, D. M. Kim, V. A. Aksyuk, R. R. Das, S. D. Bu, D. A. Felker, J. Lettieri, V. Vaithyanathan, S. S. N. Bharadwaja, N. Bassiri-Gharb, Y. B. Chen, H. P. Sun, C. M. Folkman, H. W. Jang, D. J. Kreft, S. K. Streiffer, R. Ramesh, X. Q. Pan, S. Trolier-McKinstry, D. G. Schlom, M. S. Rzechowski, R. H. Blick, and C. B. Eom, "Giant piezoelectricity on Si for hyperactive MEMS.," *Science* (New York, N.Y.), **vol. 334**, no. 6058, pp. 958–61, Nov. 2011.
- [43] P. Delobelle, G. S. Wang, E. Fribourg-Blanc, and D. Remiens, "Mechanical properties measured by nano-indentation of Pb(Zr, Ti)O<sub>3</sub> sol-gel films deposited on Pt and LaNiO<sub>3</sub> electrodes," *Surf. Coatings Technol.*, **vol. 201**, no. 6, pp. 3155–3162, Dec. 2006.
- [44] P. Delobelle, G. S. Wang, E. Fribourg-Blanc, and D. Remiens, "Indentation modulus and hardness of Pb(Zr, Ti)O<sub>3</sub> sol-gel films deposited on Pt and LaNiO<sub>3</sub> electrodes," *J. Eur. Ceram. Soc.*, **vol. 27**, no. 1, pp. 223–230, Jan. 2007.



## **General conclusion and perspectives**

---

---

Integration of functional materials, such as ferroelectric or piezoelectric oxides, on silicon has become a great challenge for developing a great variety of applications in the field of sensors, actuators, energy harvesters, and so on. The objective of this thesis has mainly focused on integration of single crystal like epitaxially grown ferroelectric thin films, i.e.  $\text{Pb}(\text{Zr}_{0.52}\text{Ti}_{0.48})\text{O}_3$  (PZT) and  $0.9\text{Pb}(\text{Mg}_{1/3}\text{Nb}_{2/3})\text{O}_3-0.1\text{PbTiO}_3$  (PMN-PT), on Si substrate. This project was initiated by CEA LETI and INL in order to study the ability of integrating single crystalline piezoelectric oxides epitaxially grown on Si with the aim to enhance the performance of piezoelectric MEMS devices. The strategy of this integration was based on the epitaxial growth of oxide template and bottom electrode, allowing the subsequent deposition of high-quality epitaxial ferroelectric films. A main part of our work has concerned the optimization of the growth conditions of ferroelectric oxides in term of crystallinity and electrical performances. In the last part, cleanroom microfabrication was performed to realize piezoelectric cantilever and membrane for device-level characterization. Using interferometry measurement, an appropriate piezoelectric response was detected under dc actuation voltage. This result indicates the successful integration of epitaxially grown ferroelectric film on silicon wafer, which could satisfy the requirement of silicon monolithic integration for future MEMS devices.

In the first step, both PZT and PMN-PT films were deposited by sol-gel method due to its simplicity and compatibility with modern MEMS manufacturing. For PZT deposition,  $\text{Gd}_2\text{O}_3$  template was first attempted on Si(111) substrate. Nearly-zero lattice misfit of  $\text{Gd}_2\text{O}_3$  and Si results in an excellent epitaxial  $\text{Gd}_2\text{O}_3$  film grown by Molecular Beam Epitaxy (MBE). However, the large lattice misfit of  $\text{Gd}_2\text{O}_3$  and PZT causes a degraded PZT film which consists of polycrystalline perovskite phase and pyrochlore phase. The formation of a non-ferroelectric pyrochlore phase with a reduction of piezoelectric performance of the PZT film allowed to not continuing the experiment on  $\text{Gd}_2\text{O}_3$  template. Another approach using  $\text{SrTiO}_3$  (STO) template and  $\text{SrRuO}_3$  (SRO) bottom electrode successfully yields an epitaxial single-crystal PZT film with pure perovskite phase. Deposition of STO was realized by MBE and SRO was grown by Pulsed Laser Deposition. The as-deposited STO and SRO films are epitaxially grown on silicon thanks to their small lattice misfit. Ultra-high vacuum conditions in the MBE chamber allow a precise interface engineering that allows the subsequent growth of epitaxial STO and SRO films. The successful deposition of epitaxial STO template is essentially important to the whole process of integration, which provides an oxide-terminated silicon surface. Different annealing temperatures

## *General conclusion and perspectives*

---

were studied for the influence on the crystalline structure and the electrical properties of the PZT films. Compared with the overheating at 700°C, 650°C annealing for 1 min is adequate for a full crystallization of the amorphous PZT film without any pyrochlore phase. The as-grown PZT/SRO/STO/Si stack follows the relationship of crystalline orientations as [100] PZT (001) // [100] SRO (001) // [100] STO (001) // [110] Si (001). The epitaxial PZT films up to 1.26 μm thickness exhibit high film quality, large remnant polarization, and piezoelectric function, which are important requirements for piezoelectric MEMS. The films show a thickness-dependent properties indicating a stress-releasing mechanism in the epitaxial film. This effect likely has strong influence on the electrical properties of the epitaxial PZT film, where the best film quality gives rise to lower permittivity and smaller remnant polarization. In addition, PFM measurement (Piezoresponse Force Microscopy) shows distinct domain dynamics between two PZT films with different film quality. The time evolution of the artificial ferroelectric domain demonstrates a back-switching mechanism in the best-quality PZT film. It can be concluded that a large residual stress appears, leading to the instability of the ferroelectric domains which will turn back to its initial orientation within a few hours.

In a second step, sol-gel deposition of PMN-PT thin films on silicon wafer was also carried out in this thesis using STO template and SRO bottom electrode. It was not easy to achieve pure perovskite PMN-PT films on silicon wafer without pyrochlore phase due to its complicated chemical composition. From the aspect of epitaxy, our successful integration of pure perovskite PMN-PT films on silicon wafer will definitely extend its practical applications. Similar to sol-gel PZT film, both 90 nm and 270 nm epitaxial PMN-PT films grown on SRO/STO/Si substrate shows a relationship of crystalline orientations corresponding to [100] PMN-PT (001) // [100] SRO (001) // [100] STO (001) // [110] Si (001) with a tensile residual stress. Although bulk PMN-PT was observed to form superlattice structure indicating the formation of chemically ordered structure, our TEM observation on epitaxial PMN-PT film shows no such structure at room temperature. Moreover, temperature-dependent infrared transmission exhibits a clear softening process towards the high temperature between 5 K and 385 K and a local ferroelectric transition occurs at around 70 K. The temperature-dependent electrical measurement shows a broad peak of dielectric permittivity without frequency dispersion, namely no feature of relaxor ferroelectrics. Besides, electrical measurement at room temperature shows a behavior between relaxor ferroelectric and ordinary ferroelectric. Since large tensile stress occurs in the epitaxial single crystal PMN-PT film, the effect of elastic stress is likely responsible for the anomalous behavior. Further experimental researches are still required to explain those phenomena.

In a last step, based on epitaxial PZT film grown on silicon wafer, microfabrication was processed in clean room to realize piezoelectric cantilevers and membranes. The membrane

## *General conclusion and perspectives*

---

structure was successfully obtained based on PZT/STO/Si stack with good piezoelectric functions. However, the cantilever structure was not well fabricated as the structural SOI (Silicon-On-Insulator) Si was accidentally etched out leading to unpredictable cantilever geometry. Although the cantilever functions well under the actuation of dc voltage, it was not possible to extract the piezoelectric coefficients. Optimization of the microfabrication process should be carried out to get a new reliable heterostructure.

In summary, this thesis draws the main focus on integration of epitaxial ferroelectric films on silicon substrate. Use of STO template and SRO bottom electrode has been experimentally proven as an appropriate way to grow epitaxial single-crystal thin film in this thesis work. Piezoelectric properties of the epitaxial PZT and PMN-PT films were clearly detected through various characterizations and different MEMS structures. However, further optimization and characterizations are still required to enhance the properties of sol-gel ferroelectric films and perform systematical study on various effects. The similar researches performed on bulk single crystal, polycrystalline film, or the film based on oxide substrates should be carefully studied for single-crystal films on Si substrate, such as strain effect, morphotropic boundary, chemical composition, bottom electrode, and so on. For sol-gel deposition, chemical profile and homogeneity of the epitaxial film are closely related to the growth condition, which thus influences various characteristics of ferroelectric film. Tensile stress is often developed in sol-gel deposited ferroelectric films, leading to the formation of a-domain. The presence of a/c/a/c domain structure can help exhausting the dielectric permittivity and the piezoelectric coefficients of the epitaxial films and, thus, deteriorate their performance in the applications. Since the tensile stress is mainly caused by different thermal expansion coefficients between PZT and Si, decrease of annealing temperature in the sol-gel deposition is likely feasible to avoid large tensile stress. This concerns the modification of the sol-gel process using a low-temperature precursor solution. In addition, SOI wafer is widely used in MEMS manufacture. Due to the addition of a buried SiO<sub>2</sub> layer, optimum deposition condition of oxide layers on SOI wafer is modified and different from those on Si wafer. This will definitely induce the derivation of the piezoelectric performance of the ferroelectric thin film away from the best one. The optimization should involve the consideration of the thermal conduction and also the thermal dilatation in the SOI wafer. Thus, the growth temperature of STO, SRO, PZT, and PMN-PT must be tuned for the new substrate to achieve the optimal properties. In order to achieve a well-defined piezoelectric cantilever, our microfabrication process needs to be improved to avoid the accidental etching of the BOX Si layer. The thick photoresist for a series of etching processes must be carefully selected to prevent burning from the plasma damage. Besides, from the aspect of MEMS device, additional characterizations are needed to measure residual stress, piezoelectric coefficient of the clamped and released ferroelectric films, and mechanical properties, like Young's modulus,

### *General conclusion and perspectives*

---

Poisson coefficient, etc. Those parameters are useful for comparison and modeling of the piezoelectric MEMS devices. Finally, new applications might be discovered due to the high performance of the epitaxial single-crystal films on Si in various effects, which could be extensively developed and studied for different electronic devices.

**Appendix**

---

---

<b>A)</b>	<b>Attempt to integrate PZT films on Si(111) using Gd<sub>2</sub>O<sub>3</sub> buffer layer...180</b>
A.1)	Introduction ..... 180
A.2)	Deposition of Gd <sub>2</sub> O <sub>3</sub> film on Si(111) by Molecular Beam Epitaxy ..... 182
A.3)	Structural characterization of Gd <sub>2</sub> O <sub>3</sub> /Si(111) substrate ..... 184
A.4)	Sol-gel deposition of PZT film on Gd <sub>2</sub> O <sub>3</sub> /Si(111) substrate ..... 185
A.5)	Conclusion ..... 188
<b>B)</b>	<b>Finite Element Method ..... 188</b>
<b>C)</b>	<b>Reference ..... 191</b>

## A) Attempt to integrate PZT films on Si(111) using Gd<sub>2</sub>O<sub>3</sub> buffer layer

### A.1) Introduction

Gadolinium oxide (Gd<sub>2</sub>O<sub>3</sub>) is one of the rare-earth (RE) metal oxides, which attracts intensive researches as high-k material to replace SiO<sub>2</sub> CMOS gate dielectric material for the future semiconductor industry [1, 2]. Gd<sub>2</sub>O<sub>3</sub> has a cubic crystalline structure (Ia $\bar{3}$ ) at room temperature, similar with that of manganese oxide (Mn<sub>2</sub>O<sub>3</sub>), called bixbyite structure. At 1200 °C, phase transition occurs and Gd<sub>2</sub>O<sub>3</sub> changes to monoclinic structure (C2/m). In the cubic structure, there are two types of gadolinium sites, both with a coordination number of 6 but with different geometry of the surrounding oxygen atoms. The lattice constant of bulk Gd<sub>2</sub>O<sub>3</sub> is 10.814 Å [3], nearly 2 times of that of silicon (5.431 Å), which produces perhaps the smallest lattice mismatch (-0.44 %) with Si. Bulk Gd<sub>2</sub>O<sub>3</sub> presents a dielectric constant of 24 [4], a bandgap of 5.3 eV [5], conduction and valence band offsets with respect to Si of 1.8 eV and 2.4 eV, respectively.

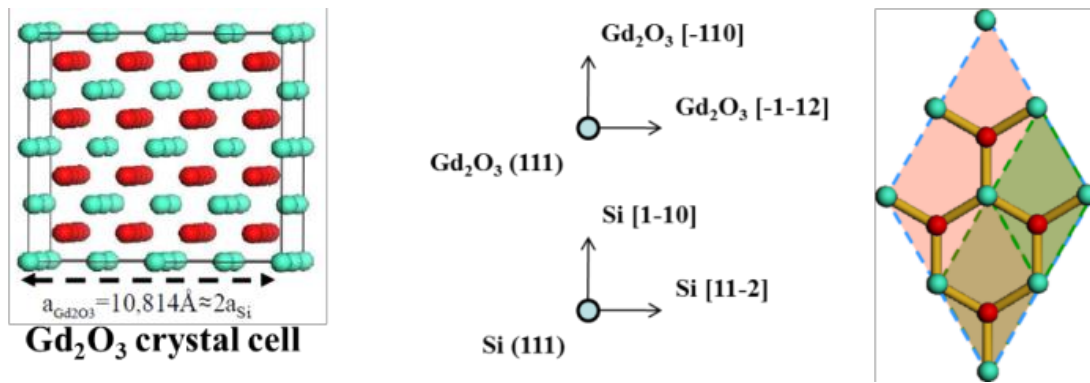


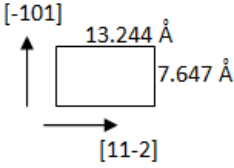
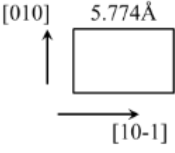
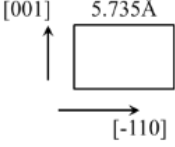
Figure A.1 - Gd<sub>2</sub>O<sub>3</sub> cubic structure and its epitaxial relationship on Si(111) substrate.

Small lattice mismatch between Gd<sub>2</sub>O<sub>3</sub> and Si allows Gd<sub>2</sub>O<sub>3</sub> being an excellent candidate for the use of buffer layer on Si substrate. On Si(001) substrate, two possible crystalline orientations usually coexist in Gd<sub>2</sub>O<sub>3</sub> film, namely  $[\bar{1}10]_{\text{Gd}_2\text{O}_3(110)} \parallel [110]_{\text{Si}(110)}$  and  $[001]_{\text{Gd}_2\text{O}_3(110)} \parallel [1\bar{1}0]_{\text{Si}(001)}$  [6]. By using vicinal Si(001) substrate (4° miscut along <110> azimuth), Kwo *et al.* successfully grew single-domain Gd<sub>2</sub>O<sub>3</sub> epitaxial layer [7, 8]. Compared with bi-domain structure of Gd<sub>2</sub>O<sub>3</sub> film, single crystalline Gd<sub>2</sub>O<sub>3</sub> film, which eliminates domain boundary effect, leads to enhanced electrical properties [9]. On Si(111) substrate, Gd<sub>2</sub>O<sub>3</sub> film is found to consist of single domain with  $[\bar{1}10]_{\text{Gd}_2\text{O}_3(111)} \parallel [1\bar{1}0]_{\text{Si}(111)}$  epitaxial orientation [10]. Figure A.1 demonstrates such epitaxial relationship for Gd<sub>2</sub>O<sub>3</sub> film on Si(111) substrate. Due to its high-quality crystalline structure and potential applications to integrate functional oxides on Si substrate, Gd<sub>2</sub>O<sub>3</sub>/Si(111) heterostructure attracts increasing interests and researches [11].

## Appendix

In order to attempt the epitaxial growth of PZT film on  $\text{Gd}_2\text{O}_3/\text{Si}(111)$ , lattice mismatch between  $\text{Gd}_2\text{O}_3$  and PZT must be taken into consideration. On  $\text{Gd}_2\text{O}_3(111)$  surface, the 2D repetitive pseudo-lattice can be regarded as a rectangle shape with dimension of  $1.32 \text{ nm} \times 0.76 \text{ nm}$ . Small lattice mismatch between  $\text{Gd}_2\text{O}_3$  and PZT can be achieved if PZT film grows with (101) or (110) growing direction. If one doubles PZT 2D pseudo-lattice, lattice mismatch will be  $-12.80\% \times 6.05\%$  for (101) growing direction, and will be  $-13.39\% \times 7.49\%$  for (110) growing direction (see Table A.1). In Ref. 12, pure perovskite PZT film was successfully deposited on  $\text{Y}_2\text{O}_3/\text{Si}(111)$  substrate, where lattice mismatch of PZT and  $\text{Y}_2\text{O}_3$  is  $-10.9\% \times 7.7\%$ , smaller than the case of  $\text{Gd}_2\text{O}_3$  buffer layer. Other templates for successful growth of epitaxial PZT films on Si(111) substrate in the references include  $\text{CeO}_2$  [13] and  $\text{Al}_2\text{O}_3$  [14]. In following section, we will mainly introduce the fabrication process of  $\text{Gd}_2\text{O}_3$  buffer layer on Si(111) substrate and the sol-gel PZT film on  $\text{Gd}_2\text{O}_3/\text{Si}(111)$ . Various characterizations on crystalline structure and electrical properties will also be addressed.

**Table A.1 - Two possible growing directions for epitaxial PZT films on  $\text{Gd}_2\text{O}_3/\text{Si}(111)$  substrate.**

$\text{Gd}_2\text{O}_3$ 2D pseudo-lattice	PZT 2D pseudo-lattice	Lattice mismatch
	<p>PZT(101)</p> 	$-12.80\% \times 6.05\%$
	<p>PZT(110)</p> 	$-13.39\% \times 7.49\%$

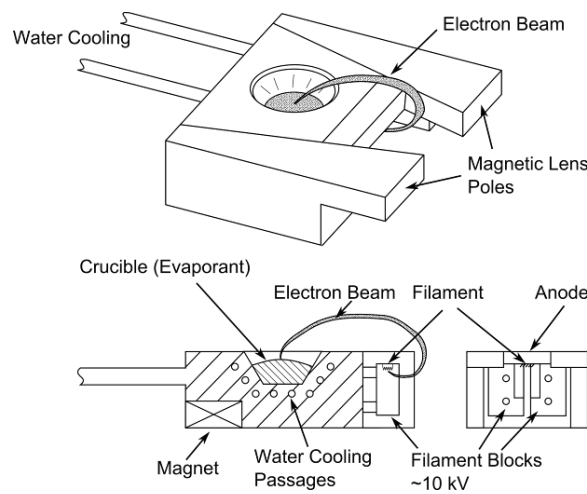


**Figure A.2 - E-beam evaporator used for deposition of  $\text{Gd}_2\text{O}_3$  in MBE growth chamber.**

## A.2) Deposition of Gd<sub>2</sub>O<sub>3</sub> film on Si(111) by Molecular Beam Epitaxy

In this thesis, epitaxial growth of Gd<sub>2</sub>O<sub>3</sub> on Si(111) substrate was carried out by an e-beam evaporator which is installed in our MBE system. Due to its binary chemical composition, direct use of granular Gd<sub>2</sub>O<sub>3</sub> target material is possible with the help of oxygen ambient<sup>[15, 16]</sup>. The e-beam evaporator is schematically illustrated in Figure A.2. In the evaporator, electron beam is generated by the thermionic emission effect of a resistive filament and then accelerated by the electric field between target material and the filament. An electromagnet is used to deflect the e-beam onto the surface of the target material. Energy transferred by the e-beam heats and evaporates the target material that will be then condensed on substrate surface. By tuning the magnetic field, the bombard position of the e-beam could scan on the surface of the target material with a preset mode to achieve a homogeneous evaporation.

Before introducing Si substrate into MBE chamber, the substrate is prepared by chemical treatment to eliminate the surface contamination and generate a relatively smooth surface for the deposition of Gd<sub>2</sub>O<sub>3</sub>. The treatment process can be found in Section III.3.3.1. After the treatment, a layer of nm-thick pure SiO<sub>2</sub> layer covers on the Si substrate, which must be removed before deposition of Gd<sub>2</sub>O<sub>3</sub>. The strategy, which uses high-temperature annealing (900°C) for 30 min to directly evaporate SiO<sub>2</sub>, is employed<sup>[17]</sup>. The annealing process holds the following chemical reaction:



After removal of SiO<sub>2</sub> layer, Si(111) surface shows a RHEED pattern of a single crystalline surface (Figure A.3 (a)). The expected 7×7 surface reconstruction is not observed in the pattern, which is mainly due to the highly rough Si surface. To improve surface smoothness, Si homoepitaxy is performed in the vacuum. During the homoepitaxy, substrate temperature is kept at 650°C and emission current of the e-beam is set at 50 mA. In few minutes, 7×7 surface reconstruction appears in the RHEED pattern, indicating an atomic-level smooth Si surface (Figure A.3 (b)). Such 7×7 reconstruction of Si surface was first demonstrated by Takayanagi *et al.* as a dimer-adatom-stacking-fault (DAS) model which involves the rearrangement of Si atoms in the first five layers (Figure A.4)<sup>[13]</sup>. In addition, 7×7 Si(111) surface changes to a disordered 1×1 structure above 850°C, which can be converted back to 7×7 structure by slow cooling.

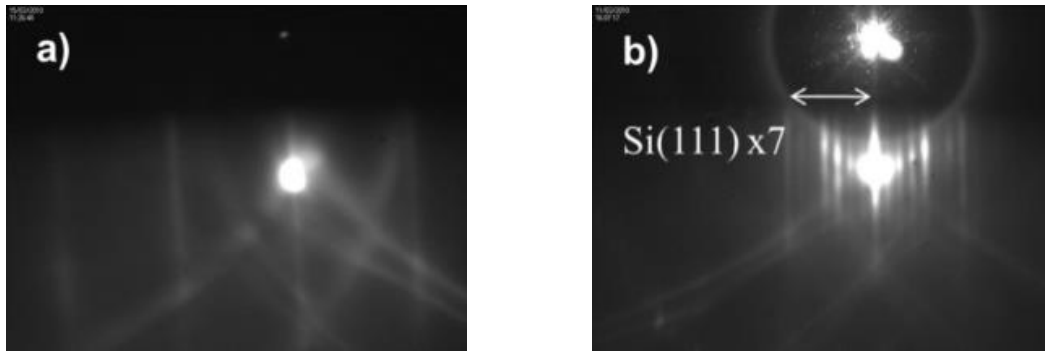


Figure A.3 - RHEED patterns of Si(111) surface along Si[110] azimuth after the chemical treatment (a) and after the Si homoepitaxial deposition (b).

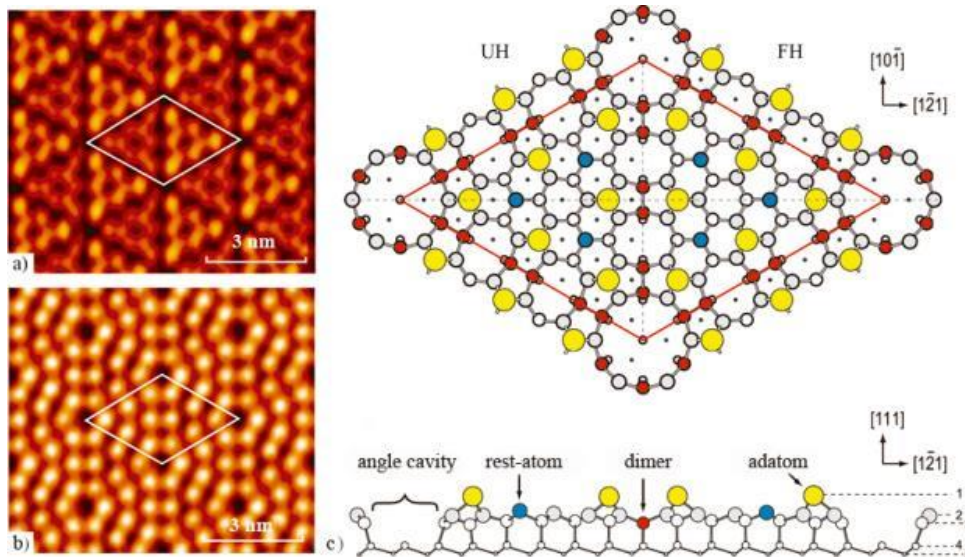


Figure A.4 -  $7 \times 7$  reconstruction of Si(111) surface. STM images of (a) filled and (b) unfilled electron states of surface; (c) schematic representation of surface (plan and side views) of Takayanagi DAS model <sup>[18]</sup>.

Once a smooth Si(111) surface was obtained with  $\times 7$  RHEED pattern,  $\text{Gd}_2\text{O}_3$  heteroepitaxy can be performed with the optimal growth condition listed in Table A.2 <sup>[19]</sup>. Under such condition, deposition rate is about  $2\sim 3 \text{ \AA}/\text{min}$ . However, for the first few monolayers (ML) of  $\text{Gd}_2\text{O}_3$ , zero oxygen pressure is required to avoid the formation of any parasitic phase at the interface. Figure A.5 shows the RHEED patterns of an as-grown 6.0nm-thick  $\text{Gd}_2\text{O}_3$  film, where bright and streaky diffraction lines are observed indicating high film quality and quite smooth surface. Besides,  $\times 4$  reconstruction is clearly seen in the pattern. It is likely caused by the oxygen vacancies, which are formed due to the low oxygen pressure in the MBE growth chamber.

## Appendix

**Table A.2 - Optimal growth condition for Si homoepitaxy and Gd<sub>2</sub>O<sub>3</sub> heteroepitaxy on Si(111) substrate.**

	Si homoepitaxy on Si(111)	Gd <sub>2</sub> O <sub>3</sub> heteroepitaxy on Si(111)
<b>Substrate temperature</b>	650°C	700°C
<b>E-beam emission current</b>	50 mA	25 mA
<b>Oxygen pressure</b>	vacuum	5×10 <sup>-7</sup> Torr

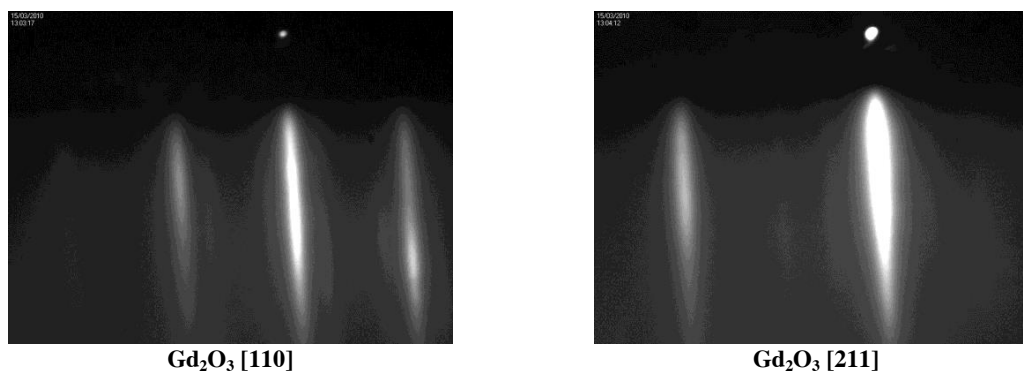


**Figure A.5 - RHEED patterns of Gd<sub>2</sub>O<sub>3</sub>(111) surface of a 6.0nm-thick Gd<sub>2</sub>O<sub>3</sub> film on Si(111) substrate along the [110] and [211] azimuths in the vacuum.**

### A.3) Structural characterization of Gd<sub>2</sub>O<sub>3</sub>/Si(111) substrate

For use of buffer layer, the most interesting characterizations are crystalline structure and surface morphology. In Figure A.6, XRD was performed on Gd<sub>2</sub>O<sub>3</sub>/Si(111) substrate using various modes. Out-of-plane 2θ/ω XRD in Figure A.6 (a) reveals a pure c-(111) crystalline structure in the as-grown Gd<sub>2</sub>O<sub>3</sub> film. The Pendellösung fringes are clearly seen in Figure A.6 (b) around Gd<sub>2</sub>O<sub>3</sub>(111) Bragg peak, demonstrating a relatively smooth film surface. In Figure A.6 (c), Φ scan XRD shows an angular difference of 60° between Gd<sub>2</sub>O<sub>3</sub>{222} and Si{111} Bragg peaks, which further confirms the epitaxial growth of single crystal Gd<sub>2</sub>O<sub>3</sub> film on Si(111). The full-width-at-half-maximum (FWHM) value derived from the rocking curve of Gd<sub>2</sub>O<sub>3</sub>(222) Bragg peak is about 0.1°. Moreover, an abrupt and sharp Gd<sub>2</sub>O<sub>3</sub>/Si interface is observed in TEM image (not shown) thanks to the zero oxygen pressure at the initial stage. This is different from the reported research in Ref. <sup>20</sup> that reveals a 9.01Å-thick Gd<sub>x</sub>Si<sub>y</sub>O layer in the MBE-grown Gd<sub>2</sub>O<sub>3</sub> film on Si. An atomic-level smooth Gd<sub>2</sub>O<sub>3</sub> surface was characterized by AFM image (Figure A.7), which clearly shows a step-flow growth mode of Gd<sub>2</sub>O<sub>3</sub>. And the root-mean-square (RMS) value of the roughness is 0.44 nm for this 6.0nm-thick Gd<sub>2</sub>O<sub>3</sub> film.

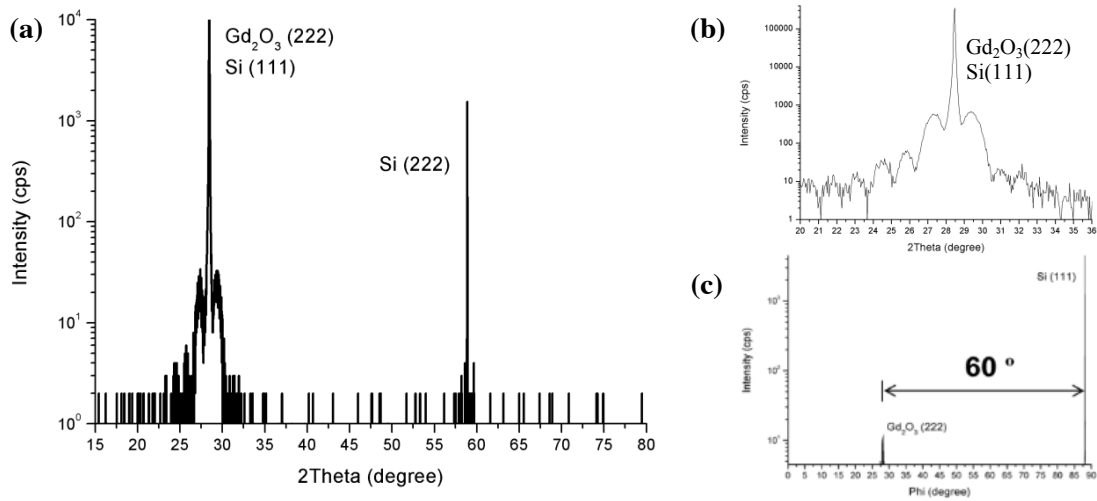


Figure A.6 - XRD characterization of  $Gd_2O_3/Si(111)$  substrate. (a) & (b) out-of-plane  $2\theta/\omega$  XRD; (c)  $\Phi$  scan XRD on  $Gd_2O_3(222)$  and  $Si(111)$  Bragg peaks.

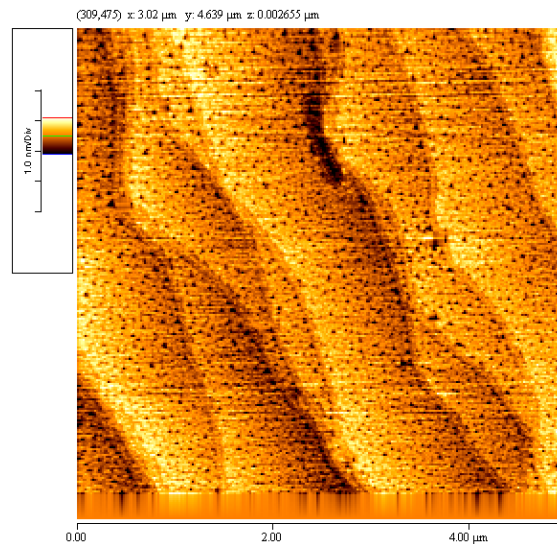


Figure A.7 -  $5 \times 5 \mu m^2$  AFM surface topography of the epitaxial  $Gd_2O_3$  film on  $Si(111)$  substrate.

#### A.4) Sol-gel deposition of PZT film on $Gd_2O_3/Si(111)$ substrate

PZT film was deposited on  $Gd_2O_3/Si(111)$  substrate by sol-gel method. The sol-gel process will be demonstrated in Section III.4.1. For one cycle of spin-coating, drying and calcination, the thickness of PZT film is about 70 nm. Out-of-plane  $2\theta/\omega$  XRD measured on PZT/ $Gd_2O_3/Si(111)$  is shown in Figure A.8. Except for the Bragg peaks of Si and  $Gd_2O_3$ , PZT film clearly shows a sharp (110) Bragg peak at  $31.27^\circ$ , which corresponds to the perovskite phase, and a diffused peak at around  $30^\circ$ , which corresponds to the pyrochlore phase (see Table A.3). The formation of the

## Appendix

pyrochlore phase likely results from the large lattice mismatch between PZT and  $\text{Gd}_2\text{O}_3$ . For the perovskite phase, PZT(110) crystalline orientation is the unique growing direction in the whole PZT film due to the fact that the lattice mismatch of PZT and  $\text{Gd}_2\text{O}_3$  along this direction is relatively small.

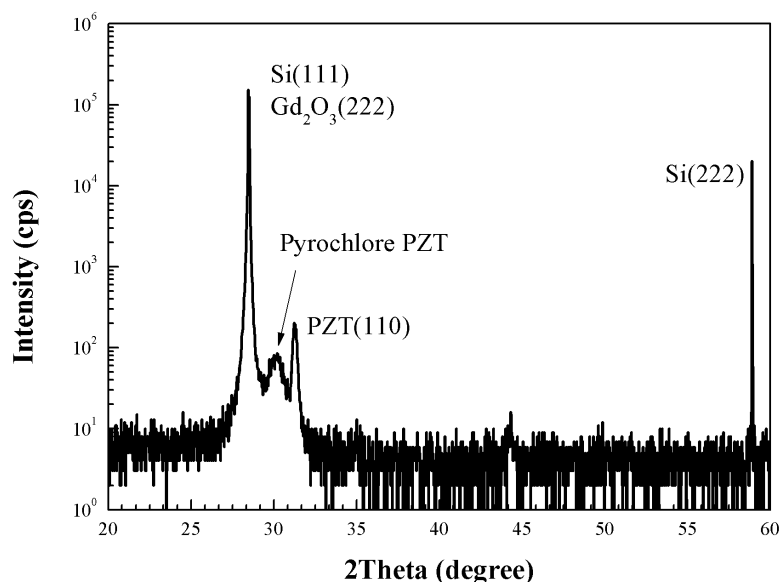


**Figure A.8 - Out-of-plane  $2\theta/\omega$  XRD on PZT/ $\text{Gd}_2\text{O}_3$ /Si(111) heterostructure.**

In Figure A.9, XRD pole figures exhibit more details on the crystalline structure of PZT/ $\text{Gd}_2\text{O}_3$ /Si(111) heterostructure. The measurement was carried out on PZT{110}, PZT{200}, and Si{111} Bragg peaks. Three Si{111} Bragg peaks around the central Si{111} Bragg peak at  $\chi = 70.53^\circ$  with 3-fold rotational symmetry confirm the single crystalline structure of the Si substrate. PZT{110} pole figure shows the Bragg peak only at the center of the image in agreement with the result of the out-of-plane  $2\theta/\omega$  XRD. Besides, PZT{200} pole figure exhibits a diffused distribution of the intensity at  $\chi = 56^\circ$ , indicating a textured structure of PZT in-plane crystalline orientation in the film. Therefore, both out-of-plane  $2\theta/\omega$  XRD and pole figures demonstrate a textured polycrystalline PZT film on  $\text{Gd}_2\text{O}_3$ /Si(111) substrate with (110) direction on the film surface.

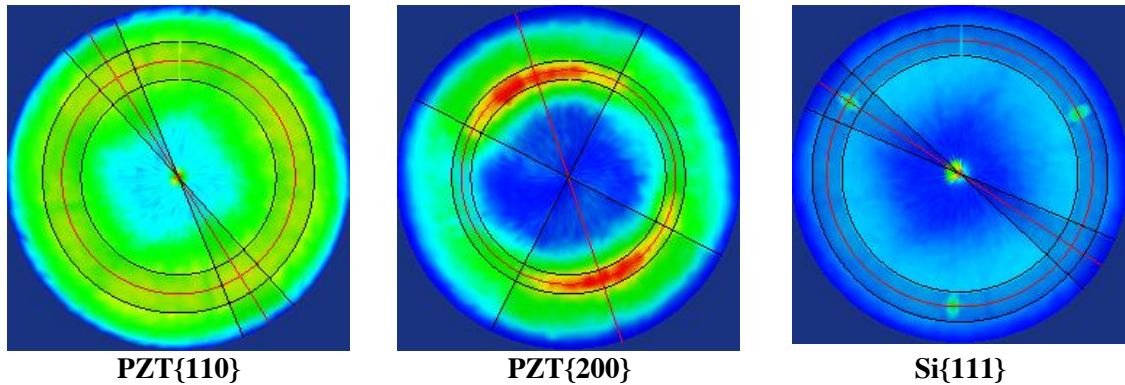


Figure A.9 - XRD pole figures of PZT/Gd<sub>2</sub>O<sub>3</sub>/Si(111) on PZT{110}, PZT{200}, and Si{111} Bragg peaks.

Dielectric permittivity and leakage current of the as-deposited PZT film on Gd<sub>2</sub>O<sub>3</sub>/Si(111) was measured based on a 100nm-thick Au/Ni top electrode. Si substrate was electrically contacted by silver paste as the bottom electrode. In Figure A.10, C-V measurement on the left image clearly shows a hysteresis loop of the dielectric permittivity as the function of dc bias voltage. Clockwise direction in the hysteresis loop is essentially different from that of ferroelectric properties, which mainly results from the charging effect in the MFIS (metal-ferroelectric-insulator-silicon). With decreasing the ac frequency, dielectric permittivity at negative dc bias gradually increases, similar to the electrical behavior of a p-n junction. Small dielectric permittivity (less than 8) implies that the most dc voltage drops on the ferroelectrically-inactive layer which has a small permittivity, like Gd<sub>2</sub>O<sub>3</sub> and SiO<sub>2</sub> layers. Therefore, other effects, like charging effect, are prevailing than ferroelectric effect, leading to an unexpected behavior in the C-V measurement. Furthermore, a weak leakage current density (less than 1  $\mu\text{A}/\text{cm}^2$ ) was measured through the PZT film (the right image in Figure A.10). And again, the direction of the hysteresis loop is clockwise due to the charging effect in the PZT film.

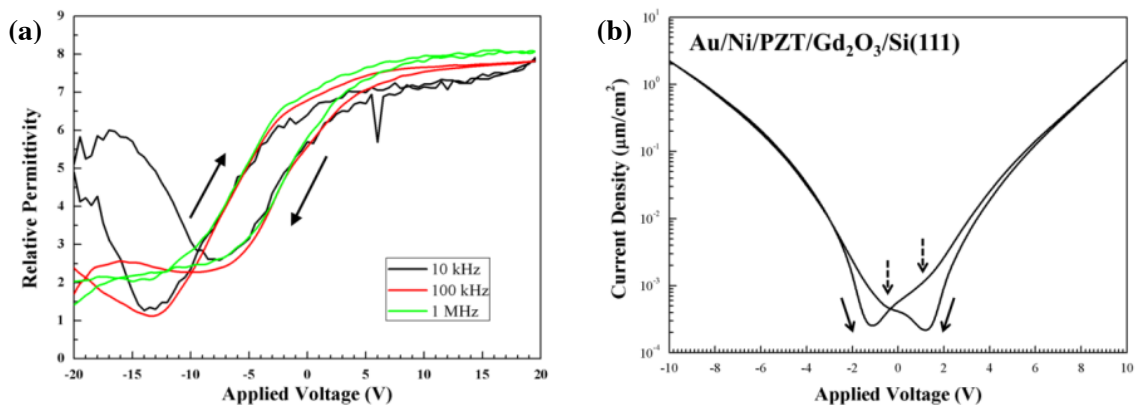


Figure A.10 - Electrical measurement on Au/Ni/PZT/Gd<sub>2</sub>O<sub>3</sub>/Si(111) capacitor: (a) dielectric permittivity vs. dc bias and (b) leakage current density vs. applied voltage.

### A.5) Conclusion

Gd<sub>2</sub>O<sub>3</sub> film deposited by e-beam evaporator in our oxide MBE system is well epitaxially grown on Si(111) substrate with single crystalline structure. However, due to the large lattice mismatch, PZT film grown on Gd<sub>2</sub>O<sub>3</sub>/Si(111) substrate consists of a large volume of unwanted pyrochlore phase in the matrix of perovskite phase. Moreover, large lattice mismatch promotes the formation of a textured perovskite structure in the PZT film instead of single crystalline structure. The non-ferroelectric pyrochlore phase definitely deteriorates the ferroelectric properties of the PZT film in the electrical measurement. Besides, the presence of ferroelectrically-inactive oxide layers, like Gd<sub>2</sub>O<sub>3</sub> and SiO<sub>2</sub>, in the heterostructure also prevents the measurement of the ferroelectric properties. As a result, a clockwise hysteresis loop is observed in the C-V measurement due to the prevailing charging effect in the PZT film.

### B) Finite Element Method

FEM analysis is a versatile numerical method that is widely used in the industry to find the approximate solution of a continuous model in various applications. The continuous model, derived from a real problem, often takes the form of a group of partial differential equations, which is insolvable in the case of a complex domain. The principal idea of the approximation by FEM is to discretize the large and continuous domain of a specific problem into a collection of small units, called "finite element", which can be simply and mathematically solved by analytic equation using finite number of the variables. The common used finite elements include tetrahedron (triangle) and hexahedron (quadrilateral), in which the former one suits an irregular domain and the latter one is usually used for a rectangular domain. This process is called "mesh discretization" which is schematically shown as follows in Figure A.11.

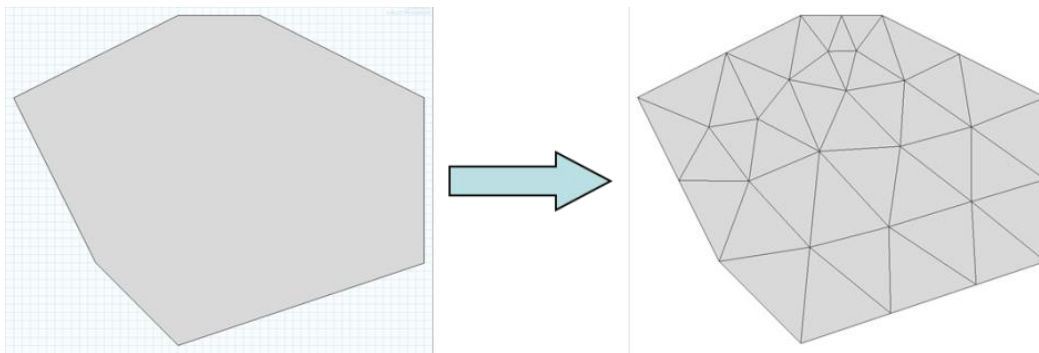
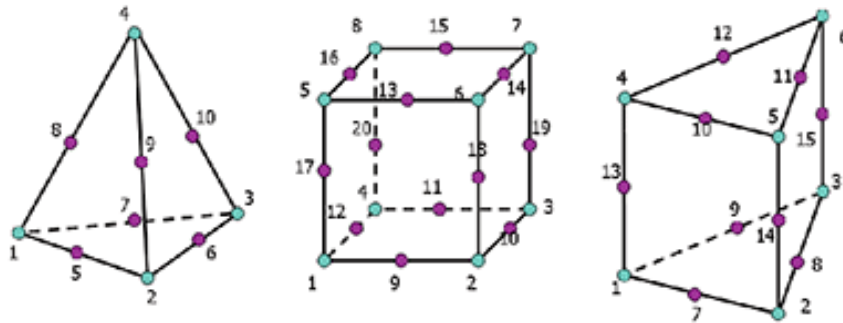


Figure A.11 - Mesh discretization using triangle within a 2-D domain.

## Appendix

The independent variables of an element are often chosen at the vertex or a point on the edge (usually the middle point) whose physical quantities can fully represent the state of this element through an analytic equation. Usually, this analytic equation can be represented by the *so-called* stiffness matrix, which is related to the element, and all the stiffness matrices of the elements in the domain can be assembled into a complete stiffness matrix of the entire domain. Figure A.12 shows several types of elements often used in FEM model and the related points usually chosen for their independent variables. For example, tetrahedron element usually has its points occupying four vertexes and six points on the middle of the edge, i.e. ten independent points.



**Figure A.12 - The nodes in several commonly used types of finite element which are chosen to represent the whole state of the element.**

With a given group of independent points of an element and a given physical model, the stiffness matrix of this element can be derived. For an example of mechanical model, the independent variable is often taken as the displacement of those points. The displacement of an arbitrary point in the element can be represented through following equation:

$$u^e = N^e(x, y, z) \cdot q^e \quad \text{Equ. A.2}$$

In the equation,  $q^e$  is the vector consisting of all the displacements of all the independent points for an element. The length of the vector equals to the freedom of this element.  $N^e(x, y, z)$  is called "shape function matrix". As the displacement of an arbitrary point in the element is known, other physical quantities of the element can be derived from  $u^e$ , like strain and stress:

$$\varepsilon^e = [\partial]u^e = [\partial]N^eq^e = B^eq^e \quad \text{Equ. A.3}$$

$$\sigma^e = D^e\varepsilon^e = D^eB^eq^e = S^eq^e \quad \text{Equ. A.4}$$

In the above equations, the strain ( $\varepsilon^e$ ) and the stress ( $\sigma^e$ ) of an arbitrary point in the element are respectively given by Equ. A.3 and A.4, where  $B^e$  is called the "geometric matrix",  $S^e$  is the "stress matrix", and  $D^e$  is the "elastic coefficient matrix". Therefore, we can calculate the total

## Appendix

---

elastic energy of the element based on the integration of the multiplication of the strain and the stress over all the space in this element.

$$\Pi^e = \frac{1}{2} \int_{\Omega^e} \sigma^e \varepsilon^e d\Omega - \left[ \int_{\Omega^e} \bar{b}^T u^e d\Omega + \int_{S_p^e} \bar{p}^T u^e dS \right] = \frac{1}{2} q^{eT} K^e q^e - P^{eT} q^e \quad \text{Equ. A.5}$$

In the above equation,  $K^e$  is the stiffness matrix of the element. Besides, the vectors of  $\mathbf{b}$  and  $\mathbf{p}$  are the external forces exerting on the volume and the surface of the element as the boundary condition, which are combined into  $\mathbf{P}^e$ . According to the principle of minimum potential energy in theory of elasticity, the above equation has minimal value at its solution. The solution can be worked out by differentiating both sides of the equation according to each independent variable, and then following equation is derived for the element:

$$K^e q^e = P^e \quad \text{Equ. A.6}$$

The above equation implies the linear relationship of the element between the displacement and the external force (boundary condition), which is represented by the stiffness matrix ( $K^e$ ). For the entire domain, the equation can be extended by considering all the elements in the domain where the stiffness matrixes of all the elements are assembled into one. Therefore, for stationary study the evaluation of the solution is actually a process to solve the above equation for the entire domain. After finding the solution, the displacements of each independent point of all the elements in the domain are known and, therefore, other physical quantities concerning the domain can be calculated by post-treatment. In addition, other study called "frequency domain analysis" is often used to study the mechanical response of a system under harmonic load. The evaluation process in this study is equivalent to finding the eigenvalues and the eigenvectors of the stiffness matrix of the domain.

In the following, the main steps in a typical FEM process are summarized:

1. Mesh discretization of the given domain by tetrahedron, hexahedron, or the other types of element.
2. Construction of the stiffness matrix for the finite element according to a specific problem.
3. Assemblage of all the stiffness matrices of the elements for the entire domain.
4. Vectorize the constraints, such as the load, the electrical potential, and eliminate the elements of the stiffness matrix according to the boundary condition.
5. Solve the equation by matrix operation and perform the post-treatment on the result.

Dependent variable is usually dependent on the specific physical model in the study, such as the displacement of the node in mechanical model. For piezoelectricity, the dependent

## Appendix

---

variables include the displacement and the voltage applying on the nodes of an element, which implies the consideration of two physical models, i.e. mechanical and electrical aspects. The interaction of these two physical models is defined by the so-called "coupling equations" of piezoelectricity:

$$\begin{aligned} S &= s^E \cdot T + d \cdot E \\ D &= d^t \cdot T + \varepsilon^T \cdot E \end{aligned} \quad \text{Equ. A.7}$$

where,  $S$  is the strain,  $s^E$  is the compliance under a constant electric field,  $T$  is the stress,  $E$  is the external electric field,  $D$  is the dielectric displacement,  $d$  is the piezoelectric coefficient, and  $\varepsilon^T$  is the dielectric constant under a constant strain. The free energy of piezoelectric model consists of both mechanical energy and electrical energy. Similar with mechanical model we discussed before, evaluation of the solution in piezoelectric model is also equivalent to solving Equ. A.6 except for that the equation takes the electrical energy into consideration.

### C) Reference

- 
- [1] H. D. B. Gottlob, T. Echtermeyer, T. Mollenhauer, J. K. Efavi, M. Schmidt, T. Wahlbrink, M. C. Lemme, H. Kurz, M. Czernohorsky, E. Bugiel, H.-J. Osten, and A. Fissel, "CMOS integration of epitaxial Gd<sub>2</sub>O<sub>3</sub> high-k gate dielectrics," *Solid-State Electronics*, **vol. 50**, no. 6, pp. 979–985, Jun. 2006.
- [2] J. Kwo, M. Hong, A. R. Kortan, K. L. Queeney, Y. J. Chabal, R. L. Opila, D. A. Muller, S. N. G. Chu, B. J. Sapjeta, T. S. Lay, J. P. Mannaerts, T. Boone, H. W. Krautter, J. J. Krajewski, A. M. Sergnt, and J. M. Rosamilia, "Properties of high-k gate dielectrics Gd<sub>2</sub>O<sub>3</sub> and Y<sub>2</sub>O<sub>3</sub> for Si," *Journal of Applied Physics*, **vol. 89**, no. 7, p. 3920, 2001.
- [3] ASTM Powder Diffraction Files, card number 12-0797.
- [4] M. Czernohorsky, E. Bugiel, H. J. Osten, A. Fissel, and O. Kirfel, "Impact of oxygen supply during growth on the electrical properties of crystalline Gd<sub>2</sub>O<sub>3</sub> thin films on Si(001)," *Applied Physics Letters*, **vol. 88**, no. 15, p. 152905, 2006.
- [5] M. Badylevich, S. Shamuilia, V. V. Afanas'ev, A. Stesmans, A. Laha, H. J. Osten, and A. Fissel, "Investigation of the electronic structure at interfaces of crystalline and amorphous Gd<sub>2</sub>O<sub>3</sub> thin layers with silicon substrates of different orientations," *Applied Physics Letters*, **vol. 90**, no. 25, p. 252101, 2007.

## Appendix

---

- [6] A. Laha, E. Bugiel, J. X. Wang, Q. Q. Sun, A. Fissel, and H. J. Osten, "Effect of domain boundaries on the electrical properties of crystalline  $\text{Gd}_2\text{O}_3$  thin films," *Applied Physics Letters*, **vol. 93**, no. 18, p. 182907, 2008.
- [7] J. Kwo, M. Hong, A. R. Kortan, K. T. Queeney, Y. J. Chabal, J. P. Mannaerts, T. Boone, J. J. Krajewski, A. M. Sergent, and J. M. Rosamilia, "High  $\epsilon$  gate dielectrics  $\text{Gd}_2\text{O}_3$  and  $\text{Y}_2\text{O}_3$  for silicon," *Applied Physics Letters*, **vol. 77**, no. 1, p. 130, 2000.
- [8] J. Kwo, M. Hong, A. R. Kortan, K. L. Queeney, Y. J. Chabal, R. L. Opila, D. A. Muller, S. N. G. Chu, B. J. Sapjeta, T. S. Lay, J. P. Mannaerts, T. Boone, H. W. Krautter, J. J. Krajewski, A. M. Sergnt, and J. M. Rosamilia, "Properties of high  $\kappa$  gate dielectrics  $\text{Gd}_2\text{O}_3$  and  $\text{Y}_2\text{O}_3$  for Si," *Journal of Applied Physics*, **vol. 89**, no. 7, p. 3920, 2001.
- [9] H. Kroemer, in *Heteroepitaxy on Si*, MRS Symposia Proceedings No. 67, edited by J. C. C. Fan and J. M. Poate (Materials Research Society, Pittsburgh, PA, 1986), and references therein.
- [10] J. X. Wang, A. Laha, A. Fissel, D. Schwendt, R. Dargis, T. Watahiki, R. Shayduk, W. Braun, T. M. Liu, and H. J. Osten, "Crystal structure and strain state of molecular beam epitaxial grown  $\text{Gd}_2\text{O}_3$  on Si(111) substrates: a diffraction study," *Semiconductor Science and Technology*, **vol. 24**, no. 4, p. 045021, Apr. 2009.
- [11] B. H. Lin, W. R. Liu, S. Yang, C. C. Kuo, C.-H. Hsu, W. F. Hsieh, W. C. Lee, Y. J. Lee, M. Hong, and J. Kwo, "The Growth of an Epitaxial ZnO Film on Si(111) with a  $\text{Gd}_2\text{O}_3$  ( $\text{Ga}_2\text{O}_3$ ) Buffer Layer," *Crystal Growth & Design*, **vol. 11**, no. 7, pp. 2846–2851, Jul. 2011.
- [12] B.-E. Park, S. Shouriki, E. Tokumitsu, and H. Ishiwara, "Fabrication of  $\text{Pb}(\text{Zr}_x\text{Ti}_{1-x})\text{O}_3$  Films on Si Structures Using  $\text{Y}_2\text{O}_3$  Buffer Layers," *Japanese Journal of Applied Physics*, **vol. 37**, no. Part 1, No. 9B, pp. 5145–5149, Sep. 1998.
- [13] B.-E. Park, I. Sakai, E. Tokumitsu, and H. Ishiwara, "Hysteresis characteristics of vacuum-evaporated ferroelectric  $\text{PbZr}_{0.4}\text{Ti}_{0.6}\text{O}_3$  films on Si(111) substrates using  $\text{CeO}_2$  buffer layers," *Applied Surface Science*, **vol. 117–118**, pp. 423–428, Jun. 1997.
- [14] D. Akai, M. Yokawa, K. Hirabayashi, K. Matsushita, K. Sawada, and M. Ishida, "Ferroelectric properties of sol-gel delivered epitaxial  $\text{Pb}(\text{Zr}_x\text{Ti}_{1-x})\text{O}_3$  thin films on Si using epitaxial  $\gamma\text{-Al}_2\text{O}_3$  Layers," *Applied Physics Letters*, **vol. 86**, no. 20, p. 202906, 2005.
- [15] T. D. Lin, M. C. Hang, C. H. Hsu, J. Kwo, and M. Hong, "MBE grown high-quality  $\text{Gd}_2\text{O}_3/\text{Si}(111)$  hetero-structure," *Journal of Crystal Growth*, **vol. 301–302**, pp. 386–389, Apr. 2007.

## Appendix

---

- [16] G. Niu, B. Vilquin, N. Baboux, C. Plossu, L. Becerra, G. Saint-Grions, and G. Hollinger, "Growth temperature dependence of epitaxial  $\text{Gd}_2\text{O}_3$  films on Si(111)," *Microelectronic Engineering*, **vol. 86**, no. 7–9, pp. 1700–1702, Jul. 2009.
- [17] T. Engel, "The interaction of molecular and atomic oxygen with Si(100) and Si(111)," *Surface Science Reports*, **vol. 18**, no. 4, pp. 93–144, Jan. 1993.
- [18] K. Takayanagi, Y. Tanishiro, S. Takahashi, and M. Takahashi, "Structure analysis of Si(111)- $7\times 7$  reconstructed surface by transmission electron diffraction," *Surface Science*, **vol. 164**, no. 2–3, pp. 367–392, Dec. 1985.
- [19] G. Niu, B. Vilquin, N. Baboux, C. Plossu, L. Becerra, G. Saint-Grions, and G. Hollinger, "Growth temperature dependence of epitaxial  $\text{Gd}_2\text{O}_3$  films on Si(111)," *Microelectronic Engineering*, **vol. 86**, no. 7–9, pp. 1700–1702, Jul. 2009.
- [20] T. D. Lin, M. C. Hang, C. H. Hsu, J. Kwo, and M. Hong, "MBE grown high-quality  $\text{Gd}_2\text{O}_3/\text{Si}(111)$  heterostructure," *Journal of Crystal Growth*, **vol. 301–302**, pp. 386–389, Apr. 2007.

*Appendix*

---

---

## **Integration of epitaxial piezoelectric thin films on silicon**

### *Abstract*

Recently, piezoelectric materials, like lead titanate zirconate  $\text{Pb}(\text{Zr}_x\text{Ti}_{1-x})\text{O}_3$  (PZT), zinc oxide ZnO, and the solid solution  $\text{Pb}(\text{Mg}_{1/3}\text{Nb}_{2/3})\text{O}_3\text{-PbTiO}_3$  (PMN-PT), increasingly receive intensive studies because of their innovative applications in the micro-electromechanical systems (MEMS). In order to integrate them on silicon substrate, several preliminaries must be taken into considerations, e.g. buffer layer, bottom electrode. In this thesis, piezoelectric films (PZT and PMN-PT) have been successfully epitaxially grown on silicon and SOI (silicon-on-insulator) in the form of single crystal by sol-gel process. In fact, recent studies show that single crystalline films seem to possess the superior properties than that of polycrystalline films, leading to an increase of the performance of MEMS devices.

The first objective of this thesis was to realize the epitaxial growth of single crystalline film of piezoelectric materials on silicon. The use of a buffer layer of gadolinium oxide ( $\text{Gd}_2\text{O}_3$ ) or strontium titanate ( $\text{SrTiO}_3$  or STO) deposited by molecular beam epitaxy (MBE) has been studied in detail to integrate epitaxial PZT and PMN-PT films on silicon. For  $\text{Gd}_2\text{O}_3/\text{Si}(111)$  system, the study of X-ray diffraction (XRD) on the growth of PZT film shows that the film is polycrystalline with coexistence of the non-ferroelectric parasite phase, i.e. pyrochlore phase. On the other hand, the PZT film deposited on STO/Si(001) substrate is successfully epitaxially grown in the form of single crystalline film. In order to measure the electrical properties, a layer of strontium ruthenate ( $\text{SrRuO}_3$  or SRO) deposited by pulsed laser deposition (PLD) has been employed for bottom electrode due to its excellent conductivity and perovskite crystalline structure similar to that of PZT. The electrical characterization on Ru/PZT/SRO capacitors demonstrates good ferroelectric properties with the presence of hysteresis loop. Besides, the relaxor ferroelectric PMN-PT has been also epitaxially grown on STO/Si and confirmed by XRD and transmission electrical microscopy (TEM). This single crystalline film has the perovskite phase without the appearance of pyrochlore. Moreover, the study of infrared transmission using synchrotron radiation has proven a diffused phase transition over a large range of temperature, indicating a typical relaxor ferroelectric material.

The other interesting in the single crystalline PZT films deposited on silicon and SOI is to employ them in the application of MEMS devices, where the standard silicon techniques are used. The microfabrication process performed in the cleanroom has permitted to realize cantilevers and membranes in order to mechanically characterize the piezoelectric layers. Mechanical deflection under the application of an electric voltage could be detected by interferometry. Eventually, this characterization by interferometry has been studied using the modeling based on finite element method and analytic method.

In the future, it will be necessary to optimize the microfabrication process of MEMS devices based on single crystalline piezoelectric films in order to ameliorate the electromechanical performance. Finally, the characterizations at MEMS device level must be developed for their utilization in the future applications.

### *Key words*

Micro-electromechanical system (MEMS); PZT; PMN-PT; STO; SRO; Gadolinium oxide; Heteroepitaxy; Functional oxides; Single crystalline oxides; Piezoelectric materials; Molecular beam epitaxy (MBE); Pulsed laser deposition (PLD); Sol-gel process; Micro-structuration; X-ray diffraction (XRD); Electrical measurement; Transmission electron microscopy (TEM); Atomic force microscopy (AFM);

# Intégration de film mince piézoélectrique épitaxiale sur silicium

## Résumé

Les matériaux piézoélectriques, comme le titanate-zirconate de plomb  $Pb(Zr_xTi_{1-x})O_3$  (PZT), l'oxyde de zinc ZnO, ainsi que la solution solide de  $Pb(Mg_{1/3}Nb_{2/3})O_3$ - $PbTiO_3$  (PMN-PT), sont actuellement l'objet d'études de plus en plus nombreuses à cause de leurs applications innovantes dans les systèmes micro-électromécaniques (MEMS). Afin de les intégrer sur substrat de silicium, certaines précautions doivent être prises en compte concernant par exemple des couches tampon, les électrodes inférieures. Dans cette thèse, des films piézoélectriques (PZT et PMN-PT) ont été épitaxiés avec succès sous forme de monocristaux sur silicium et SOI (silicon-on-insulator) par procédé sol-gel. En effet, des études récentes ont montré que les films piézoélectriques monocristallins semblent posséder des propriétés supérieures à celles des films polycristallins, permettant ainsi une augmentation de la performance des dispositifs MEMS.

Le premier objectif de cette thèse était de réaliser l'épitaxie de film monocristallin de matériaux piézoélectriques sur silicium. L'utilisation d'une couche tampon d'oxyde de gadolinium ( $Gd_2O_3$ ) ou de titanate de strontium ( $SrTiO_3$  ou STO) déposés par la technique d'épitaxie par jets moléculaires (EJM) a été explorée en détail pour favoriser l'épitaxie du PZT et PMN-PT sur silicium. Sur le système  $Gd_2O_3/Si(111)$ , l'étude par diffraction des rayons X (XRD) de la croissance du film PZT montre que le film est poly-phasé avec la présence de la phase parasite pyrochlore non ferroélectrique. Cependant, le film PZT déposé sur le système STO/Si(001) est parfaitement épitaxié sous forme d'un film monocristallin. Afin de mesurer ses propriétés électriques, une couche de ruthenate de strontium conducteur  $SrRuO_3$  (SRO) déposée par ablation laser pulsé (PLD) a été utilisée comme l'électrode inférieure à cause de son excellente conductibilité et de sa structure cristalline pérovskite similaire à celle du PZT. Les caractérisations électriques sur des condensateurs Ru/PZT/SRO démontrent de très bonnes propriétés ferroélectriques avec présence de cycles d'hystérésis. Par ailleurs, le matériau relaxeur PMN-PT a aussi été épitaxié sur STO/Si comme l'a confirmé la diffraction des rayons X ainsi que la microscopie électronique en transmission (TEM). Ce film monocristallin est de la phase de pérovskite sans présence de pyrochlore. En outre, une étude en transmission du rayonnement infrarouge au synchrotron a prouvé une transition de phase diffuse sur une large gamme de température, comme attendue dans le cas d'un relaxeur.

L'autre intérêt d'avoir des films PZT monocristallins déposés sur silicium et SOI est de pouvoir utiliser les méthodes de structuration du silicium bien standardisées maintenant pour fabriquer les dispositifs MEMS. La mise au point d'un procédé de micro-structuration en salle blanche a permis de réaliser des cantilevers et des membranes afin de caractériser mécaniquement les couches piézoélectriques. Des déplacements par l'application d'une tension électrique ont ainsi pu être détectés par interférométrie. Finalement, cette caractérisation par interférométrie a été combinée avec une modélisation basée sur la méthode des éléments finis.

Dans le futur, il sera nécessaire d'optimiser le procédé de microfabrication du dispositif MEMS afin d'en améliorer les performances électromécaniques. Enfin, des caractérisations au niveau du dispositif MEMS lui-même devront être développées en vue de leur utilisation dans de futures applications.

## Mot clés

Microsystème électromécanique (MEMS ou MST); PZT; PMN-PT; STO; SRO; Gadolinium oxyde; Hétéroépitaxie; Oxydes fonctionnels; Oxydes monocristallins; Matériaux piézoélectriques; Epitaxie par jets moléculaires (EJM); Ablation laser pulsé (PLD); Procédé sol-gel; Micro-structuration; Diffraction des rayons X (XRD); Mesures électriques; Microscopie électronique en transmission (TEM); Microscope à force atomique (AFM);